Investigation of steady and unsteady flow in annular vaneless diffusers.

Abir, Arie

Award date:
1983

Awarding institution:
University of Bath

INVESTIGATION OF STEADY AND UNSTEADY FLOW IN ANNULAR VANELESS DIFFUSERS.

Submitted by

ARIE ABIR

for degree of PhD of University

of Bath 1983.

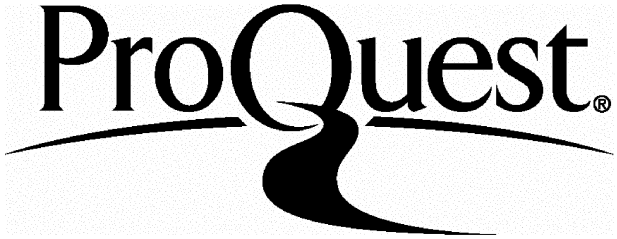

TO SHALVA, ROY AND JOHNATAN

THE IMPORTANT "ELEMENTS" OF MY LIFE

WITH LOVE.

ACKNOWLEDGEMENTS

My thanks are due to the follow:
to Dr A. Whitfield for his thorough and helpful supervision and advice during the performing of this work and espically in the writting up of this thesis.
I am also indebted to Prof. F.J. Wallace for his general and stimulating interest in the work.
Acknowledgement is also due to the staff of the School of Engineering workshop and laboratories, University of BATH, and to Mr. A. Coggins and Mr. N. HAMLIN for valuable assistance in the laboratory.
To BNAI-BRITH for their financial support for the writting up of this thesis.

Finally, I wish to express my gratitude to my wife Shalva and childern Roy and Jhonatan for their love, patience, and understanding.

SUMMARY

Three types of annular diffusers associated with radial and mixed flow turbocharger compressors have been studied both experimentally and theoretically. The investigations have been carried out on model diffusers six times larger than the normal turbocharger in order to enable detailed flow traverse measurements to be carried out. These measurements have been obtained using both a five hole yaw probe and a hot wire anemometer in order to observe the development of the flow profiles throughout the diffuser with particular reference to flow stability. To measure the onset and development of unstable flow flush mounted wall pressure transducers were employed.

Radial, curved annuler and straight annuler diffusers have been tested in order to study their relative merits. Two curved diffusers, which are used with mixed flow compressor impellers, have been studied. It has generally been observed that the straight annular diffuser was the least stable, with the radial diffuser having the best stability characteristics. For mixed flow compressor designs, therefore, the curved annular diffuser, which turns the flow from the conical to radial

direction, is to be prefered.

The theoretical analysis employed the finite element method to solve the basic Navier-Stokes equations using a stream function-vorticity formulation, with the common two equation, k-ϵ turbulence model. In order to obtain solutions at high Reynolds numbers a dynamic mesh system was used which solved for the required properties at the centre node only using the variational method. The mesh was then regenerated so that each non-boundary node become a centre node in turn.

The theoretical analysis has been used to study the effect of inlet velocity profiles upon the stability of the diffuser. The analysis indicated the type of velocity profiles which should be avoided if possible.

CONTENTS

NOMENCLATURE

A^+ - Van Driet damping constant

A - Area

C - Logarithmic law constant,convective term

$C\mu$ - Eddy viscosity factor

D - Diffusion term, Domain area

E - Hot-wire anemometer output

E_0 - Hot-wire output in zero velocity

e - Hot-wire r.m.s output

F - Flow forces

H - Global stiffnes matrix

h - Element stiffnes matrix

I - Integral

J - Jacobian matrix

k - Turbulent kinetic energy

k_1 - Hot-wire yaw coefficient

k_2 - Hot-wire pitch coefficient

L - Element lenght vector

l - Diffuser width

l - Mixing lenght

l_D - Mixing lenght

l_z - Normal vector in the r direction

l_z - Normal vector in the z direction

M - Weight function

m - Mass flow rate

N - Element shape function

n - Normal distance to the surface, normal direction

P - Pressure

R - Hot-wire resistence

R_c - Hot-wire cold resistence

R - Residual

Re - Reynolds number

r - Radius

S - Source term, contour

T - Temperture

T - Time

U - Mean velocity

U_τ - Friction velocity

y - Distance normal to the surface

y^+ - A Reynolds number = $yU_\tau\rho/\mu$

α - Element angle

α_h - Overheat ratio

α_r - Relaxation factor

β - Element angle, yaw angle

γ - Upwind factor

δ - Boundary layer thickness, Kronecker delta

ϵ - Turbulence kinetic energy dissipation rate

μ - Kinematic viscosity

μ_t - Turbulent viscosity

μ_{eff}- Eddy viscosity

θ - Pitch angle

κ - Logarithmic law constant

ρ - specific mass

Ψ - Stream function

ω - Vorticity

τ - Shear stress

σ - Turbulent Prandtl/Schmidt number

Subscripts

r,z,θ -direction

m - Meridonal direction

i,j - Tensor subscripts

w - wall

Superscripts

- -Mean value

0 - Intial value

' -Instantaneous value

CHAPTER 1

INTRODUCTION AND LITERATURE SURVEY

1.1 INTRODUCTION

In many turbomachines such as turbines, pumps, and compressors the flow inside the diffuser has considerable effect upon the efficiency of the machine.

The aim of a diffuser is to convert kinetic energy to pressure by reducing the absolute velocity; this is usually accomplished by increasing the cross sectional area. This aim is difficult to achieve efficiently and is regarded as one of the central problems of turbomachinery design. The difficulty arises from the fact that in an adverse pressure gradient the boundary layer on the wall grows rapidly and in some cases leads to the development of a separation area and large losses in stagnation pressure. Separation can also lead to unstable flow and rotating stall inside the diffuser which can then affect the stability of the whole system. For the annular diffusers studied here the flow has a high degree of swirl, and it is the reduction of the swirl component of velocity which is most significant in

the diffusion process. This is usually accomplished, in the absence of vaned diffusers, by increasing radius. For radial flow centrifugal compressors the radial vaneless diffuser is usually employed. For mixed flow compressors a choice lies between the use of straight and curved annular diffusers, see fig. 1.1. ATKEY(1975) used a number of curved annular diffusers with his mixed flow impeller designs but did not test any straight conical diffusers, believing them to be less stable. The flow stability in the vaneless diffusers of centrifugal and mixed flow compressors is a significant parameter in the development of compressor surge and the overall stable operating range of the compressor.

In this work the three diffusers of fig. 1.1 have been studied. The experimental investigation has been carried out on a six times full size model of the turbochargers used by ATKEY(1975) so that internal flow measurements with hot-wire anemometers and a five hole yaw probe could be readily made.

A theoretical analysis using the finite element method, has been developed to predict the development of the internal flow with the aim to identify the situations which lead most readily to separation and unstable flow conditions.

1.2 LITERATURE SURVEY ON EXPERIMENTAL STUDIES

Experimental diffuser studies have been carried out by many investigators for a variety of diffuser geometries and applications. Excellent surveys of experimental work on different types of diffusers were presented by COCKRALL and MARKLAND(1963) and by EL-GERESY(1982).
This survey is confined to flow in radial and mixed flow diffusers, as shown in fig. 1.1 and refers only to reports which are directly concerned with the subject of this thesis.

1.2.1 Steady flow investigations.

Early work to study the geometric effects of vaneless diffusers was presented by BARINA(1947) who compared the performance of conical and curved diffusers, which gave similar performance. SAKAI et al(1978) examined the relationship between inlet and internal flow patterns in pure conical mixed flow diffuser to find the optimum configuration which would enable a stable and effective flow to be established. He compared the pressure recovery to that obtained with a curved diffuser and found that it was not as good but the difference was small. EL-GERESY(1982) also compared curved and conical

annular diffusers and showed that it was clear that the curved diffuser was superior to the conical diffuser in both performance and stability. HONAMI et al(1971) studied the flow behavior and relation between the flow patterns and the diffuser losses in a conical diffuser. They found that the boundary layer on the inner wall become more complex as the main flow shifted towards the outer wall due to the wall curvature, and also as the flow yielded to a pressure gradient normal to the diffuser wall. WHITFIELD et al(1979) investigated and compared the preformance of a curved diffuser to a curved diffuser with contraction. They found that the diffuser with intial contraction gave better efficiency at optimum operating condition than the constant width diffuser. That conclusion was supported theoretically by an inviscid analysis developed by WALLACE et al(1975), and experimentally by testing six times full size models of the above mentioned curved diffusers, BARBOTIN(1977).

The simple geometry of the vaneless radial diffuser allowed studies of the flow mechanism from many aspects such as boundary layer development, pressure recovery, and the effect of inlet conditions.

Experimental studies of the three dimensional boundary layer in vaneless diffusers were carried out by

GARDOW(1958), JANSEN(1964) and MATES(1963) in an attempt to resolve the flow phenomena in vaneless diffusers. The separation problem which leads to high losses was the main concern of many researchers e.g. BROWN(1947), ELLIS(1964), JOHNSTON(1966). BROWN studied the effect of friction coefficients on the flow in the diffuser and found that it was necessary to vary the friction factor with the radius. He found that the highest value of friction loss occurred at the inlet. For this reason BROWN and BRADSHAW(1947) suggested that the diffuser should incorporate a short inlet section tapering to a throat which would convert the non-uniform flow profile at inlet into a uniform steady flow. WATSON et al(1971) investigated this suggestion by using convergent-divergent and convergent parallel vaneless radial diffusers. They showed that these configurations gave similar pressure recovery coefficients and that they generated more uniform velocity profiles at outlet compared to the parallel diffusers. By a theoretical investigation VOLOV and SHAKHOV(1978) came to the same conclusion, that a convergent walled diffuser would give better preformance than a parallel one.

The effect of the inlet conditions was studied by ELLIS(1964) who presented the total pressure in terms of

vorticity and showed that the amount of vorticity generated varied with the mass flow rate through the diffuser. Increasing the vorticity led to separation downstream. He also showed that the shear stress near to the wall had a negligible effect on the flow compared to that of the vorticity. This phenomenon of the total pressure gradient at inlet was investigated both theoretically and experimentally by REBERNIK(1972). He showed that a gradient in the total pressure would create a separation area downstream.

JOHNSTON and DEAN(1966) developed a method to predict losses in vaneless diffusers and compared their results to the DEAN-SENOO(1960) model, and to experimental data. They showed that their model could replaced the more complex SENOO model and still provide good agreement with the experimental results.

1.2.2 Rotating stall and unstable flow investigations.

Reduction of the mass flow rate through a centrifugal compressor system leads, at a critical value, to a highly unstable flow known as system surge. This unstable flow can be distinguished by two types of self-excited oscillations, a rotating stall in the impeller or

diffuser. It is generally assumed that rotating stall can lead to surge in the compression system.

SANDBORN and KLINE(1961) reviewed previous work in order to obtain a definition for stall and separation in turbulent flow. They showed that the flow separation leading to stall in turbulent flow cases is usually preceded by local intermittent separation involving three dimensional streaks of backflow near the wall.

One of the earliest works concerning rotating stall in annular vaneless diffusers was reported by JANSEN(1964b). He carried out a theoretical and experimental investigation into this phenomenon and linked the occurrence of the oscillations to the existence of a radially inward flow within the skewed boundary layer on the hub or shroud surfaces. He suggested a theoretical inviscid, incompressible model with the assumption that the disturbances could be expressed in terms of periodic waves. The approximate solution gave the rotational speed and number of rotating stall cells, and the unsteady velocity distribution. Fig. 1.2 shows the perturbed path of a fluid partical for different numbers of flow cells. JANSEN showed good agreement between theoretically predicted wave speed and experimental values when the disturbance was two lobed and generally

related the rotating stall to separation area along the diffuser side walls.

IMAICHI et al(1979) used rotating screens to generate the swirl velocity in an annular vaneless diffuser and compared his experimental results to JANSEN's theoretical results. He found that the theoretical results did not agree well with his experimental results for pressure fluctuations. In his experimental work IMAICHI came to the conclusion that the rotating stall occurs automatically when a back flow occupies some radial extent (dependent upon the diffuser geometry) on the diffuser wall and is proportional to the flow resistance at diffuser exit.

ABDELHAMID(1980b) also suggested an analytical solution using the linearized equations of motion for unsteady flow. solutions of the differential equations were made to satisfy boundary conditions at diffuser inlet and exit. He concluded from the theoretical results that the generation of self-excited oscillations in vaneless diffusers is dependent on the coupling between the impeller and diffuser. He further showed that the stability limits of diffuser are strongly dependent upon the difuser radius ratio if the conditions at the diffuser inlet are such that low speed rotating stall patterns are generated. He supported his theoretical

studies with experimental investigations to determine the effect of vaneless diffuser radius ratio on the occurrence of self- excited flow oscillations in a compression system (see ABDELHAMID(1980a,1981)). He found that complete system flow stability does not necessarily follow from a condition of reversed flow in the diffuser. In order to control and supress the onset of rotating stall he tested radial diffusers with a throttlring at discharge, see reference ABDELHAMID (1982).

SENOO and KINOSHITA(1978) specified a criterion for the onset of rotating stall in a vaneless diffuser based on SENOO's earlier work (SENOO et al(1977a)). This criterion was based upon the geometrical parameter exit/inlet radius ratio and diffuser width ratio. Fig. 1.3 shows these parameters as a function of the inlet flow angles which created a reverse flow zone and led to a rotating stall.

LIGRANI et al(1982) verfied experimentally the effect of inlet conditions and especially the flow angle on the onset of rotating stall in vaneless diffusers. His results showed how flow behavior varied in stable, rotating stall and surge regimes of compressors operation. He measured the critical flow angle at the

onset of rotating stall confirming the importance of diffuser inlet width and diffuser inlet flow angle on the onset of rotating stall in vaneless diffuser.

These rotating stall and flow instability studies have concentrated upon radial vaneless diffusers and no investigations have been concerned with the mixed flow type of diffuser.

1.3 THEORETICAL SOLUTION FOR FLOW IN VANELESS DIFFUSERS

Theoretical attemps to predict two and three dimensional flow in diffusers has been made by many investigators, JANSEN(1964a), ELLIS(1964), REBERNIK(1972), WALLACE(1975).

Three main numerical techniques have been used, a) The streamline curvature method (WALLACE et al(1975)). b) The finite difference method, REBERNIK(1972). c) The finite element method HIRSCH and WARZEE (1975), KIRMEREMAN and ADLER(1975) both of whom developed the method especially for rotating machines (impeller) but could be modified for application to vaneless diffusers. A comparison between the different methods for turbomachinery was given by DAVIS(1975), JAPIKSE(1976), ADLER(1982).

In recent years with the development of the finite element method many investigators have used this approach for fluid flow problems. HIRSCH et al(1975, 1978) used the Galerkin approach for axial turbomachines and KRIMERMAN (1975) used the Variational approach to obtain a finite element solution for three dimensional inviscid flow based upon the models of WU(1952) for radial turbomachines. In both cases a stream function formulation was used and good agreement with experimental results was shown.
PFOERNER et al(1977) used the velocity-pressure model with the Galerkin method to predict the inviscid flow in diffusers, whilst a three dimensional potential flow was presented by LASKARIS(1978) and by METU(1982).

The main concern of many theoretical studies was to predict the separation area in vaneless diffusers. this had been done by REBERNIK(1972) who studied the effect of inlet total pressure gradient on the separation area and ELLIS(1963) who represented the total pressure in terms of vorticity. EL-GERESY(1982) modified the streamline curvature method of WALLACE(1975) to a direct analytical solution by assuming a linear variation of all variables between hub and shroud. Although EL-GERESY showed good agreement to other methods for radial

vaneless diffusers, the error in the predicted solution increases for cases with curved surfaces. All theoretical methods assumed inviscid flow and were incapable of predicting a truly separation flow.

To obtain a solution close to real flow conditions JOHNSTON and DEAN(1966), BARBOTIN(1977) and BAMMERT et al(1978) included the effect of internal friction in the inviscid analysis of the flow. Although good prediction of the flow was obtained no correlation could be obtained between the friction coefficient and the flow conditions. The friction coefficient had to be found independently for each case. The failure of the inviscid model to predict the flow in diffusers with complicated shapes or to deal with separation encouraged the use of the viscous solution. These solutions have been based upon

a) Boundary layer techniques.

b) Solution of the Navier-Stokes equations.

1.3.1 Boundary layer techniques.

Boundary layer techniques have been extensively used for prediciting the flow in diffusers e.g. MAGER(1952), NASH and PATEL(1972), DAVIS(1976). VOORDE and BOS(1972) predicted the flow in radial vaneless diffusers but for the case of non-swirling flow only. Their solution was

for a two dimensional flow and used Cole's velocity profiles in the boundary layer. The theoretical solution agreed well with their experimental results. ANTONIA (1968), KAWAGUCHI and FURUYA(1966) gave a full interactive solution between the main flow and the boundary layer. They assumed that the swirl flow had a weak effect upon the shear stress, although ANTONIA mentioned that this assumption could be justified for small values of flow angle only. The predicted velocity distribution remained invariant with respect to the radial direction, and was symmetrical across the diffuser.

JANSEN(1964b) suggested a model which could handle high swirl flows by imposing the "power law" for velocity components in the radial and tangential directions. Although JANSEN's theoretical results agreed well with his experimental results DEAN criticized his work because the radial momentum equation was not satisfied by the analysis, and for assuming that the tangential and radial boundary layers had equal displacement thicknesses.
SENOO et al(1977b) evaluated the flow behavior in vaneless diffusers in which the flow was not symmetric between the walls. The "power law" was used to describe the velocity components in both radial and tangential

directions. The solution satisfied the energy and conservation of angular momentum equations for the main flow. SENOO's method succeeded in predicting the flow inside the diffuser but failed for cases of high swirl flow and when the boundary layers megred.

MICHEL(1972) used a three dimensional model based on COLE's model of velocity to predict the flow in vaneless diffusers, and showed good agreement between the predicted and experimental results of the velocity components and boundary layer thicknesses.

The effect of radius of curvature upon boundary layer development was reviewed by BRADSHAW(1973), it was found that the effect is less important on the outer wall of annular diffuser. PEARSON and HILL(1973) studied the effect of curvature on two dimensional diffuser flows and suggested the use of the Richardson number to take into account curvature.

1.3.2 Solution of the Navier-Stokes equations

The development of new numerical methods in recent years has led to attempts to solve the full Navier-Stokes equations in order to predict the flow in different configurations.

The solution of The Navier-Stokes equations, including turbulence models, was used recently in many problems (see GOLDSTEIN(1965), GOSMAN et al(1968) and TAYLOR(1981)), little application has been made to solve the equations for predicting the flow in diffuser.

Many investigators simplified the differential equations by assuming constant viscosity, this allowed them to ignore all the non-linear terms in the equations. this method was used by CRANE et al(1974a,b) to study the effect of different swirl flows in annular diffusers, and the conditions which lead to separation inside the diffuser. DODGE(1977) presented a solution to the Navier-Stokes equations by separating the momentum and continuity equations into coupled elliptic and parabolic groups.
A three dimensional solution was given by SHEORAN(1982) which used the vorticity-stream function approach and the finite difference technique.

A further step was taken by PATANKAR and SPALDING(1972) who initiated three dimensional viscous flow calculations in ducts using a parabolized system of flow equations. MOORE(1979) gave a three dimensional turbulent flow solution in ducts using the two equation turbulence model. FISTER et al(1982) calculated the three

dimensional turbulent viscous flow in vaneless return channels of multi-stage radial flow turbomachines by the finite different technique.

More details with respect to the application of the finite element method to the solution of the Navier-Stokes equations will be given in the next chapter.

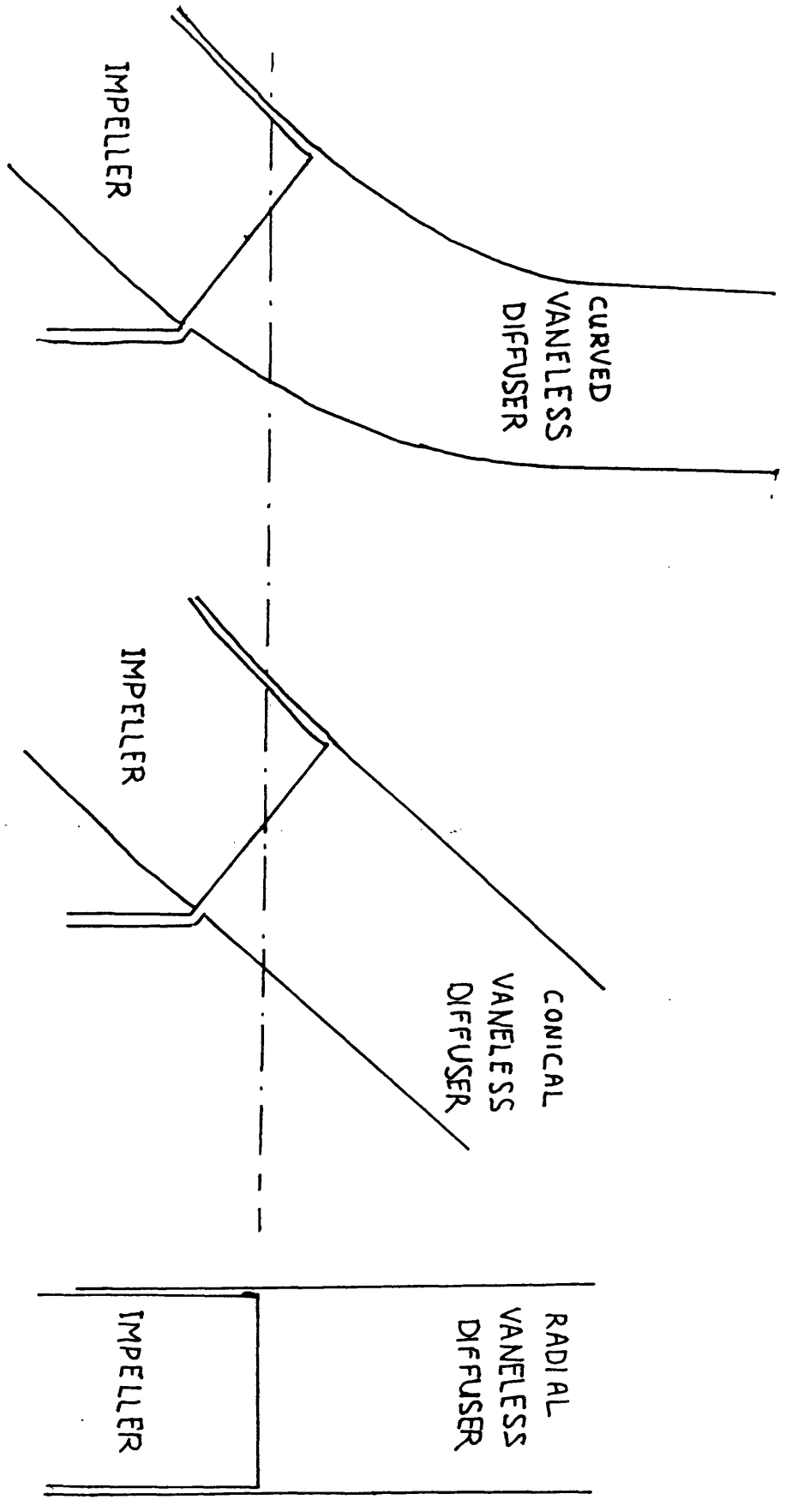

FIGURE 1.1: Alternative mixed flow and radial diffuser designs.

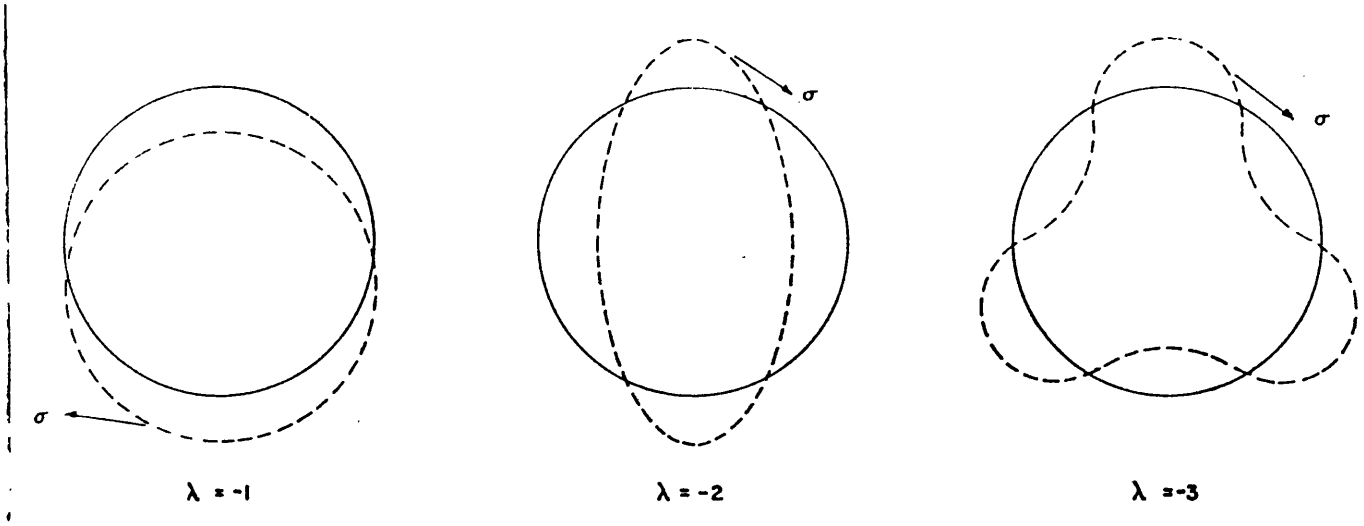

FIGURE 1.2: Perturbed path of a fluid particle for different values of λ (JANSEN(1964)).

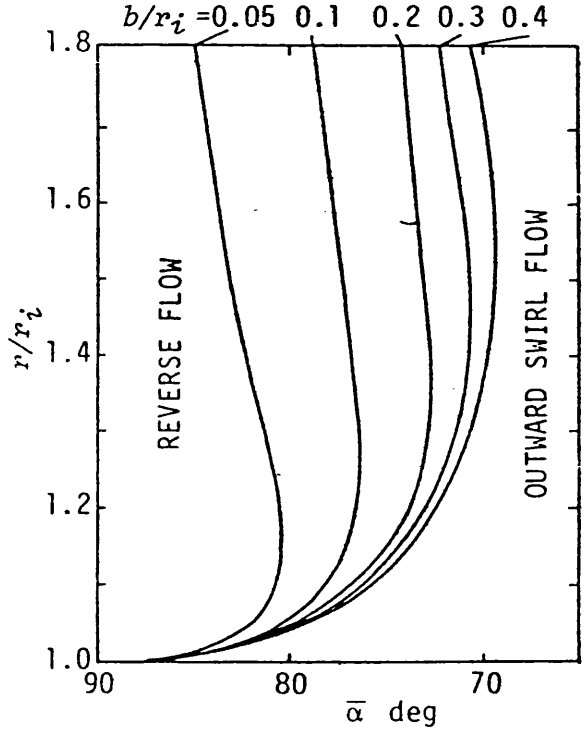

FIGURE 1.3: Reverse flow zone versus mean inlet flow anfle relation for parallel wall diffuser, incompressible flow. (SENOO et al(1978)

CHAPTER 2

THE FINITE ELEMENT METHOD IN FLUID FLOW

2.1 INTRODUCTION

The Navier-Stokes equations can be used to represent physical fluid flow problems. To solve the equations it is necessary to introduce simplifications based upon the nature of the physical problem, see Appendix 2.

For many years the main numerical method to solve the Navier-Stokes equations has been based upon the finite difference technique which involves a direct approximation of the governing differential equations, at the discrete points, by the value of the functions at other mesh points. But in cases of irregular geometry or mixed boundary conditions difficulties have arisen which could only be avoided by using a large number of uniform elements in the mesh or substantial computation time. These difficulties may be overcome by the use of the finite element method which allows the use of non-uniform mesh systems and can thereby deal with irregular geometry.

The following chapter discusses the application of the finite element method in fluid flow problems.

2.2 LITERATURE SURVEY

A number of finite element methods are available for solving the Navier-Stokes equations for compressible and incompressible fluids. The different methods can be classified into three main categories:

a) Pressure-velocity model.

b) Stream function model.

c) Stream function-vorticity model.

The pressure-velocity approach employs the values of velocity and pressure as unknown variables with a polynomial interpolation function used to describe them at each point inside or on the boundary of a fluid element. The solution for these variables can be obtained directly by solving simultaneously the Navier-Stokes equations and the continuity equation. This method has been used by many investigators e.g. ODEN(1972), TAYLOR(1973), KAWAHARA(1976), McCOMBER et al(1978). They applied the Galerkin method to each of the equations to yield a system of linear equations for the solution. By choosing the same interpolation function for both pressure and velocity errors arise in

the solution for velocity. To obtain better accuracy HOOD and TAYLOR(1974) suggested the use of a shape function for pressure one order lower than that used for the velocity components. This mixed interpolation procedure was investigated by HUYAKORN et al(1978) and they found that a nine node Lagrangian element and four node quadrilateral element gave the best accuracy for pressure and velocity distributions. SCHNEIDER et al(1978), however, observed that the mixed model was adequate if viscous effects were dominant, but if internal effects dominated then the pressure should be interpolated to an equal or higher order than the velocity. To overcome this difficulty of using two shape functions, which limits the size of problems which can be dealt with, ZIENKIEWICZ and GODBOLE(1975) used a penalization method where a "penalty" function replaced the pressure and satisfied the continuity equation. BERCOVIER and ENGELEMAN(1979) used a reduced integration technique on a 9 noded parabolic element to eliminate the pressure unknown from the system of equations. The main advantage of the pressure-velocity model is the simplicity of the equations and the convenience for defining the boundary conditions. The use of this formulation is however limited to flow with relatively low Reynolds numbers (see BAR-YOSEPH(1976)) or with the

use of upwind methods.

The second method uses the Navier-Stokes equations as fourth order non-linear differential equations, and only uses the stream function and it's first derivative as unknown variables. This approach has been used by VRIES et al(1974) and KAWAHARA et al(1976), were it is shown that the main advantage of this approach is in using one equation only to describes the fluid behavior, the stream function definition fulfilling the continuity condition. It is clear however that the method requires high order elements and the specification of the boundary conditions is more complicated.

The third approach is the stream function-vorticity model with the Navier-Stokes equation as second order non-linear differential equation with vorticity and the stream function as unknowns. In this method the continuity equation is implicitly satisfied by the definition of the stream function. This avoids the instability of the solution which arise due to the necessity of coupling of the equations in the pressure-velocity model. The solution, however, is not as straight-forward as it first appears from the mathematical equations because the vorticity is not defined on the wall boundaries. In most cases it is necessary to develop an iterative procedure

to solve the basic equations and the vorticity boundary condition. The pressure can not be found directly from the equations and the final solution needs another equation to solve for the pressure distribution. Various investigators e.g. CENG(1972) have used the variational approach, whilst BAKER(1973) and TAYLOR et al(1973) have applied the weighted residuals method with the stream function-vorticity model. The difficulty of introducing the vorticity boundary condition is handled in an iterative manner by solving separately the vorticity transport equation and the stream function equation. The solution converges only for low Reynolds numbers because with high Reynolds numbers the vorticity transport equation ceases to be diagonally dominanted. To overcome this problem IKEGAWA(1979) and MOULT et al(1979) modified the equations and used the "upwind differencing scheme" for high Reynolds numbers. OLSON and TUANR(1976) claimed that in the stream function-vorticity method the equations can not be solved simultaneously because the vorticity boundary conditions are not known a priori. However CAPION-RENSON et al(1978), DHATT et al(1981) employed the Galerkin method in a manner which allowed them to solve the equations simultaneously without resorting to an iterative procedure to satisfy the boundary condition. DHATT also used a mixed

interpolation function for the stream function and vorticity and solved the non-linear equations with a Newton-Raphson iterative scheme which was then satisfactory for flows with high Reynolds numbers.

Although the governing equations for a constant viscous fluid have been solved by many investigators using the finite element method, the solution of the Navier-Stokes equations to boundary layer flow (laminar and turbulent) is more complicated and often at present impossible. Applying the finite element method to the pressure-velocity model of the Navier Stokes equations BAKER(1972, and 1976) gave the solution for three dimensional laminar flow by using an algebraic model for the eddy viscosity. TAYLOR et al(1977, and 1978) used the pressure-velocity model of the Navier-Stokes equations with the Van-Driest algebraic model for the eddy viscosity to solve laminar and turbulent flow in pipes. They assumed that the viscosity inside the element could be interpolated in a similar maner to that for the other physical variables i.e.

$$\mu_t = \sum_{i=1}^{m} N_i \mu_i$$

To calculate the shear stress on the wall a logarithmic element was used. This element was developed for use near the wall region so that the element shape function

described a typical velocity profile in the region. The elements are described in fig. 2.1. It can be seen that the shape function associated with nodes 5,6,7 are not required since the boundary velocity is always zero.

TAYLOR and HARPER(1978) suggested an alternative technique which could be employed to remove the need for fine discretisation of the region near the wall, or the use of wall elements. The technique is to define a solution domain which does not extend to the wall but terminates inside the fully turbulent region at some distance from the wall. A more sophisticated turbulence model has been used by TAYLOR(1978b) to solve two dimensional incompressible shear flow. In this approach the velocity and the turbulence kinetic energy are approximated over each element by a quadratic interpolation function, whilst a linear function is used for pressure. Then for every node four unknowns are defined and the unknown vector for node i is:

$$\delta_i = \begin{Bmatrix} u \\ v \\ p \\ k \end{Bmatrix}_i$$

To obtain a solution the turbulence kinetic energy equation is solved simultaneously with the Navier-Stokes equations and the continuity equation. TAYLOR(1980) and THOMAS et al(1981) used this one equation turbulent model

for solving turbulent flow over a downstream facing step. They found that the use of the upwind method in laminar flow problems greatly improved the accuracy of the results but the use of the "upwind technique" was not required in the turbulent flow. HUTTON(1976) used the two equation turbulence model by applying the Galerkin approximations. He used a special logarithmic wall element which was able to model velocity variations close to arbitrary shaped walls. The elements were located to a position h within the flow. The increment h was chosen sufficiently small so that the mesh boundary remained sensitive to the geometrical detail of the wall. The k-ϵ model, set as a boundary value problem, was used by SCHAMBER and LAROCK(1980) who applied the Galerkin method. They followed TAYLOR's experience about choosing the interpolation function for velocity and pressure, but restricted their solution to one dimensional problems which had been solved by the Newton-Raphson procedure.

Although previous investigations have solved the two equation turbulent model for different Reynolds numbers, the stream function-vorticity model has not been discussed in relation to the finite element method.

In this work the stream function-vorticity model, and the

two equation turbulence model, coupled with the third momentum equation, are solved by the finite element method for low and high Reynolds numbers by applying both Weighted residual and Variational methods.

2.3 THE BASIC EQUATIONS

The objective of the theoretical analysis was to develop a procedure to predict the turbulent flow in the three type of vaneless diffusers encountered with radial and mixed flow compressors. In such cases the flow usually has a high degree of swirl and high Reynolds numbers.

2.3.1 The Navier-Stokes equations

The equations governing laminar and turbulent flow of a fluid are the conservation of momentum equations, known as the Navier-Stokes equations (see Appendix 2 for detail of the turbulence equations). These are most easily represented in the vector form as:

$$\frac{D\bar{u}}{Dt} = \bar{F}_B - \nabla\left(\frac{P}{\rho}\right) + \frac{\mu}{\rho}\nabla^2\bar{u} \qquad (2.3.1)$$

The Navier-Stokes equations are solved in conjunction with the continuity equation i.e.

$$\nabla(\rho\bar{u}) = 0 \qquad (2.3.2)$$

The Navier-Stokes equations in their most general form are difficult to solve and it is necessary to introduce simplifications in order to develop a tractable solution procedure. In this the following assumptions were applied.

1) The fluid motion was assumed to be steady, incompressible and without body forces.

2) The flow was axisymmetric, i.e. there were no property variations in the θ direction, then $\frac{\partial}{\partial \theta} = 0$.

3) For turbulent flow the eddy viscosity concept was applied.

4) The second order derivatives of the turbulent viscosity were considered negligible.

With this assumptions the Navier Stokes equations become

$$u_r \frac{\partial u_r}{\partial r} + u_z \frac{\partial u_r}{\partial z} - \frac{u_\theta^2}{r} = -\frac{1}{\rho}\frac{\partial P}{\partial r} + \frac{\mu_{eff}}{\rho}\left(\frac{1}{r}\frac{\partial u_r}{\partial r} + \frac{\partial^2 u_r}{\partial r^2} + \frac{\partial^2 u_r}{\partial z^2} - \frac{u_r}{r}\right)$$

$$u_r \frac{\partial u_z}{\partial r} + u_z \frac{\partial u_z}{\partial z} = -\frac{1}{\rho}\frac{\partial P}{\partial z} + \frac{\mu_{eff}}{\rho}\left(\frac{1}{r}\frac{\partial u_z}{\partial r} + \frac{\partial^2 u_z}{\partial r^2} + \frac{\partial^2 u_z}{\partial z^2}\right) \qquad (2.3.3)$$

$$u_r \frac{\partial u_\theta}{\partial r} + u_z \frac{\partial u_\theta}{\partial z} + \frac{u_r u_\theta}{r} = \frac{\mu_{eff}}{\rho}\left(\frac{1}{r}\frac{\partial u_\theta}{\partial r} + \frac{\partial^2 u_\theta}{\partial r^2} + \frac{\partial^2 u_\theta}{\partial z^2} - \frac{u_\theta}{r^2}\right)$$

where $\mu_{eff} = \mu + \mu_t$

and μ_t is the turbulent viscosity.

In order to solve these equations in conjunction with the continuity equation

$$\frac{\partial}{\partial r}(r u_r) + \frac{\partial}{\partial z}(r u_z) = 0 \qquad (2.3.4)$$

the pressure terms in equations 2.3.3a and b were eliminated by differentiating with respect to z and r respectively and subtracting. Also the dependent variables U_r and U_z were replaced by the stream function Ψ and the vorticity ω defined as:

$$\frac{1}{r}\frac{\partial \Psi}{\partial r} = \rho u_z$$

$$-\frac{1}{r}\frac{\partial \Psi}{\partial z} = \rho u_r \qquad (2.3.5)$$

and $$\omega = \frac{\partial u_r}{\partial z} - \frac{\partial u_z}{\partial r}$$

The definition of stream function ensures that the continuity equation 2.3.4 is automatically satisfied, leaving equations 2.3.3c the combined form of equations 2.3.3a and b, and equation 2.3.6 to be solved for Ψ , ω and U_θ.

The resulting equations can be expressed in the general form as

$$a_\phi\left[\frac{\partial}{\partial z}\left(\phi\frac{\partial \Psi}{\partial r}\right) - \frac{\partial}{\partial r}\left(\phi\frac{\partial \Psi}{\partial z}\right)\right] - \frac{\partial}{\partial z}\left[b_\phi r \frac{\partial (c_\phi \phi)}{\partial z}\right] - \frac{\partial}{\partial r}\left[b_\phi r \frac{\partial (c_\phi \phi)}{\partial r}\right]$$

$$+ r d_\phi = 0 \qquad (2.3.7)$$

The dependent variable Φ represent vorticity (ω/r), stream function (Ψ) and tangential velocity (rU_θ) when the appropriate parameters a_Φ, b_Φ, c_Φ and d_Φ are applied as given in table 2.1.

With the use of an effective viscosity, μ_{eff}, equation 2.3.7 represents turbulent as well as laminar flow. The turbulence model used is that based upon the kinetic energy of turbulence (k) and the rate of dissipation of turbulence(ϵ), and is described in Appendix 2. This turbulence model leads to two further equations with k and ϵ as the unknowns from which the turbulent viscosity μ_t can be calculated. These equations can be written in the form of equation 2.3.7 where the parameters a_Φ, b_Φ, c_Φ, d_Φ are given in table 2.2. The development of the full turbulence equations, Appendix 2, also modifies the vorticity equation, equation 1b in table 2.1, by the additional source term Sw such that the parameter d_Φ become

$$d_\Phi = -\frac{\rho}{r^2}\frac{\partial (r U_\theta)^2}{\partial z} - 2r\underbrace{\left[\frac{\partial u_z}{\partial r}\frac{\partial^2 \mu_{eff}}{\partial z^2} - \frac{\partial u_r}{\partial z}\frac{\partial^2 \mu_{eff}}{\partial r^2} + \frac{\partial^2 \mu_{eff}}{\partial r \partial z}\left(\frac{\partial u_r}{\partial r} - \frac{\partial u_z}{\partial z}\right)\right]}_{Sw} \qquad (2.3.8)$$

This additional parameter, Sw, is zero for laminar flows, and for fully developed turbulent flows which show no variation in the radial direction. GOSMAN et al(1968) omit this parameter as it is often zero and because they considered that knowledge with respect to the laws of

turbulence was not precise enought to allow for an accurate calculation of Sw. OLIVER(1975) investigated the importance of the Sw term and considered it negligible for boundary layer flows where variations normal to the wall exceed those parallel to the wall. For recirculating flows OLIVER considerd it unclear as to whether Sw could be neglected or not. He did, however, neglect the Sw term and this procedure has been adopted here.

2.4 THE BOUNDARY CONDITION

In order to solve the fluid dynamic equations using the finite element method it is necessary to specify the boundary conditions, inlet, discharge, and solid wall boundaries, for all the variables involved, i.e, Ψ, ω, rU_θ, k, ϵ. The boundary conditions can be specified in three ways (a) Dirichlet condition, where the variable is specified (b) Neuman condition, where the gradient normal to the boundary is specified, and (c) nature boundary conditions, where the required variable is computed from other known parameters. The boundary conditions for a typical problem are shown schematically in fig. 2.2 and discussed below.

2.4.1 Upstream and downstream boundary condition.

For the inlet boundary most of the variables can be specified directly or are readily calculated. The stream function can be calculated from the known or specified inlet velocity and the stream function definition, equation 2.3.5, e.g for the radial diffuser

$$\Psi = \int_{2:0} f r \, dr \qquad (2.4.1)$$

with the stream function on the hub set to zero.

By assuming that the vorticity can be calculated from the definition, equation 2.3.6, as

$$\omega = \frac{\partial v_r}{\partial z} \qquad (2.4.2)$$

The angular momentum, rv_θ, can be calculated directly from the known or specified tangential component of velocity.

For turbulent flows the turbulent kinetic energy (k) and the rate of dissipation of turbulent energy (e) would be difficult to determine without detailed experimental data for each flow situation. In this case an experimental correlation proposed by BOBKOV(1973), see YAMAMATO(1979), was used to calculate the turbulent kinetic energy from the known inlet velocities, then

$$k = (0.02 v_{in})^2 \left(1 - \frac{r}{r_{in}}\right)^2 \qquad (2.4.3)$$

where A and B are constant given by YAMAOTO(1979) as 0.7225 and 2.54 respectively.

$\overline{Z}$ is the distance normal to the wall divided by the distance from the wall to the point of maximum velocity.

$$U^2 = \left(U_r^2 + U_z^2 + U_\theta^2\right)$$

and U_{av} and U_{max} are the average and maximum velocities respectively.

The dissipation rate (ϵ) was shown by OLIVER(1975) to be unimportant due to the dominanting influence of the wall. The dissipation rate has, therefore, been considered to be zero or calculated from a specified turbulent viscosity μ_t and the turbulent kinetic energy, given by equation 2.4.3, through the relationship

$$\varepsilon = C_\mu \rho k^2 / \mu_t \qquad (2.4.4)$$

At the downstream boundary Neuman boundary conditions have been generally applied, see fig. 2.2, because it was assumed that this boundary was in a region where the flow would be fully developed. In cases where the flow would not be fully developed the stream function values could be specified by points at the outlet boundary and the vorticity and k-ϵ values derived in the same way as at the inlet.

2.4.2 Wall boundary conditions.

The stream function and swirl velocity can be readily specified on the wall boundaries. A constant value of stream function can be specified for each wall surface and due to the no slip boundary condition the tangential component of velocity is zero.

The wall vorticity can not be directly specified and fixed but must be computed from known stream function values. Consequently the wall boundary vorticity varies from iteration to iteration. From the definition of vorticity and stream function it follows that

$$\omega = -\left[\frac{1}{\rho r}\left(\frac{\partial^2 \psi}{\partial z^2} + \frac{\partial^2 \psi}{\partial r^2}\right)\right]$$

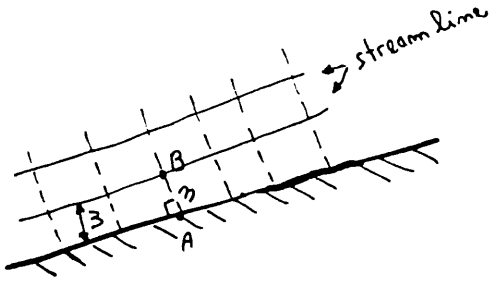

Assuming that close to the wall there is no velocity normal to the wall it follows that

$$\omega = -\frac{1}{\rho r}\frac{\partial^2 \psi}{\partial m^2} \qquad (2.4.5)$$

The stream function variation in the normal direction is derived through a Taylor series expansion such that

$$\Psi_B = \Psi_A + n\left(\frac{\partial \Psi}{\partial n}\right)_A + \frac{n^2}{2}\left(\frac{\partial^2 \Psi}{\partial n^2}\right)_A + \ldots \qquad (2.4.6)$$

With the no slip condition on the wall

$$\left(\frac{\partial \Psi}{\partial n}\right)_A = 0$$

then

$$-\rho \omega_A r_A = \frac{\Psi_B - \Psi_A}{n^2/2}$$

$\omega_w = \omega_A$

i.e.

$$\omega_w = \frac{2}{r_w \rho n^2}\left[\Psi_A - \Psi_B\right] \qquad (2.4.7)$$

GOSMAN et al(1969) by assuming that the vorticity varied linearly with distance from the wall derived a similar representation for the vorticity as

$$\omega_w = -\left[\frac{3}{r_w \rho n^2}\left(\Psi_B - \Psi_A\right) + \frac{\omega_B}{2}\right] \qquad (2.4.8)$$

It was found that the use of equation 2.4.8 improved the convergence stability of the numerical analysis due to the inclusion of the internal vorticity ω_B.

For turbulent flows rapid variations can occur near the wall in the normal direction and the above equation becomes invalid. The use of a fine mesh close to the wall surface can be used to overcome this problem. Whilst the finite element method can accommodate different mesh sizes such a procedure led to a demand for large computer storage and time. It was, therefore,

decided to adopt the technique commonly applied in finite difference schemes where wall functions are used to describe the rapidly varying properties close to the wall; see Appendix 2 and HEINZE(1959). The wall velocity profile was expressed by the logarithmic law of the wall, i.e.

$$\frac{U}{U_\tau} = 2.5 \ln\left(\frac{y U_\tau \rho}{\mu}\right) + 5.5 \qquad (2.4.9)$$

where

$$U_\tau = \sqrt{\frac{\tau_w}{\rho}} \qquad (2.4.10)$$

$$y = n$$

With the first nodal point close to the wall equation 2.4.9 can be solved iteratively for U_τ and hence the wall shear stress τ_w can be found from equation 2.4.10. With the no slip condition on the wall the vorticity, equation 2.4.4, can be written as

$$\frac{w}{r} = -\frac{1}{r}\frac{\partial u}{\partial n} \qquad (2.4.11)$$

The wall shear stress is given by

$$\tau_w = \mu_t \left|\frac{\partial u}{\partial n}\right| \qquad (2.4.12)$$

where

$$\tau_{w,r} = \mu_t \left|\frac{\partial u_r}{\partial n}\right|$$

and

$$\tau_{w,\theta} = \mu_t \left|\frac{\partial u_\theta}{\partial n}\right|$$

Combining equations 2.4.11 and 2.4.12 gives the vorticity function as

$$\left(\frac{w}{r}\right)_w = -\frac{\tau_w}{r_w \mu_t} \qquad (2.4.13)$$

or in terms of the friction velocity U_τ

$$\left(\frac{w}{r}\right)_w = -\frac{\rho u_\tau^2}{r_w \mu_t} \qquad (2.4.14)$$

The turbulence wall functions were derived by method suggested by LAUNDER(1970) and followed by OLIVER(1975). Experimental results for near turbulence indicate that convection and diffusion of turbulence energy are negligible compared to its production and dissipation, consequently by omiting the convective and diffusion terms form the k transport equation (see Appendix 2), the equation reduces to

$$\mu_t\left[2\left(\frac{\partial u_z}{\partial z}\right)^2 + 2\left(\frac{\partial u_r}{\partial r}\right)^2 + \left(\frac{\partial u_\theta}{\partial z}\right)^2 + \left[r\frac{\partial}{\partial r}\left(\frac{u_\theta}{r}\right)\right]^2 + 2\left(\frac{u_r}{r}\right)^2\right]$$
$$- C_\mu k^{3/2}\rho/l_D = 0 \qquad (2.4.15)$$

where l_D is the turbulence dissipation length scale.
By assuming the turbulence viscosity to be a scalar quantity and the derivatives in the radial direction to be negligible (no slip condition), equation 2.4.15 reduces to

$$\mu_t^2\left[\left(\frac{\partial u_r}{\partial z}\right)^2 + \left(\frac{\partial u_\theta}{\partial z}\right)^2\right] = C_\mu k^2 \rho \qquad (2.4.16)$$

Taking $l=l_D$ and $\mu_t = \rho l k^{0.5}$ equation 2.4.16 becomes

$$k_w = \tau_{w,m} / \rho C_\mu^{\frac{1}{2}} \qquad (2.4.17)$$

where

$$\tau_{w,m}^2 = \tau_{w,r}^2 + \tau_{w,\theta}^2$$

For the dissipation near the wall the convective terms may be neglected and the ϵ transport equation, (equation 2A.6 in Appendix 2), reduces to

$$\frac{d}{dz}\left(\frac{\mu_t}{\rho\sigma_\epsilon}\frac{\partial\epsilon}{\partial z}\right) + \frac{C_1 \mu_t \epsilon}{\rho k}\left[\left(\frac{\partial u_r}{\partial z}\right)^2 + \left(\frac{\partial u_\theta}{\partial z}\right)^2\right] - \frac{C_2 \epsilon^2}{k} = 0 \qquad (2.4.18)$$

The turbulent viscosity can be calculate as

$$\mu_t = C_\mu \cdot \rho k^{3/2} / \epsilon \qquad (2.4.19)$$

and the relationship between k and ϵ is given by

$$\epsilon = C_\mu k^{3/2} / l \qquad (2.4.20)$$

Substituting into equation 2.4.18 and solving for ϵ gives

$$\epsilon_w = \left(\frac{\tau_{w,m}}{\rho}\right)^{3/2} \frac{1}{y\left[\sigma_\epsilon C_\mu^{\frac{1}{2}}(C_2 - C_1)\right]^{\frac{1}{2}}} \qquad (2.4.21)$$

2.5 THE FINITE ELEMENT TECHNIQUE EMPLOYED

For the full turbulence model five equations of the form given by equation 2.3.7 have to be solved. Two commonly applied finite element techniques, the Weight Residual method and the Variational principle, have been used to solve the equations. The detailed solution procedure is presented in the next chapter, the two finite element technique employed are presented here.

2.5.1 The Weight Residual Method

In the finite element the unknown stream function, vorticity, kinetic energy of turbulence, rate of dissipation, turbulence viscosity and swirl flow are expressed in terms of interpolation formulae over each element. Through the use of shape functions N the approximate solution fields take the form

$$\Psi = \sum_{i=1}^{m} N_i \Psi_i \qquad K = \sum_{i=1}^{m} N_i K_i$$

$$\frac{\omega}{r} = \sum_{i=1}^{m} N_i \left(\frac{\omega}{r}\right)_i \qquad \varepsilon = \sum_{i=1}^{m} N_i \varepsilon_i \qquad (2.5.1)$$

$$u_\theta r = \sum_{i=1}^{m} N_i (u_\theta r)_i \qquad \mu_t = \sum_{i=1}^{m} N_i \mu_{ti}$$

where N_i is the element shape function at node i.

Employing the Galerkin method or the Galerkin-Petrov method by choosing weighting functions M the differential equation 2.3.7 for a typical nodal point l becomes

$$I_1 = \int_A M_l a_\alpha \left[\frac{\partial}{\partial z}\left(\phi \frac{\partial \Psi}{\partial r}\right) - \frac{\partial}{\partial r}\left(\phi \frac{\partial \Psi}{\partial z}\right)\right] dA \qquad (2.5.2)$$

$$I_2 = \int_A M_l \left[\frac{\partial}{\partial z}\left(b_\phi r \frac{\partial (c_\phi \phi)}{\partial z}\right) - \frac{\partial}{\partial r}\left(b_\phi r \frac{\partial (c_\phi \phi)}{\partial r}\right)\right] dA$$

$$I_3 = \int_A M_l r d_\phi dA$$

$$I_l = I_1 + I_2 + I_3 = 0$$

Substituting equation 2.5.1 into equation 2.5.2 and using the general form $\Phi = \sum_{i=1}^{m} N_i \Phi_i$ yields a system of linear equations of which the component of the l(th) equation for the convective term is

$$I_{1l} = \sum_{i=1}^{l} \int_A M_l a_\phi \left[\frac{\partial}{\partial z}\left(\left(\sum_{i=1}^{m} N_i \phi_i\right)\frac{\partial \Psi}{\partial r}\right) - \frac{\partial}{\partial r}\left(\left(\sum_{i=1}^{m} N_i \phi_i\right)\frac{\partial \Psi}{\partial z}\right)\right] dA \qquad (2.5.3)$$

In the same way the integral of the diffusion and source terms can be presented.

Equation 2.5.2 is a non-linear equation and it is necessary, therefore, to use an iterative procces for its solution in which values from the previous iteration are used in the calculation of the new variable. It is assumed for the iteration m+1 that the viscosity part of the coefficients c_Φ or b_Φ, and the terms $\frac{\partial \Psi}{\partial r}$ and $\frac{\partial \Psi}{\partial z}$ in

the convective term are given by:

$$\mu_{eff} = \mu + \sum_{i=1}^{m} N_i \mu_{ti}$$

$$\frac{\partial \mu_{eff}}{\partial r} = \sum_{i=1}^{m} \frac{\partial N_i}{\partial r} \mu_{ti}$$

$$\frac{\partial \mu_{eff}}{\partial z} = \sum_{i=1}^{m} \frac{\partial N_i}{\partial z} \mu_{ti} \qquad (2.5.4)$$

$$\frac{\partial \Psi}{\partial r} = \sum_{i=1}^{m} \frac{\partial N_i}{\partial r} \Psi_i$$

$$\frac{\partial \Psi}{\partial z} = \sum_{i=1}^{m} \frac{\partial N_i}{\partial z} \Psi_i$$

A typical example of how the Galerkin method is applied to a differential equation and transforms it into set of linear equations consider the stream function equation, equation 2.3.7a, in the differential form can be written as

$$\frac{1}{\rho r^2}\left(\frac{\partial^2 \Psi}{\partial r^2} + \frac{\partial^2 \Psi}{\partial z^2}\right) = -w \qquad (2.5.5)$$

For a nodel point 1 in an element equation 2.5.5 can be written as

$$I_l = \int_A M_l \left[\frac{1}{\rho r^2}\left(\frac{\partial^2 \Psi}{\partial r^2} + \frac{\partial^2 \Psi}{\partial z^2}\right)\right] dA + \int_A M_l \, w \, dA = 0 \qquad (2.5.6)$$

where 1 is any number of a nodal point in the element. The variable r is a geometric variable and can be taken as an average for each element i.e. $r = 1/n \sum_{i=1}^{m} r_i$. For each element the approximate variation of Ψ is given by

equation 2.5.1 and equation 2.5.6 becomes

$$I_l = \frac{1}{\rho r^2}\int_A M_l\left[\frac{\partial^2\left(\sum_{i=1}^{m}(N_i\psi_i)\right)}{\partial r^2} + \frac{\partial^2\left(\sum_{i=1}^{m}(N_i\psi_i)\right)}{\partial z^2}\right]dA + \int_A M_l\sum_{i=1}^{m}(N_i w_i)\,dA \qquad (2.5.7)$$

To obtain the equation in a suitable form for the application of Green's first theorem equation 2.5.7 can be written as

$$\frac{1}{\rho r^2}\int_A\left[\frac{\partial M_l}{\partial r}\left(\sum_{i=1}^{m}\left(\frac{\partial N_i}{\partial r}\psi_i\right)\right) + \frac{\partial M_l}{\partial z}\left(\sum_{i=1}^{m}\left(\frac{\partial N_i}{\partial z}\psi_i\right)\right)\right]dA \qquad (2.5.8)$$

$$= -\int_A M_l\left(\sum_{i=1}^{m}(N_i w_i)\right)dA + \frac{1}{\rho r^2}\oint_S M_l\left[\left(\sum_{i=1}^{m}\frac{\partial N_i}{\partial r}\psi_i l_r\right) + \left(\sum_{i=1}^{m}\frac{\partial N_i}{\partial z}\psi_i l_z\right)\right]ds$$

where lr and lz are direction cosines between the outward normal of the element and the axis. The right hand side of equation 2.5.8 is a contour integral which can be evaluated by assuming that on rigid boundaries the condition of zero tangential and normal velocity components can be applied. Then the value of the contour integral of equation 2.5.8 is immaterial on these surfaces, since the nodal stream function or velocity is known, and consequently these contour integrals are not required for the determination of equation 2.5.8.

The integral equation 2.5.8 can be written as a set of equations for equilibrium of all the nodes in the domain and can be expressed in a general form as

$$[H]\{\psi\} = \{f\} \qquad (2.5.9)$$

The vector $\{\Psi\}$ contains the stream function at all the nodal points. The square matrix [H] is the overall stiffness (viscous) matrix, and the vector $\{f\}$ contains all the flow forces applied on the nodal points.

Let H_{ij} be typical coefficients of the overall stiffness matrix, where i and j are in the range 1 to m (where m=number of nodal points in the domain), and h_{kl} be typical coefficients of the element stiffness matrix where k and l are in the range 1 to n (where n=number of nodes in an element). Now h_{kl} can be interpreted as the flow forces that must be applied to the typical element at the k node in order to maintain equilibrium due to the forces at the l node in the element. In the same way H_{ij} can be interpreted for all the overall forces in the system applied at node i due to those at node j. The process of assembling for the overall matrix takes the form of

$$H_{ij} = \sum_{m=1}^{e} h_{k,l}$$

where e = the number of elements in the domain.

The assembly process can be shown with an example for two elements as shown in fig. 2.3.

The six nodal points are designated the letters a to f

throughout the domain, whilst for each element the nodes are numberd 1 to 4.

For element B equation 2.5.9 is

$$\begin{bmatrix} h_{11} & h_{12} & h_{13} & h_{14} \\ h_{21} & & \vdots & \\ h_{31} & & \vdots & \\ h_{41} & \cdots\cdots & & h_{44} \end{bmatrix}_B \begin{Bmatrix} \psi_1 \\ \vdots \\ \psi_4 \end{Bmatrix}_B = \begin{Bmatrix} f_1 \\ \vdots \\ f_4 \end{Bmatrix}_B$$

where the stiffness matrix coefficients are derived from equation 2.5.8, as for example

$$h_{11} = \frac{1}{\rho \bar{r}_e^2} \int_{Ae} \left(\frac{\partial M_1}{\partial r} \frac{\partial N_1}{\partial r} + \frac{\partial M_1}{\partial z} \frac{\partial N_1}{\partial z} \right) dA_e$$

$$h_{21} = \frac{1}{\rho \bar{r}_e^2} \int_{Ae} \left(\frac{\partial M_2}{\partial r} \frac{\partial N_1}{\partial r} + \frac{\partial M_2}{\partial z} \frac{\partial N_1}{\partial z} \right) dA_e$$

$$f_1 = \int_{Ae} M_1 \left(N_1 w_1 + N_2 w_2 + N_3 w_3 + N_4 w_4 \right) dA_e$$

$$f_2 = \int_{Ae} M_2 \left(N_1 w_1 + N_2 w_2 + N_3 w_3 + N_4 w_4 \right) dA_e$$

and Ae is the element area

Similarly all the coefficients can be derived. For element C also

$$\begin{bmatrix} h_{11} & h_{12} & h_{13} & h_{14} \\ h_{21} & & \vdots & \\ h_{31} & & \vdots & \\ h_{41} & \cdots\cdots & & h_{44} \end{bmatrix}_C \begin{Bmatrix} \psi_1 \\ \vdots \\ \psi_4 \end{Bmatrix}_C = \begin{Bmatrix} f_1 \\ \vdots \\ f_4 \end{Bmatrix}_C$$

where

$$h_{11} = \frac{1}{\rho \bar{r}^2} \int_{A_e} \left(\frac{\partial M_1}{\partial r} \frac{\partial N_1}{\partial r} + \frac{\partial M_1}{\partial z} \frac{\partial N_1}{\partial z} \right) dA_e$$

$$f_1 = \int_{A_e} M_1 (N_1 w_1 + N_2 w_2 + N_3 w_3 + N_4 w_4) \, dA_e$$

In element B 1,2,3,4 corresponds to a,b,c,d and in element C 1,2,3,4 corresponds to d,c,f,e respectively. For equilibrium of forces acting on the six nodes the two matrices can be added together to give

$$\begin{bmatrix} h_{11}^B & h_{12}^B & h_{13}^B & h_{14}^B & 0 & 0 \\ h_{21}^B & h_{22}^B & h_{23}^B & h_{24}^B & 0 & 0 \\ h_{31}^B & h_{32}^B & (h_{33}^B + h_{22}^C) & (h_{34}^B + h_{21}^C) & h_{23}^C & h_{24}^C \\ h_{41}^B & h_{42}^B & (h_{43}^B + h_{21}^C) & (h_{44}^B + h_{11}^C) & h_{13}^C & h_{14}^C \\ 0 & 0 & h_{31}^C & h_{32}^C & h_{33}^C & h_{34}^C \\ 0 & 0 & h_{41}^C & h_{42}^C & h_{43}^C & h_{44}^C \end{bmatrix} \begin{Bmatrix} \psi_a \\ \psi_b \\ \psi_c \\ \psi_d \\ \psi_e \\ \psi_f \end{Bmatrix} = - \begin{Bmatrix} f_1^B \\ f_2^B \\ f_3^B + f_2^C \\ f_4^B + f_1^C \\ f_3^C \\ f_4^C \end{Bmatrix}$$

where the superscripts on the stiffness coefficients refer to the element B or C from which they are derived. The stiffness coefficients can be now written in a general form as

$$H_{ij} = \sum_{m=1}^{e} \int_{A_e} \frac{1}{\rho \bar{r}_m^2} \left(\frac{\partial M_e}{\partial r} \frac{\partial N_k}{\partial r} + \frac{\partial M_e}{\partial z} \frac{\partial N_k}{\partial z} \right) dA_e$$

$$f_i = \sum_{m=1}^{e} \int_{A_e} M_e \left(\sum_{i=1}^{m} N_i w_i \right) dA_e \qquad (2.5.10)$$

Equation 2.5.9 is a set of linear equations which can be solved to find the values of the stream function at each nodal point.

General methods for solving sets of simultaneous linear equations are well known and described by FENNER(1974) and ZIENKIEWICZ(1978). The most commonly used techniques are the direct Gaussian elimination and iterative Gauss Seidel method. These were modified by HOOD(1970) and BERCOVIER(1979) for better use in the finite element method.

Similarly the other differential equations of equation 2.3.7 can be obtain by including also the non-linear terms using suitable iteration procedures to obtain their value from the previous iteration until convergence has been reach.

2.5.2 The Pseudo-Variational method.

A variational formulation does not exist for equation 2.3.7. However the variational is known for the Poisson equation which is of the form

$$\nabla^2 \phi = g \qquad (2.5.11)$$

where g is a constant function.

Assuming that the stream function and the eddy viscosity are known functions of the coordinates for the case of turbulent flow, equation 2.3.7 may be rewritten as

$$a_\phi\left(\frac{\partial\phi}{\partial z}\frac{\partial\Psi}{\partial r}-\frac{\partial\phi}{\partial r}\frac{\partial\Psi}{\partial z}\right)-rb_\phi\left[\mu_{eff}\nabla^2\phi+2\left(\frac{\partial\phi}{\partial z}\frac{\partial\mu_{eff}}{\partial z}+\frac{\partial\phi}{\partial r}\frac{\partial\mu_{eff}}{\partial r}\right)\right]$$

$$+rd_\phi=0 \qquad (2.5.12)$$

and rearranged to give

$$\nabla^2\phi=G\left(\frac{\partial\phi^\circ}{\partial z}\frac{\partial\Psi^\circ}{\partial r}-\frac{\partial\phi^\circ}{\partial r}\frac{\partial\Psi^\circ}{\partial z}\right)$$

$$-\frac{2}{\mu_{eff}}\left(\frac{\partial\phi^\circ}{\partial z}\frac{\partial\mu_{eff}}{\partial z}+\frac{\partial\phi^\circ}{\partial r}\frac{\partial\mu_{eff}}{\partial r}\right)+Qd_\phi \qquad (2.5.13)$$

where

$$G=a_\phi/rb_\phi\mu_{eff}$$

$$Q=1/b_\phi\mu_{eff}$$

If the right hand side of equation 2.5.13 is assumed to be fixed during the variation and using the values of the previous iteration as Ψ^0 and Φ^0, then equation 2.5.13 has a variational form similar to that of the Poisson equation which can be written as

$$\chi(\phi)=\int_A\left\{\frac{1}{2}(\nabla\phi)^2+\phi\left[G\left(\frac{\partial\phi^\circ}{\partial z}\frac{\partial\Psi^\circ}{\partial r}-\frac{\partial\phi^\circ}{\partial r}\frac{\partial\Psi^\circ}{\partial z}\right)\right.\right.$$

$$\left.\left.-\frac{2}{\mu_{eff}}\left(\frac{\partial\phi^\circ}{\partial z}\frac{\partial\mu_{eff}}{\partial z}+\frac{\partial\phi^\circ}{\partial r}\frac{\partial\mu_{eff}}{\partial r}\right)\right]+\phi Qd_\phi\right\}dA \qquad (2.5.14)$$

and the variation will be completed only when Φ^0 is equal to Φ. Minimising equation 2.5.14 with respect to Φ_i gives

$$\frac{\partial \chi(\phi)}{\partial \Phi_i} = \underbrace{\int_A \nabla \phi \frac{\partial \phi}{\partial \phi_i} dA}_{D} + \underbrace{\frac{\partial \phi}{\partial \phi_i}\left[G\left(\frac{\partial \phi^\circ}{\partial z}\frac{\partial \psi^\circ}{\partial r} - \frac{\partial \phi^\circ}{\partial r}\frac{\partial \psi^\circ}{\partial z}\right)\right] dA}_{C}$$

$$\underbrace{-2\int_A \frac{\partial \phi}{\partial \phi_i}\left[\frac{1}{\mu_{eff}}\left(\frac{\partial \phi^\circ}{\partial z}\frac{\partial \mu_{eff}}{\partial z} + \frac{\partial \phi^\circ}{\partial r}\frac{\partial \mu_{eff}}{\partial r}\right) dA}_{S_1}$$

$$+ \underbrace{\int_A \frac{\partial \phi}{\partial \phi_i} Q d_\phi \, dA}_{S_2} = 0 \qquad (2.5.15)$$

$$D + C + S_1 + S_2 = 0$$

The term D of equation 2.5.15 can be evaluated by minimising the effect of quadrature error on the approximate solution of the integral as used in the "patch work" approximation presented by AZIZ(1972) and WACHSPREN(1975). MOULT(1975) presented the term D in the same form by deriving the equation from the variational formulation of the equation.

Assume a typical linear triangular element as shown in fig. 2.4 and the term D given as

$$D = \int_A \nabla \phi \frac{\partial \phi}{\partial \phi_i} dA \qquad (2.5.16)$$

where A is the triangular element area.

By using the definition of the function for a triangular

element in Appendix 1 for node 0 in the element

$$\frac{\partial \phi}{\partial \phi_0} = a_0 = \frac{1}{2A}\left[(r_1 - r_2)(z_2 - z_0) + (r_0 - r_2)(z_1 - z_2)\right]$$

$$\nabla\phi = \frac{1}{2A}\Big[\phi_0\big((z_1 - z_2) + (r_2 - r_1)\big) + \phi_1\big((z_2 - z_0) + (r_0 - r_2)\big) + \phi_2\big((z_0 - z_2) + (r_2 - r_0)\big)\Big] \qquad (2.5.17)$$

Substituting into equation 2.5.16 and assuming the integrand is independent of r and z leads to

$$D = \frac{1}{4A}\Big\{\big[(r_1 - r_2)(z_2 - z_0) + (r_0 - r_2)(z_1 - z_2)\big]\cdot\big[\phi_0\big((z_1 - z_2) + (r_2 - r_1)\big) + \big((z_2 - z_0) + (r_0 - r_2)\big)\phi_1 + \phi_2\big((z_0 - z_1) + (r_1 - r_0)\big)\big]\Big\} \qquad (2.5.18)$$

If the vector $\bar{L}_1$ and $\bar{L}_2$ are defined as shown in fig. 2.4. Equation 2.5.18 can be rewritten as

$$D = \frac{1}{4A}\left(\bar{L}_2 - \bar{L}_1\right)\left[(\phi_2 - \phi_0)\bar{L}_1 - (\phi_1 - \phi_0)\bar{L}_2\right]$$

but

$$\frac{(\bar{L}_2 - \bar{L}_1)\bar{L}_2}{A} = \frac{|\bar{L}_1 - \bar{L}_2||\bar{L}_2|\cos\gamma_2}{\frac{1}{2}|\bar{L}_2 - \bar{L}_1||\bar{L}_2|\sin\gamma_2} = 2\cot\gamma_2$$

In the same way

$$\frac{(\bar{L}_2 - \bar{L}_1)\,\bar{L}_1}{A} = -2\cot\gamma_1$$

and therefore

$$D = \frac{1}{2}\left[(\phi_0 - \phi_1)\cot\gamma_2 + (\phi_0 - \phi_2)\cot\gamma_1\right] \qquad (2.5.19)$$

In the same way term D can be presented for nodes 1 and 2 in the element.

To calculate the term C it is necessary to transform the area integral to a contour integration by use of the Gauss's divergence theorem. By using the definition of the stream function and substituting into term C gives

$$C = r G \int_A \left(\frac{\partial(\phi^\circ u_r^\circ)}{\partial r}\right) + \left(\frac{\partial(\phi^\circ u_z^\circ)}{\partial z}\right) dA \qquad (2.5.20)$$

which transforms to

$$C = r G \oint_{\text{Contour}} \left[u_r^\circ l_r - u_z^\circ l_z\right] \phi^\circ \, dl \qquad (2.5.21)$$

where $U_r^{\,0}$ and $U_z^{\,0}$ are calculated from the previous value of Ψ, and l_r and l_z denote the direction cosines of those normals drawn outward from the boundary.

Equation 2.5.21 can be rewritten as

$$C = r G \int_A u_m^\circ \, \phi^\circ \, dl \qquad (2.5.22)$$

By summing for each side of the triangle equation 2.5.22 becomes

$$C = \Gamma G \left[U^{\circ}_{m,0} \int_0^1 \phi^{\circ} dl + U^{\circ}_{m,1} \int_1^2 \phi^{\circ} dl + U^{\circ}_{m,2} \int_2^0 \phi^{\circ} dl \right] \qquad (2.5.23)$$

The variable Φ^0 can be described by a linear interpolation function as

$$\phi^{\circ} = \langle N_0; N_1; N_2 \rangle \begin{Bmatrix} \phi^{\circ}_0 \\ \phi^{\circ}_1 \\ \phi^{\circ}_2 \end{Bmatrix}$$

and the velocity U_m^0 is the fluid velocity normal to the side of the element. The average value of U_m^0 is given by

$$\bar{U}_m = \frac{1}{\Gamma} \frac{\partial \psi^{\circ}}{\partial l} = \frac{1}{\Gamma} \frac{\psi^{\circ}_1 - \psi^{\circ}_2}{\Delta l} \qquad (2.5.24)$$

where

$$\Delta l = l_1 - l_2$$

Substituting these relationships into equation 2.5.23 leads to

$$C = -\frac{G\Gamma}{6} \left[(\psi^{\circ}_1 - \psi^{\circ}_0)(\phi^{\circ}_2 - \phi^{\circ}_0) - (\psi^{\circ}_2 - \psi^{\circ}_0)(\phi^{\circ}_1 - \phi^{\circ}_0) \right] \qquad (2.5.25)$$

The term S1 is needed only in the turbulence model where the viscosity is treated as a variable. (Assuming that

the second derivative of the viscosity function can be neglected.)

The viscosity in the element is described in the same way as the variable Φ i.e.

$$\mu_{eff} = \langle N_0; N_1; N_2 \rangle \begin{Bmatrix} \mu^{\circ}_{eff,0} \\ \mu^{\circ}_{eff,1} \\ \mu^{\circ}_{eff,2} \end{Bmatrix} \qquad (2.5.26)$$

The first derivative of μ_{eff} and Ψ in a linear triangular element is constant, then the term S_1 can be rearranged as

$$S_1 = -\frac{2}{\mu^{\circ}_{eff}} \left[\frac{\partial \mu^{\circ}_{eff}}{\partial r} \frac{\partial \phi^{\circ}}{\partial r} \int_A dA + \frac{\partial \mu^{\circ}_{eff}}{\partial z} \frac{\partial \phi^{\circ}}{\partial z} \int_A dA \right. \qquad (2.5.27)$$

Using the expression for the first derivative in a triangular element equation 2.5.27 becomes, for node 0 in the triangular element

$$S_{10} = -\frac{1}{3A_{012}} \mu^{\circ}_{eff} \left[\left\{ (\mu^{\circ}_{eff,0} - \mu^{\circ}_{eff,1}) \left[(z_0 + z_2)(r_0 + r_2) \right] - (\mu^{\circ}_{eff,0} - \mu^{\circ}_{eff,2}) \left[(z_0 + z_1) + (r_0 + r_1) \right] \right\} \right.$$

$$\left. + \left\{ (\phi^{\circ}_0 - \phi^{\circ}_1) \left[(z_0 + z_2)(r_0 + r_2) \right] - (\phi_0 - \phi_2) \left[(z_0 + z_2) + (r_0 + r_1) \right] \right\} \right]$$

(2.5.28)

The term S_1 is different in each form of equation 2.3.7. in a problem with swirl flow the term S_2 for the vorticity equation can be written as

$$S_2 = \rho \int_A \frac{\partial (u_\theta r)}{\partial z} \, dA \qquad (2.5.29)$$

in a triangular element 0,1,2

Assuming that $\partial(U_\theta r)/\partial z$ is constant in the element

$$S_2 = \rho \frac{\partial (u_\theta r)}{\partial z} \int_A dA$$

which leads for node 0 in the triangular element to:

$$S_2 = -\frac{\rho}{6}\left[(\phi_0 - \phi_1)(r_0 - r_2) + (\phi_0 - \phi_2)(r_1 - r_2)\right] \qquad (2.5.30)$$

where $\phi = U_\theta r$

For the turbulence equation S_2 can be calculate in a similar manner to S_1 which will give an average value for all nodes in the element.

Collecting together the expressions for D, C, S_1 and S_2 equation 2.5.15 can be written for node 0 in the element 0, 1, 2 as

$$\frac{\partial \chi(\phi_0)}{\partial \phi_0} - \frac{1}{2}\left[(\phi_0 - \phi_1)\cot\gamma_3 + (\phi_0 - \phi_2)\cot\gamma_2\right] - \frac{\sigma r}{6}\left[(\psi_1^\circ - \psi_0^\circ)(\phi_2^\circ - \phi_0^\circ) - (\psi_2^\circ - \psi_0^\circ)(\phi_1^\circ - \phi_0^\circ)\right] + S_{10} + S_{20} = 0 \qquad (2.5.31)$$

Equation 2.5.31 is an algebraic equation and can be written in the same manner for all the n nodes in the domain. By assuming the values of Φ_1 and Φ_1 in each element equation, equation 2.5.31 can be solved to find the value of Φ_0.

TYPE OF EQUATION	ϕ	a_ϕ	b_ϕ	c_ϕ	d_ϕ	code
Stream function	Ψ	0	$\rho\frac{1}{r^2}$	1	$-\frac{\omega}{r}$	a
Vorticity	$\frac{\omega}{r}$	r^2	r^2	μ	$-\frac{\rho}{r^2}\frac{\partial(ru_\theta)^2}{\partial z}$	b
Swirl flow	$u_\theta r$	1	μr^2	$\frac{1}{r^2}$	0	c

TABLE 2.1: Coefficients of the basic equations for constant viscosity problem.

TYPE OF EQUATION	ϕ	a_ϕ	b_ϕ	c_ϕ	d_ϕ	code
Stream function	Ψ	0	$\rho\frac{1}{r^2}$	1	$-\frac{\omega}{r}$	a
Vorticity	$\frac{\omega}{r}$	r^2	r^2	μ_{eff}	$-\frac{\rho}{r^2}\frac{\partial(ru_\theta)^2}{\partial z}$	b
Swirl flow	ru_θ	1	$\mu_{eff}r^2$	$1/r^2$	0	c
Turbulence kinetic energy	k	1	$\mu+\frac{\mu_t}{\sigma_k}$	1	$\rho\varepsilon-\Delta\mu_t$	d
The rate of dissipation of turbulence	ε	1	$\mu+\frac{\mu_t}{\sigma_\varepsilon}$	1	$\frac{c_2\varepsilon\rho}{k}$ $-\frac{c_1\varepsilon\mu_t\Delta}{k}$	e

TABLE 2.2: Coefficients of the basic equations for turbulent flow.

$$\Delta = 2\left(\frac{\partial u_z}{\partial z}\right)^2 + 2\left(\frac{\partial u_r}{\partial r}\right)^2 + \left(\frac{\partial u_\theta}{\partial z}\right)^2 + 2\left(\frac{u_r}{r}\right)^2 + \left[r\frac{\partial}{\partial r}\left(\frac{u_\theta}{r}\right)\right]^2 + \left(\frac{\partial u_z}{\partial r}+\frac{\partial u_r}{\partial z}\right)^2$$

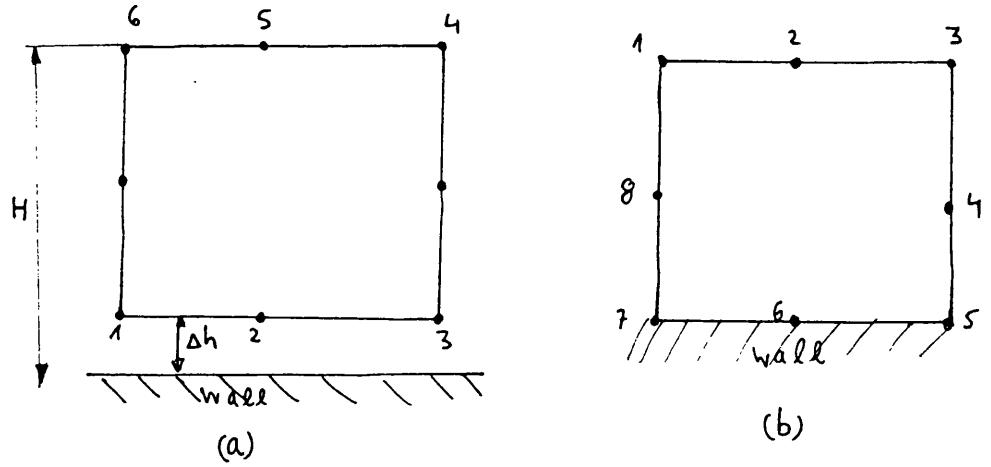

FIGURE 2.1: Logarithmic wall elements

a) HUTTON (1976)

b) TAYLOR (1980)

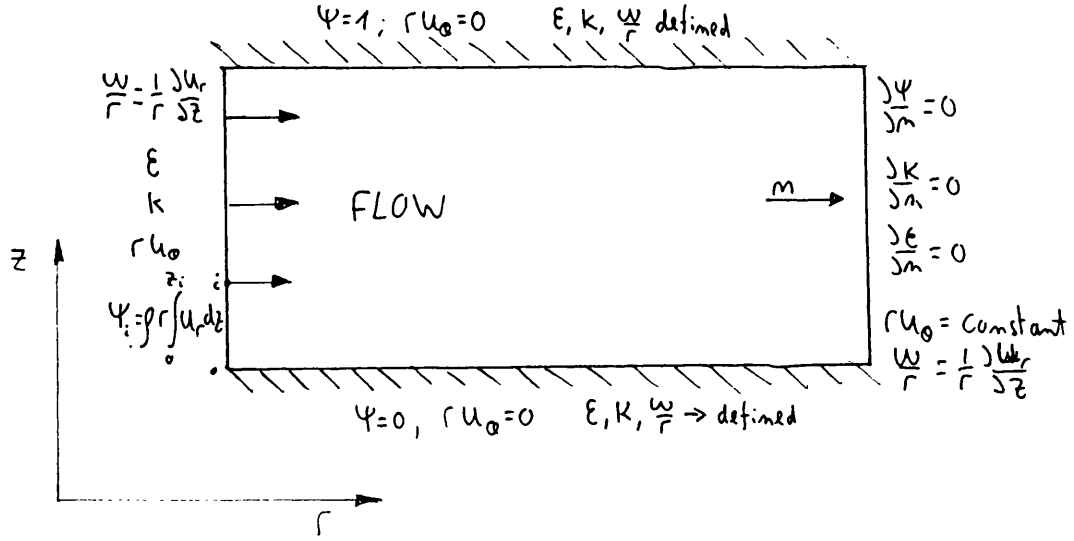

FIGURE 2.2: Schematic drawing of boundary conditions

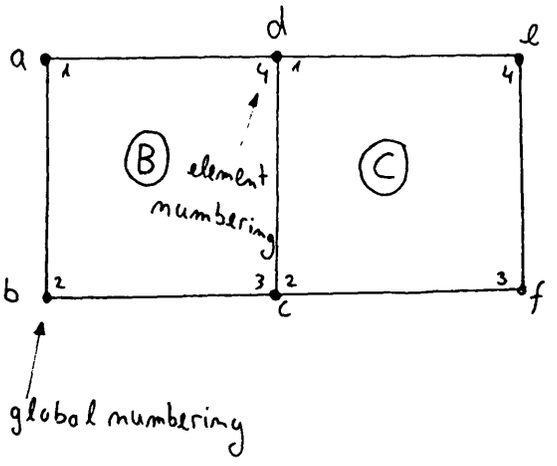

FIGURE 2.3: A simple elements mesh

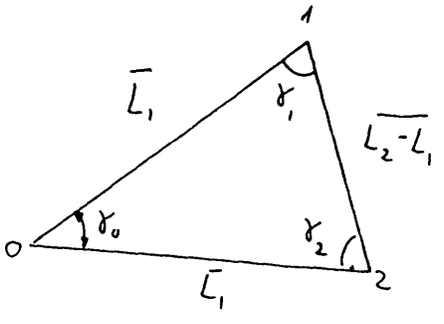

FIGURE 2.4: A triangular element.

CHAPTER 3

THE METHOD OF SOLUTION

3.1 INTRODUCTION

The aim of the theoretical work has been to develop a method to solve equation 2.3.7 which is a non-linear partial differential equation of eliptic form for predicting the laminar and turbulent flow in vaneless diffusers.

By choosing the stream function-vorticity model two finite element methods can be applied:

a) The Galerkin method.

b) The variational approach.

In the present study the variational approach has been chosen to solve the transport equations equations 2.3.7b, c, d, e, because the solution of these equations by the Galerkin method became unstable with high Reynolds numbers (this depends upon the mesh size) due to the convective term becoming dominant.

The remainder of this chapter gives the main factors which affected the numerical solution together with an

outline description of the resulting computer program.

3.2 THE NUMERICAL SCHEME

The numerical solution of equations 2.3.7 is an iterative process, each equation being solved separately and coupled by boundary conditions and / or values of variables which were calculated during the previous iteration.

This technique had two advantages: a) each equation could be treated by different numerical methods which suited the particular equation best, b) at each stage the number of unknowns per nodal point is only one and consequently the coefficient matrix dimension is minimised. the disadvantages were: a) the method needed a long computing time, b) the use of relaxation factors was necessary to ensure convergence of the equations.

As mentioned before different finite element techniques have been applied to the equations depend upon the nature of the differential equation. The stream function equation 2.3.7a is in the form of a Poisson equation therefore, the solution can be achieved by the straight forward application of the Galerkin method. The element that has been used is a nine noded Lagrangian element (fig. 3.1a). The set of linear equations were solved

using the direct method based on the Gauss elimination technique modified by IRON(1970) to the frontal solution.

To solve the turbulence transport equations and the momentum equations (equation 2.3.7b,c,d,e) the Variational method was applied. The same nine noded element was used, however instead of describing the variables by second order interpolation functions the element was divided into a number of triangles which have a common point at the center of the element. Each triangle was then considered as a 3 noded element with linear interpolation functions, as described in Appendix 1. This type of element is refered to as a "sub element", the number of triangular sub elements in the element can be changed and fig. 3.1b, c, d show different types of "sub element". The node 0 in the center of the element is affected by the "sub element" triangles only and their average contribution to node 0 is proportional to the triangular area of the sub element.

Using this type of element and equation 2.5.19 for a triangular element, for the center node 0 the diffusion term of equation 2.3.7 can be represented by

$$D = \frac{1}{2}\sum_{i=1}^{n} (\phi_o - \phi_i)(\cot\beta_i + \cot\lambda_i) \qquad (3.2.1)$$

where n represents the element nodes (number of sub

elements) except the centre node 0, and the angles α_i and β_i in the element are defined in fig. 3.2.

The convective term can be treated in a similar manner and by using the expression of equation 2.5.25, and the sub element model it can be written as

$$C = -\frac{G}{6}\sum_{i=1}^{m}(\phi_i - \phi_0)(\Psi_{i+1} - \Psi_{i-1}) \qquad (3.2.2)$$

where G includes the Reynolds number.

Equations 3.2.1 and 3.2.2 can be combined to yield

$$D + C = \sum_{i=1}^{m}(\phi_i - \phi_0) f_i \qquad (3.2.3)$$

where $f_i = \frac{1}{2}(\cot\alpha_i + \cot\beta_i) - \frac{G}{6}(\Psi_{i+1} - \Psi_{i-1})$

For a case of swirling flow the swirl term in the vorticity equation is given by (using equation 2.5.30)

$$S_2 = \frac{Q_0}{6}\sum_{i=1}^{m}\Theta_i(r_{i+1} - r_{i-1}) \qquad (3.2.4)$$

The contribution to the node 0 of all the source terms can be taken as an average value in each element i.e.

$$S_1 = \sum_{i=1}^{n} S_{1i} \qquad (3.2.5)$$

where n is the number of triangular sub elements in the Lagrangian element.

All the terms can be combined to yield

$$I = D + C - S_1 + S_2 = 0$$

$$I = \sum_{i=1}^{m} (\phi_i - \phi_0) f_i - \frac{Q}{6} \sum_{i=1}^{m} \Theta_i (r_{i+1} - r_{i-1}) + \sum_{i=1}^{m} S_{i1} = 0 \qquad (3.2.6)$$

The restriction that the matrix of the coefficients must be diagonally dominant for convergence means that the term f_i must be positive i.e.

$$\frac{1}{2}(\cot \alpha_i + \cot \beta_i) > \frac{G}{6}(\Psi_{i+1} - \Psi_{i-1})$$

If all the angles in the triangular sub element are less than 90 degrees then $(\cot\alpha_i + \cot\beta_i)/2$ will be positive. Therefore the restriction is that $G(\Psi_{i+1} - \Psi_{i-1})/6$ must be less than $(\cot\alpha_i + \cot\beta_i)/2$. To ensure that this condition is achieved it is necessary to use the finite difference "upwind" method. This is applied on a typical element as illustrated in fig. 3.3 where the direction of the flow is indicated by the arrow. The equation 3.2.2 can be written as

$$C = \frac{G}{6}\Big[(\phi_1 - \phi_0)(\Psi_2 - \Psi_8) + (\phi_2 - \phi_0)(\Psi_3 - \Psi_1) + (\phi_3 - \phi_0)(\Psi_4 - \Psi_2)$$

$$+ (\phi_4 - \phi_0)(\Psi_5 - \Psi_3) + (\phi_5 - \phi_0)(\Psi_6 - \Psi_4) + (\phi_6 - \phi_0)(\Psi_7 - \Psi_5)$$

$$+ (\phi_7 - \phi_0)(\Psi_8 - \Psi_6) + (\phi_8 - \phi_0)(\Psi_1 - \Psi_7)$$

From the flow direction it is clear that $(\Psi_2 - \Psi_8)$, $(\Psi_1 - \Psi_7)$, $(\Psi_3 - \Psi_1)$, $(\Psi_4 - \Psi_2)$ are greater than zero whilst the other terms are less then zero. The "upwind" method replaces the terms $(\Phi_1 - \Phi_0)(\Psi_2 - \Psi_8)$ by $(\Phi_5 - \Phi_0)(\Psi_6 - \Psi_4)$ and treat all the positive terms in the same way.

Equation 3.2.2 is therefore re-written as

$$C = \frac{G}{6}\sum_{i=1}^{m}(\Phi_i - \Phi_0)\left[(\Psi_{i+1} - \Psi_{i-1}) - |\Psi_{i+1} - \Psi_{i-1}|\right] \qquad (3.2.7)$$

The basic equation 3.2.6 can be transformed to an algebraic equation for node 0 in an element as

$$\Phi_0 = \left[\sum_{i=1}^{m}\Phi_i g_i - \frac{Q}{6}\sum_{i=1}^{m}\theta_i(r_{i+1} - r_{i-1}) + \sum_{i=1}^{m}S_{4i}\right] \Big/ \sum_{i=1}^{m} g_i \qquad (3.2.8)$$

where

$$g_i = \frac{1}{2}(\cot\alpha_i + \cot\beta_i) - \frac{G}{6}\left[(\Psi_{i+1} - \Psi_{i-1}) - |\Psi_{i+1} - \Psi_{i-1}|\right.$$

An indirect iterative procedure known as "point successive over/under relaxation" has been employed to solve these equations. Gosman et. al(1968) used a relaxation factor to improve convergence and equation

3.2.8 was modified to

$$\phi_o^{m+1} = \phi_o^m + \alpha_R \left[\sum_{i=1}^{n} (\phi_i^m - \phi_o^m) g_i - \frac{Q}{6} \sum_{i=1}^{n} \theta_i^m (r_{i+1} - r_{i-1}) + \sum_{i=1}^{n} S_{4i}^m \right] \Big/ \sum_{i=1}^{n} g_i \qquad (3.2.9)$$

where α_R is the relaxation factor, which can be different for each equation ,and the superscript m indicates the value from the previous iteration.

The node 0 in the centre of the element is only influenced by other nodes in the element. The "point successive under relaxation" method was used to solve the equation for the centre node of each element. The mesh was then regenerated so that the computed values are no longer centre nodes and are used instead to compute the value at the new centre nodes. The mesh was modified in steps, as shown in fig. 3.4, so that all nodes, except the boundary values, became centre nodes during the process.

The method of solution for equation 2.3.7 is therefore:

a) Make an initial guess for all variables.

b) Calculate the vorticity (equation 2.3.7b).

c) Calculate the stream function (equation 2.3.7a).

d) Calculate the vorticity boundary condition.

e) Calculate the other variables (equation 2.3.7c, d, e)

This sequence of steps b, c, d, e is repeated until convergence is reached.

The flow chart of the procedure is given in fig. 3.5.

3.3 STABILITY AND CONVERGENCE

A non-linear differential equation needs an iterative process to converge to the exact solution. The rate and/or success of convergence depends upon 1) The initial estimated values for all the variables and 2) Selection of the relaxation factors. These initial estimates and selections differ from problem to problem. The relaxation factor in the vorticity equation has to be of the order of the nondimensional distance of the first internal node from the wall (see GOSMAN et al(1968)).

The criterion applied for convergence is that

$$\frac{\phi_i^{m+1} - \phi_i^{m}}{\phi_i^{m}} < \lambda \qquad (3.3.1)$$

at each point of the mesh.

Equation 3.3.1 has to be satisified by all the variables in the problem. Of all the equations it was found to be most difficult to obtain convergence of the vorticity field; however the vorticity is an important parameter and a convergence factor λ of 0.005 was used. For the

turbulence model k-ϵ were converged to a factor of λ=0.01 The convergence of the stream function and swirl flow parameter was better than 0.5%.

Flow with high Reynolds numbers may lead to instability in the numerical solution; and in some cases to a divergent solution; in these cases the "upwind method" was used.

3.4 COMPUTATIONAL DETAILS

Equation 3.2.9 is an algebraic equation which leads to the use of the "point successive over/under relaxation" numerical method.

The convergence of any numerical solution depends upon two major factors

a) The mesh size.

b) The magnitude of the relaxation factors.

A typical problem of a uniform flow through a radial diffuser was chosen to study the effect of these parameters on the solution. The first task in the finite element method is to determine the mesh size in the radial and axial direction, if the mesh size is poorly chosen divergence or an inaccurate solution will result.

Fig 3.6 shows a typical mesh used.

As it is known that the velocity has a significant variation near the wall and at the inlet, relatively small elements were employed in these regions.

The accuracy of the solution depends also upon the vorticity boundary condition which is not clearly defined and calculated from the wall stream function values and those at the node point located at a distance y from the wall, (this is the first node point from the wall)
Fig. 3.7 presents the vorticity and stream function distribution at a cross section a distance of 0.25 widths from inlet. The solution is given with different mesh sizes in the z direction for a constant viscosity case. The stream function equation was solved by the Galerkin method whilst the remaining momentum equations were solved using the variational sub element method described in section 3.2. In order to test this Variational sub element numerical method a full Galerkin analysis was also carried out for this constant viscosity and low Reynolds number analysis. The results show that the vorticity distribution is effected more significantly by the mesh size especially close to the wall. The stream function distribution is not significantly changed by reducing the mesh size. The vorticity distribution

predicted by the Galerkin and the Variational sub element methods show a satisfactory agreement when a mesh size of 15*19 was used. The close agreement on stream function is as expected as the Galerkin method was used for all calculations. A mesh size with a minimum of 17 nodes across the width has been generally used in the theoretical investigations.

In fluid flow problems optimum mesh size is a function of Reynolds number. In problems with high Reynolds numbers the "upwind" method has to be used to avoid instability of the numerical solution, this leads to reduced accuracy (see DENNIS and CHANG(1969)). By decreasing the element size the use of the "upwind" method can be avoided, this however leads to a large number of elements and uneconomical computer requirements.

No general theory exists for prediction of the optimum relaxation factors for non-linear coupled equations. The optimum relaxation factor depends on the mesh size, the Reynolds number, number of variables in the problem and changes from problem to problem. The effect of different relaxation factors on the convergence of the solution for a typical problem can be seen in fig. 3.8 where a high or low relaxation factor does not lead to convergence. It was found that the relaxation factor in the vorticity

equation is strongly affected by the distance of the first node from the wall, when this distance was decreased the relaxation factor had also to be reduced. For the majority of the calculations a relaxation factor of $0.1<\alpha_{rv}<0.7$ was satisfactory for the vorticity and $0.3<\alpha_{r}<0.5$ for the other variables.

3.5 ASSESSMENT OF THE VARIATIONAL SUB-ELEMENT METHOD.

The Variational sub-element method developed in this work was assessed by comparing it with a standard Galerkin solution for a constant viscosity case. In the previous section satisfactory comparison was shown for the vorticity distribution when using four sub-elements, see fig. 3.1d, and a Reynolds number of 100. However the method was further tested by using 6 and 8 sub-elements, see fig. 3.1c and b, and with different Reynolds numbers. Table 3.1 compares the calculated magnitude of vorticity at internal nodes A and B of fig. 3.6 , using both computational methods. In all cases the Variational sub-element has been used with and without the application of the upwinding technique. At the low Reynolds number, Re=10, good agreement is shown between both numerical techniques no matter which type of

sub-element is employed. However, the introduction of upwinding leads to a worsening of the comparison and this was most significant when using 8 sub-elements and least significant using 4 sub-elements. With a Reynolds number of 100 good agreement is shown in all cases and the appliciation of the upwind method didnot lead to a worsening of the comparisons.

When the Reynolds number was increased to 1000 the two methods did not agree satisfactorily unless the "upwind" technique was applied to the Variational sub-element method. The results shown for the Galerkin method did not employ the "upwind" technique, however it was necessary to increase the mesh size from 17*19 to 31*31.

At the high Reynolds number of 10000 no comparatve solution was obtained with the Galerkin method.

When using 8 sub-elements the numerical method proved to be unstable for Reynolds numbers in excess of 1000. Whilst the stability was improved by reducing the width of the element (z direction) it was not always possible to obtain a converged solution. The cause of this instability has not been investigated. The use of 6 sub-elements proved to be the most stable, however a large number of iterations were required when compared to

the use of 4 sub-elements (48 iterations compared to 35). Generally, therefore, 4 sub-elements have been used in the theoretical investigations.

For a typical problem at high Reynolds numbers using the $k-\epsilon$ turbulence model and 441 nodes the computation time was approximately 1 minute of CPU time per iteration when using the HONEYWELL MULTICS system.

POSITION	METHOD	Re=10	Re=100	Re=1000	RE=10000
	G.M	0.250117	0.5423	0.593	no sol.
	VE4(c)	0.2501	0.5424	no sol	no sol.
	VE6(c)	0.2501	0.5481	no sol	no sol.
	VE8(c)	0.2501	0.5513	no sol	no sol.
2,2	VE4(w)	0.2512	0.5418	0.5931	0.6762
	VE6(w)	0.2734	0.5421	0.5822	0.6781
	VE8(w)	0.3169	0.5321	0.6772	no sol.
	G.M	0.069	0.0687	0.0695	no sol.
	VE4(c)	0.069	0.0687	no sol	no sol.
	VE6(c)	0.069	0.0694	no sol	no sol.
	VE8(c)	0.069	0.0694	no sol	no sol.
19,2	VE4(w)	0.0688	0.06878	0.0592	0.05868
	VE6(w)	0.0668	0.06876	0.0593	0.05868
	VE8(w)	0.0761	0.06851	0.0754	no sol.

TABLE 3.1: Comparison of the vorticity values between different elements and method.

G.M- Central Galerkin method

VE4- Variational method with type 4 sub-element

VE6- Variational method with type 6 sub-element

VE8- Variational method with type 8 sub-element

(c)- Central method

(w)- Upwind method

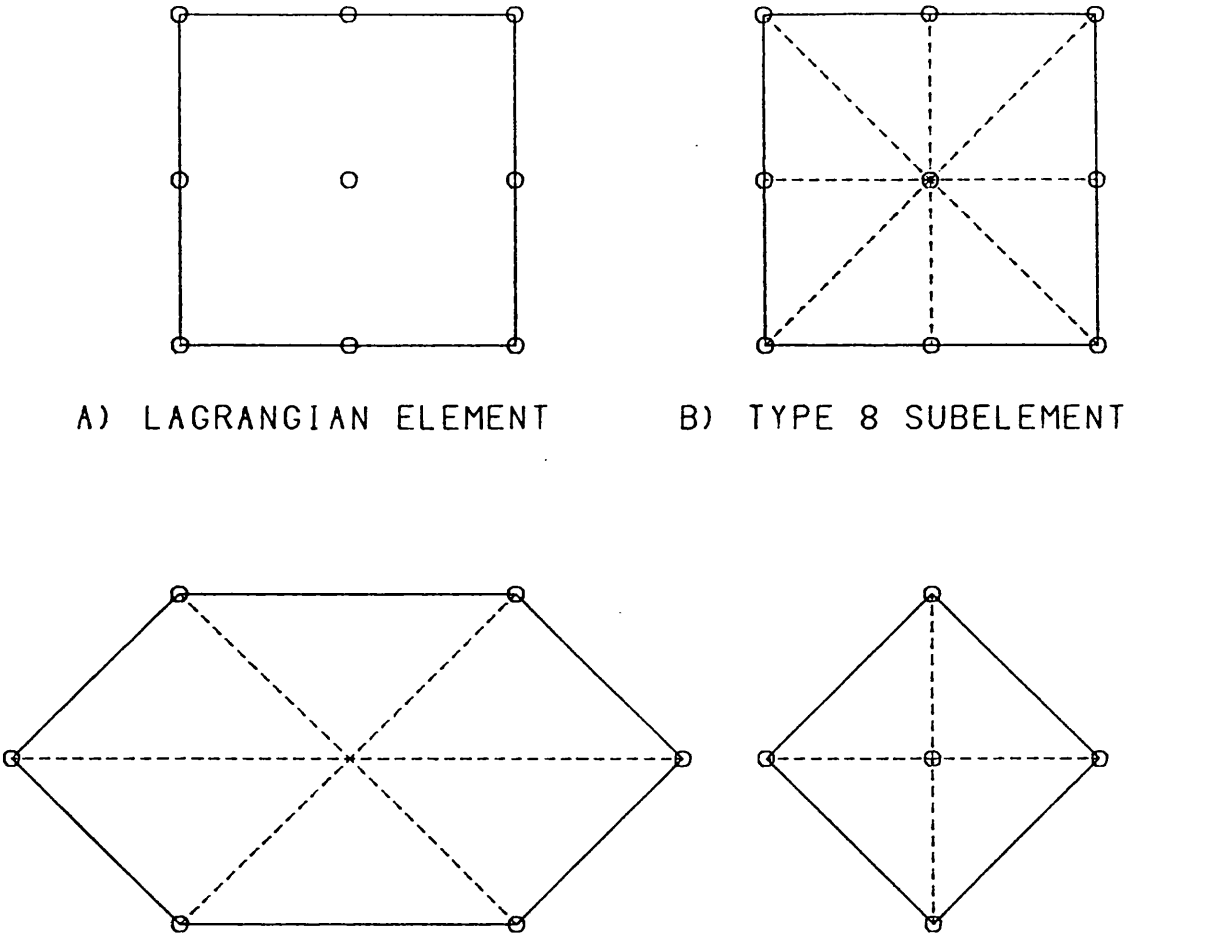

FIGURE 3.1: Type of elements which have been used in the present work.

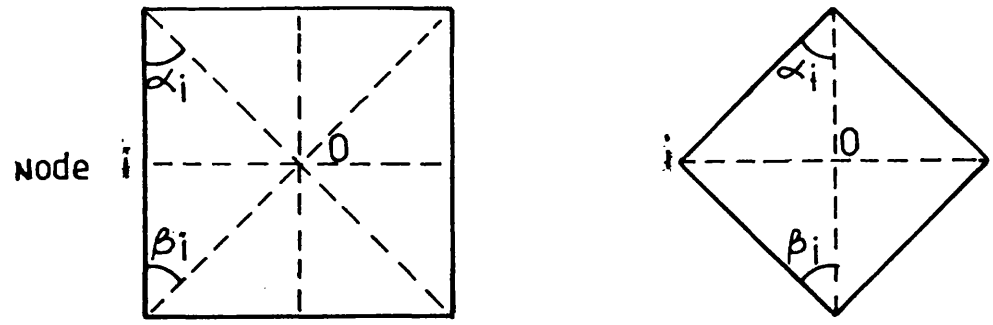

FIGURE 3.2: The definition of the element angles.

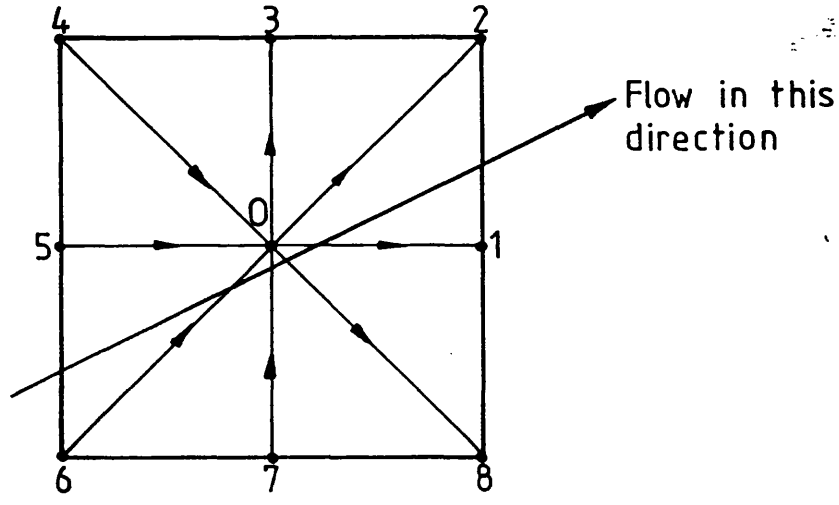

FIGURE 3.3: A typical element with direction of the flow.

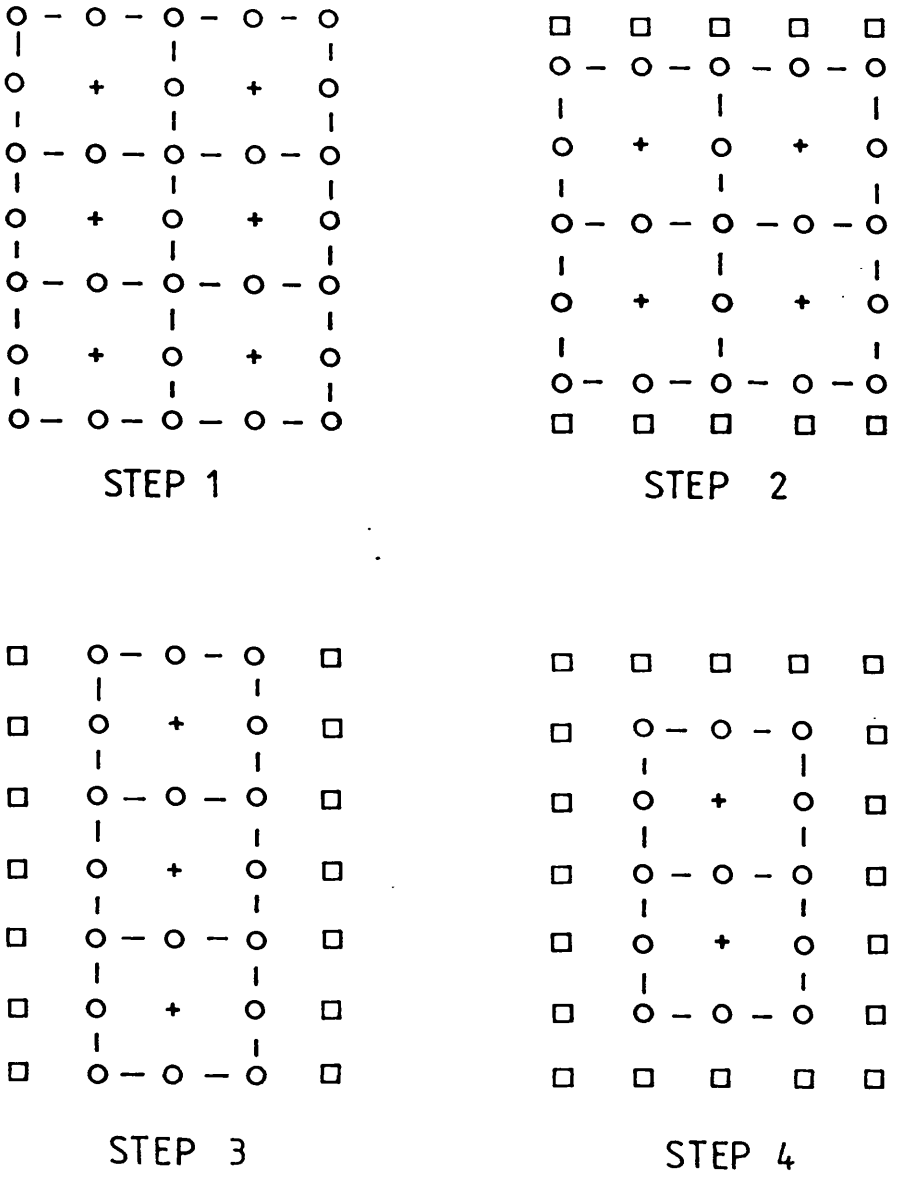

FIGURE 3.4: Regeneration of the mesh for the "point successive under relaxation" method.

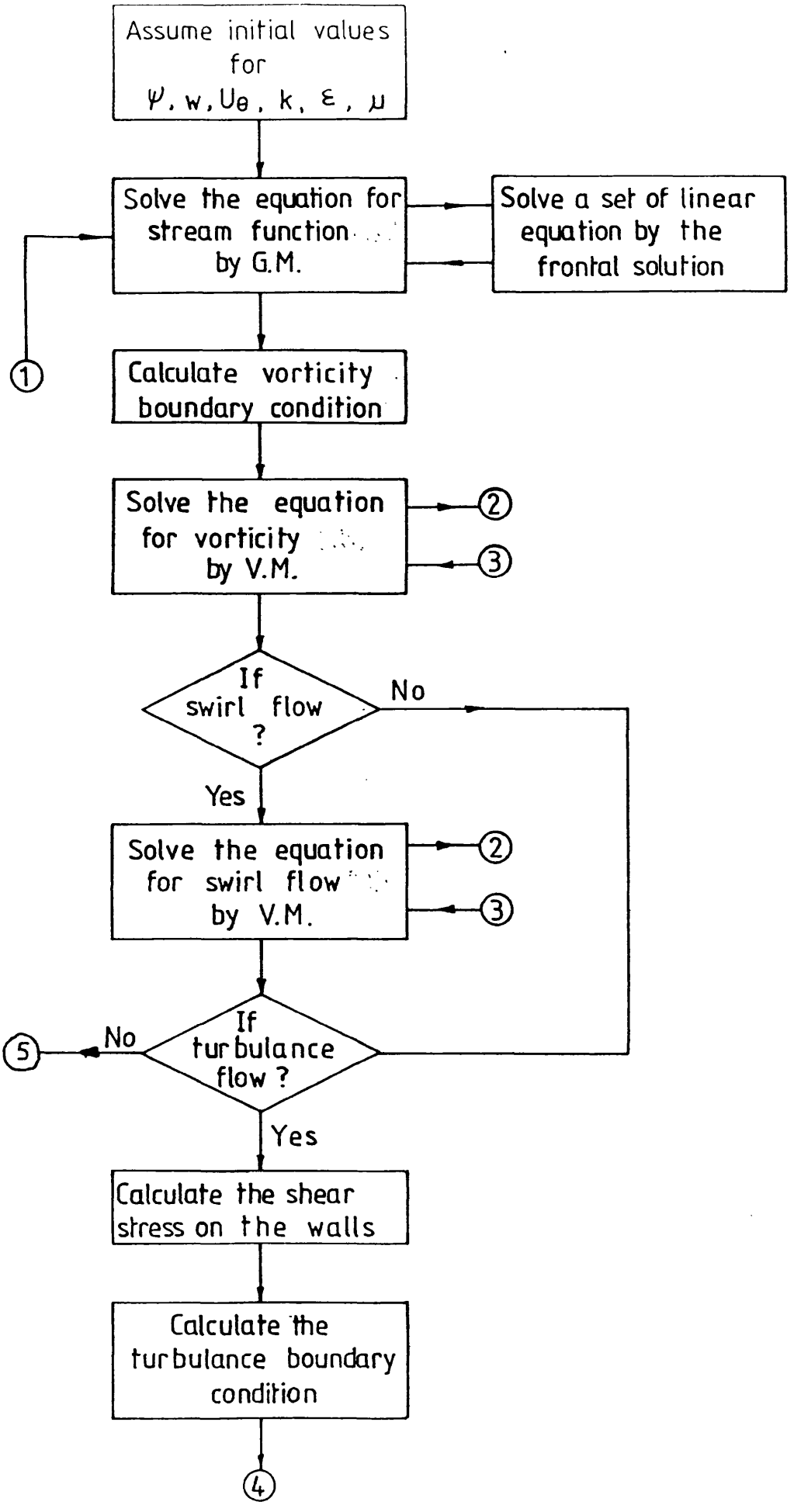

FIGURE 3.5: The flow chart of the present procedure.

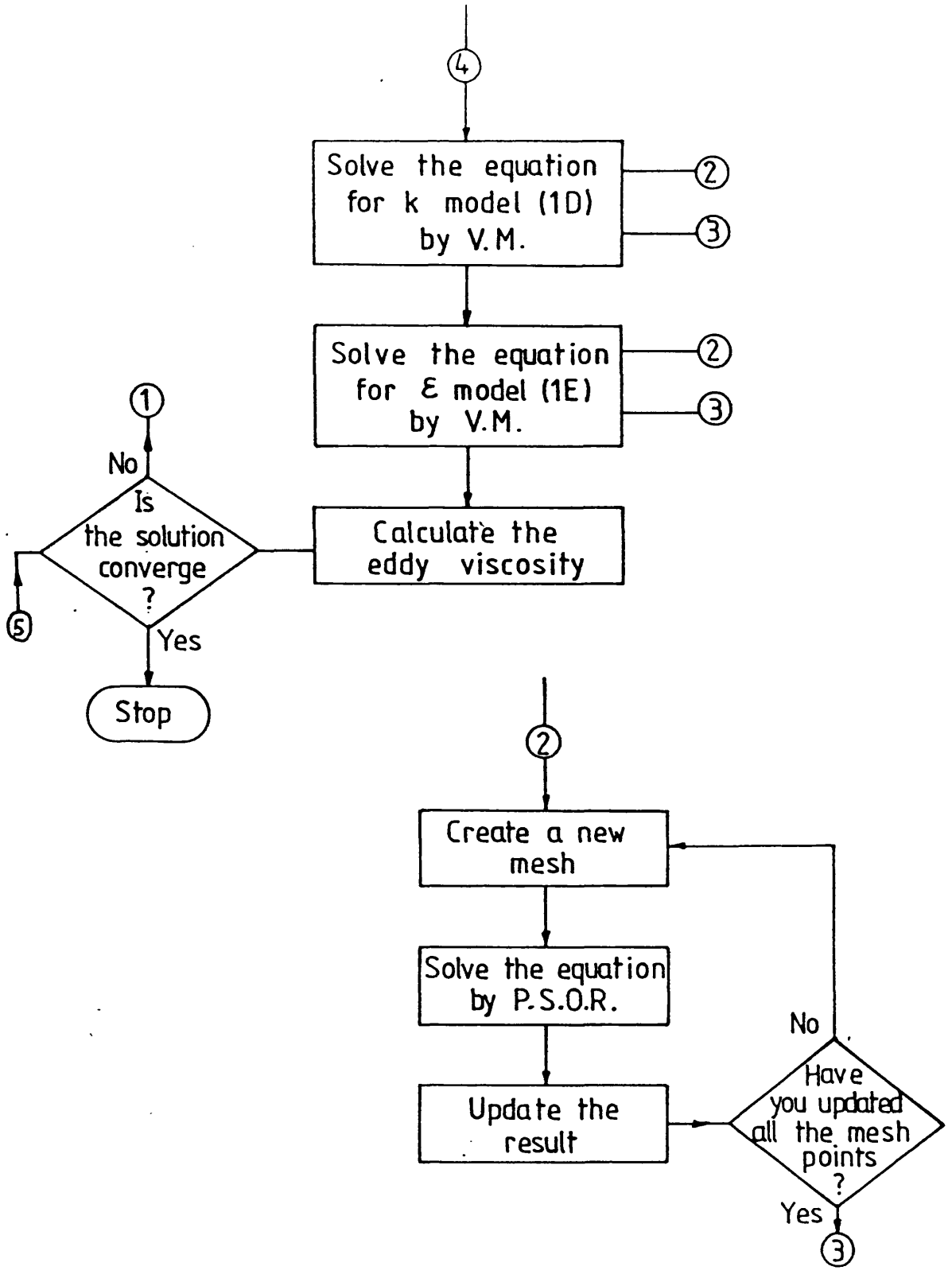

G.M. - Galerkin method
V.M. - Variational method
P.S.O.R. - Points successive over relaxation

FIGURE 3.5: Continued

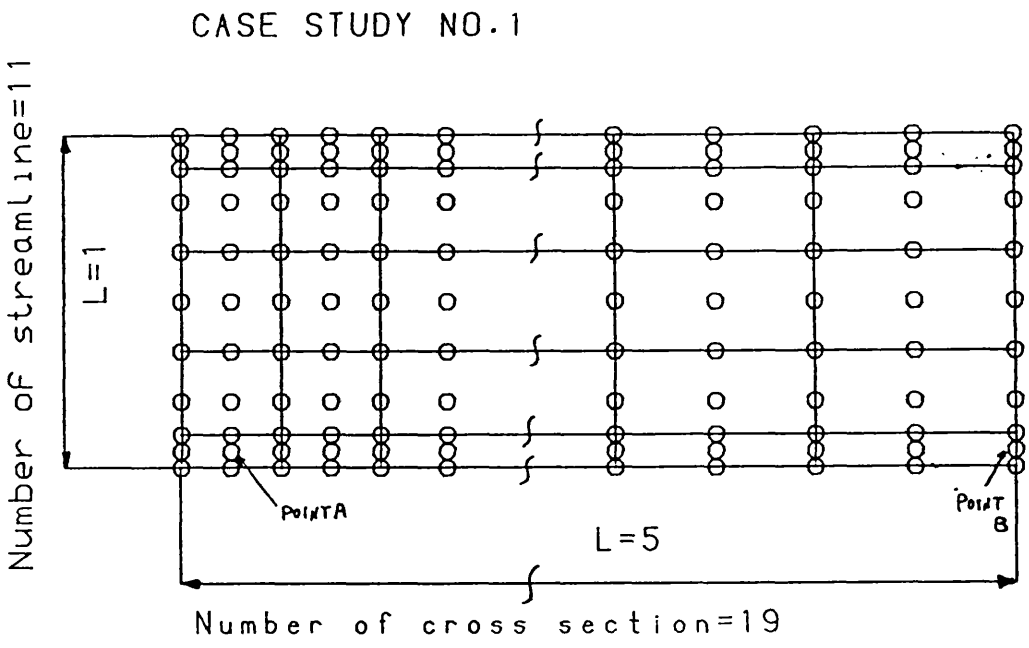

FIGURE 3.6: Typical finite element mesh.
(Lagrangian elements)

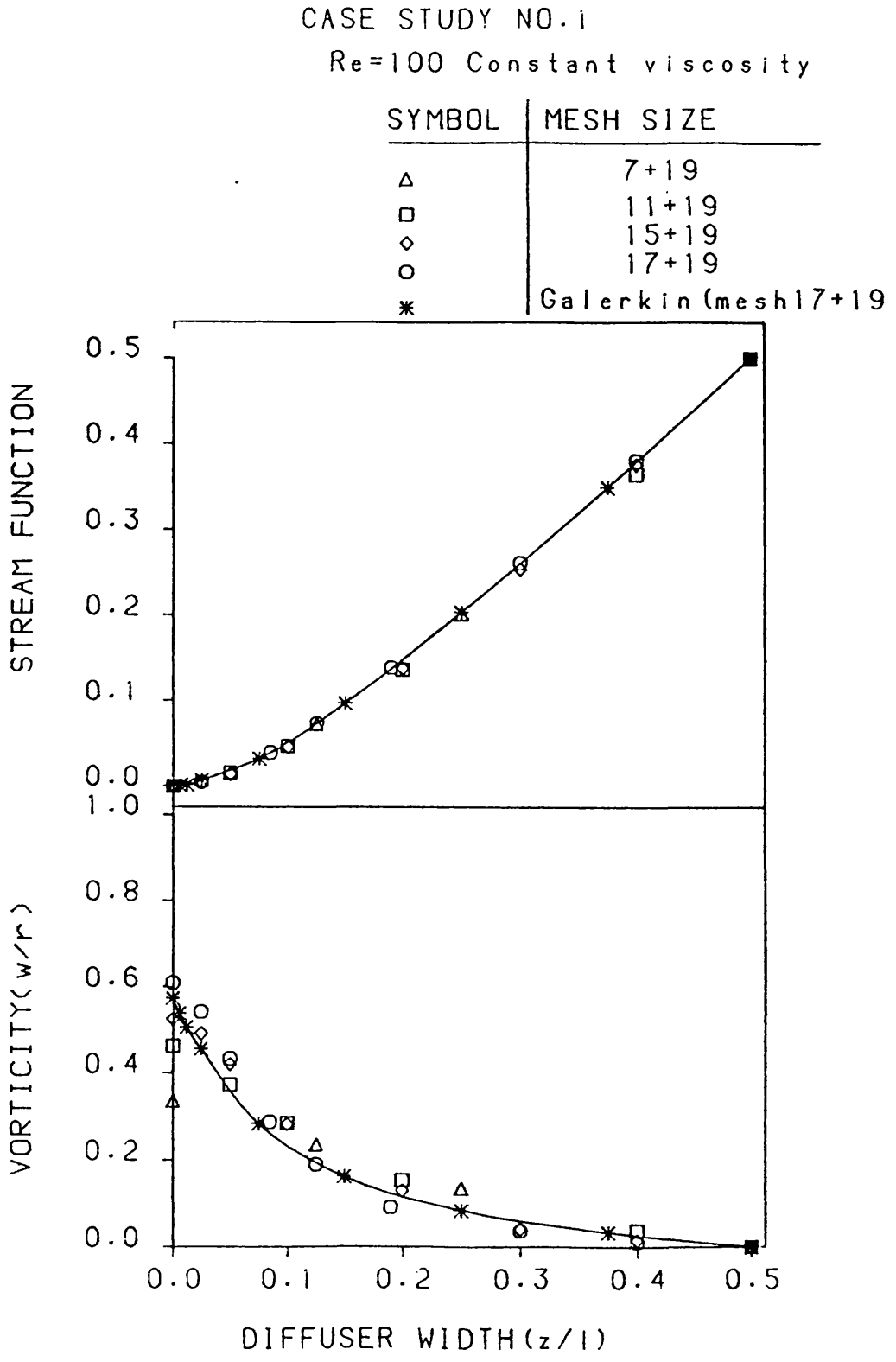

FIGURE 3.7: Effect of mesh size on the numerical solution.

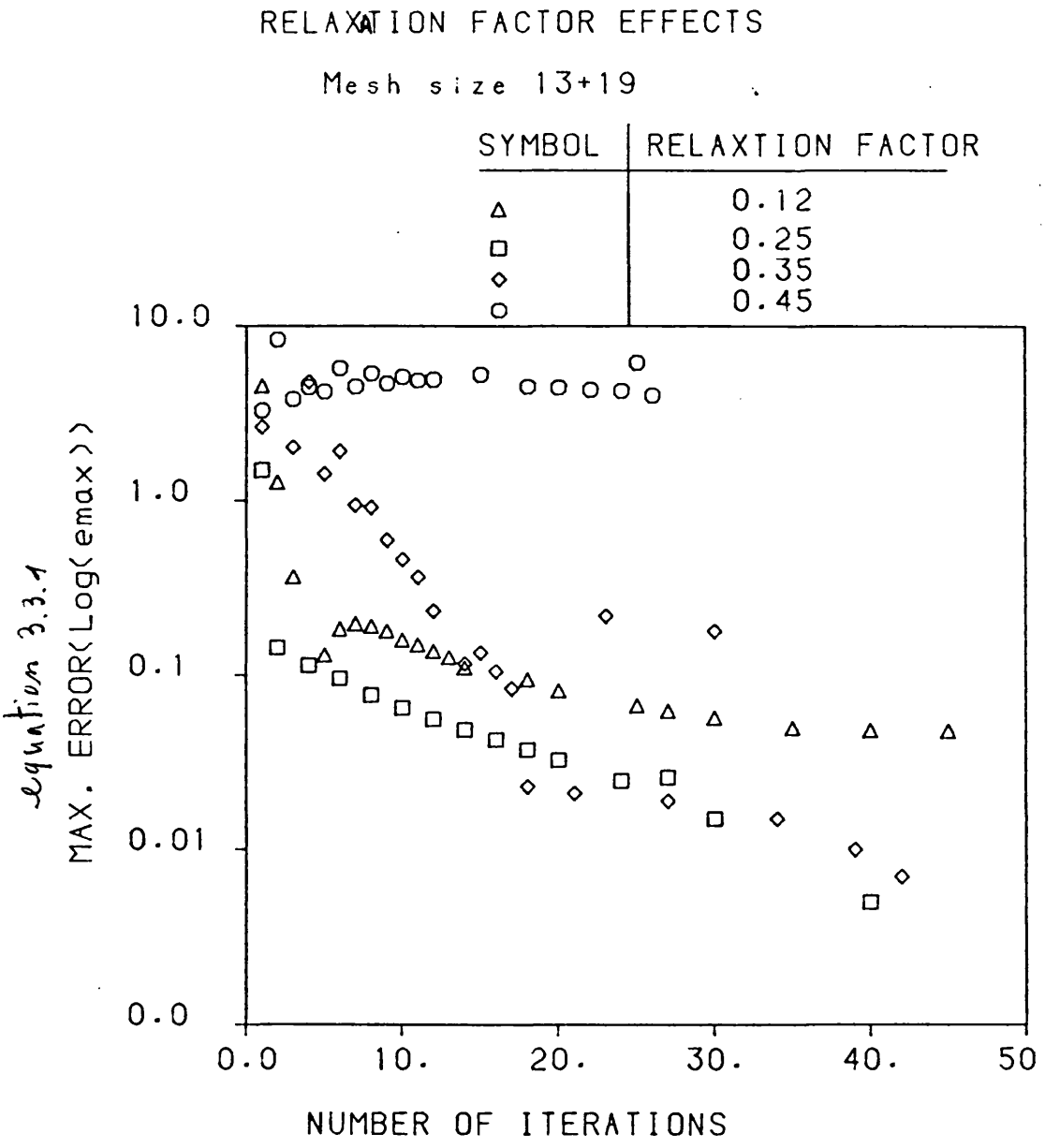

FIGURE 3.8: Effect of the vorticity relaxation factor upon the convergance of the solution.

CHAPTER 4

APPLICATION OF THE THEORETICAL ANALYSIS TO FLOW IN ANNULAR DIFFUSERS.

The initial development of the theoretical analysis and numerical procedure was carried out by applying it to existing published data. The numerical procedure was then further studied by investigating the effect of specified inlet flow conditions upon the predicted flow structure in the diffuser. With the development of the experimental investigation reported here the theoretical analysis was applied to a number of typical experimental configurations. All calculations have assumed "isotropic" turbulence where equal radial and tangential effective viscosities are used.

4.1 DEVELOPMENT WITH RESPECT TO PUBLISHED DATA

The simplest flow situation relevant to this investigation is that of non-swirling flow through a radial diffuser. VOORDE and BOS(1972) presented experimental results for such a situation with a diffuser

having inlet and discharge radii of 0.25m and 0.61m. For the theoretical analysis a uniform inlet flow with no boundary layer and a Reynolds number of 3*10 was assumed. The development of the predicted boundary layer thickness and friction velocity with radius ratio is compared with the results of VOORDE and BOS in fig. 4.1. Satisfactory agreement is shown and the differences are considered to be due to not specifying the inlet conditions precisely and due to the interpolation procedure, based upon the fixed mesh of the finite element method, used to calculate the boundary layer thickness and by using the logarithmic law of the wall for calculating the friction velocity.

For the full swirling flow in radial diffusers the analysis was applied to the diffuser configuration reported by JANSEN(1964). The theoretical analysis was applied to flow conditions which gave inlet flow angles of 47 and 70.5 degrees. The specified inlet conditions assumed uniform meridional and tangential velocity profiles with the no slip condition specified for the tangential velocity at the wall surfaces. The predicted tangential and meridional velocity profiles are compared with JANSEN's results at three radial stations in fig. 4.2 and 4.3. For both flow conditions satisfactory

agreement has been achieved at each station, with only the discharge tangential velocity profiles showing any significant difference from JANSEN's results. Differences at the two inner radius ratios, fig 4.3, are considered to be due to the specified inlet conditions which were not identical to those given by JANSEN.

4.2 EFFECT OF INLET FLOW PROFILES ON RADIAL DIFFUSER PERFORMANCE

Having developed the numerical procedure it was employed to investigate the effect of inlet flow conditions upon the internal flow pattern of the different types of diffuser. The meridional and tangential velocity profiles were changed systematically in order to vary the diffuser inlet flow conditions. The bulk of this study was concentrated on the radial diffuser and table 4.1 gives details of all the cases presented. The accuracy of the solution depends largely upon the mesh size used. Typically for the radial diffuser 8 quadrilateral elements have been used across the width of the diffuser and 11 in the radial direction. As is shown in fig. 4.4 a fine mesh has been used closed to the diffuser walls where large velocity gradients exist.

4.2.1 Uniform velocity profiles

The first three flow conditions presented maintained a uniform inlet velocity profile, but by increasing the magnitude of the tangential velocity component, while keeping the meridional velocity constant, the inlet flow angle was systematically increased, see table 4.1. The predicted results at three radial stations show that the meridional velocity distribution developed a parabolic profile at discharge indicating a fully developed turbulent flow, figs. 4.5, 4.6 and 4.7. In addition the increasing inlet flow angle has no effect upon the development of the meridional velocity profile, the predicted results in each case being identical showing that it is governed strongly by the continuity requirement. The tangential velocity profile clearly shows the development of the boundary layer, whilst the core flow shows a reduction in magnitude as expected from the basic free vortex relationship. If the tangential velocity was presented non-dimensionally based upon the inlet tangential velocity, then it would not be possible to see any significant change in profile as the flow angle was increased. The relocation of the imposed discharge boundary condition to an increased radius ratio of 2.6 had no effect upon the predicted flow profile at

the radius ratio of 1.6 .

It is known from the experimental results of JANSEN, and those presented here, that as flow angle is increased eventually separation and flow reversal will occur. It was accepted during the development of the theoretical analysis that it would not be possible to predict flow profiles where separation occurs. Predictions were made up to an inlet flow angle of 85 degrees, however beyond this it was not possible to obtain a converged solution. A number of calculations were performed with different mesh sizes and relaxation factors but convergence was not achieved. The divergence of the numerical solution is due to the dominance of the source term in the vorticity equation when the flow angle became large.

4.2.2 Shear meridional velocity profile

The effect of three linear meridional velocity distributions at diffuser inlet have been studied whilst maintaining a uniform tangential velocity profile and a constant mean flow angle of 51 degrees. Fig. 4.8 shows a moderate degree of shear flow at inlet, while fig. 4.9 and 4.10 show a more progressively highly distorted flow with the velocity increasing linearly from hub to shroud. The modest change from uniform flow conditions shown in

fig. 4.8 has no significant effect on the diffuser flow. Of the more severely distorted inlet flows that shown in fig. 4.10 leads to the most significant modification to the internal flow structure. At the a radius ratio of 1.254 indications of reverse flow on the hub surface are present. To handle separation and reverse flows the computation was continued by applying a constant kinematic viscosity when the turbulence model was not satisfactory. The meridional velocity gradient at inlet has also led to the development of a gradient in tangential velocity at radius ratio 1.254. At the discharge radius ratio of 1.6 a fully developed parabolic profile is shown; this, however, is due to the location of the outlet boundary condition. By moving the outlet boundary from a radius ratio of 1.75 to 2.5 the predicted profiles at the radius ratio 1.6 were modified for test 16, fig. 4.10, but not significantly for case 15, fig 4.9. The modified flow profiles are presented in fig. 4.11.

The predicted results show that vorticity at inlet cause a separation in the flow downstream, this phenomenon was studied by ELLIS(1964). This theory can explain why no flow revesal are predicted for the cases with uniform velocity profiles.

4.2.3 Effect of tangential velocity profile

The effect of a gradient in tangential velocity at inlet was investigated in a similar manner to that described for the meridional velocity profile. By keeping the meridional velocity constant and the same mean tangential velocity the mean inlet flow angle was 51 degrees in each case. The effect of introducing a gradient in tangential velocity was not as significant as that for the meridional velocity profile. For test case No. 17, fig. 4.12, the tangential velocity gradient diminished through the diffuser passage but persisted to the final radius ratio. With an increase in velocity gradient, case No. 19, fig. 4.13, a shear flow profile was developed in the meridional component of velocity but no tendency towards flow separation was detected. For these case no modification to the predicted results occurred by moving the discharge boundary condition downstream. Further increases in the tangential velocity gradient led to instabilities in the numerical solution.

4.3 STUDY OF CURVED AND CONICAL MIXED FLOW DIFFUSERS

In the previous section the geometry of the diffuser was kept the same and only the the inlet flow conditions were changed. For non-radial flow diffusers a choice exists between straight conical and curved diffusers and the theoretical study was, therefore, extended to these diffusers in order to assess the effect of introducing curvature upon the predicted flow structure and stability.

4.3.1 Curved diffusers

A curved diffuser with an overall size equal to that used in the experimental work was chosen to study the flow structure.

Three different inlet condition were chosen, see table 4.1 cases 20, 21, 22. In all cases the tangential velocity increased from hub to shroud due to the increase in radius of the rotating conical screen. To avoid the need to modify the turbulence equations for curved surfaces a very fine mesh, 25*23 nodes, was introduced, see fig. 4.14.

For test 20 in which a uniform meridional velocity was

assumed, no separation area was observed near the hub or shroud, see fig. 4.15. The effect of curvature on the meridional velocity profile can be seen at the outer radius ratio of 1.55 where a non symmetrical profile has developed.

The effect of introducing a gradient in the meridional velocity at inlet was investigated in cases 21 and 22, see figs. 4.16 and 4.17. In case 21, fig. 4.16, it is clear that a low velocity area develops near the hub at a radius ratio 1.16, which could lead to separation. This low velocity area reduces downstream in the radial part, and at a radius ratio of 1.55 it can no longer be seen. By introducing a meridional velocity gradient in the oposite direction, Fig. 4.17, no tendency towards separation can be observed, and the flow profile is similar to that of case 20. Fig. 4.18 and fig. 4.19 show a schematic velocity distribution throughout the curved diffuser for cases with an increased meridional velocity gradient (52 deg.). Whilst it was difficult to obtain a good converged solution, an error of approximately 15% existed, a separation area was indicated near the hub or shroud corresponding to the direction of the velocity gradient.

4.3.2 Conical diffuser

The geometry of the diffuser studied was identical to that used in the experimental investigation. The finite element mesh is shown in fig. 4.20 and again a fine mesh near the wall was introduced to avoid the need to modify the turbulence equations.

For cases 23 and 24 the tangential velocity profile was the same as in the curved diffuser. For case 23, fig. 4.21, a uniform meridional velocity profile was assumed and no separation area was observed; however at the discharge radius ratio of 1.55 the meridional velocity profile is asymmetric and a low velocity zone has developed on the hub surface. By introducing a small gradient in the meridional velocity (26 deg.), case 24, a separation area was indicated at a radius ratio of 1.254 which disapeared down stream, see fig. 4.22. This result was obtained with the exit boundary at a radius 20 times the diffuser width. The numerical procedure was not fully converged and an error of the order of 10% existed.

In all cases studied the continuity equation strongly dominates the solution. For the application to the curved and conical diffusers the boundary layer equations, which are applicable to flat surfaces, have

not been extended to curved surfaces. However it is felt that this is not a serious limitation for cases presented here as a fine mesh has usually been applied.

CASE No.	DIFFUSER TYPE	MERIDIONAL VELOCITY	TANGINTIAL VELOCITY	FLOW ANGLE
11	radial	uniform	uniform	37
12	radial	uniform	uniform	51.3
13	radial	uniform	uniform	63
14	radial	shear(11)	uniform	51.3
15	radial	shear(37)	uniform	51.3
16	radial	shear(47)	uniform	51.3
17	radial	uniform	shear(35)	51.3
18	radial	uniform	shear(45)	51.3
19	radial	uniform	shear(52)	51.3
20	curved	uniform	shear	63
21	curved	shear(26)	shear	63
22	curved	shear(-26)	shear	63
23	conical	uniform	shear	63
24	conical	shear 26	shear	63

TABLE 4.1: Diffuser types and flow conditions in the theoretical

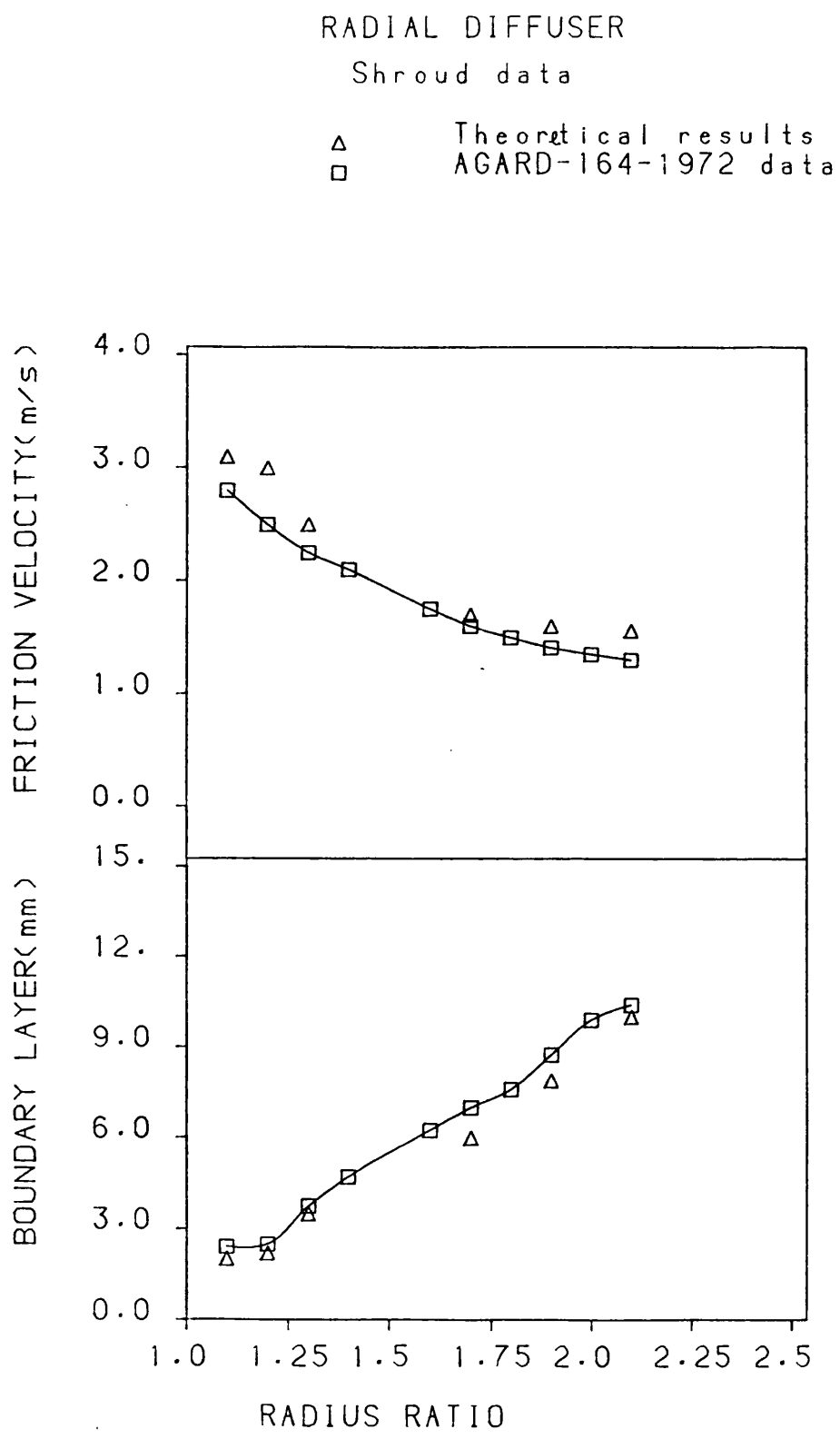

FIGURE 4.1: Comparison of the boundary layer thickness and the friction velocity between VOORDE (AGARD-164-1972) data and the present method.

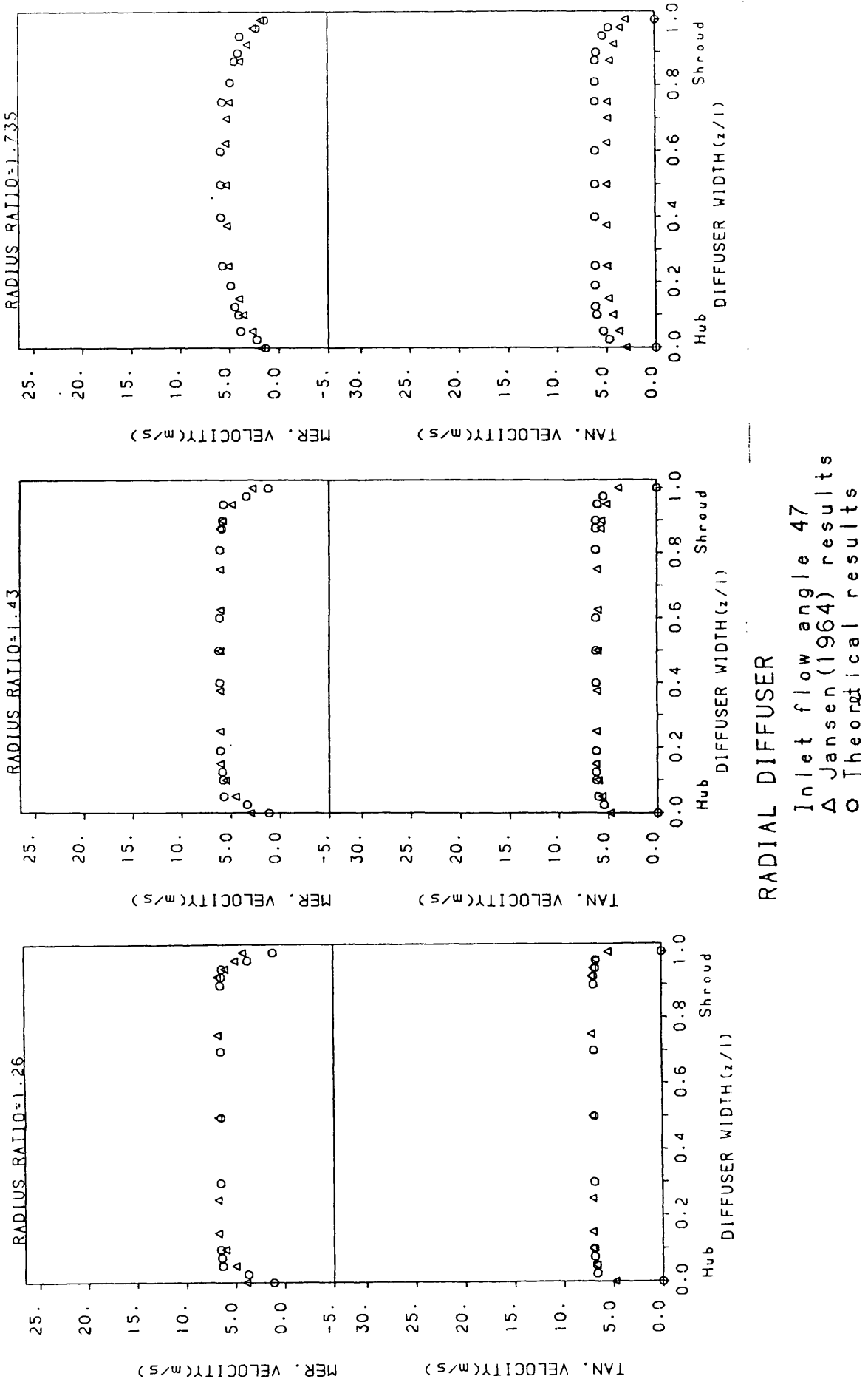

FIGURE 4.2: Comparison of the velocity profiles at different cross sections between JANSEN (1964) and the present method.

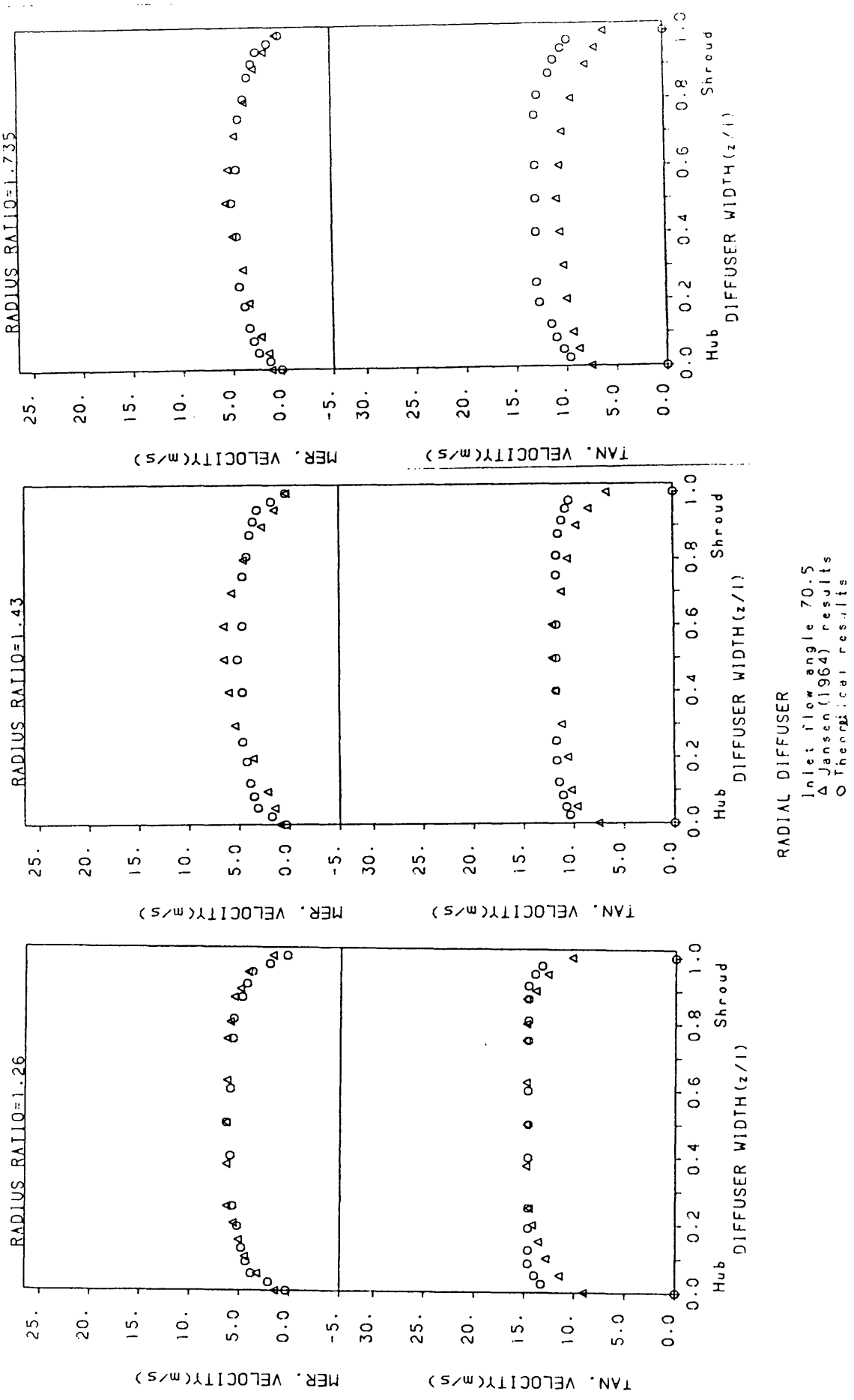

FIGURE 4.3: Comparison of the velocity profiles at different cross sections between JANSEN (1964) and the present method.

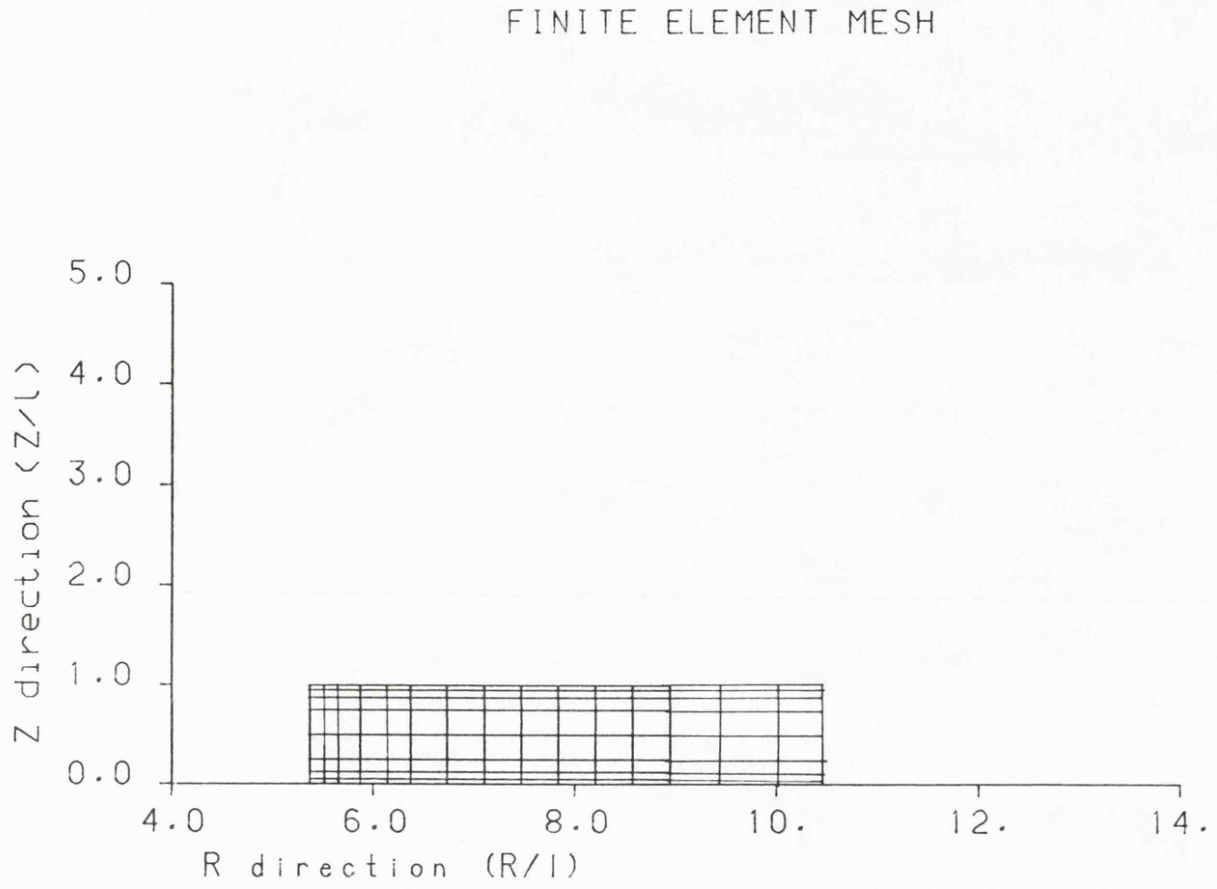

FIGURE 4.4: A typical finite element mesh for a radial diffuser.

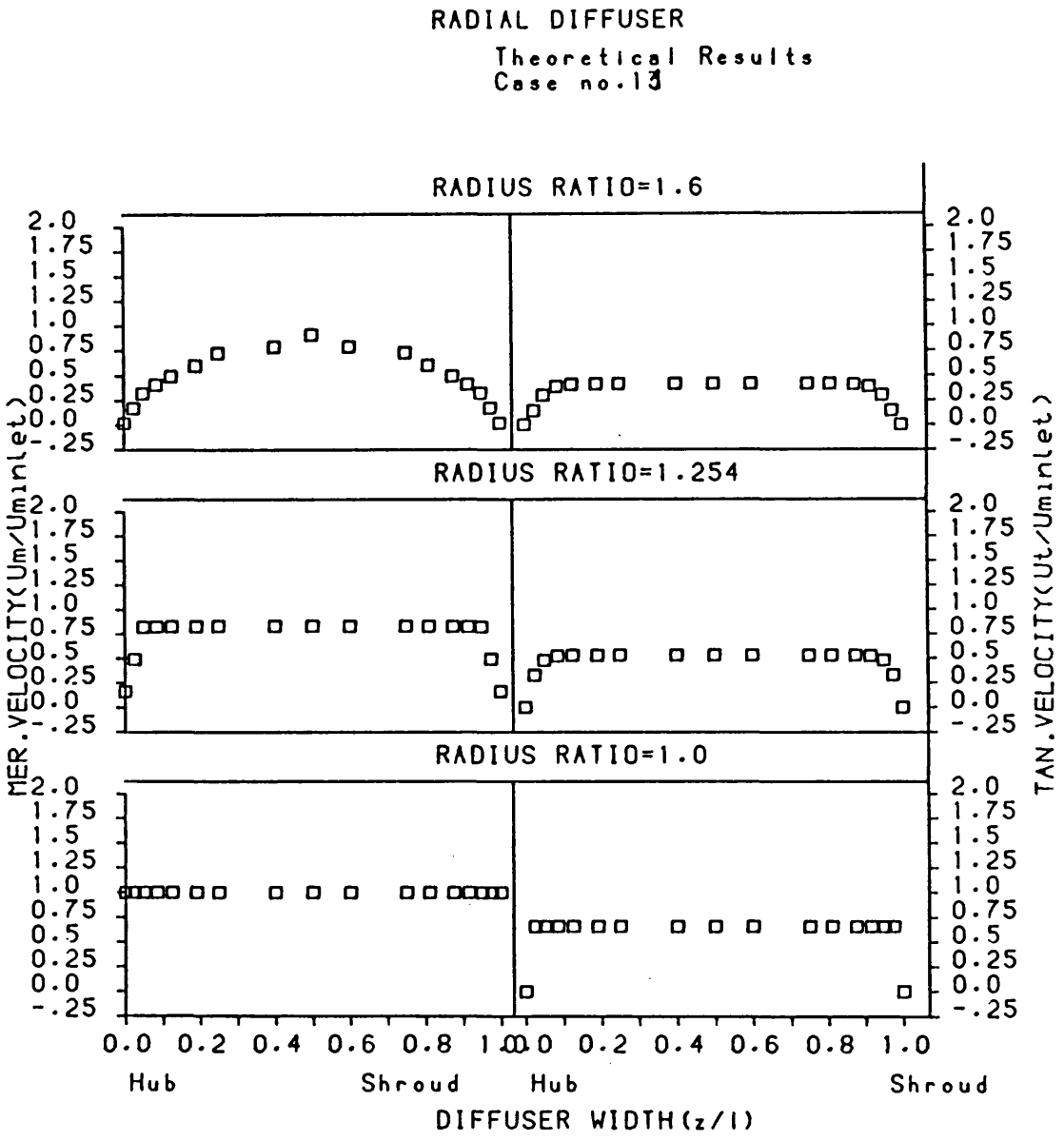

FIGURE 4.5: Predicted velocity distribution in a radial diffuser, with an inlet flow angle of 33.7 degrees.

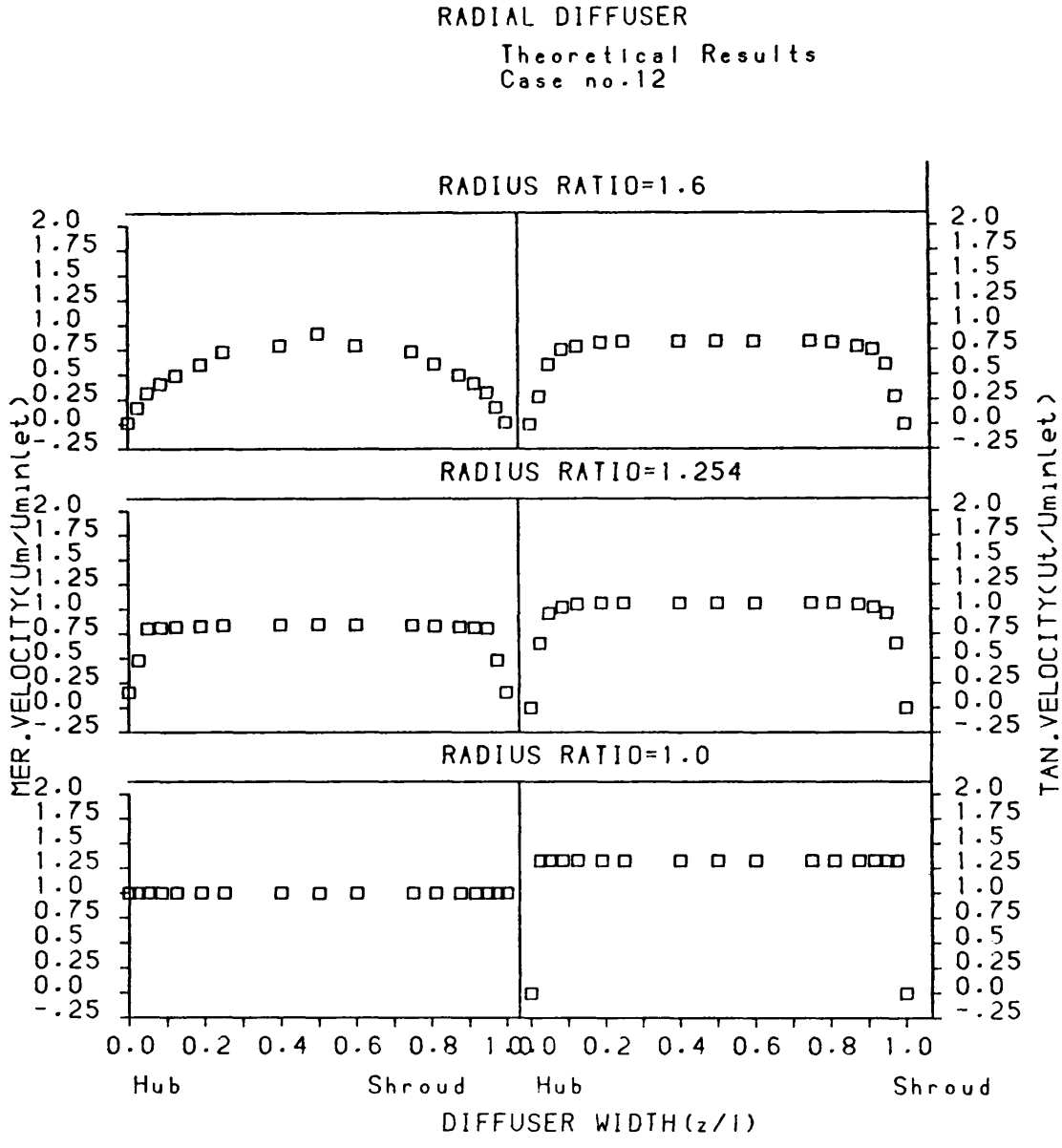

FIGURE 4.6: Predicted velocity distribution in a radial diffuser, with an inlet flow angle of 53. degrees.

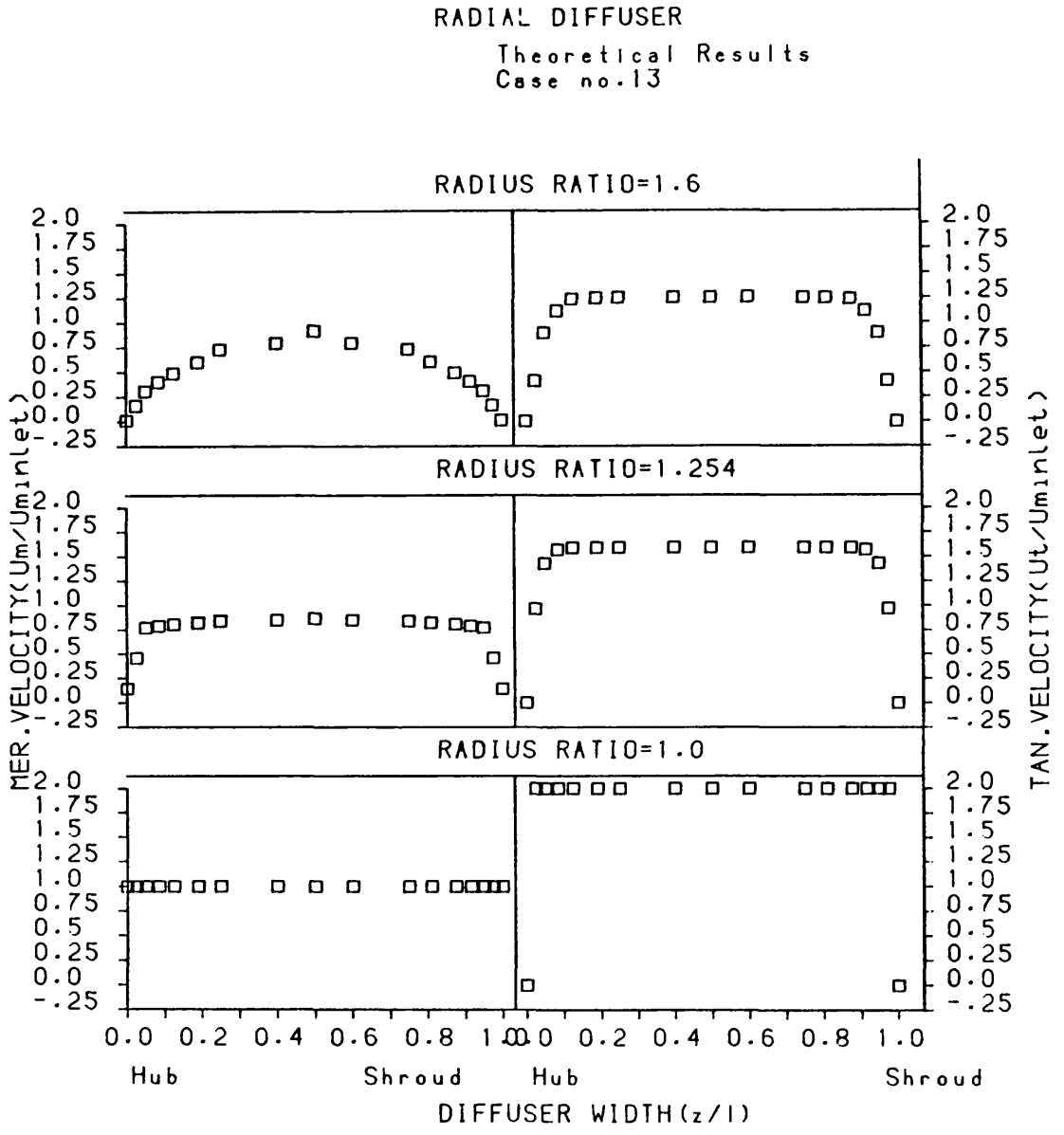

FIGURE 4.7: Predicted velocity distribution in a radial diffuser, with an inlet flow angle of 63.4 degrees.

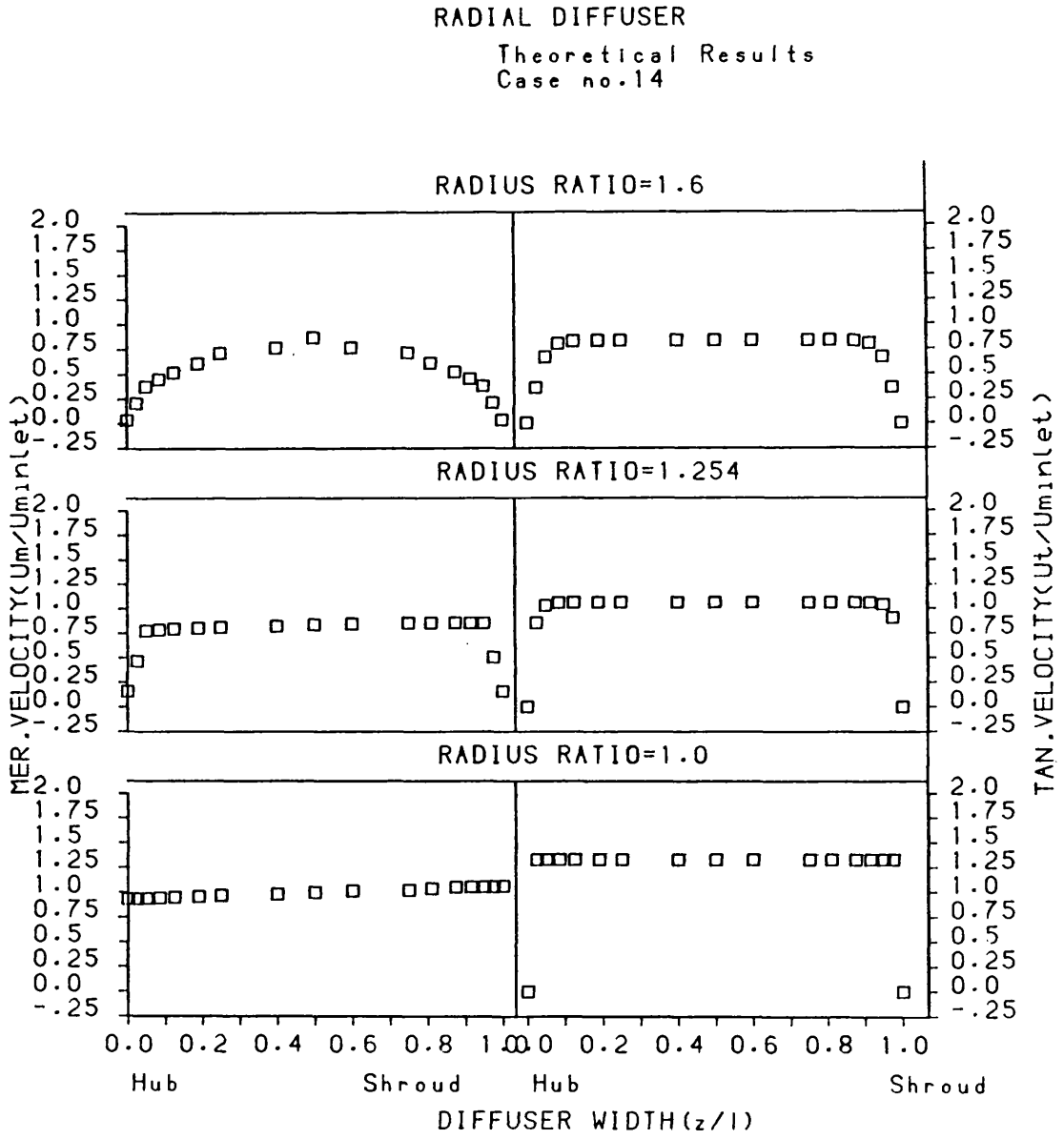

FIGURE 4.8: Predicted velocity distribution in a radial diffuser.
(Inlet shear meridional velocity of 10.)

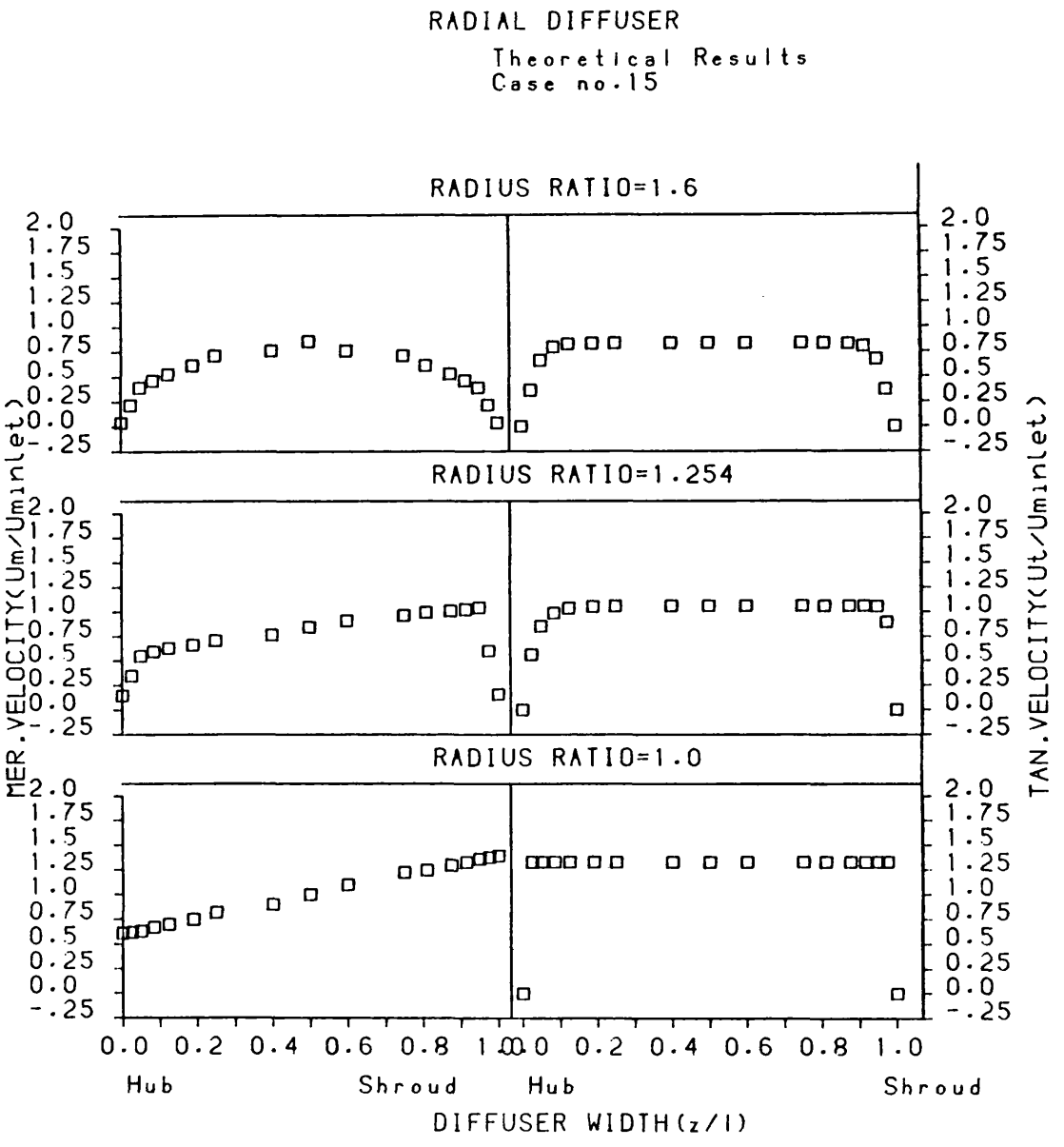

FIGURE 4.9: Predicted velocity distribution in a radial diffuser.
(Inlet shear meridional velocity of 37°.)

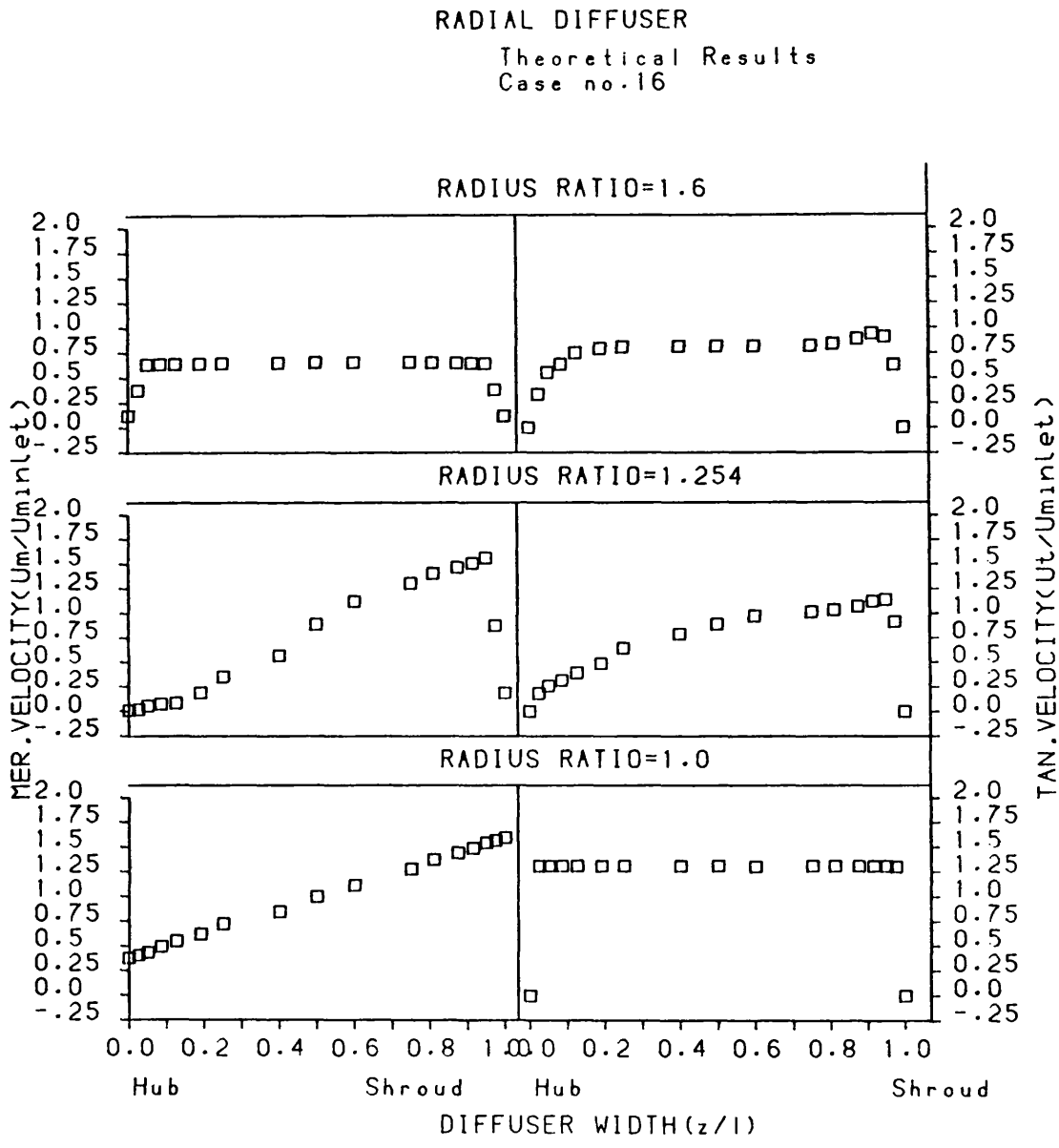

FIGURE 4.10: Predicted velocity distribution in a radial diffuser.

(Inlet shear meridional velocity of 47.°)

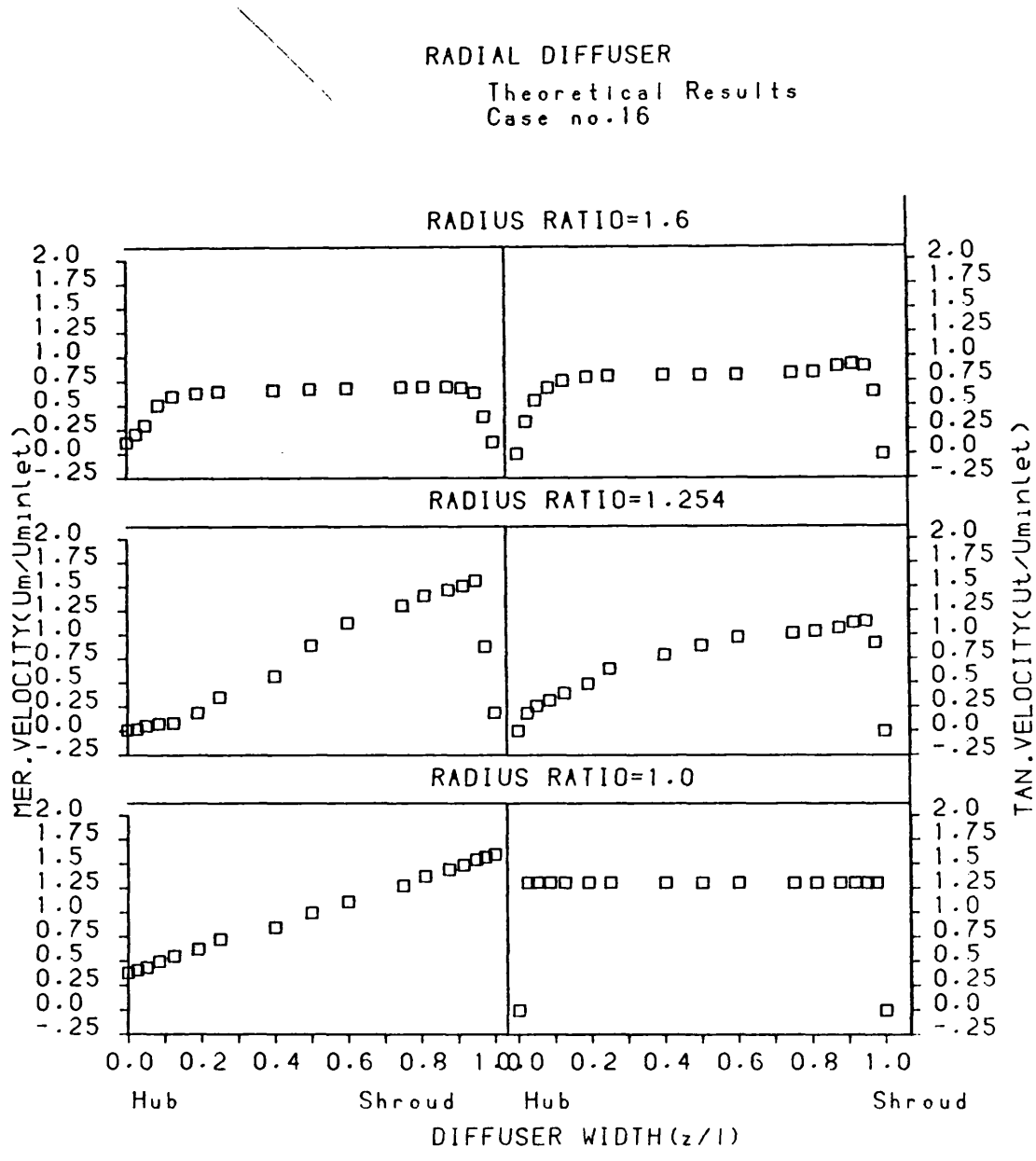

FIGURE 4.11: Predicted velocity distribution in a radial diffuser with a more remote outlet boundary condition.
(Inlet shear meridional velocity of 47)

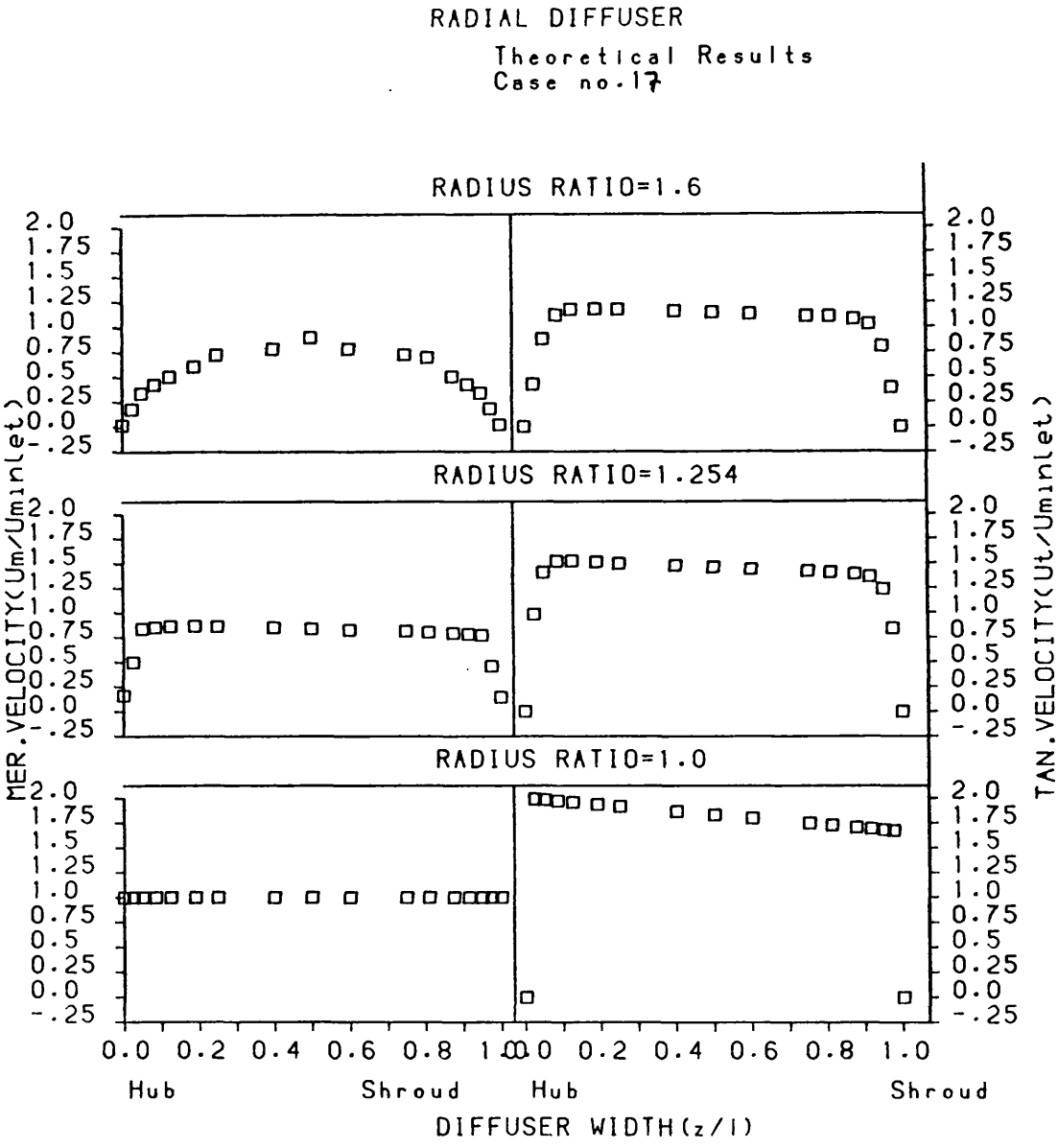

FIGURE 4.12: Predicted velocity distribution in a radial diffuser.
(Inlet shear tangential velocity of 45°)

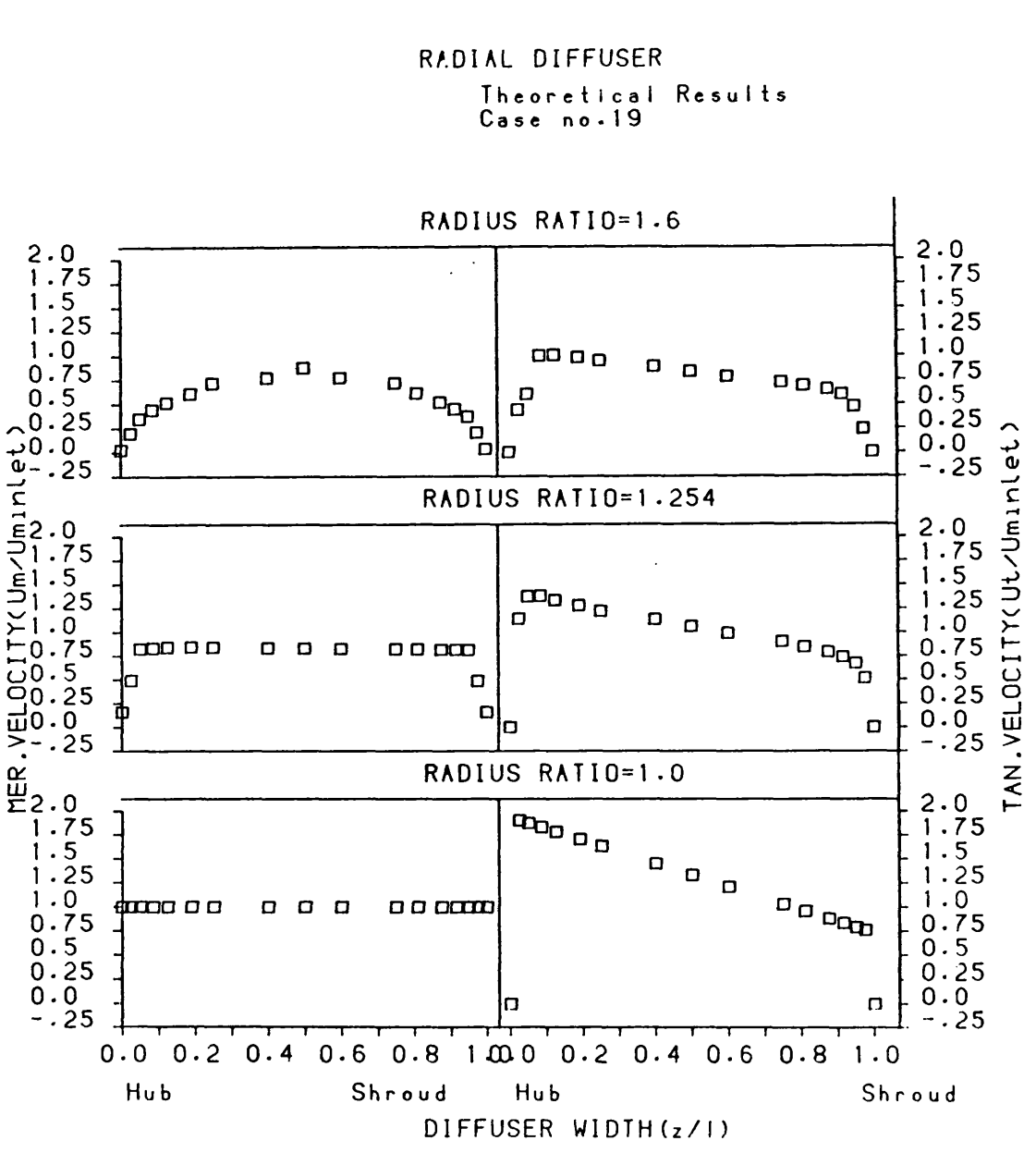

FIGURE 4.13: Predicted velocity distribution in a radial diffuser.
(Inlet shear tangential velocity of 52°)

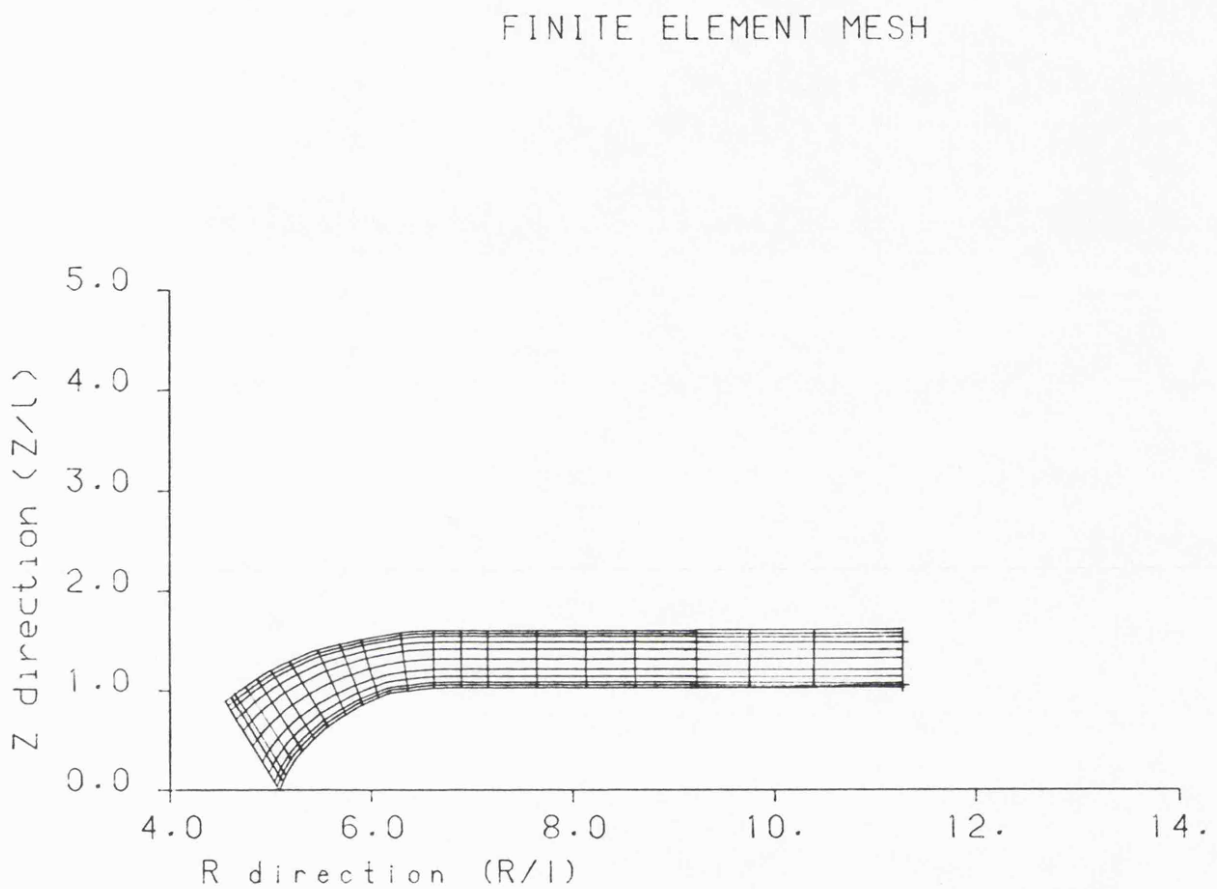

FIGURE 4.14: A finite element mesh for a curved diffuser.

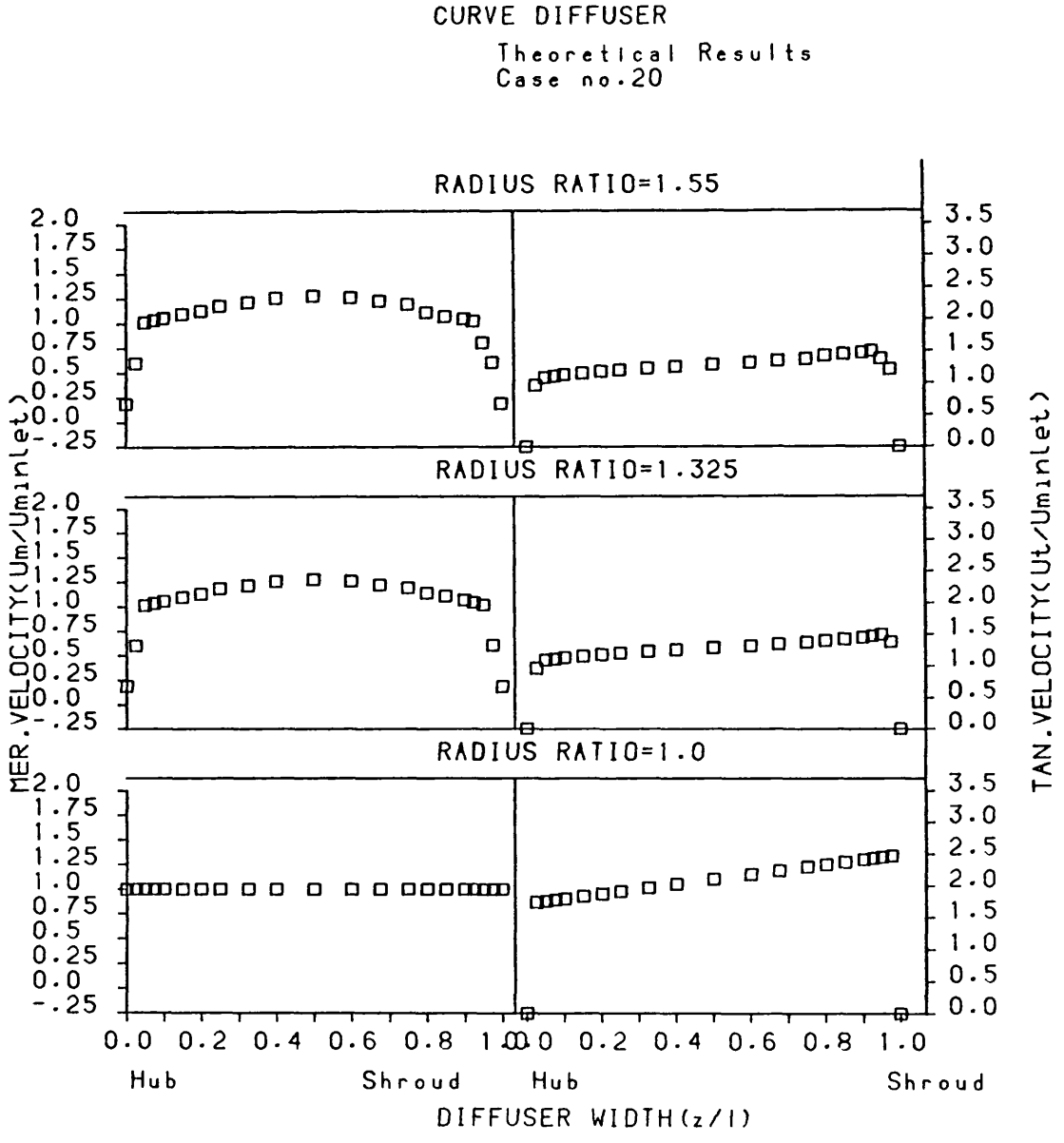

FIGURE 4.15: Predicted velocity distribution in a curved diffuser.

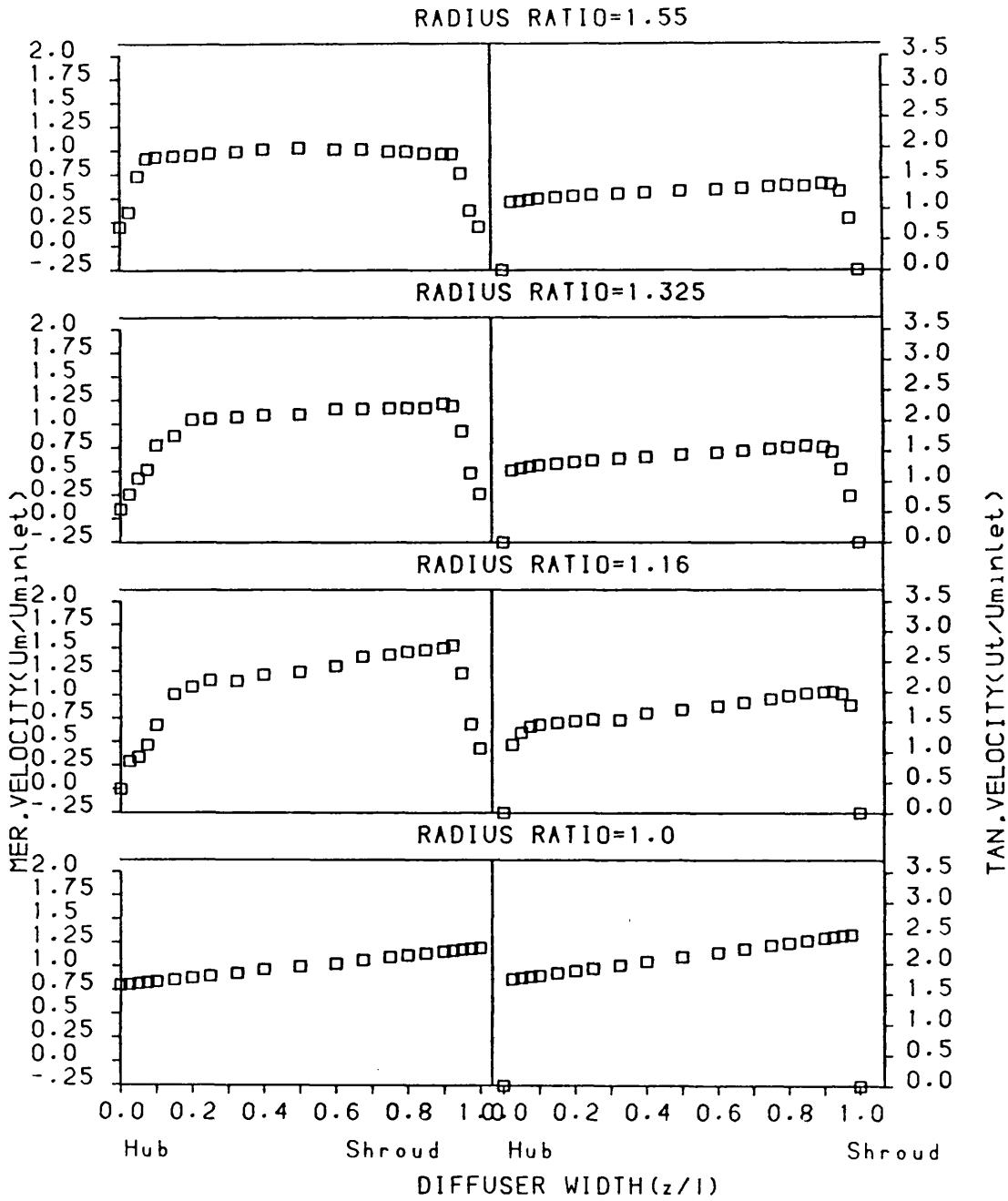

FIGURE 4.16: Predicted velocity distribution in a curved diffuser.
(Inlet shear meridional velocity of 26.^{o})

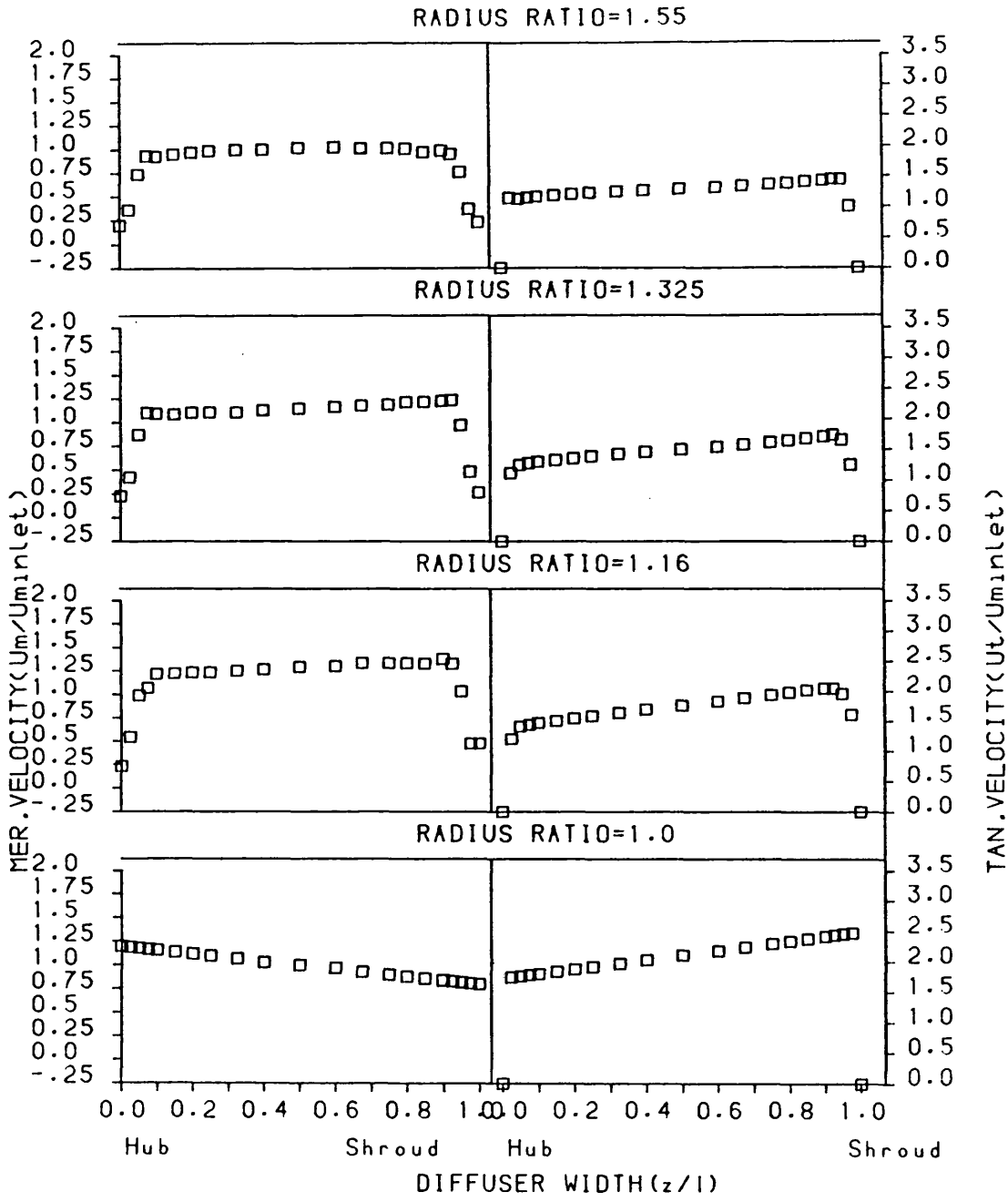

FIGURE 4.17: Predicted velocity disttribution in a curved diffuser.
(Inlet shear meridional velocity of -26°.)

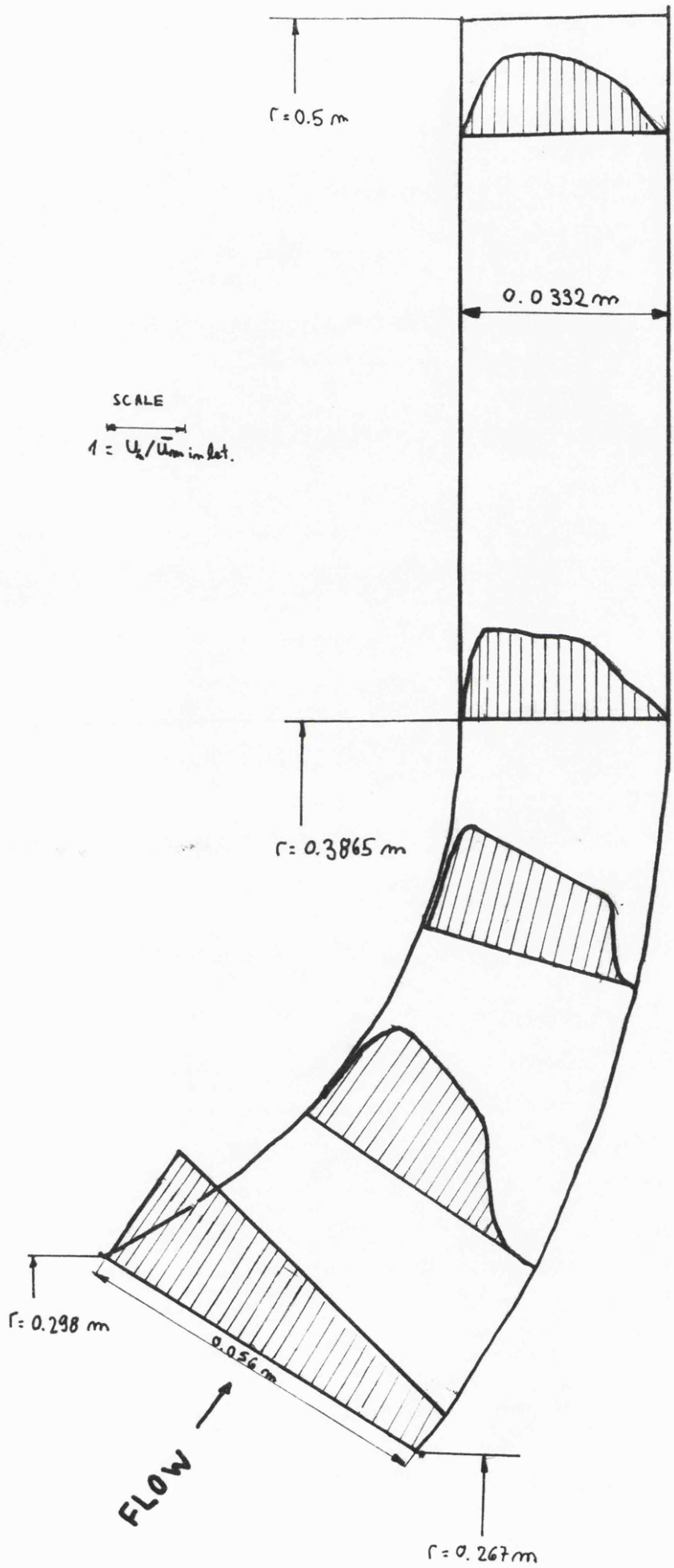

FIGURE 4.18: Qualitative representation of the predicted velocity distributions. (Inlet shear meridional velocity of 52°.)

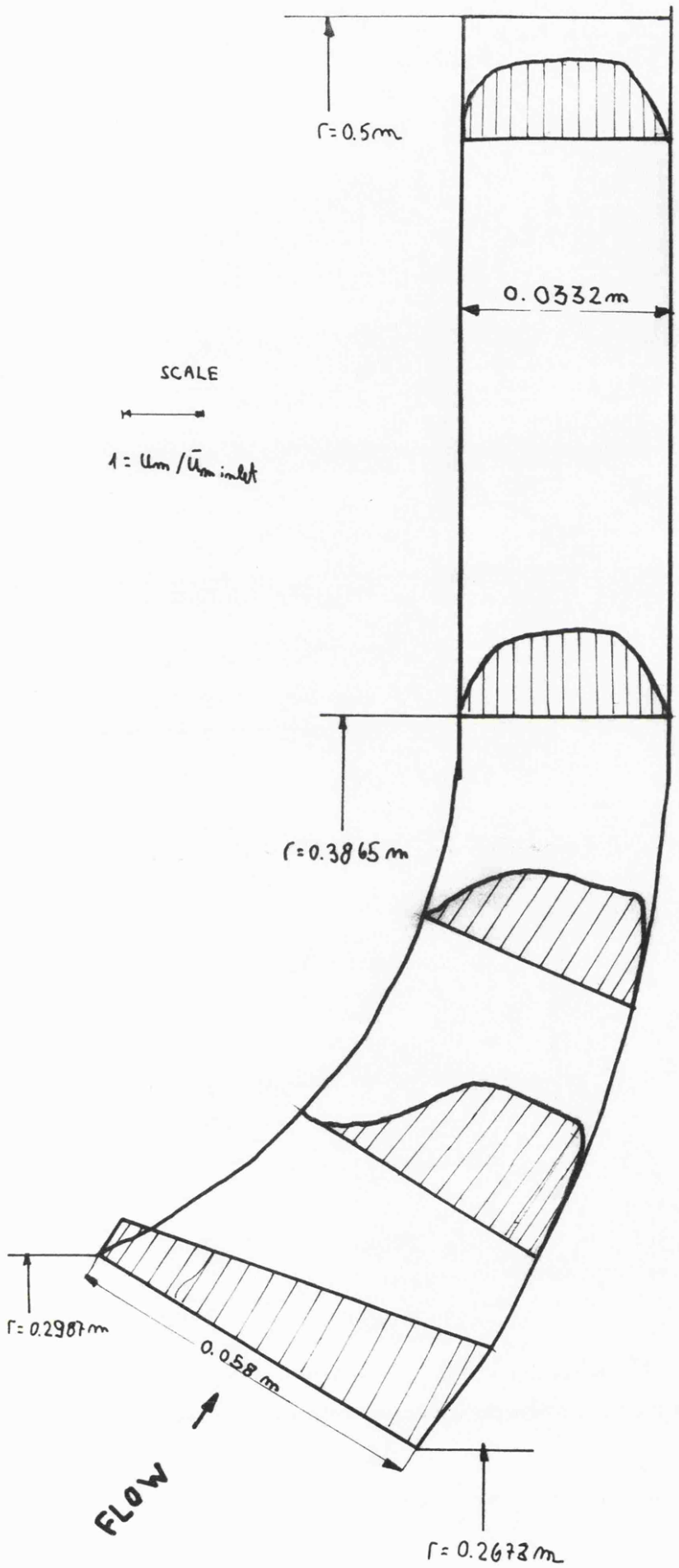

FIGURE 4.19: Qualitative representation of the predicted velocity distributions. (Inlet shear meridional velocity of -52^{o}.)

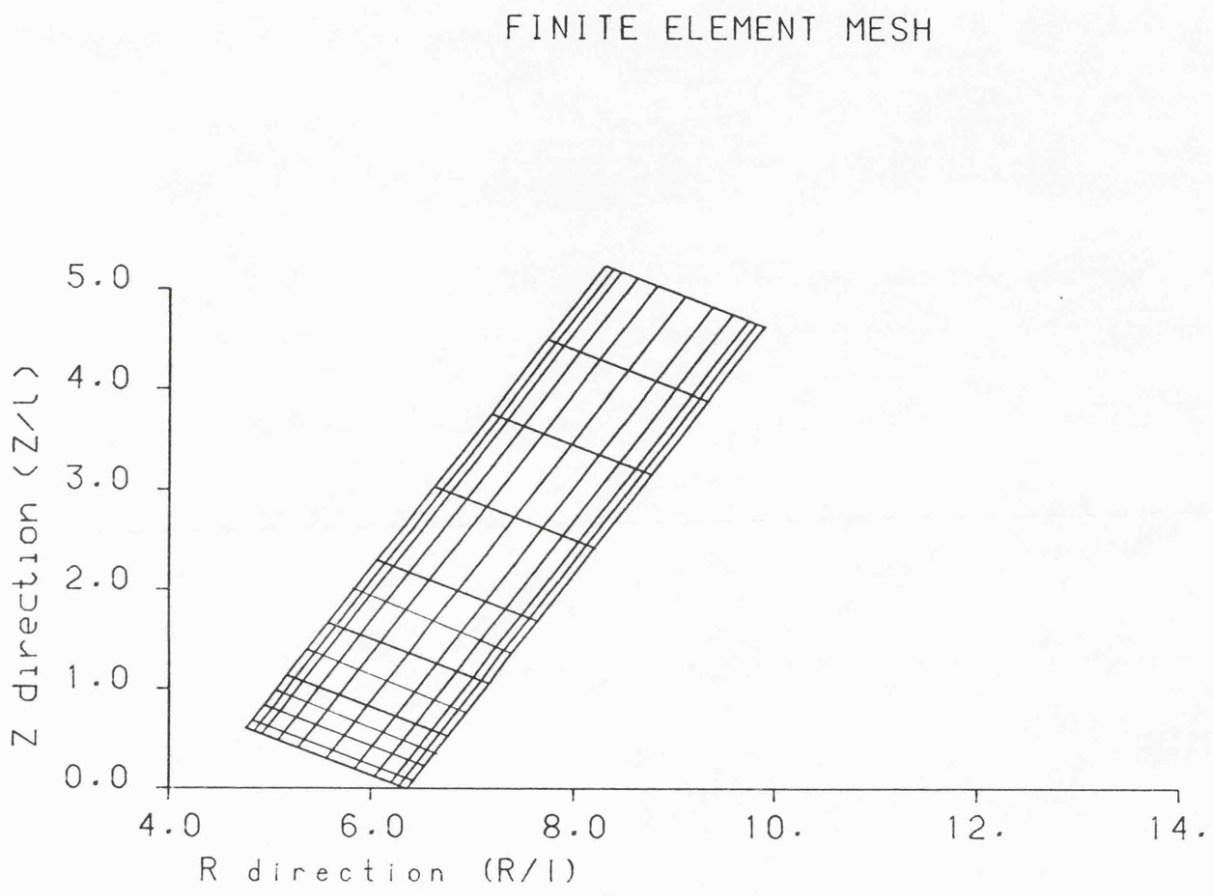

FIGURE 4.20: A finite element mesh for a conical diffuser.

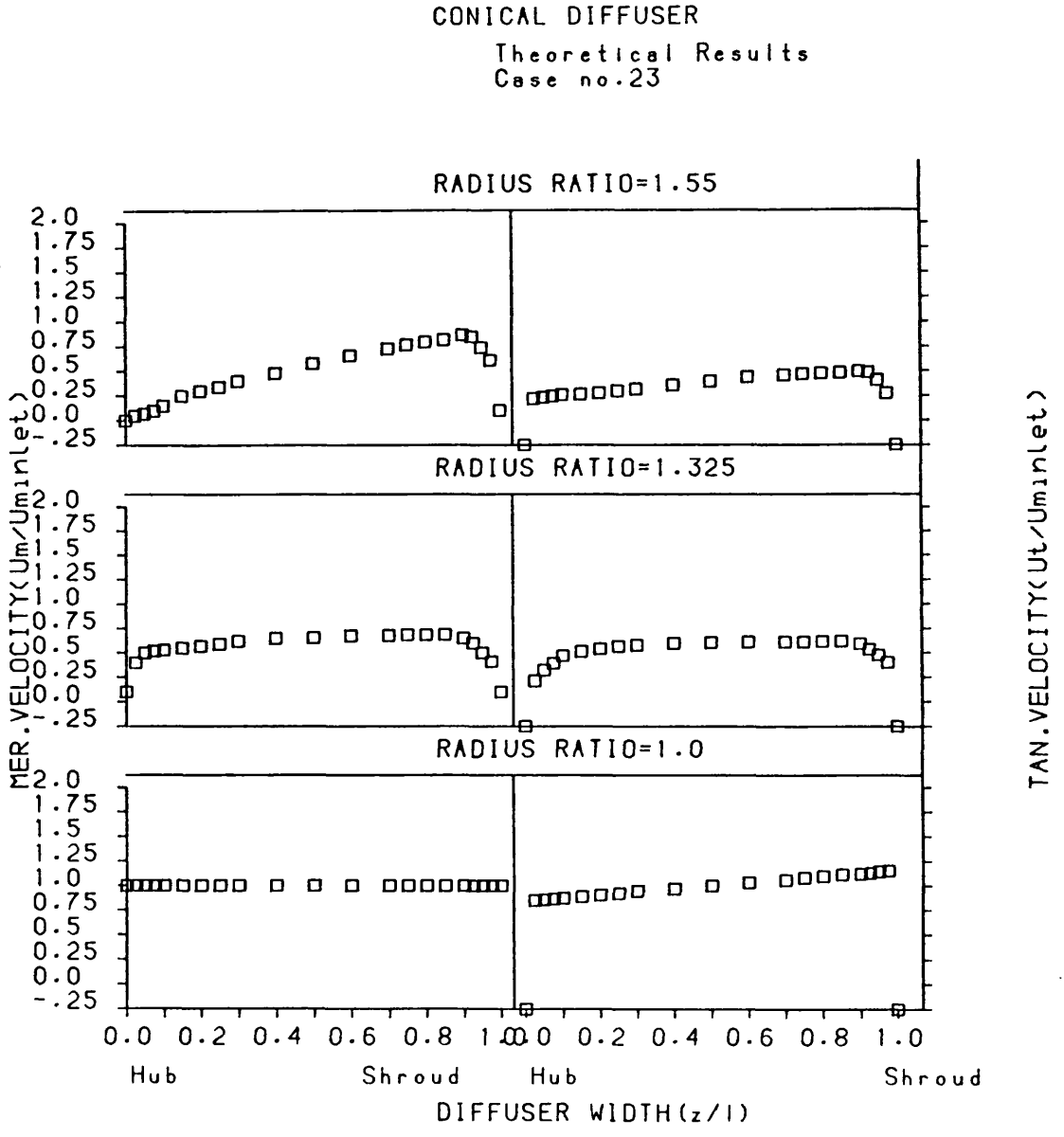

FIGURE 4.21: Predicted velocity distribution in a conical diffuser.

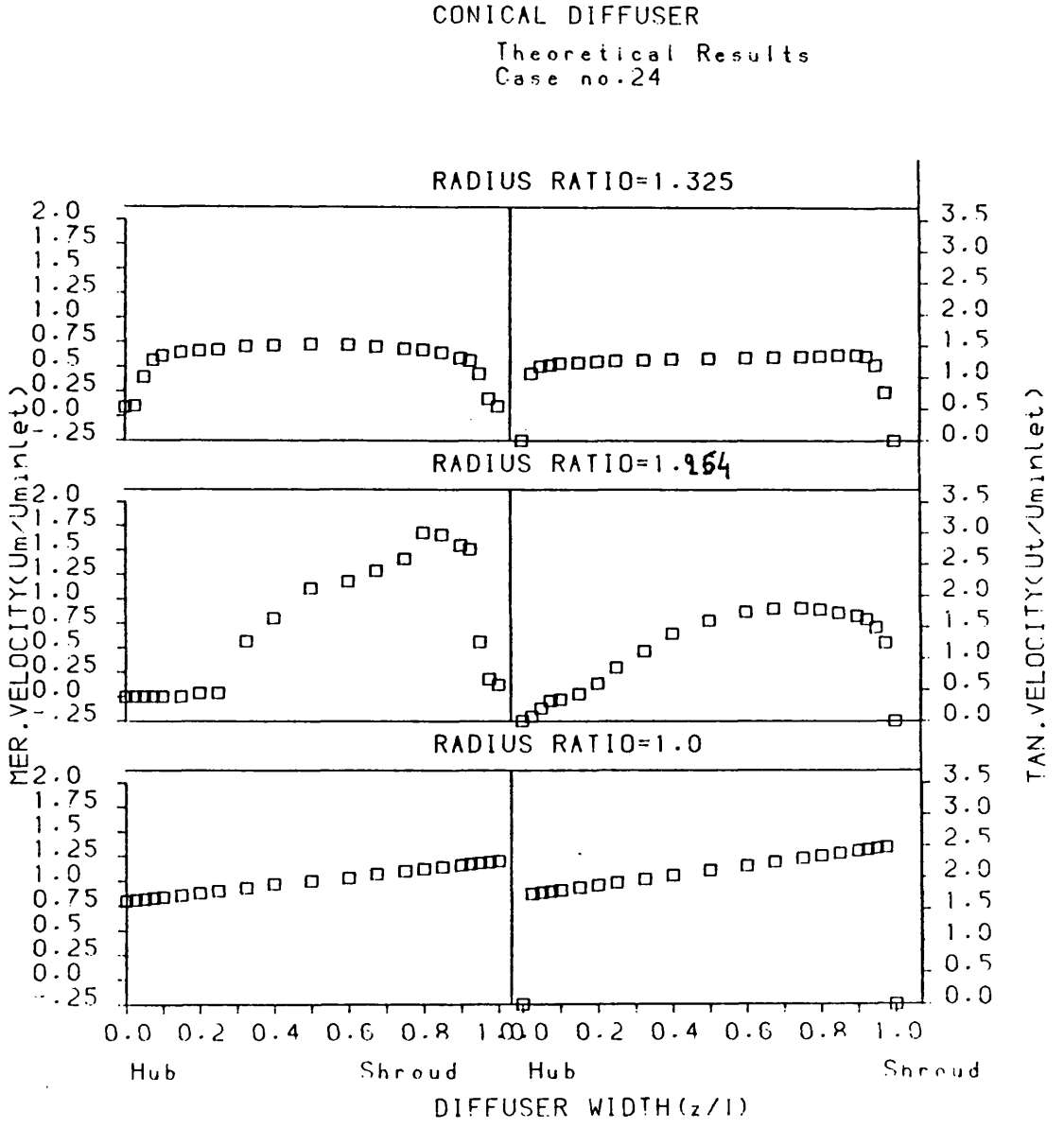

FIGURE 4.22: Predicted velocity distribution in a conical diffuser. (Inlet shear meridional velocity of 26.)

CHAPTER 5

TEST RIG AND INSTRUMENTATION.

The experimental program consisted of the measurement of mean and turbulent quantities in the core flow, and the boundary layer developing on the shroud and hub surfaces of three diffuser geometries.
The flow measurement included the mean velocity and flow angle relative to the radial direction, and total and static pressure distributions across the width of the diffuser at several radial stations.
Transient static pressure measurements on the diffuser walls were measured to indicate the onset and development of rotating stall in the diffuser.

5.1 THE EXPERIMENTAL TEST RIG.

A schematic layout of the test rig is given in fig. 5.1. The test rig which is a six-times full size model of a turbocharger diffuser used two rotating screens to develop the required swirling motion at the inlet of the diffuser. Two axial fans upstream of the rotating

screens could be operated separately or together in order to provide the main air flow. The flow rate was varied by operating with either two, one or no fans, further reduction in flow rate was achieved by throtlling the duct at inlet if it was necessary to develop an unstable flow condition.

Two types of rotating screen were used one with the radial diffuser and the other with the mixed flow diffusers, see fig. 5.2. In both cases the mesh size was 25*35, and the mean radius approximately 300 mm, two screens were used to create a smooth velocity profile at the diffuser inlet.

The screens were belt driven by an electric motor and the rotational speed of the screens could be varied between 1300 to 2600 r.p.m to provide varying degrees of swirl flow.

Three different types of diffuser were tested as illustrated in fig. 5.3. All the diffusers had the same width at inlet approximately 56 mm, and inlet and discharge radii of 300 mm and 508 mm respectively. The curved diffuser, fig. 5.3b was also tested with a second shroud profile. The first curved diffuser design was a six times full size model of the MKI diffuser tested by ATKEY(1975) and had a discharge width of 41.28 mm. The

second curved diffuser had a discharge width of 33.21 mm and corresponded to the MKIV diffuser of ATKEY. These curved diffusers and the location of the measurement stations are shown in fig. 5.4. The measurement stations used for the radial and straight conical diffusers are shown in figures 5.5 and 5.6.

The pressure transducers used for measuring the wall static pressure fluctuations were located at the same radii as the hot-wire traveres but off set from each other by 45 or 90 degrees.

5.2 INSTRUMENTATION

Measurement of a three dimensional flow field requires the precise measurement of flow parameters at many points across the diffuser width. The majority of the velocity measurements were made with a hot-wire probe. The basic hot-wire circuit consists of a P.S.I. (PROSSER SCIENTIFIC INSTRUMENTS) Model 6110 constant temperature anemometer. The r.m.s fluctuations were obtained by feeding the output from the P.S.I 6151 (meter unit) to a DISA 55D35 r.m.s unit and averaging for 1 sec to 5 sec. Two standard probes were used a) P.S.I 6505/W05 single sensor 5μ tungsten wire and b) P.S.I 6510/W05 Right angle

(45 deg.) single sensor 5μ tungsten wire was. The hot-wire was calibrated using velocity values obtain from a pitot tube in the outlet of a calibration rig where the velocity range was 1-70 m/sec. No significant drift due to dirt on the wire or change in ambient temperature occurred during most of the tests. The average life of the wire was about 80 hours and in most cases failure was due to mechanical damage.

Two types of pressure measurements were taken a) Total and static pressure at different cross sections through the flow. These measurements used a 5 hole pitot tube, UNITED SENSOR type DA. This three dimensional directional probe measured also the yaw and pitch angle of the fluid flow.

b) Static pressure fluctuations by means of DRUCK PDCR10 pressure transducers which were located on the shroud and hub surfaces.

5.2.1 Mechanical traverse arrangement.

The hot-wire probes were traversed from shroud to hub to measure the velocity and the flow direction with reference to the radial direction. For this purpose a traverse mechanism was designed with two degrees of movement

a) Axial movement.

b) Rotational movement about the probe axis.

Some running conditions of the the rig caused mechanical vibration which could damage the wire, to avoid this effect the traversing system was erected separately from the rig and couple to it with a flexible coupling. A detail picture of the traversing system is shown in fig. 5.7.

Two drive units were chosen, a SIGMA Model 20-2220D200-E5.1 stepper motor for the rotational movement and a SIGMA Model 20-3437D200-F075 for the axial movement. The axial drive motor was coupled directly to a lead screw that moved a disc guided by 3 steel rods and translated the rotating movement to axial movement.

The rotational drive stepper motor was mounted on the traversing disc and coupled directly to the probe holder giving it the required rotational movement. The probe holder was guided by guide tubes which reduced the deviation from the center line perpendicular to the surface.

The resolution of the system is given in table 5.1.

To obtain maximum advantage of the accuracy of the traversing system a reliable zero setting procedure was required. The probe holder was fixed to the rig at a

fixed distance from the hub with the wire position perpendicular to the radial direction. Two L.E.D units were set up on the traverse mechanism with an axial distance equal to that between the hub and shroud on the rig. The traversing disc was then moved to a point the same distance from the L.E.D (which represented the hub) as the probe holder was fixed from the hub. The probe holder was then connected to the traversing system and since the probe holder was at a fixed relative angular position traversing of the unit did not affect the zero setting of the rotating movement. The disc was then traversed until the flag on the disc reach the L.E.D which represented the shroud and the axial movement changed direction. This point was set up as zero, i.e. on the shroud.

The stepper motors were controlled by a PET 2001 micro-computer and the position of the probe was recorded as the number of motor steps from the zero point.

5.3 MEASUREMENT TECHNIQUES

5.3.1 Hot-wire techniques

A single hot-wire was used to measure the velocity and turbulence components. The main advantages of using a single wire are that the single wire is cheap for replacement and repair and needs a relatively simple calibration procedure. On the other hand the disadvantages are the time taken to measure all data and the fact that all relevant readings cannot be taken simultaneously.

A spherical coordinate system was introduced where the probe axis was perpendicular to the diffuser wall as shown in fig. 5.8. Two angles were defined, β the yaw angle (the angle between the velocity vector and the radial direction) and θ the pitch angle defined as the angle between the velocity vector and the velocity component parallel to the surface.

The measurement of the three dimensional flow was divided into two stages. First a single wire in the R,β plane searched for the maximum velocity vector and secondly a slant wire was used in the R,θ plane to find the pitch angle. As the pitch angle was usually small this second

stage was later dispensed with.

A typical example of the effect of yaw angle on the wire output with the flow direction normal to the probe axis is given in fig. 5.9. It is clear from this figure that the effective cooling velocity is a function of the sin of the yaw angle. The maximum wire output occurs when the flow is normal to the wire and decreases symmetrically when the yaw angle is bigger or lesser than zero. From the results it was found that the wire output is not very sensitive for yaw angles less than ± 10 deg. or greater than ± 60 deg. Measurements were, therefore, always taken in the range ±10 to ±60 degrees only.

To find the magnitude and direction of the maximum velocity the following procedure was used. The probe was located at a known yaw angle β_n from the radial direction, in this position the wire output was recorded. The probe was then rotated until the wire output was the same as that in the original β_n position, see fig. 5.10. The symmetrical behavior of the wire output enables the direction of the maximum velocity to be determined. To ensure maximum sensitivity the angle $(\gamma-\beta_n)$ was always greater than 10 and less than 60 degrees. In order to determine the Reynold stresses the probe was rotated to two positions shifted 45 degrees from the maximum

velocity direction.

To determined the true value of the velocity the pitch angle must also be measured. The method which was presented by MATES(1963) was used. A slant wire was calibrated for the change of the effecting cooling velocity as a function of the angle. Fig. 5.11a defines the direction of the flow relative to the slant wire. A typical calibration curve showing the ratio between the wire output to that when the wire was perpendicular to the flow direction against the pitch angle is given in fig. 5.11b. This calibration is valid for $\theta < 31$ degrees only, and it was found to be independent of the magnitude of the air velocity. The calibration curve is described by

$$\frac{E^2 - E_0^2}{E_{MAX}^2 - E_0^2} = \sqrt{Sin(\beta_w - \theta)}$$

The following procedure was used to find the pitch angle: first the wire was located in the direction of the maximum velocity as found in the first stage and the output was recorded. The wire was then rotated through 90 degrees and another reading was taken. By calculating the ratio required for the calibration curve the pitch angle could be found.

The calculated results for the pitch angle compared

closely to these measured with the 5 hole probe see fig. 5.12. The differences near the wall is due to inaccurate measurements of the pitot tube near the wall surface. Once it had been verified that the pitch angle was small and less then 10 degrees this second stage was often dispensed with.

Fig. 5.13 gives the flow chart of the computer program which controls the hot-wire instrumentations used.

5.3.2 Static pressure measurement techniques to detect rotating stall.

Static pressure fluctuations on the walls at various locations in the diffuser were detected by strain gauge differential pressure transducers. The pressure transducers were flush mounted and there amplitudes were calibrated and found to be phase matched.

In order to detect any unstable flow three pressure transducers were located on the same radius but shifted from each other by 45 and 90 degrees respectively. The oscillatory output of the transducers were then compared with each other to determine the variation of the phase and amplitude of the pressure fluctuations. Fig. 5.14 presents a typical output of two pressure transducers

which indicate an average time shift, ΔT.

The number of stall cells can be determined from fig. 5.14 by the equation

$$\text{number of cells} = \frac{\Delta T}{\varphi} \qquad (5.1)$$

Equation 5.1 shows that if there is no phase difference between the two signals then no rotating stall is detected.

5.4 DATA REDUCTION

5.4.1 The data collection and analysis system.

The data collection and analysis system is shown in fig. 5.15. The system which was based upon a PET 2001 computer could handle data from three sources a) A hot-wire anemometer b) A thermocouple, and c) Pressure transducers. The reading could be taken simulataneously or separately for all the sensors.

Two types of analysis were made. The first was a time and frequency analysis where the signal from the sensor was passed through a two channel GOULDS OS4000 digital oscilliscope and an HP 3582A spectrum analyzer. The time and frequency analysis gave the power spectrum of the

pressure and the velocity fluctuations and the phase difference analysis for the rotating stall phenomena. An example of the display is given in fig. 5.16.

In order to find the magnitude of the mean velocity and pressure the output from the hot-wire sensor and the pressure transducer were recorded approximately 10000 times for each data point. This information was stored as raw floating point numbers on a cassette tape and analysed at a later time on a main frame computer.

5.4.2 Velocity and Turbulence measurements.

It was assumed that the hot-wire output followed the "KINGS Law" relationship given by

$$E^2 = A + B\,U_{eff}^{n} \qquad (5.2)$$

where A, B and n are the calibration constants.
By using the inverse calibration equation (see Appendix 3 for more details) the effective velocity can be obtained by

$$\bar{U} = \left[\left(\frac{E^2}{E_{01}^2} - 1 \right) A_t \Big/ B E_{01}^2 \right]^{\frac{1}{n}} \quad m/sec \qquad (5.3)$$

A_t is a compensation for temperature change suggested by WOOD(1981) and given by: $A_t = 1 + \frac{\alpha_h}{\sigma_h}$

where

$\sigma_h = \frac{T_{flow} - T_{cal}}{T_{flow}}$

α_h = over heat ratio

$E_{01} = 0.92 \cdot E_0$

The turbulence intensity $\overline{u_x^2}$ was evaluated by using the method given by MOJOLA(1974) as

$$\frac{\sqrt{\bar{u}_x^2}}{\bar{u}} = S\sqrt{\bar{e}^2} \qquad (5.4)$$

where e^2 is the r.m.s of the fluctuation of the bridge voltage, and S given by

$$S = \left(\frac{2}{m}\right)\left(\frac{\bar{E}}{E^2 - E_{01}^2}\right)$$

The other terms for Reynolds stress were determined by using the method given by CHANPUGNE and SLEIDNER(1967) and RODI(1975). The wire was located at three different angles from the direction of the absolute velocity as shown in fig. 5.10 and the terms calculated from

$$\overline{u_y^2} = \frac{\bar{e}^2(\beta=+45^\circ) + \bar{e}^2(\beta=-45^\circ) - (1+k_1^2)\,\bar{e}^2(\beta=0)}{S^4(1-3k_1^2)} \qquad (5.5)$$

$$\overline{u_x u_y} = \frac{\bar{e}^2(\beta=45^\circ) - \bar{e}^2(\beta=-45^\circ)}{2S^4(1-k_1^2)}$$

where kl is a constant and evaluated from the calibration.

Equation 5.5 was derived from the general equation 3A.7, see Appendix 3, by substituting the values of β=45 and

β=-45 degrees.

5.5 ERROR ANALYSIS.

The errors which occur in any experimental investigation can be categorised into two groups.

a) Fixed errors which include errors in the calibration of the instruments used for measurement.

b) Random experimental errors.

To minimise the effect of fixed errors a careful calibration of the instruments was taken and was checked by using a second instrument. Fig. 5.17 shows a comparison of the absolute velocity distribution obtained with both a 5 hole pitot-tube and the hot-wire anemometer. It can be seen that in the main flow region the measurements are approximately the same within 5% . Near the wall, due to the uncertainty of the measurements with the pitot-tube, the comparison is not as good.

Table 5.2 gives the estimated uncertainty interval for measured quantities which depends upon the fixed error.

The second type of error is random error that occurs during the experiment and cannot be estimated. It is clear that when the flow became unstable the uncertainty

in the measurements increased and errors of the turbulence intensity could be of the order of 30%. The accuracy of the flow angle, because of the technique used, was also affected and the error became approximately 2.7 degrees.

	SIGMA 20-2220D200E5.1	SIGMA 20-3437D200E075
1 pulse of motor =	0.9°	0.9°
1 pulse of motor = shaft axial movement (mm)	-	0.00635
Maximum working torque (N m)	0.34	1.87

TABLE 5.1: Resolution of the Traversing System

MEASURED QUANTITY	UNCERTAINTY INTERVAL
Pressure trasducers location	On radius ±1 mm. Phase different ±2 deg.
Zero set-up on the shroud	±1 mm.
Traversing position	0.005 mm.
Angle position	±0.9 degrees
Static pressure	±0.5 mm of water
Velocity	±1%
Turbulence intensity	For $\overline{u_1^2}$ 2%. $\overline{u_2^2}$ and $\overline{u_1 u_2}$ 10%

TABLE 5.2: Uncertainly error for measured quantities

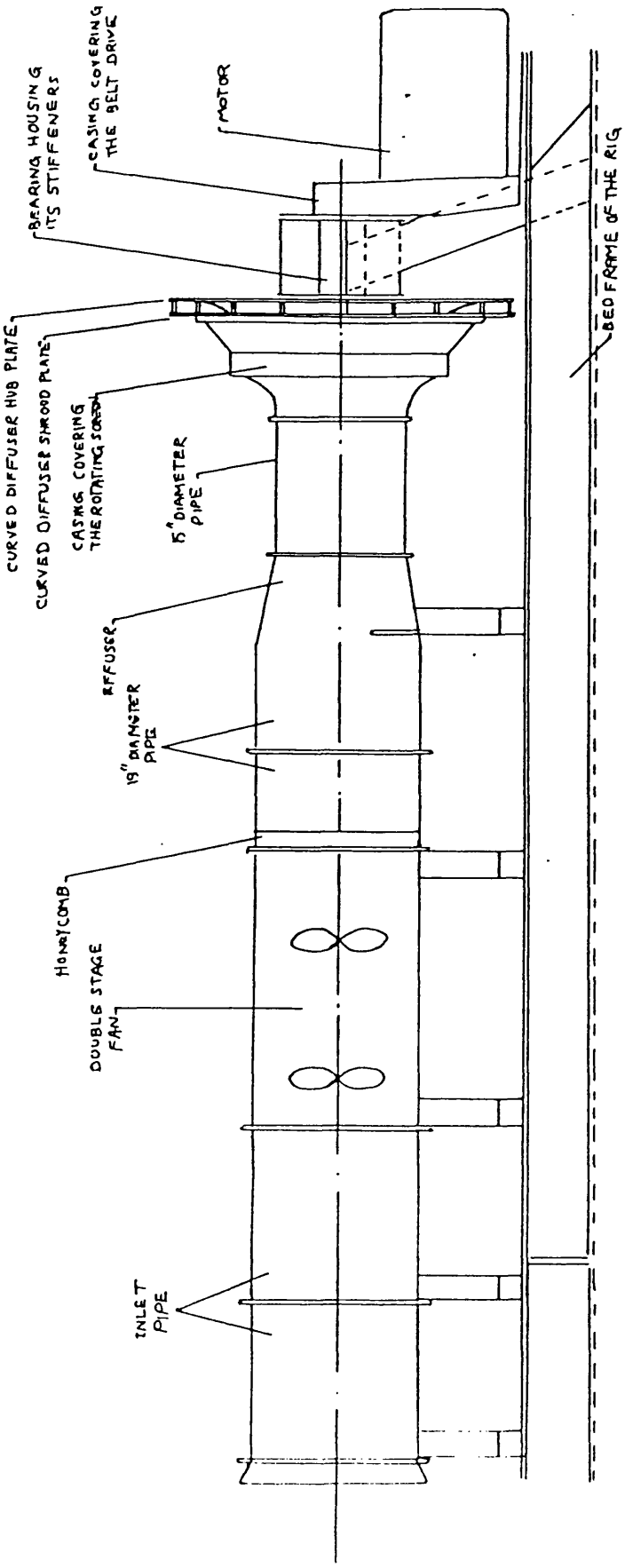

FIGURE 5.1: Schematic view of the test rig.

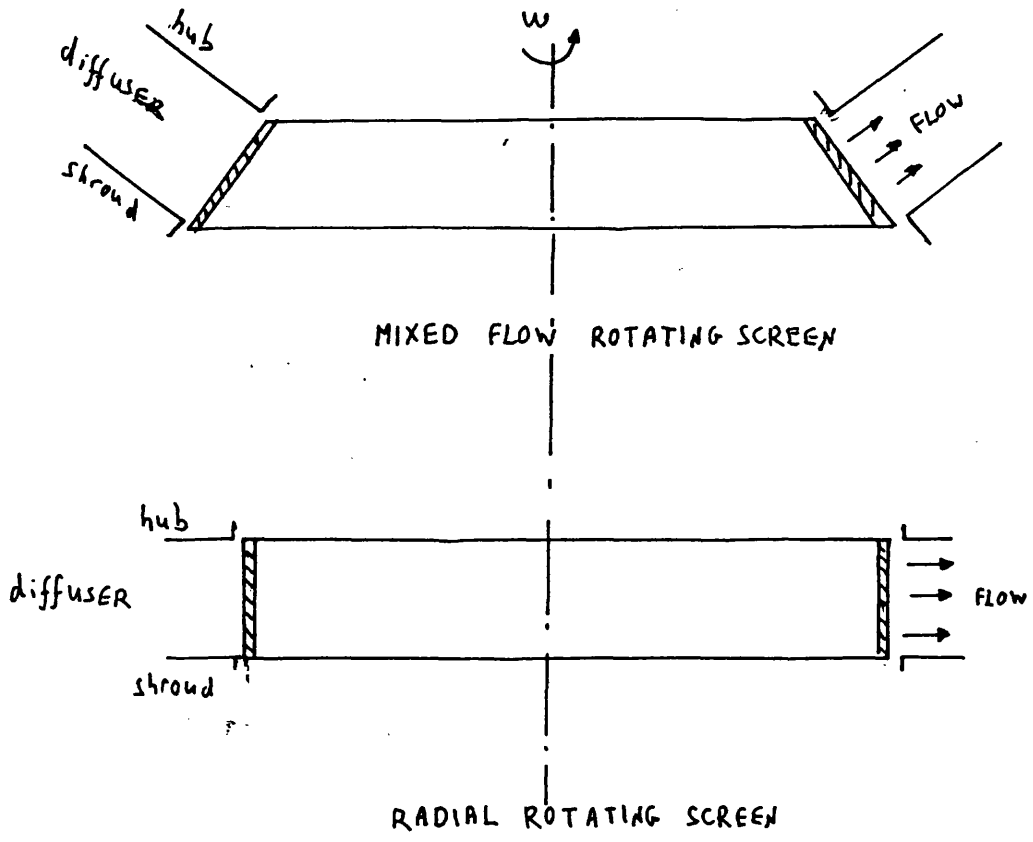

FIGURE 5.2: Rotating screens.

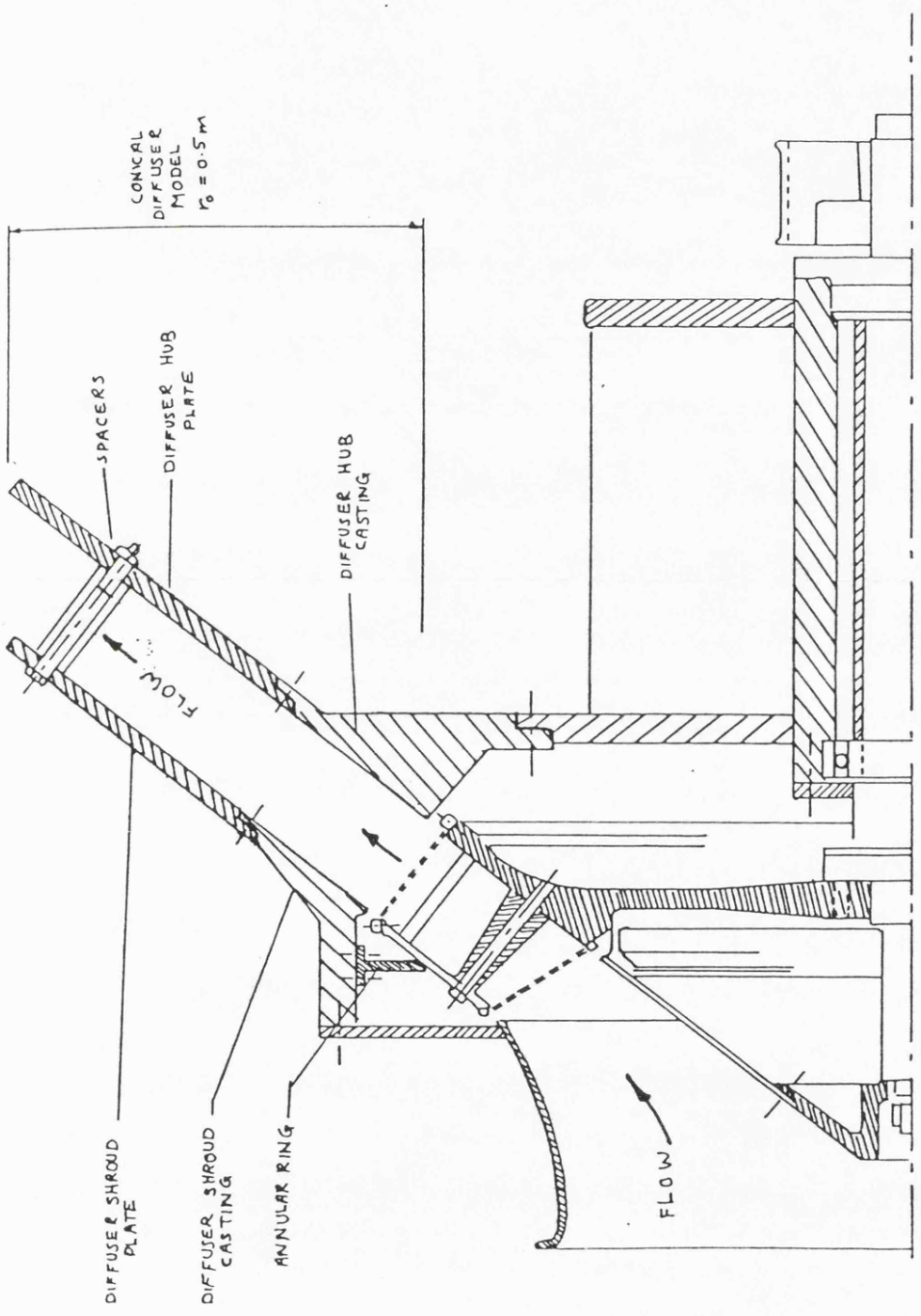

FIGURE 5.3a: Rotating assembly for conical diffuser.

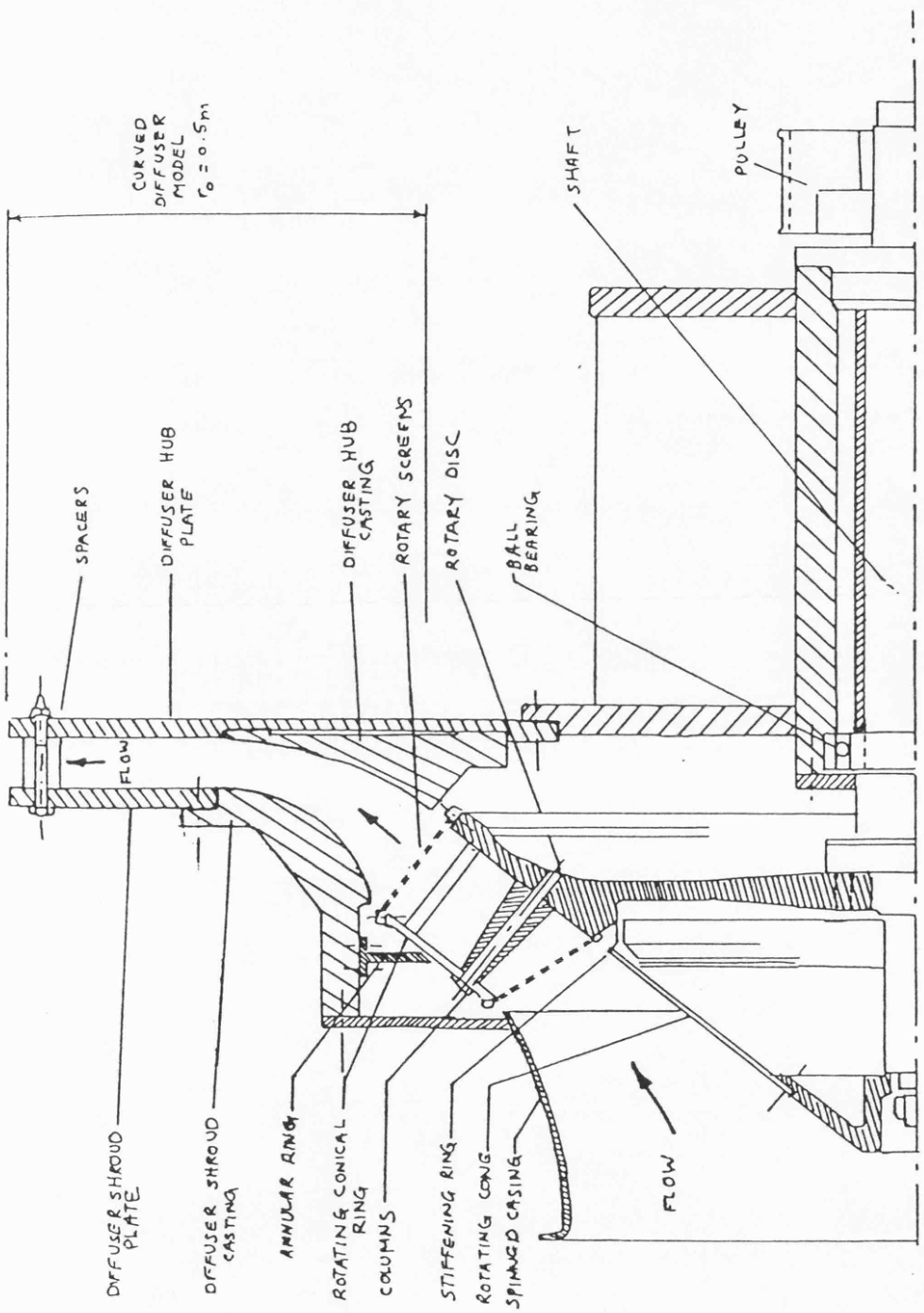

FIGURE 5.3b: Rotating assembly for curved diffuser.

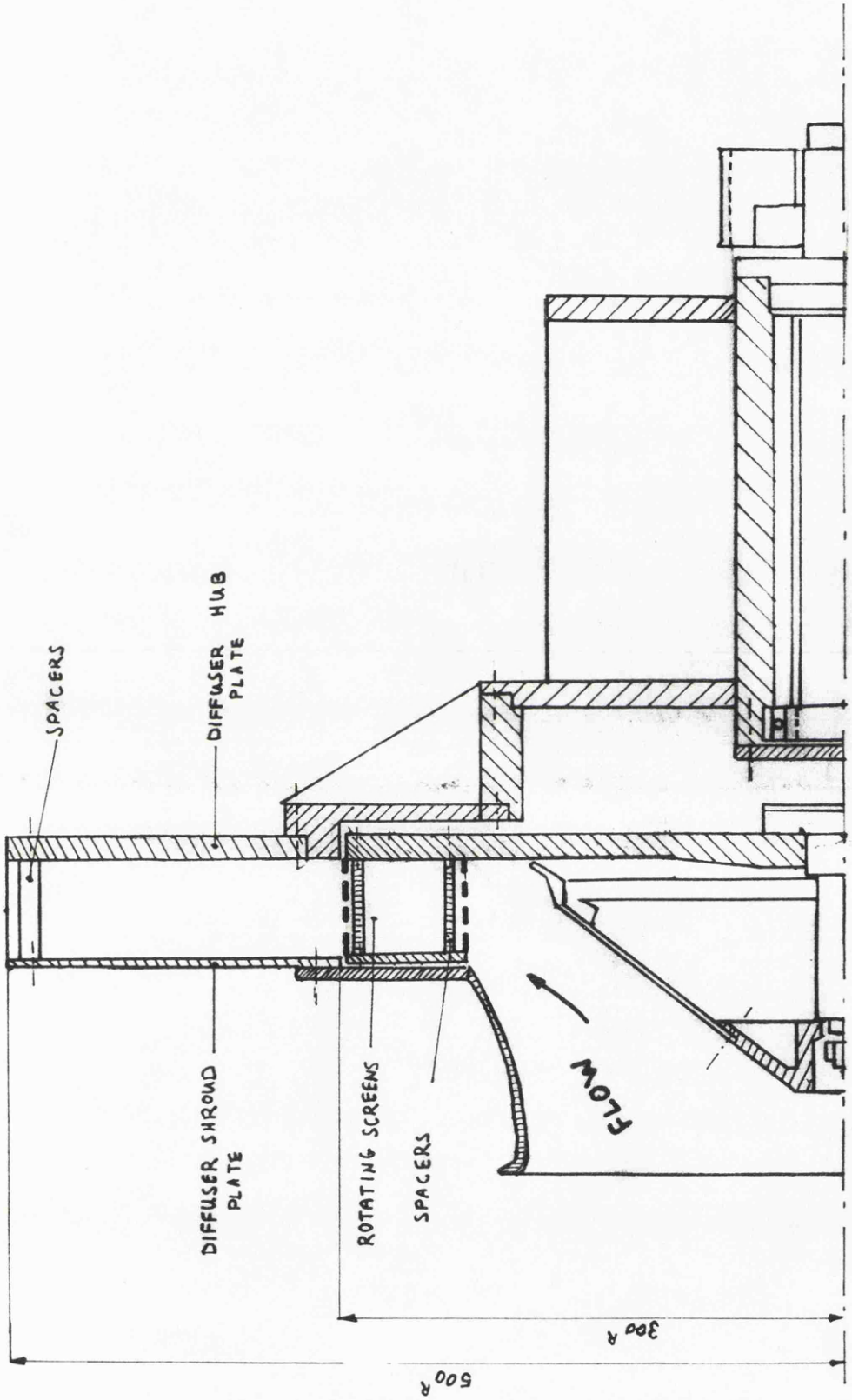

FIGURE 5.3c: Rotating assembly for radial diffuser.

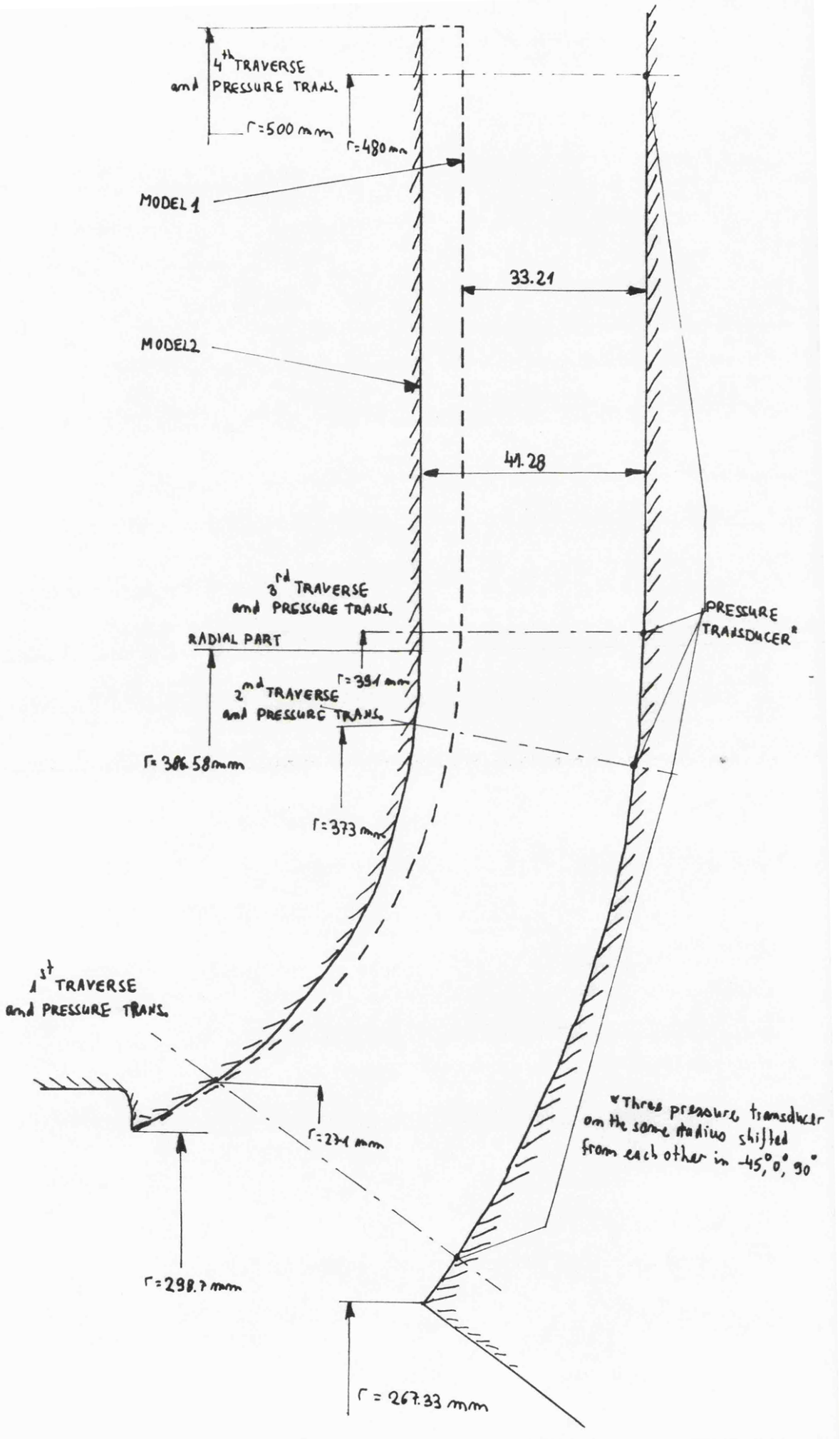

FIGURE 5.4: Different curved diffuser profiles and

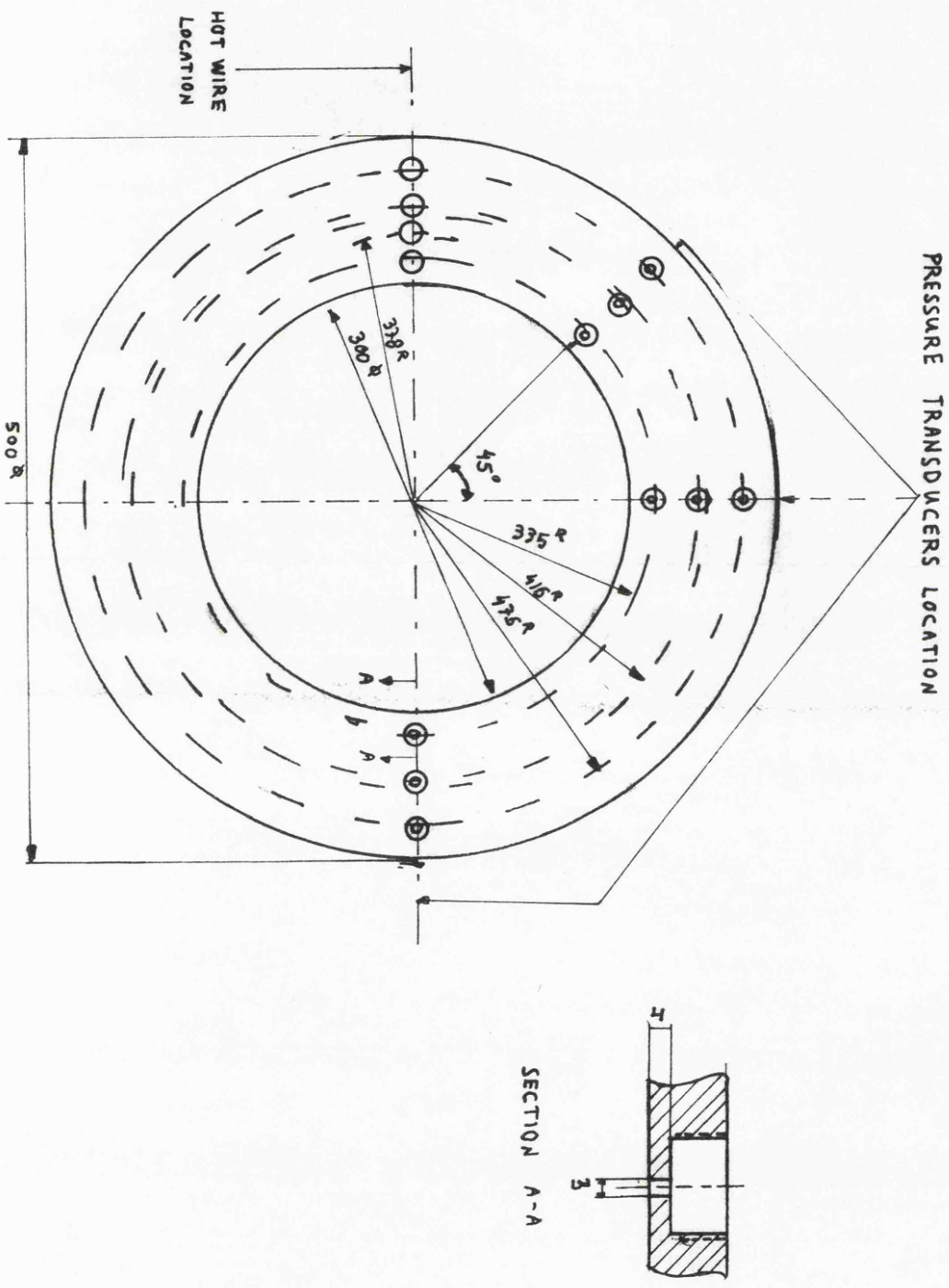

FIGURE 5.5: Location of instrumentation position for the radial diffuser.

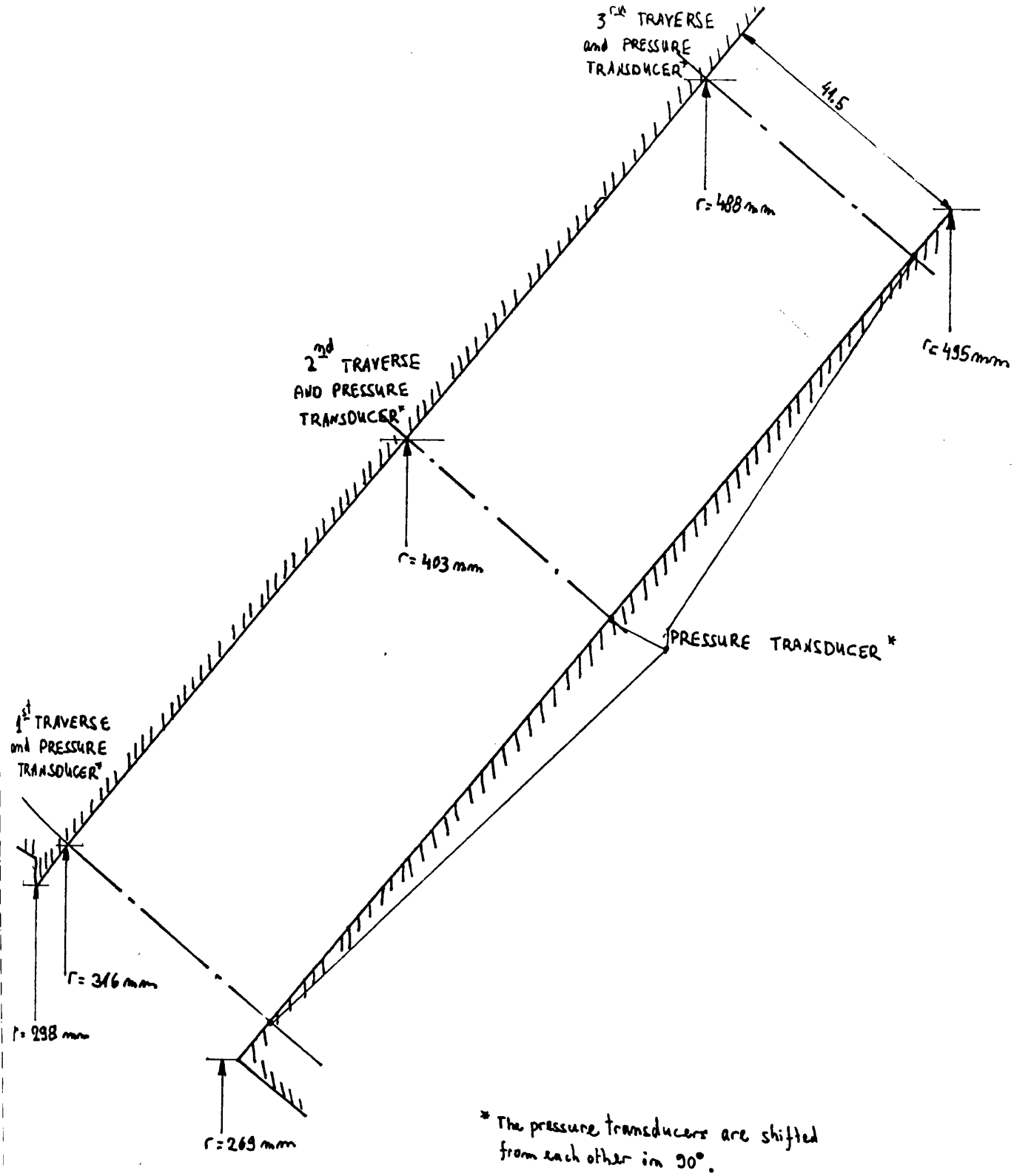

FIGURE 5.6: Conical diffuser profile and travers stations.

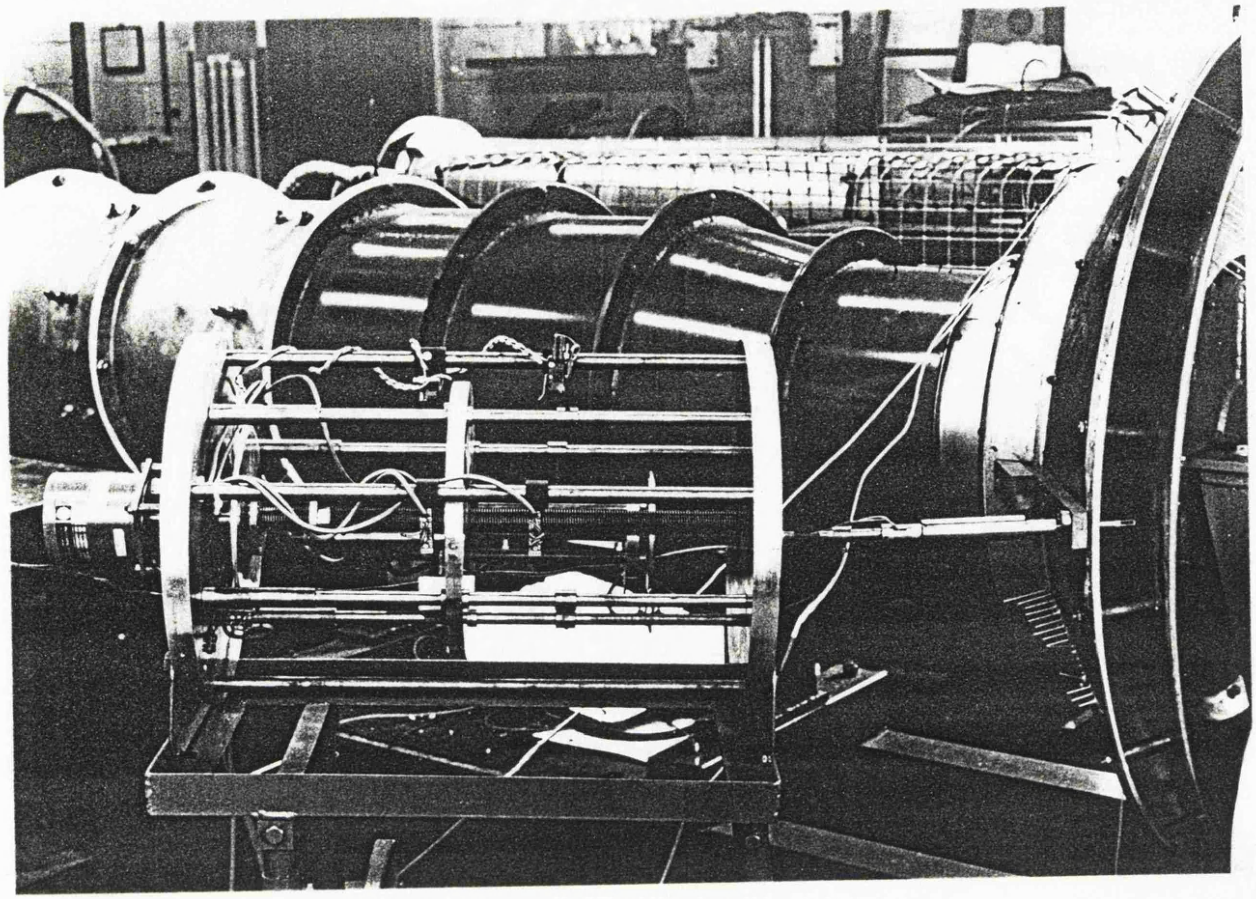

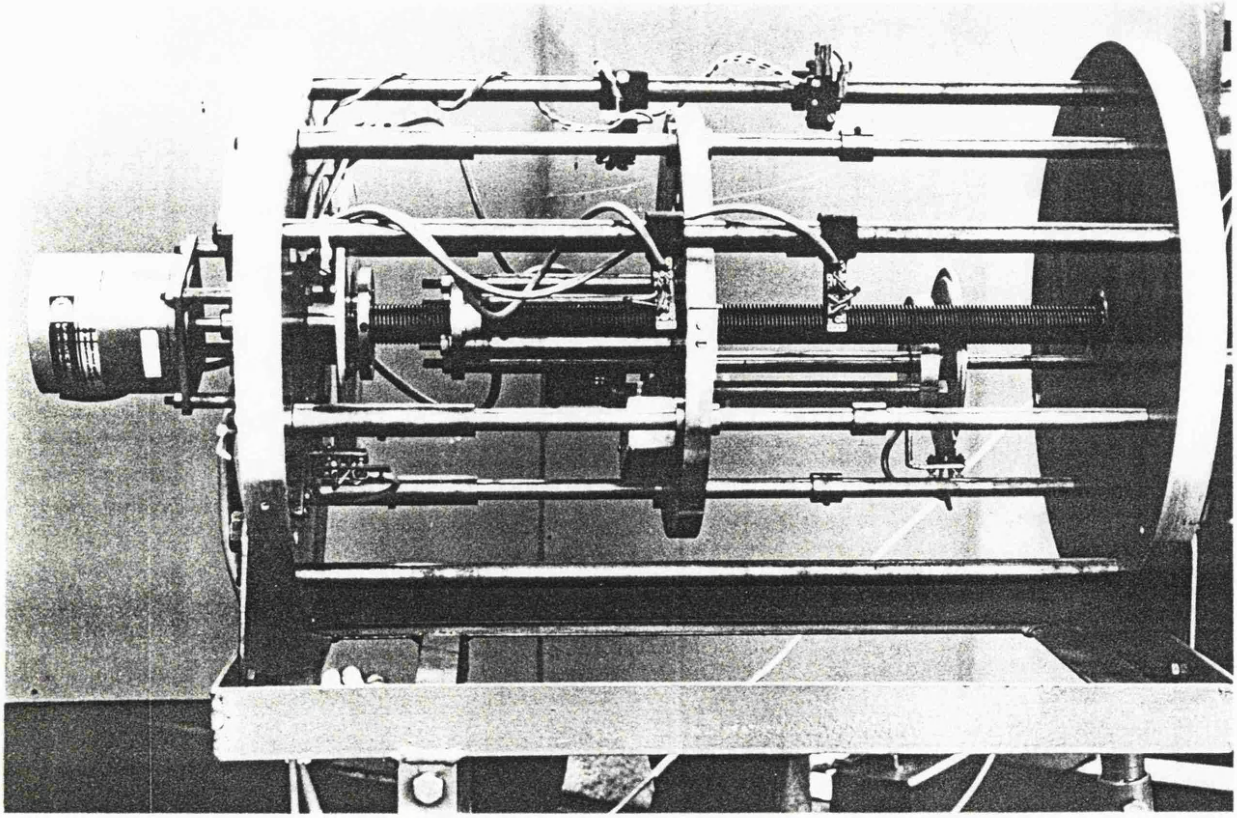

FIGURE 5.7: The traversing system.

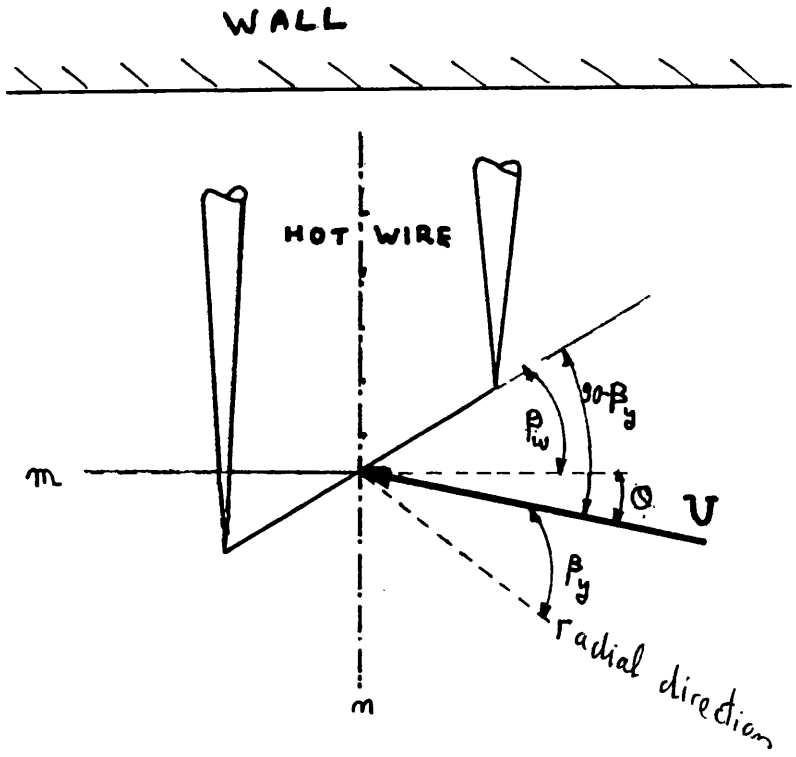

FIGURE 5.8: Probe coordinate system.

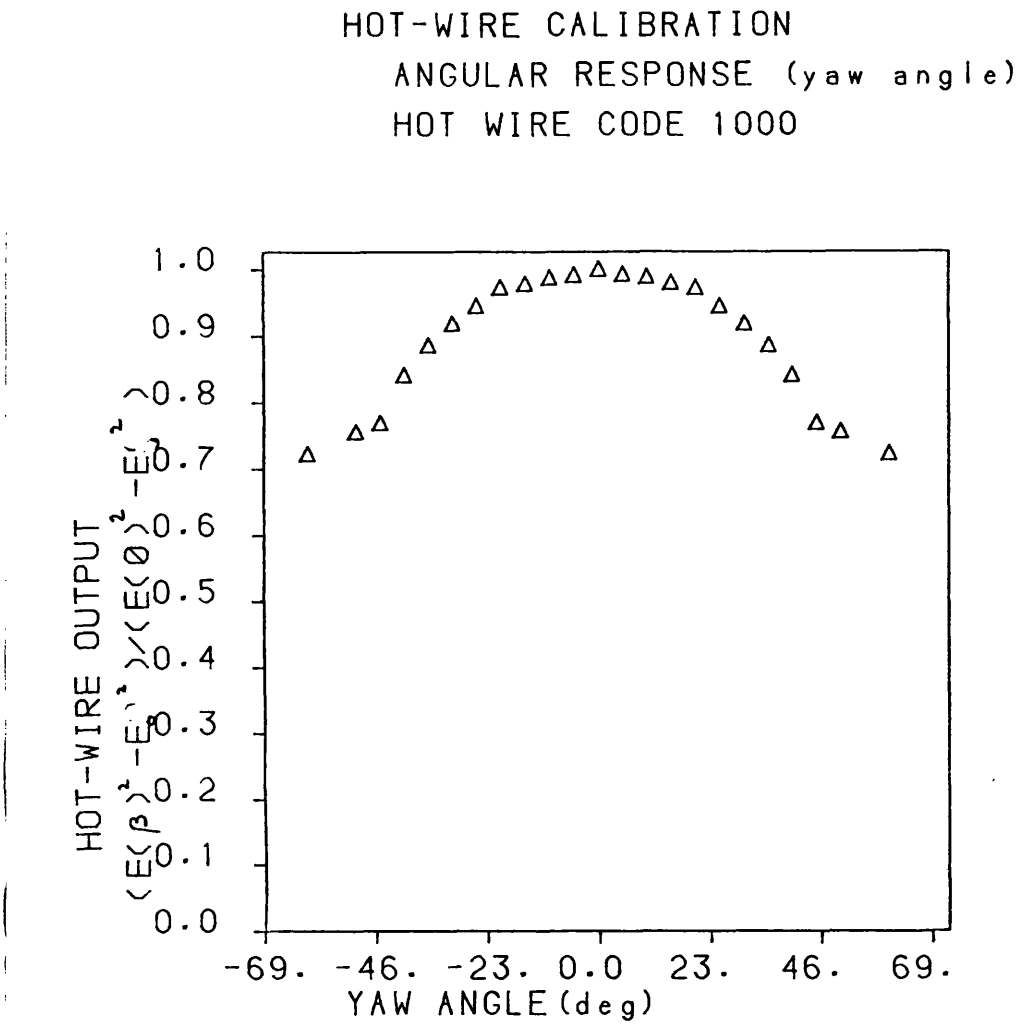

FIGURE 5.9: The effect of the yaw angle on a single wire output.

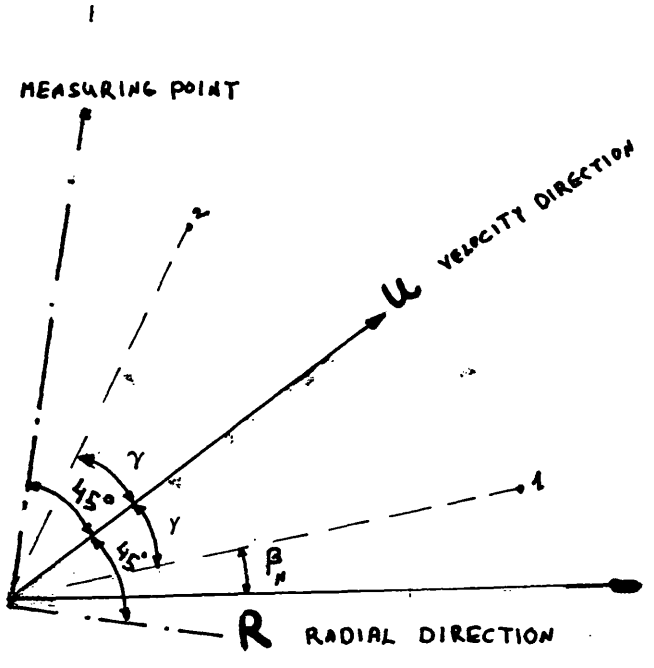

FIGURE 5.10: Probe location and angle definition.

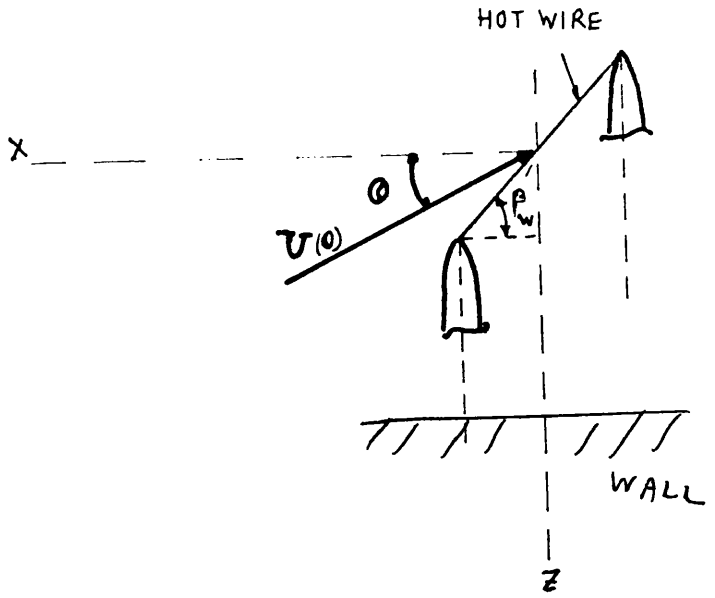

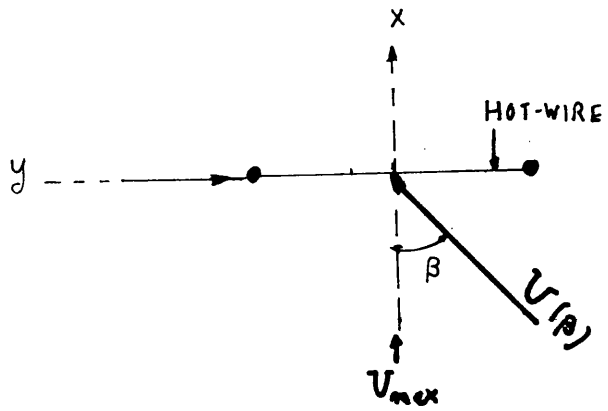

FIGURE 5.11a: Direction of the flow relative to the wire.

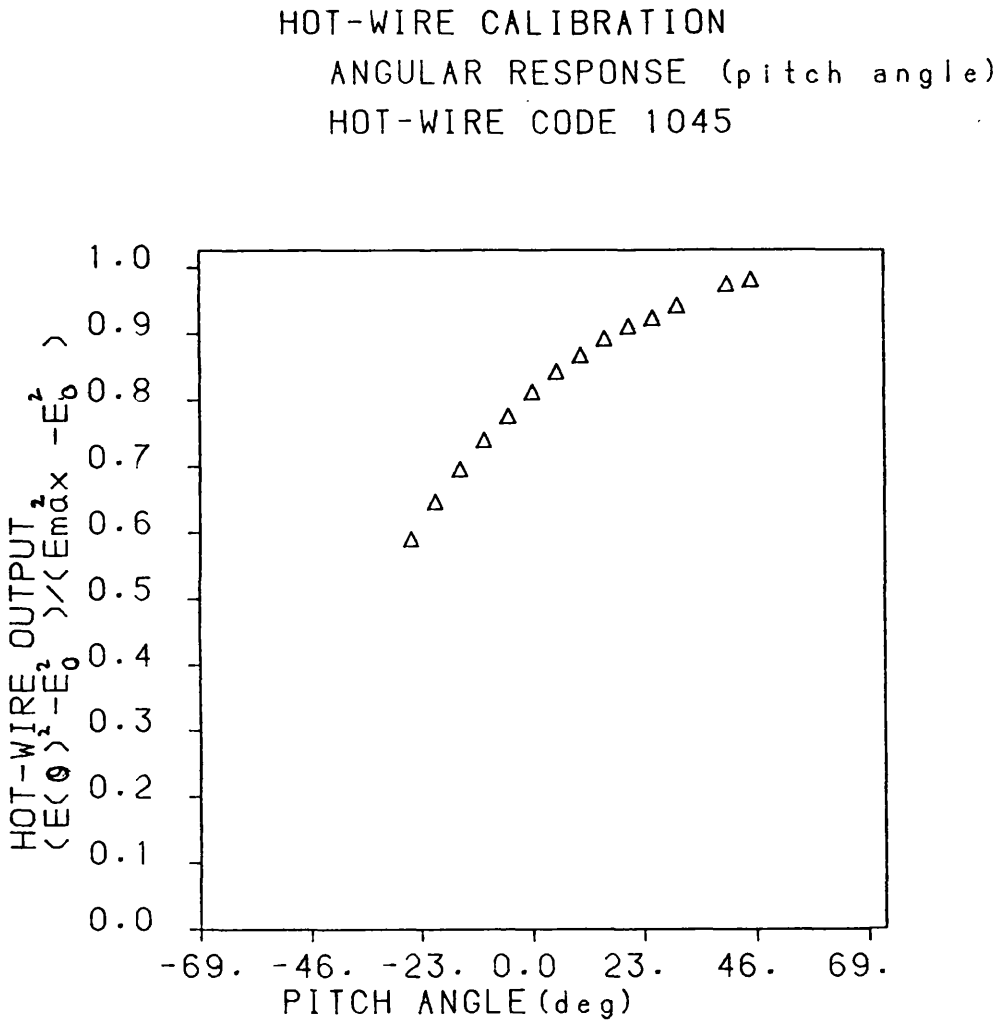

FIGURE 5.11b: Calibration curve for the effect of the pitch angle.

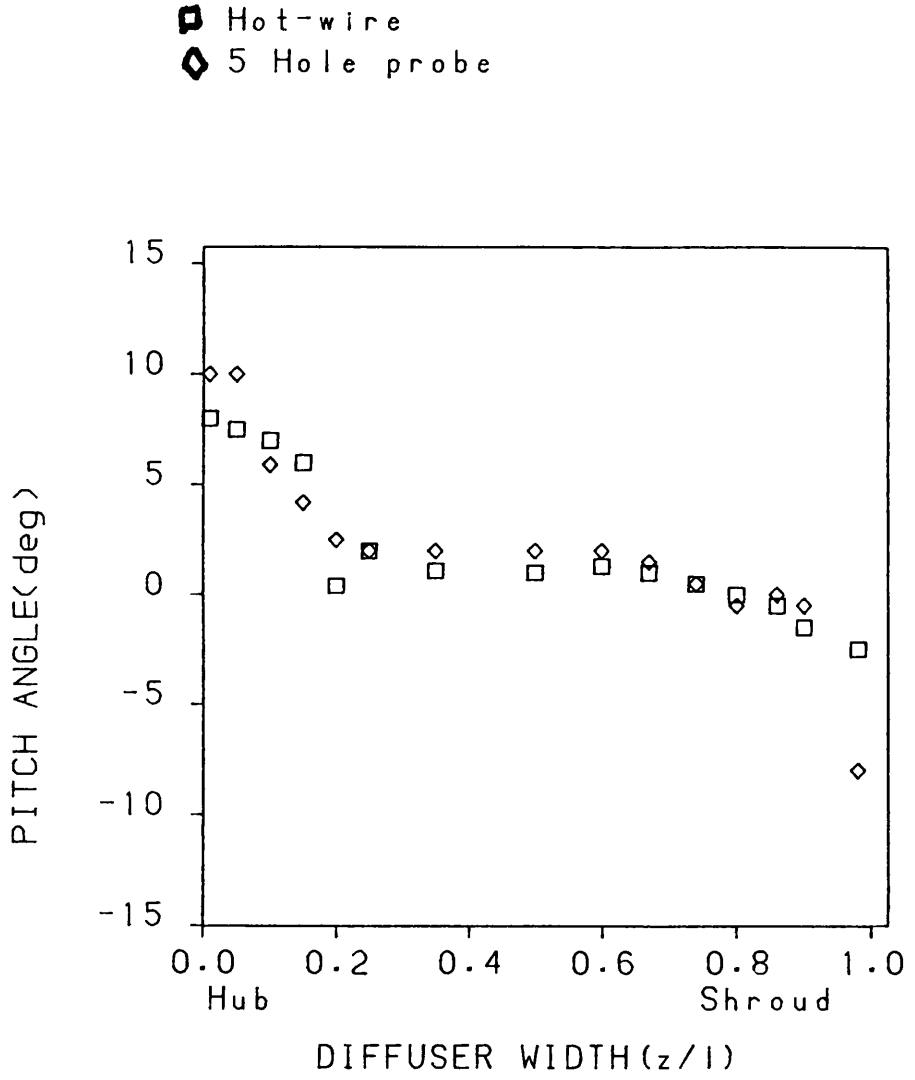

FIGURE 5.12: Comparison between the hot-wire and five hole probe measurement of the pitch angle.

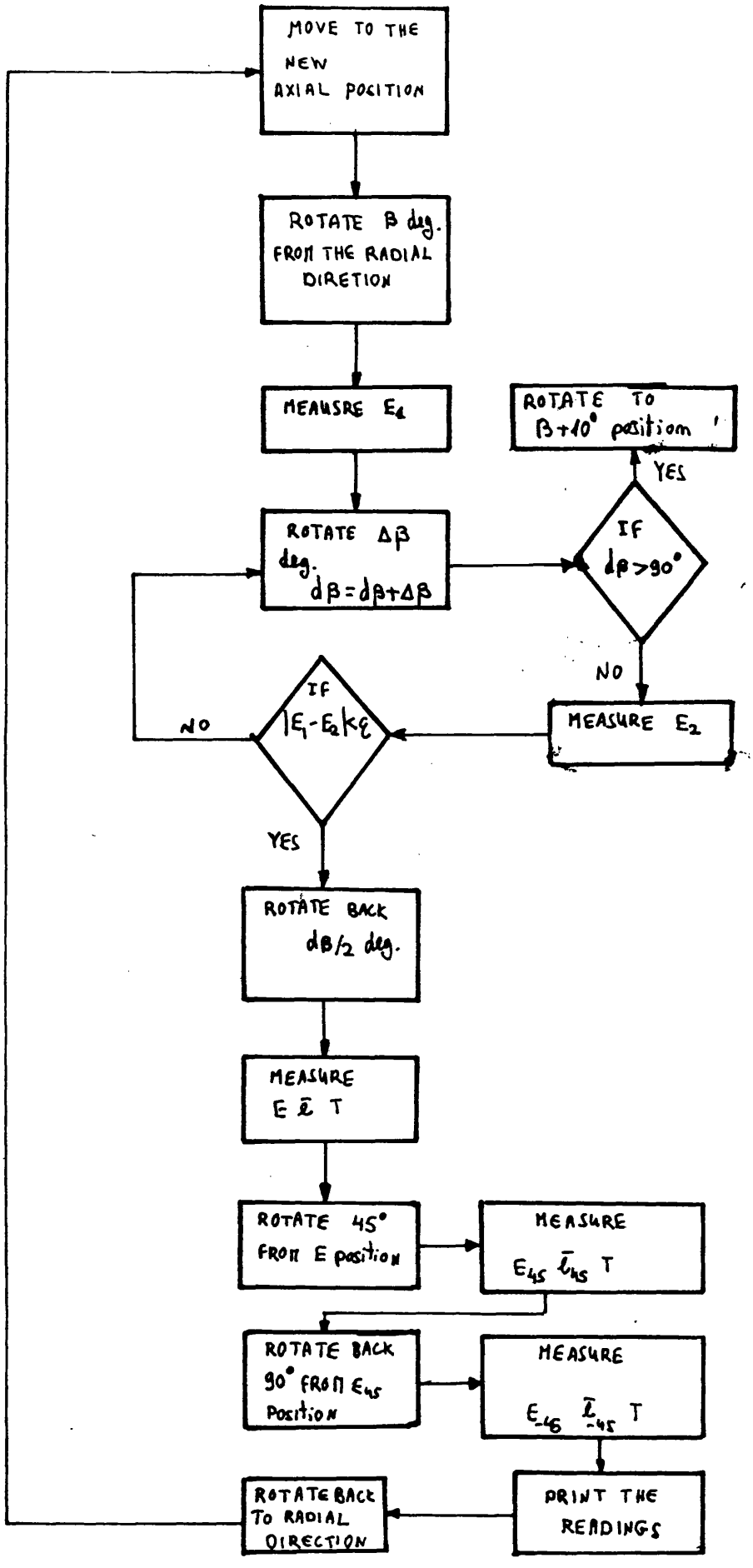

FIGURE 5.13: Flow chart of the computer program which controls the hot-wire measurement.

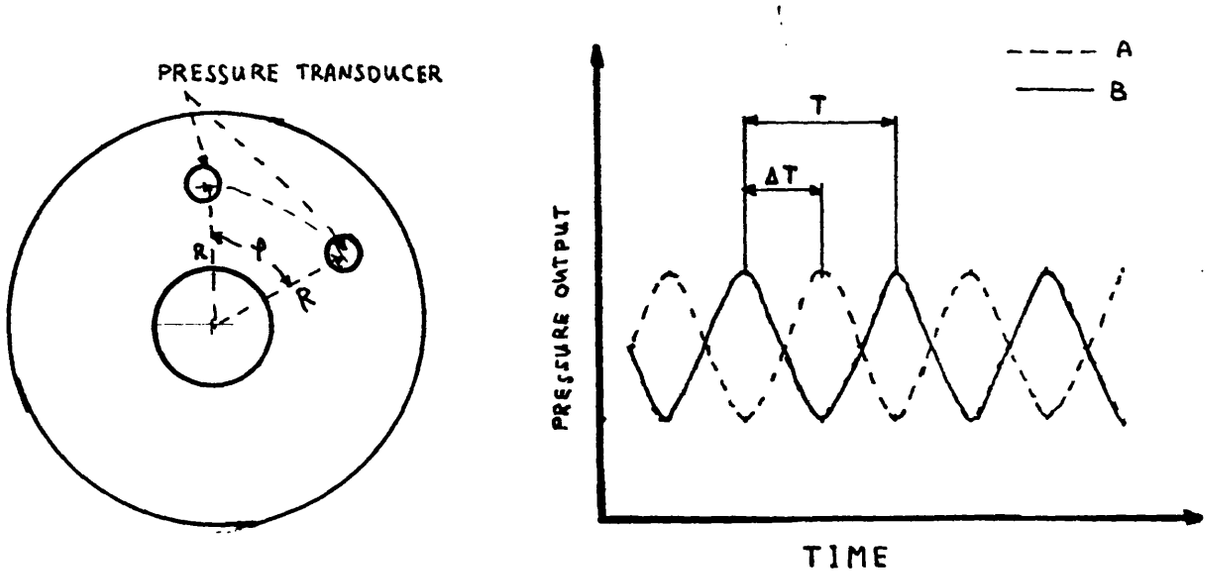

FIGURE 5.14: Schematic output of two pressure transducers and their phase difference.

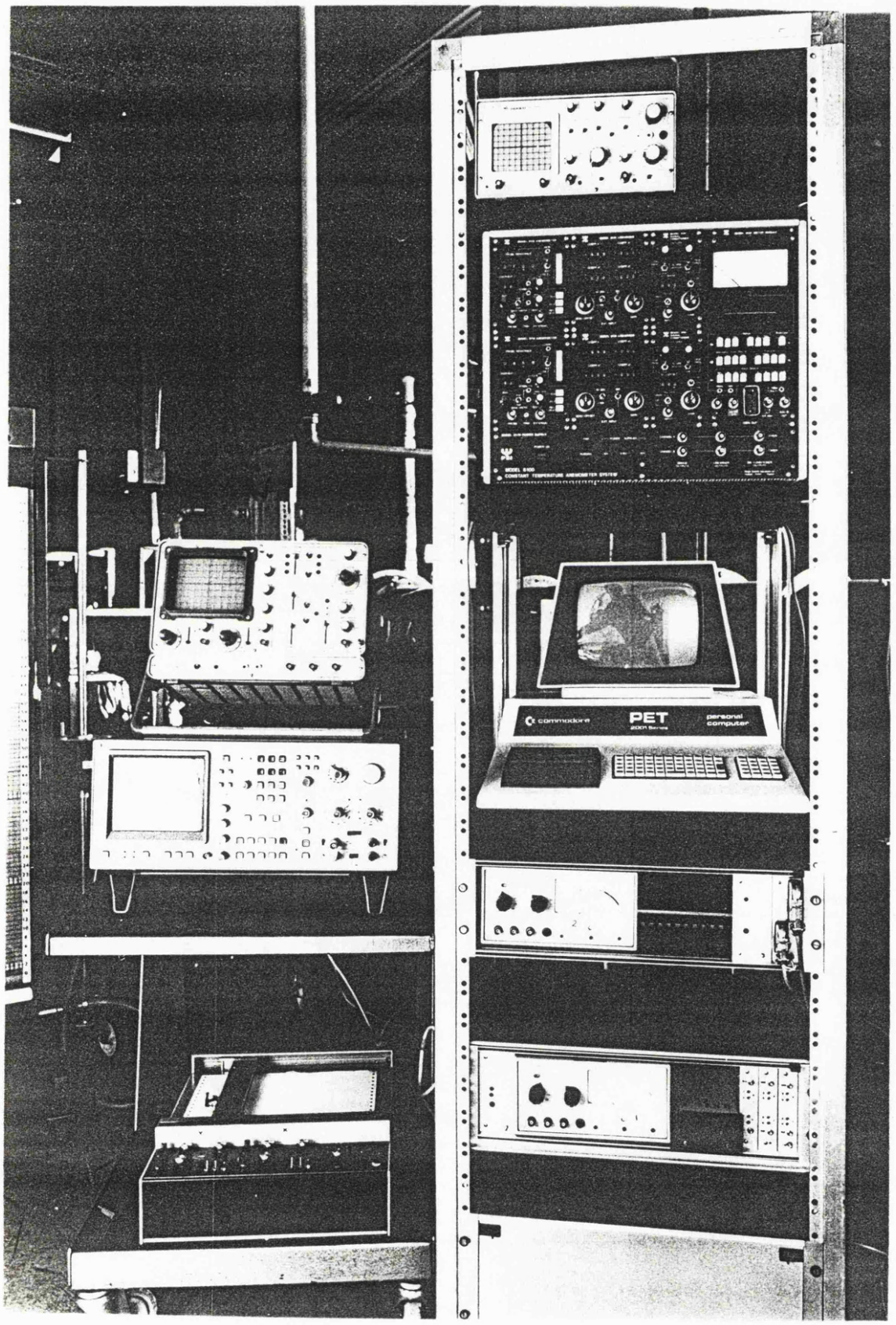

FIGURE 5.15: Data collection system.

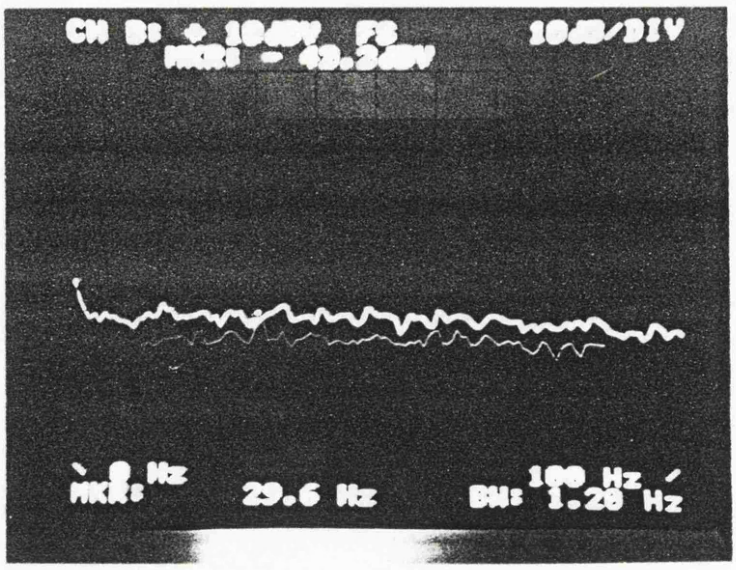

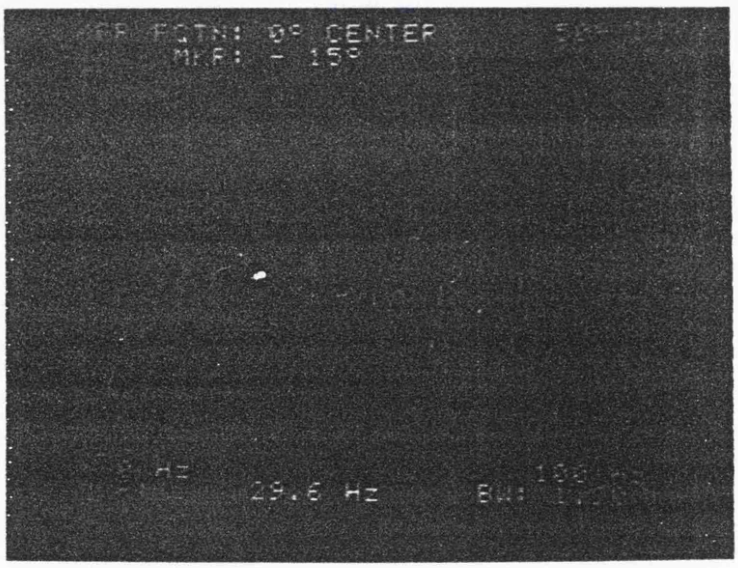

FIGURE 5.16: An example of the spectrum anaylaser display.

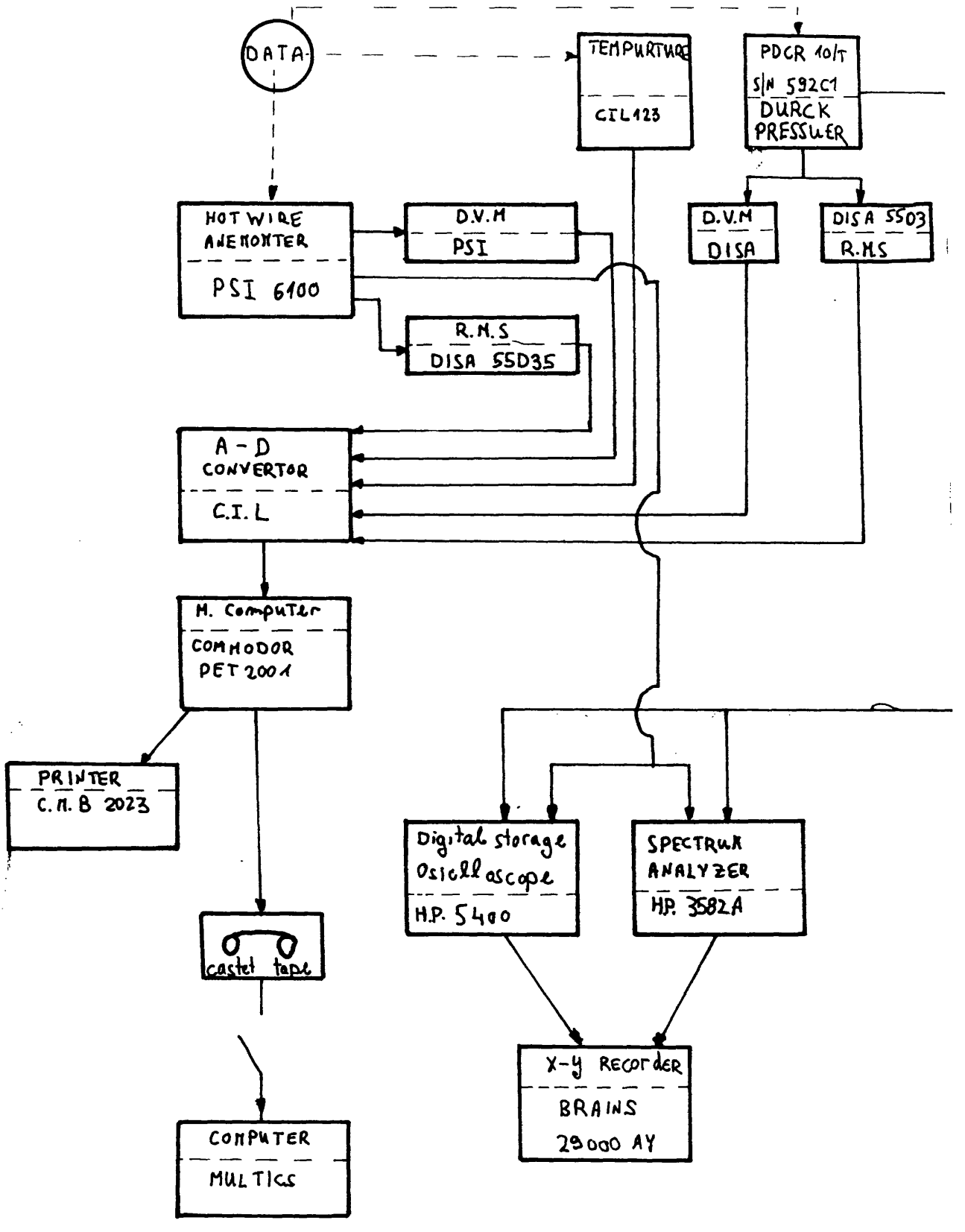

FIGURE 5.15: continued.

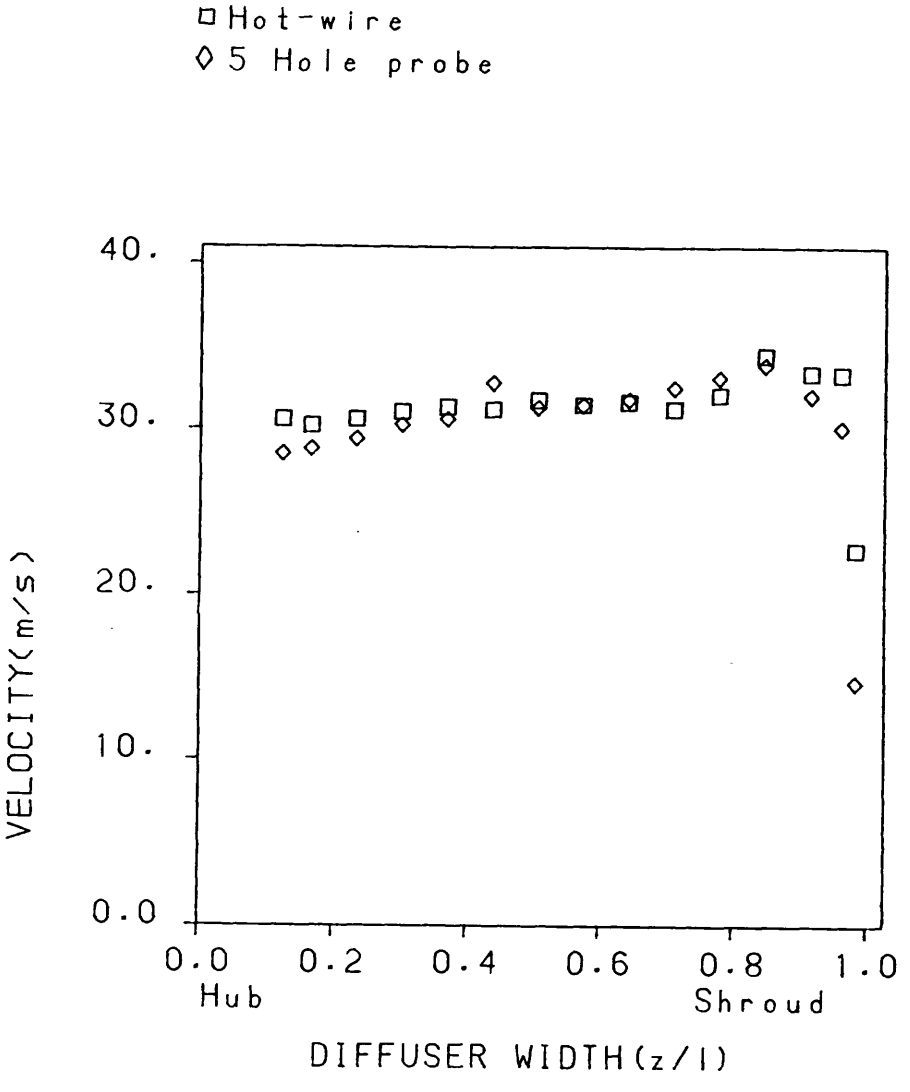

FIGURE 5.17: Comparison between the measurement of velocity in the diffuser betwwen the five hole probe and hot-wire anemometer.

CHAPTER 6

PRESENTATION AND DISCUSSION OF EXPERIMENTAL RESULTS.

6.1 INTRODUCTION

The experimental program was conducted to obtain better understanding of the flow pattern and the transient structure in radial, curved and conical vaneless diffusers. A wide range of flow conditions were studied including rotating stall and highly unsteady flows.

The diffusers were tested with different inlet flow conditions by varying the mass flow rate through the operation of one or two axial fans with the rotating screen, or the rotating screen alone. In addition by varying the screen speed and throttling the duct inlet further flow rates were achieved. Hence it was possible to systematically vary the mass flow rate and inlet flow angle.

To each test a code was given which refers to the type of diffuser and operation conditions as show below:

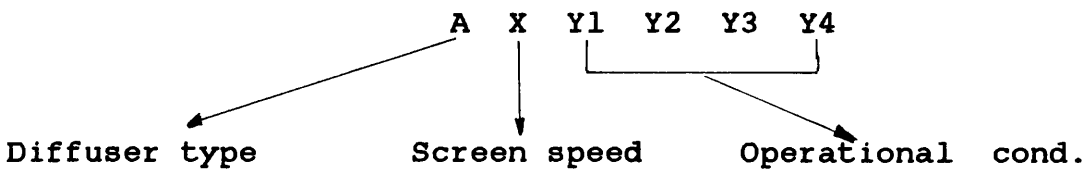

R-radial	0=2600 r.p.m	Y1-Fan 1
C-conical	1=2085 r.p.m	Y2-Fan 2
K-curved (model 1)	2=1789 r.p.m	Y3-Screen
L-curved (model 2)	3=1290 r.p.m	Y4-Inlet throtle
		0=not working
		1=working

e.g. code R01110 indicates a radial diffuser operated with 2600 r.p.m screen speed, and axial fans 1 and 2 .

In each test the flow properties were recorded by traversing the width of the diffuser passage at different stations. The mass flow rate was calculated from the integrated inlet meridional velocity profile. Integrated meridional velocity profile at other cross sections showed a disagreement on the mass flow of approximately 10% between each cross section. This was considered to be measurement and numerical errors, particular close to a surface.

Finally some experimental results were chosen to compare with the numerical results where similar inlet condition

were applied in order to check the validity of the numerical procedure.

6.2 VANELESS RADIAL DIFFUSER

The radial flow diffuser has been tested with a number of different inlet conditions which eventually led to an unstable flow pattern inside the diffuser. The inlet flow conditions were controlled by varying the flow rate, and/or the rotational speed of the screens, This meant that the flow angle and tangential component of velocity could be varied independently. The test conditions used and the associated code numbers are detailed in table 6.1. An artificial separation was created at inlet with test number 1 by displacing the shroud surface 5mm relative to the rotating screen, see fig. 6.1. An unstable operating state was reached when the inlet flow angle become higher than a critical value, this could be achieved by either reducing the flow rate or increasing the rotational speed of the screen.

6.2.1 Development of a stable flow profile throughout the diffuser

The inlet flow profiles developed with four flow conditions are shown in fig. 6.2. Tests 6(code R21010)and 2(code R11110), in fig. 6.2a yield similar inlet flow angles of approximately 62 degrees, see table 6.1, with different flow rate. Similarly tests 3 (code R10010)and 7 (code R20010), fig. 6.2b, yield inlet flow angles of 72 degrees with different flow rates. In all cases the velocity and flow angle remains approximately constant over 70% of the channel width. Near the shroud surface there is a tendency for the velocity to fall and the flow angle to increase. This increase in flow angle is possibly due to a non uniform flow through the rotating screens as illustrated in fig. 6.3.

As part of the assessment of the inlet flow conditions the pitch angle was calculated from the five hole probe measurements. The results for two flow rates, tests 2 and 6, are shown in fig. 6.4. At both inlet and outlet the pitch angle is approximately zero over 80% of the diffuser width. The high pitch angles near the wall are considered to be due to probe reading errors when it is close to the wall surface. In general the effect of

pitch angle has, therefore, been considered negligible and the meridional velocity can be refered to as the radial velocity.

Tests 2 and 6, fig. 6.2a, are examples of flow situations which led to stable operation of the diffuser. The development of the velocity and flow angle distributions throughout the diffuser is shown in fig. 6.5 and 6.6. Both the tangential and meridional velocities are constant across the inlet section except near the shroud. As the flow progresses through the diffuser the boundary layer becomes clearly defined on both surfaces at the outer radius. The velocity profile in the core flow remains uniform. With the low flow rate, fig. 6.6, the flow angle becomes close to 90 degrees on both surfaces. The growth of the boundary layer thicknes as a function of radius ratio is presented in fig. 6.7 and 6.8. In both cases the boundary layer grows most rapidly, and is finally thicker, on the shroud. For the low flow rate, fig. 6.8, the hub and shroud boundary layers almost merge at the discharge section. The friction velocity was estimated from the velocity profile using the "Cole's model" outside the laminar sublayer, .i.e. in the range $30<y^{+}<100$.

The hub and shroud boundary layer velocity profiles are presented in figs. 6.9 and 6.10. The commonly applied seventh power law provides a reasonable fit to the experimental data.

The distribution of the turbulence intensity across the passage, for each radius ratio, is shown in fig. 6.11. Two different regions can be distinguished (i)a high level of turbulence intensity in the boundary layer, particularly on the shroud surface(up to 0.2), and (ii)a low level of turbulence intensity in the core flow (approximately 0.08). The high level of turbulence at inlet is due to the effect of the rotating screen. The turbulence intensity first falls on the hub surface and then increases again as the boundary layer builds up.

The first test case listed in table 6.1 had an artificial separation on the inlet shroud surface. The resultant velocity and flow angle profiles at three measuring stations are shown in fig. 6.12. It can be seen that the reverse flow generated at inlet on the shroud surface persisted throughout the diffuser. The flow along the hub surface reached the point of separation at the final measuring station, whilst on the shroud surface at discharge the magnitude of the reverse flow has reduced

and is almost zero. This phenomenon of the separation zone shifting from one side to the other has been reported by ELLIS(1964) and REBENIK(1972). ELLIS attributed this to the fact that the vorticity was sufficiently strong to rotate the meridional velocity profile until separation occurred on the opposite surface.

6.2.2 Development of unstable flow profile

In order to develop an unstable flow pattern the inlet to the test rig was gradually throttled until the flow become clearly unstable. Results are presented for two rotational speeds of the screen, test 4 (code R10011) and test 8 (code R20011). From table 6.1 it can be seen that the unstable flow occurred at similar inlet flow angles. The inlet flow conditions for both cases are presented in fig. 6.13. From the flow angle profile it is clear that reverse flow occurred on both the hub and shroud surfaces, in the the passage center, however, the main core flow is constant over 60% of the the passage width.

In order to detect and measure the nature of the unsteady flow two pressure transducers were located on the diffuser walls and a hot wire traversed across the

internal flow. The development of the unsteady flow with reducing flow rate, as seen by the hot wire located normal to the absolute velocity and in passage center at the inlet measuring station, is presented in fig. 6.14. Three flow conditions are shown (i)a steady flow with only turbulent fluctuations superimposed upon it (ii) a flow condition prior to the onset of strong pulsations, and (iii) the fully unstable flow were the pulsations can be clearly observed. In order to study these results in more detail a spectrum frequency analyser was used. Fig. 6.15a and b shows the spectra of pressure fluctuations at diffuser inlet and discharge for three flow rates with the rotational screen operating at 2600 rev/min. The pressure transducers were located on the hub and shroud surface at the same radial and angular coordinates. For the steady flow case the dominant frequency was that of the rotating screen, 44.8 Hz, and persisted through to the diffuser discharge.

Just before the onset of unstable flow the frequency of the rotating screen ceases to be dominant and other frequencies appear approximately 23 Hz at the inlet, whilst at discharge no dominant frequency is apparant. With the onset of strong pulsations a low frequency was

detected of approximately 15 Hz, along with the higher harmonics, which persisted through to the diffuser discharge.

The presence of rotating stall cells in the diffuser passage were detected by placing three wall pressure transducers at the same radius but at angular positions of -45 ,0 ,90 degrees. The results presented ,figs. 6.16-6.19, were for test case 8 (table 6.1) in which the rotational speed of the screen was 1789 rev/min. Before the onset of unstable flow no phase difference in the pressure fluctuations was observed and the level of the pressure spectra was low and no frequency was dominant. When the unstable flow region was reached low frequency pulsations were dominant when observed with either the pressure transducers, fig. 6.16, or the hot wire anemometer, fig. 6.17. The nature of the pressure pulsations and the dominant frequencies remained unchanged throughout the diffuser, figs. 6.16 and 6.18. The phase difference between the pressure transducers displaced by 45 degrees is illustrated in fig 6.19. The rotating stall frequency and the number of rotating cells were found using the techniques described in chapter 5. Table 6.2 summarises the results obtained for the three

rotational speeds of the screen. The frequency of the rotating stall lies between 24% and 34% of the rotating screen frequency. In all cases the onset of flow pulsations occurred when the inlet flow angle was approximately 85 degrees.

6.3 CURVED ANNULAR DIFFUSER

Two curved diffuser configurations have been studied by using two shroud profiles. Both diffusers had the same inlet cross section, but by employing different shroud curvatures the discharge width of Model 1 and Model 2 diffuser was 33mm and 41.33mm respectively. Both diffusers were tested through a range of flow conditions by varying both the flow rate and screen rotational speed. The test conditions employed are given in table 6.3.

6.3.1 Development of a stable flow profile throughout the diffuser.

The inlet flow conditions for a range of tests with both diffusers are illustrated in figures 6.20 to 6.21. The results presnted have been selected to cover a broad

range of inlet flow angles. The test condition have been obtained by varying the rotational speed of the screen and/or the number of fans used, as illustrated in table 6.3. In all cases the absolute velocity and flow angles remained approximately constant over 80% of the channel width. At the lowest flow rates, tests 16 and 19, a reverse flow region exists on the hub surface where the flow angle exceeds 90 degrees. The pitch angles, figs. 6.22 and 6.23, were calculated from hot wire anemometer and five hole probe measurements. Again results are presented for a range of flow angles. At the highest flow rate, lowest flow angle, see fig. 6.22(i), the inlet pitch angle is approximately constant and close to zero over 60% of the passage width but rises to 10 degrees on the hub surface. Measurments close to a surface are subject to errors. With inlet flow angles of 61 and 77 degrees, figs. 6.23(i) and 6.22(i), the inlet pitch angle is positive with a tendency to increase towards the shroud surface. With the highest flow angle, test 16 fig. 6.22(ii), where a flow reversal occurred on the hub surface, the pitch angle lies between 5 and 10 degrees throughout the channel width. Figures 6.22 and 6.23 also show pitch angles measured at other radial stations through the diffuser. Generally, fig. 6.23, the pitch

angle decreases as flow passes through the diffuser except near the shroud surface. For the tests presented with Model 1 diffuser flow reversals developed on the shroud surface leading to a large variation in pitch angle with high values near the shroud.

As examples of stable flow operation of the Model 1 diffuser test 14 and test 15 were chosen, whilst for Model 2 diffuser tests 20 and 21 are presented. The rotating screen speed was the same for each pair of tests whilst the flow rate was varied by not using the fans for tests 15 and 21. Consequently the inlet tangential velocity components were approximately equal in both pairs of tests, whilst the flow angles were significantly higher for test 15 and 21 due to the reduced meridional component of velocity, see figs 6.24, 6.25, 6.26 and 6.27. The effect of the different diffuser passage widths can be seen in the variation of the meridional component of velocity. With the narrow diffuser, Model 1, there is an increase in meridional velocity through the curved part of the diffuser, fig. 6.24, and consequently the flow angle decreases. With Model 2 diffuser, fig. 6.26 test No.20, the meridional velocity shows no significant change up to the radial part of the

diffuser. By reducing the mass flow rate flow reversals developed on the hub surface, this can be most clearly observed where the flow angle exceeds 90 degrees. The wide passage diffuser, Model 2, proved to be move prone to separation, with a reverse zone being detected at the second measuring station, radius ratio 1.19.

The boundary layer velocity distribution, fig. 6.28, can be reasonably represented by a seventh power law in the radial part. On the curved surfaces however, fig. 6.28(i) and (ii), the magnitude of the power must be reduced in order to obtain a satisfactory representation. Whilst it is difficult to detect any difference due to the different curvature of the two diffuser shroud surfaces there is a clear change in boundary layer profile with position along the curved surface. This uncertainty in the magnitude of the power parameter led to the use of the "Logarithmic law of the wall" in the theoretical model to predict the diffuser flows. Fig. 6.29 shows that this logarithmic curve provides a satisfactory fit to the experimental data at all radial stations and in the range $0.3 < y/\delta < 1.0$.

The distribution of the turbulence intensity across the diffuser passage for each radius ratio is shown in fig.

6.30, (Model 1) and fig. 6.31 (Model 2). Again tests 14 and 15 and tests 20 and 21 are used to illustrate typical results. In all the tests the level of turbulence intensity at inlet is approximately constant over 80% of the passage width and varied between 0.08 with the low flow rates to 0.12 for the high flows. At the high flow rates, figs. 6.30a and 6.31a, there is little significant change in turbulence intensity as the flow passes through the diffuser. At the low flow rate, figs. 6.30b and 6.31b, the effect of the change of diffuser design is clearly indicated. With the wide passage diffuser, Model 2, the turbulence intensity clearly increases with radius ratio and exceeds 25% in the reverse flow zones. With the narrow passage diffuser, fig. 6.30b, similar changes in turbulence intensity are not observed despite similar inlet flow conditions.

6.3.2 Unstable diffuser flow

In order to develop a highly unstable flow the inlet to the test rig was gradually throttled in order to reduce the mass flow rate. Tests 16 and 19, see table 6.3, are presented as examples of low flow rates generated by throttling the inlet. Both tests yielded an average inlet flow angle of approximately 82 degrees (81 and 83

degrees in table 6.3), whilst test 19 had a high flow rate compared to test 16 due to the high rotational speed of the screen. Details of the mean flow profiles at all measurement stations are presented in figs. 6.32 and 6.33. In both cases reverse flow existed at the first measuring station. With the wide passage diffuser, fig. 6.33, the reverse flow persisted on the hub throughout the diffuser and at the discharge radius there is a tendency for reverse flow to commence on the shroud also. With Model 1 diffuser, fig. 6.32, the reverse flow zone moves from the hub to the shroud surface and at the discharge radius there is no clear indication of reverse flow on either side. In both cases the flow was extremely unsteady.

In order to measure the details of the unsteady flow pressure transducers were located on the diffuser walls and the output, along with that from the hot wire anemometer, were analysed with a spectrum analyser. The development of the unstable flow is illustrated in fig 6.34. For test 14, fig 6.34(i), the flow was stable and the dominant frequency was that of the rotating screen. Reducing the flow rate to that of test 15, fig 6.34(ii), leads to an unsteady flow but with no dominant frequency.

The traces labelled A and B were obtained from two pressure transducers offset from each other by an angle of 45 degrees. As can be seen from fig. 6.34(ii) there was no phase difference between the traces, thereby indicating no rotating stall. Further reduction of the flow rate by throttling the inlet, test 16, led to the pressure traces of figs. 6.34(iii) and 6.34(iv). In this case a low frequency pulsation of 4.8 Hz is clearly indicated. The phase difference, at this frequency, between the two traces was 47 degrees thereby indicating a single rotating stall cell. By locating the pressure transducers at the same angular and radial position on the hub and shroud the pressure traces of fig. 6.34(iv) were obtained with the same dominant frequency but in this case without any phase difference between the pulsations. Further reduction of the flow rate slightly reduced the pulsation frequency to 4.0 Hz and no phase difference was indicated.

The operating condition for test 13 were similar to those of test 16 except the rotational speed of the screen was increased from 1296 rev/min to 1789 rev/min. In this case, fig. 6.35, the lowest dominant frequency was 5.6 Hz, a high frequency of 20 Hz, which is not a harmonic of

the low frequency, was also clearly indicated. ABDELHAMID(1980) reported a similar observation and assumed the existence of two types of stall in the system. For the results of fig. 6.35 the pressure transducers were located: (i) opposite each other on the hub and shroud and (ii) at the same angular position but a three radial locations on the shroud. In both cases similar traces were observed with no phase difference between the pulsations. This indicates that the unsteady flow extended radially from inlet to outlet and filled the passage width. Spectrum frequency traces of the pressure transducer at inlet and outlet are compared with hot wire anemometer traces in fig. 6.36. Very similar results are clearly shown.

For the Model 2 diffuser test 22 and 19 are presented. Fig. 6.37 shows the velocity fluctuations at inlet and outlet as recorded directly from a hot wire anemometer, along with the associated frequency spectra. A low dominant frequency of 6.8 Hz is clearly indicated at both inlet and outlet. The frequency spectra obtained from two inlet pressure transducers off set from each other by 45 degrees is shown in fig. 6.38. The low dominant frequency is 6.4 Hz approximately equal to that given by

the hot wire anemometer. The phase difference between the two traces is shown in fig. 6.38(i). At the frequency of 6.4 Hz the phase difference is approximately 20 degrees whilst at the first harmonic 12.8 Hz the phase angle is 70 degrees. At the highest rotating screen speed, test 19 fig. 6.39, the frequency spectra indicates dominant frequencies of 9.6 Hz and 19.6 Hz with a phase difference, not shown, of 50 degrees. The lower dominant frequencies obtained with each diffuser and with three rotational screen speeds are showned in table 6.4, Whilst it was clear that the Model 2 diffuser was less stable then the Model 1 diffuser, reverse flow commencing at higher inlet flow angles with the Model 2 diffuser, there was no measurable difference between the diffuser flow behavior once a fully established unsteady flow commenced.

6.4 ANNULAR CONICAL DIFFUSER TESTS

The annular conical diffuser had the same inlet cross section as the curved diffusers and employed the same rotating screen. The diffuser was constructed of parallel conical surfaces with a cone angle of 52.5

degrees. The diffuser was tested through a range of flow conditions by varying the flow rate and speed of rotation of the screen. The test conditions are summarised in table 6.5.

6.4.1 Development of a stable flow profile throughout the diffuser.

The inlet conditions for four typical tests are shown in fig. 6.40. In all cases the velocities and flow angles remain effectively constant across the passage width. The flow pitch angle is presented in fig. 6.41 for tests 27 and 29. With a high flow rate, test 29, the main core flow pitch angle at inlet is approximately -5 degrees, whilst with a reduced flow, test 27, it increased to -10 degrees. In both cases the pitch angle increased near the diffuser walls, however the measurement accuracy can not be considered to be very good in this region. In all tests the pitch angle was considered small and was not included in the analysis of the results.

The results for test 28 and 29 in which the flow rates were approximately equal are presented in figs. 6.42 and 6.43. Due to the differing rotational screen speeds used the mean inlet angles were 66 and 61 degrees for tests 28

and 29 respectively. The tangential velocity at inlet shows a gradual increase from hub to shroud due to the higher screen velocity at the shroud radius. The inlet meridional velocity is substantially constant; however the profile develops a significant gradient, with low velocity on the hub surfaces, as the flow passes through the diffuser. This is particular clear for test 28, fig. 6.42, where a significant reverse flow zone has developed at the first measurement radius (radius ratio 1.35). For test 29 the flow reversal is not detected until the discharge measurement position. Clearly flow reversals occurred at much lower inlet flow angles (66 degrees) than was observed with the curved diffusers (73 degrees) and the reduction of flow stability with the straight conical diffuser was readily apparent.

The distribution of turbulence intensity for tests 28 and 31 are shown in figs. 6.44 and 6.45. On fig. 6.44 three regions can be distinguished:

(i) A high level of turbulence in the shroud boundary layer.

(ii) A uniform intensity level in the main flow.

(iii) The hub region where a separation zone occurred.

In the region between the main through flow and the reverse flow zone the turbulence intensity increases but falls again in the separated flow. For test 31 the mean inlet flow angle was 71 degrees and consequently the degree of flow reversal was greater than that of test 28. The turbulence intensity, as a consequence, increases from that at inlet and whilst the three regions described above are not so clearly defined they still exist.

The shroud surface boundary layer profiles are shown in fig. 6.46 for test 27 and 28. In all cases the power law with a coefficient between 5.5 and 6.0 can be applied to fit the experimental data except near the wall, i.e. not for the first 30% of the boundary layer. At the inlet, fig. 6.46(i), the curve fit is unsatisfactory for 50% of the boundary layer. This is due to the inlet flow pattern near the shroud and the uncertainty of measurements close to the wall.

The "logarithmic law of the wall" was used with Cole's model outside the laminar sublayer($y^+ > 30$) to calculate the wall shear stress. The friction velocity and the boundary layer thickness for two test conditions are presented in fig. 6.47. The friction velocity is high for test 28 compared with test 29 whilst the boundary

layer thicknesses are identical. This correlates with the large reverse flow zone observed with test 28.

6.4.2 Unstable diffuser flow

The most severe pulsating flow conditions studied occurred with test No.27 where a reverse flow zone existed at all measurement stations on the hub surface. The mean flow profiles are shown in fig. 6.48 where the negative meridional velocities and the high flow angles on the hub clearly show a reverse flow zone throughout the diffuser. The mean inlet flow angle for this cases was 75 degrees and was the largest tested, see table 6.5. To measure the fluctuating nature of the flow two pressure transducers were located at the same radius but off set from each other by 90 degrees. The resulting pressure traces on the hub and shroud are shown in fig. 6.49(i) and (ii). Similar results are shown in both cases with a phase difference of approximately 180 degrees between the two traces. This indicated two rotating stall cells and compares with only one observed with the curved diffuser. Location of the pressure transducers without any angular offset but at either different radii, inlet and outlet or on different

surfaces, hub and shroud, showed no phase difference between the pressure pulsations. This showed that the stall cells filled the diffuser passage in both width and radial location.

The development of the unstable flow condition at the low rotational screen speed, tests 29 to 31, was studied with a spectrum frequency analyser. The resultant traces for test 29, stable flow, and test 31, unstable flow, are shown in fig. 6.50. For the stable flow measurements were taken at inlet and outlet and in both cases the dominant frequency was that of the rotating screen. For the pulsating flow the pressure transducers were located on the hub and shroud inlet surface. The dominant pulsation frequencies are most clearly indicated by the hub surface measurements which show a low frequency of 7.2 Hz. The rotating stall frequencies measured with the three rotating screen speeds tested are given in table 6.6.

6.5 COMPARISON OF THEORETICAL AND EXPERIMENTAL RESULTS

The experimental results presented in the previous sections were used to test the validity of the finite

element computational methods presented in chapter 3. The experimentally determined inlet conditions to the diffuser were used to specify the theoretical inlet boundary, whilst the discharge boundary was set sufficiently far from the actual discharge radius so that it did not significantly effect the computed results within the diffuser. For the theoretical inlet boundary condition the meridional velocity was integrated and presented in terms of stream function. The tangential component of velocity was presented in terms of angular momentum and the vorticity was calculated from the gradient of the meridional velocity at each point of the cross section. The theoretical analysis has been applied to stable flow conditions in each of the four diffusers studied experimentally.

6.5.1 Application to the radial diffuser

The experimental results from tests No. 2 and 6, flow codes R11110 and R21010, were selected for comparison with the theoretical study. In this experimental study the mean inlet flow angle was approximately 62 degrees in both cases and no flow reversals occurred in the diffuser. The theoretically specified inlet boundary

assumed a uniform tangential component of velocity, whilst the meridional velocity had a similar profile to that obtained experimentally. The differences shown in fig. 6.51, test No.2, between the theoretical and experimental meridional velocity at inlet reflects the process of converting the measured velocity to a stream function boundary condition and then back to a velocity. At the second measurement station, radius ratio 1.235, the experimental tangential component of velocity is high relative to that predicted , fig. 6.51. The predicted meridional component of velocity compares satisfactorily with that measured. At the discharge, radius ratio 1.55, both the tangential and meridional components of velocity compare well with those measured. The effect of the distorted tangential velocity at inlet on the shroud surface is still apparent at the diffuser discharge.

The comparison between the predicted and experimental results for test No. 6 are presented in fig. 6.52. In this case a finer mesh was used with reduced mesh size near the walls (25 nodes at each cross section compared to 19 nodes for the previous analysis). In this case the boundary layers are more prominent as in the previous test and with the exception of the discharge tangential

velocity. The velocity profiles are predicted satisfactorily at all stations.

The differences shown between the experimental and theoretical results could be due to errors and inaccuracies in both the experimental measurements and the numerical analysis. In order to assess the accuracy of the experimental measurements the conservation of mass and momentum at the three measurement stations was checked. The mass flow rate obtained from an integration of the velocity profiles is given by $m = r\, U_m dz$. The parameter rU_m is therefore presented for each cross section in fig. 6.53. The area under each curve is proportional to the mass flow rate and should, therefore, be the same at each cross section. The greatest discrepency is approximately 10% for test No. 6 between the first station and the third station. The angular momentum at each cross section is given by

$$\int_{z=0}^{z=z_t} r^2 U_m U_\theta \, dz$$

and the parameter $r^2 U_m U_\theta$ is, therefore , presented for each cross section in fig. 6.54. Again if the angular momentum is to be conserved the area under the curve should be equal. The relatively high values for the second measurement station with test No. 2 is clearly

shown. For test No. 6 the relative discrepancies are not readily apparent.

In the theoretical analysis no attempt has been made to distinguish between the effective radial and tangential viscosities. YAMAMOTO(1980) showed that the calculated decay of tangential velocity exceeded that obtained experimentally due to the large calculated viscosities. He concluded that accurate estimation of the viscosity is more important for swirling flows than for non-swirling flows, since the tangential velocity is affected more by the viscosity than is the axial velocity. In this case the radial, velocity is governed strongly by the continuity requirement rather than by the the value of viscosity.

The discrepercy shown in fig. 6.51, radius ratio 1.235, appears to be largely experimental, see fig. 6.54(i), whilst the discrepercy at the discharge radius for test No. 6, fig. 6.52, is probably related to the use of a high effective viscosity in the tangential direction.

6.5.2 Application to the curved diffuser

The theoretical analysis was applied to both diffuser models tested and the predictions compared with tests No. 14 and 20, both of which had mean inlet flow angles of approximately 60 degrees and consequently no flow reversals occurred. In both cases, figs. 6.55 and 6.56, satisfactory agreement is shown except for the discharge tangential component of velocity which is low relative to that measured experimentally. Again the use of high effective viscosity is considered to be the cause of this high decay in predicted tangential velocity. No attempt has been made to include the effect of curvature on the transfered using the Richardson number as recommended by BRADSHAW(1973). Instead a very fine mesh was employed in the curved section and near the walls, see fig. 6.57.

6.5.3 Application to the conical diffuser.

For the conical diffuser test No. 29 has been used for comparative purposes see, fig. 6.58. In this case the mean inlet flow angle was approximately 61 degrees and was the most steady flow case tested. However, the conical diffuser flow was generally unstable relative to the curved diffuser design and a small reverse flow zone

existed on the hub surface at the discharge radius. The theoretical computation was similarly unstable and it was necessary to employ a fine mesh arrangement, 29 nodes at each cross section, in order to obtain a converged solution. Again satisfactory comparisons are achieved, with the decay of the tangential velocity component exceeding that measured experimentally.

TEST NO.	FLOW CODE	FLOW RATE (m 3) sec	INLET FLOW ANGLE (deg)	OPERATING CONITION SCREEN SPEED (r.p.m)	FAN 1	FAN 2	SCREEN	INLET
1	R01110	1.72	65	2600	+	+	+	-
1a	R00011	-	84	2600	-	-	+	+
2	R11110	1.67	62	2085	+	+	+	-
3	R10010	0.96	72	2085	-	-	+	-
4	R10011	0.43	85	2085	-	-	+	+
5	R21110	1.51	54	1789	+	+	+	-
6	R21010	1.1	61	1789	+	-	+	-
7	R20010	0.55	72	1789	-	-	+	-
8	R20011	0.25	87	1789	-	-	+	+

TABLE 6.1: Flow condition for radial diffuser

TEST NO.	FLOW CODE	SCREEN SPEED [Hz]	INLET FLOW ANGLE (deg)	LOWER RORATING STALL FREQUENCY [Hz]	NUMBER OF CELLS
1a	R00011	44.8	84	15.	2
4	R10011	34.8	85	9.8	2
8	R20011	29.8	87	7.2	1

TABLE 6.2: Rotating stall data for different rotating screen speeds. (RADIAL DIFFUSER)

TEST NO.	FLOW CODE	FLOW RATE (m 3) sec	INLET FLOW ANGLE (deg)	OPERATING CONITION SCREEN SPEED (r.p.m)	FAN 1	FAN 2	SCREEN	INLET
9	K01110	1.68	69	2600	+	+	+	-
10	K00010	1.32	72	2600	-	-	+	-
10a	K00011	-	-	2600	-	-	+	+
11	K21110	1.29	61	1789	+	+	+	-
12	K20010	0.73	75	1789	-	-	+	-
13	K20011	0.55	80	1789	-	-	+	+
14	K31110	1.14	60	1296	+	+	+	-
15	K30010	0.426	77	1296	-	-	+	-
16	K30011	0.344	83	1296	-	-	+	+
17	L01110	1.64	71	2600	+	+	+	-
18	L00010	1.008	72	2600	-	-	+	-
19	L00011	0.752	81	2600	-	-	+	+
20	L21110	1.34	61	1789	+	+	+	-
21	L20010	0.694	76	1789	-	-	+	-
22	L20011	0.49	81	1789	-	-	+	+
23	L30010	0.51	71	1296	-	-	+	-
24a	L30011	-	79	1296	-	-	+	+

TABLE 6.3: Flow conditions for curved diffuser.

TEST NO.	FLOW CODE	SCREEN SPEED [Hz]	INLET FLOW ANGLE (deg)	LOWER RORATING STALL FREQUENCY [Hz]	NUMBER OF CELLS
10a	K00011	44.5	-	10.4	1
13	K20011	29.8	80	5.6 20.	1 2
16	K30011	21.6	83	4.8	1
19	L00011	44.5	81	9.6	1
22	L20011	29.8	81	6.4	1
23a	L30011	21.6	79	4.8	1

TABLE 6.4: Rotating stall data for different rotating screen speeds. (CURVED DIFFUSER)

TEST NO.	FLOW CODE	FLOW RATE (m 3) sec	INLET FLOW ANGLE (deg)	OPERATING CONITION SCREEN SPEED (r.p.m)	FAN 1	FAN 2	SCREEN	INLET
24	C01110	1.64	68	2600	+	+	+	-
25	C00010	0.72	73	2600	-	-	+	-
26	C11110	1.14	72	2085	+	+	+	-
27	C10010	0.61	75	2085	-	-	+	-
28	C21110	1.14	66	1789	+	+	+	-
28a	C20010	-	71	1789	-	-	+	-
29	C31110	1.19	61	1296	+	+	+	-
30	C31010	0.96	66	1296	+	-	+	-
31	C30010	0.58	71	1296	-	-	+	-

TABLE 6.5: Flow condition for conical diffuser

TEST NO.	FLOW CODE	SCREEN SPEED [Hz]	INLET FLOW ANGLE (deg)	LOWER RORATING STALL FREQUENCY [Hz]	NUMBER OF CELLS
27	C10010	44.5	75	10.7	2
28a	C20010	29.8	71	9.5	2
31	C30010	21.6	71	7.2	2

TABLE 6.6: Rotating stall data for different rotating screen speeds. (CONICAL DIFFUSER)

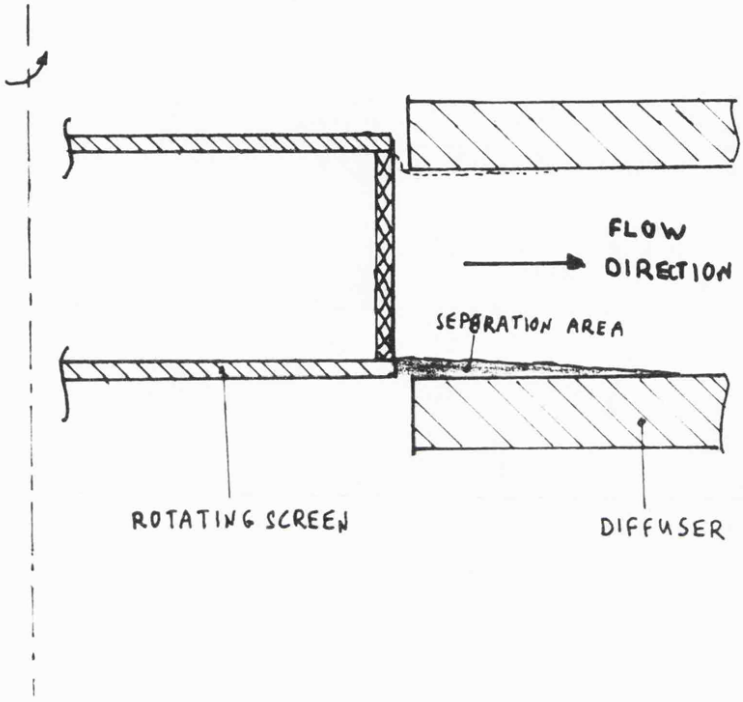

FIGURE 6.1: Illustration of artificial separation in a radial diffuser.

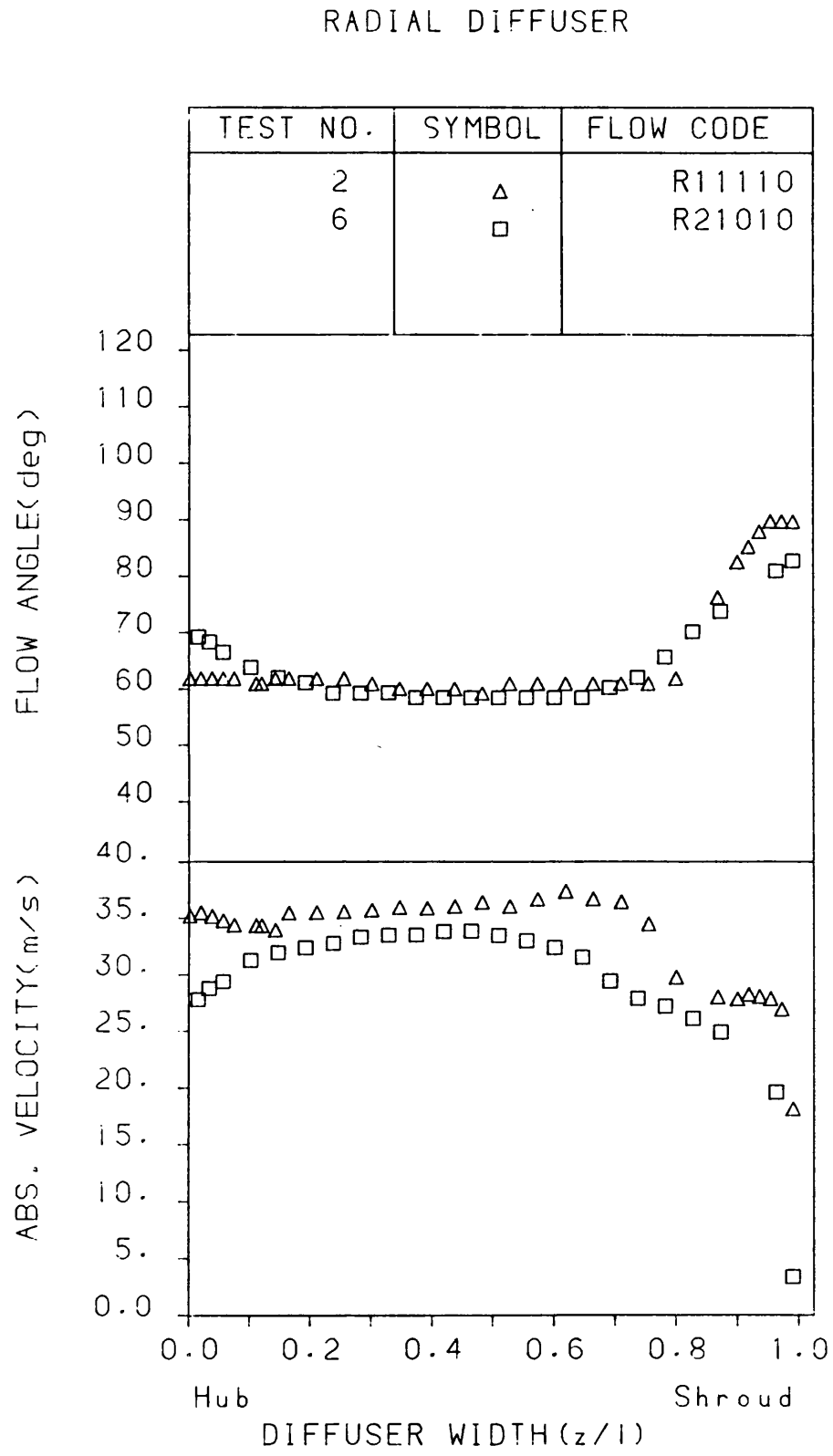

FIGURE 6.2a: Distribution of absolute velocity and flow angle at the inlet of the diffuser.

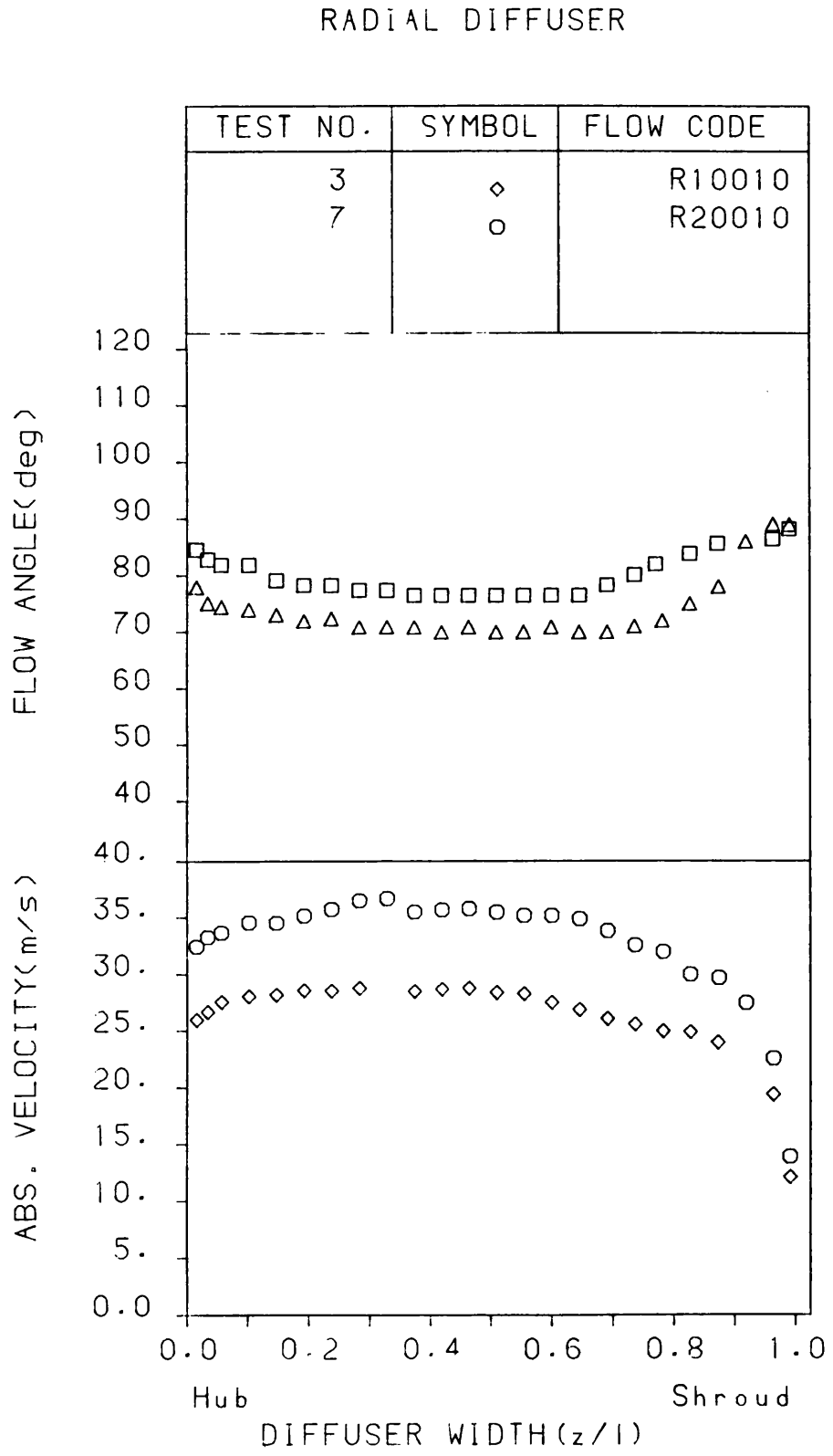

FIGURE 6.2b: Distribution of absolute velocity and flow angle at the inlet of the diffuser.

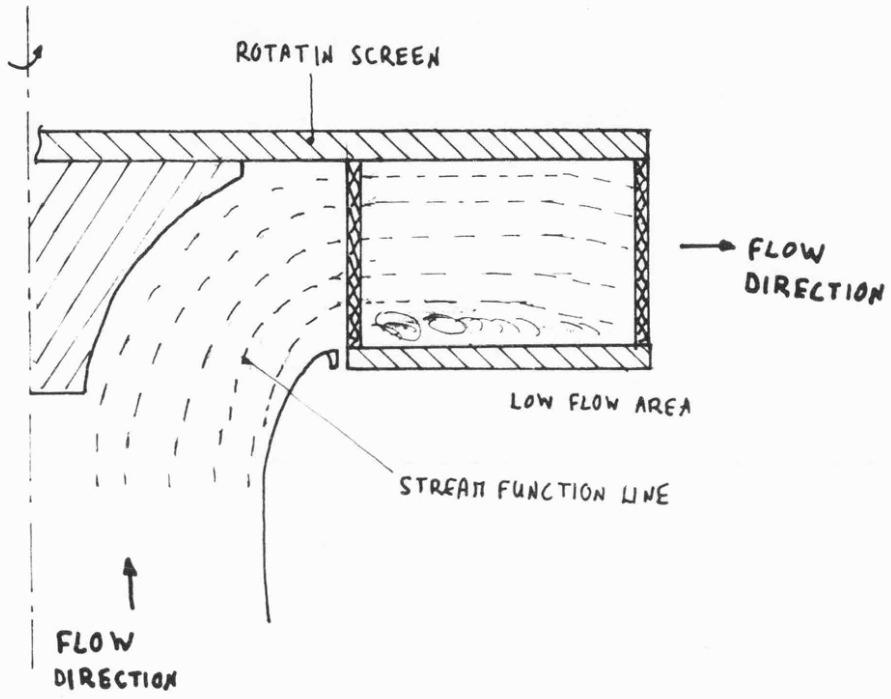

FIGURE 6.3: Flow pattern through the rotating screens.

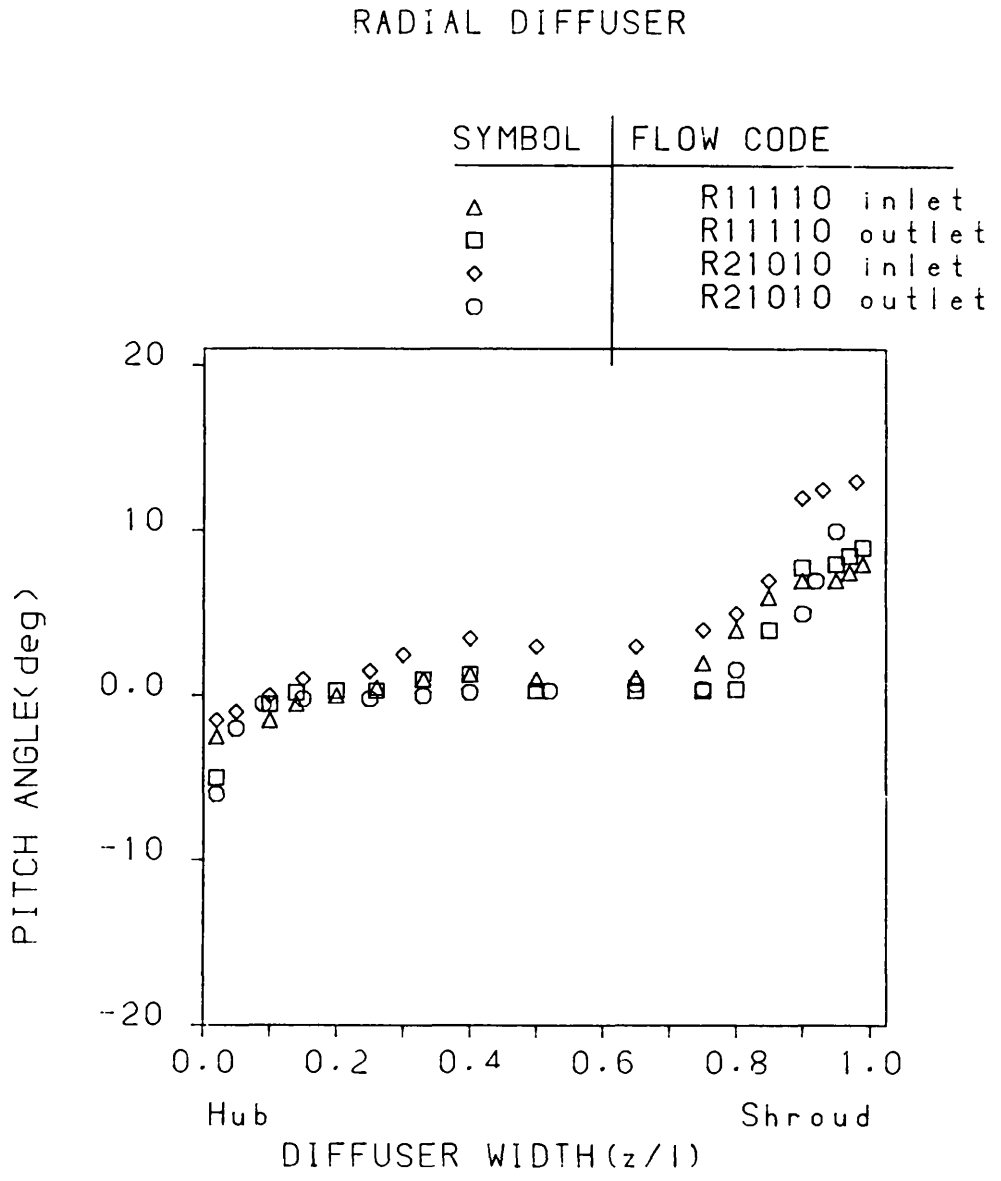

FIGURE 6.4: Pitch angle distribution across diffuser width for different flow rates.

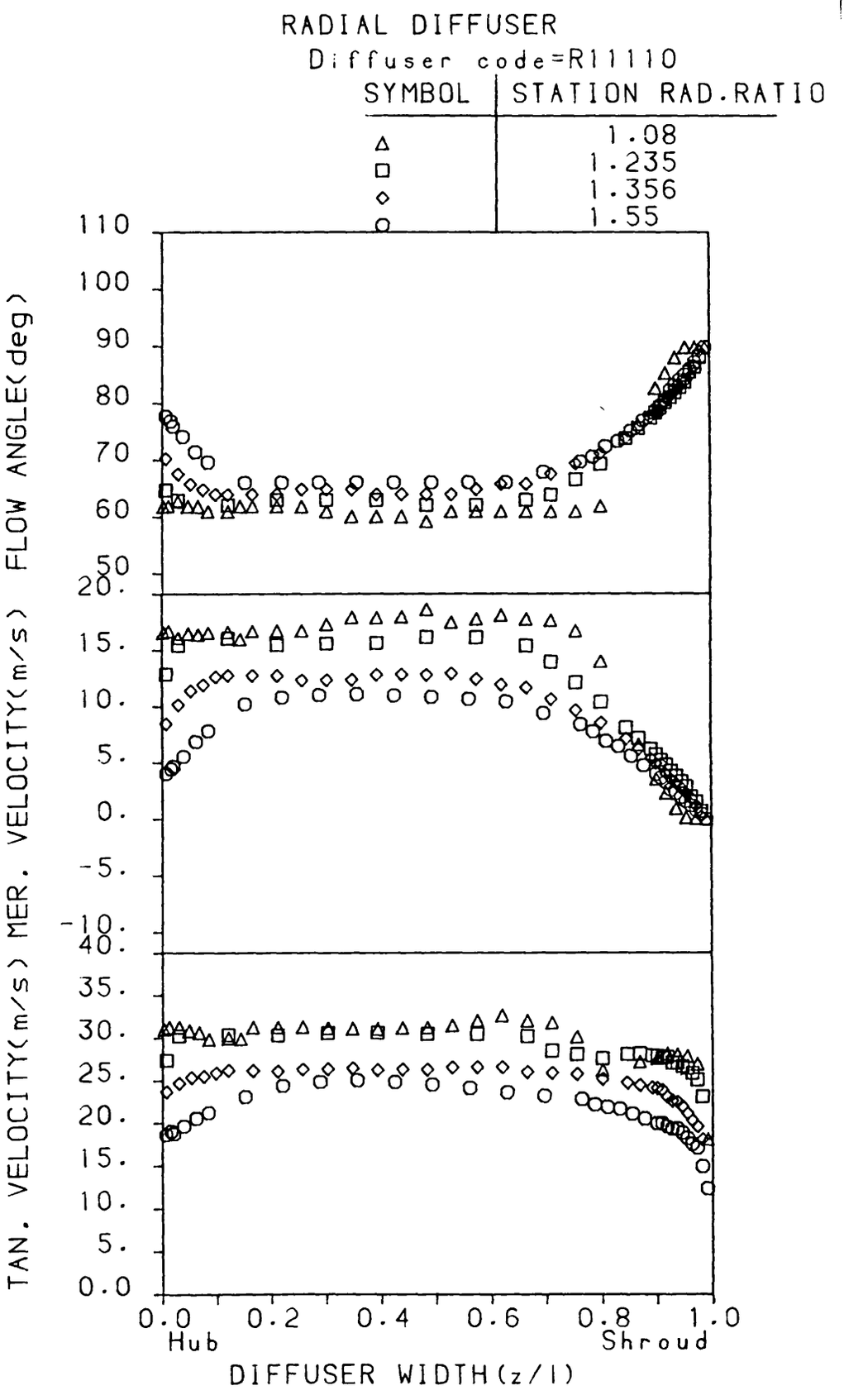

FIGURE 6.5: Velocity distribution in a radial diffuser at different radial stations.

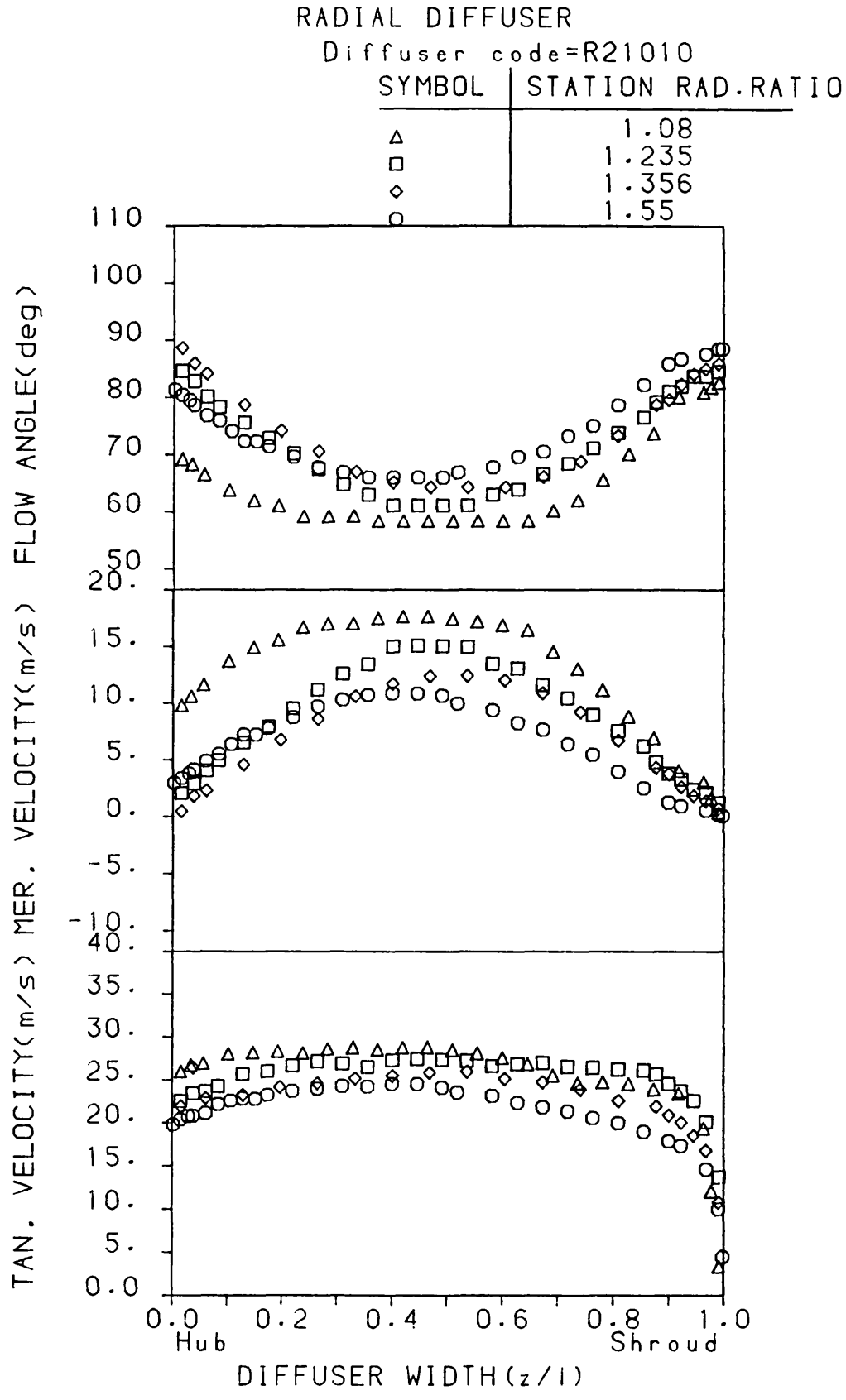

FIGURE 6.6: Velocity distribution in a radial diffuser at different radial stations.

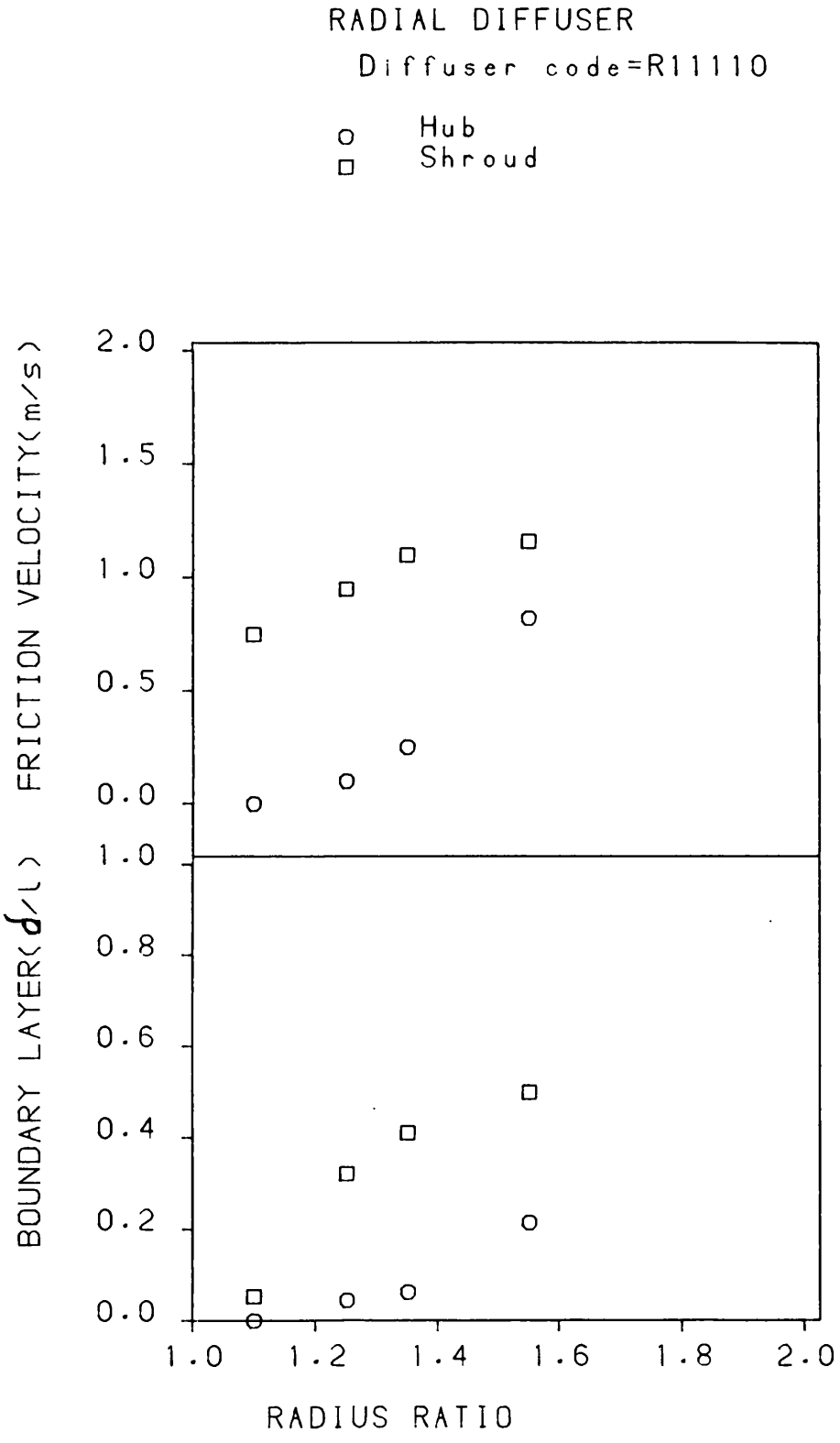

FIGURE 6.7: Boundary layer thickness and friction velocity throughout the radial diffuser.

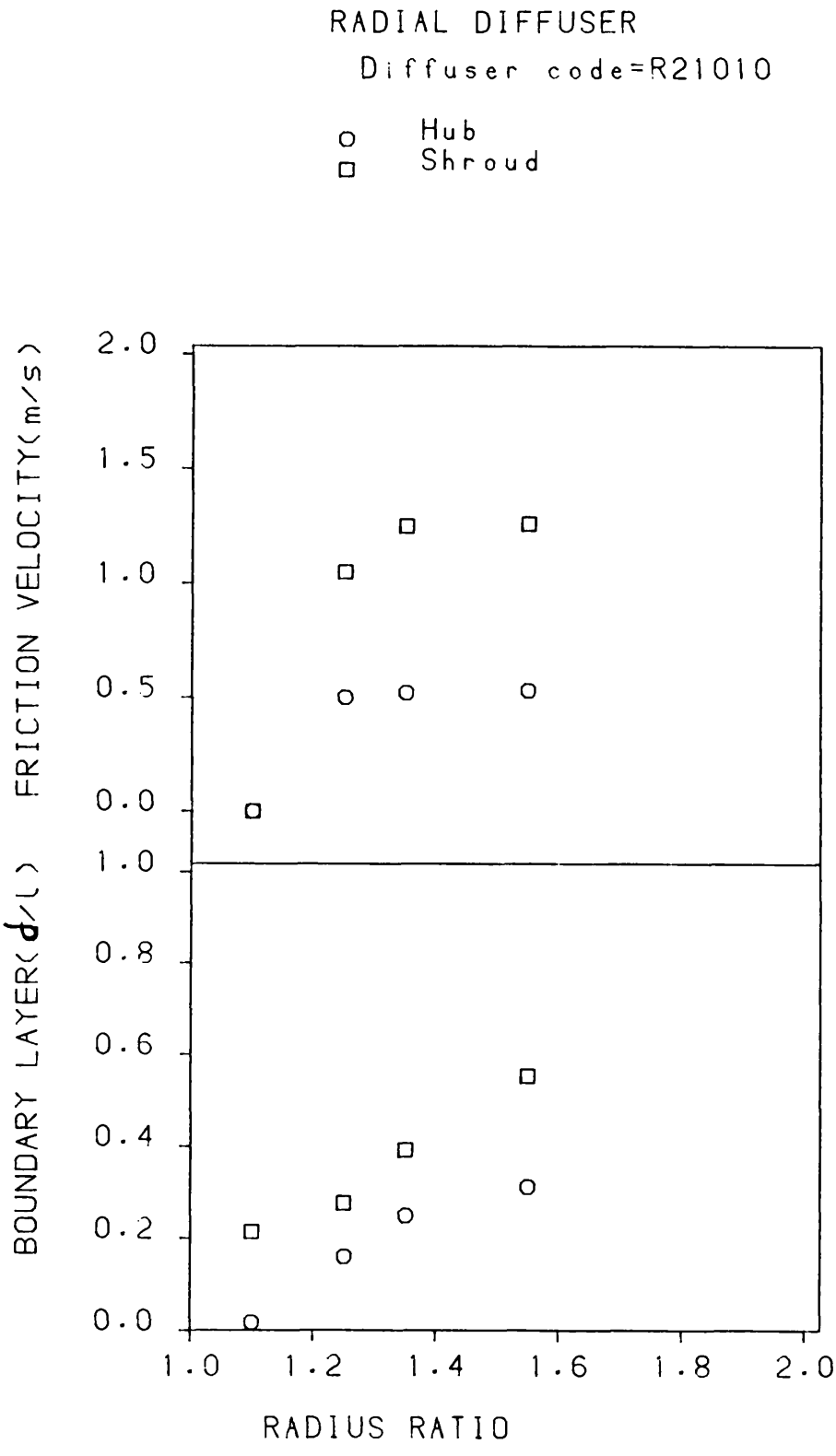

FIGURE 6.8: Boundary layer thickness and friction velocity throughout the radial diffuser.

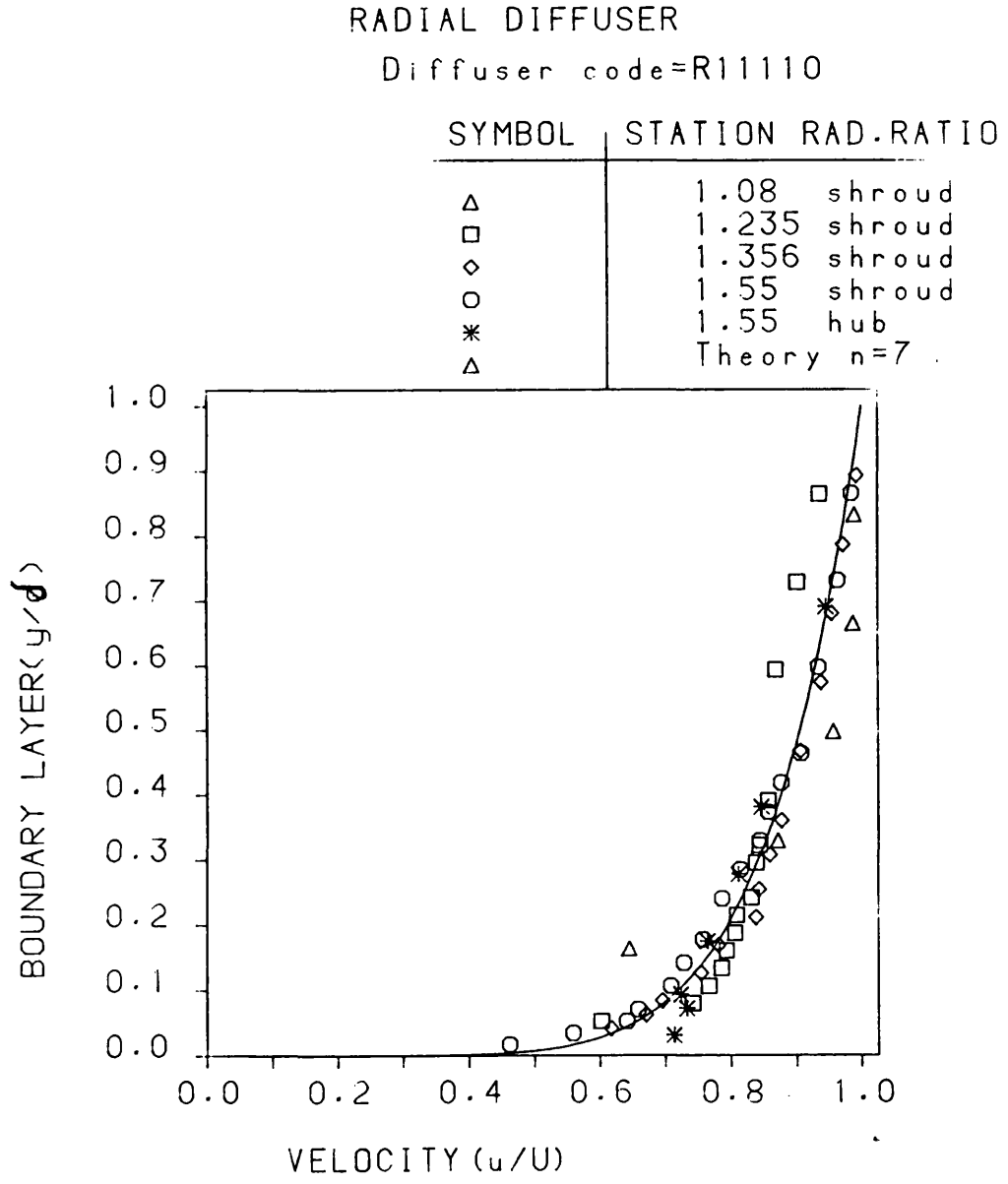

FIGURE 6.9: Velocity distribution in the boundary layer

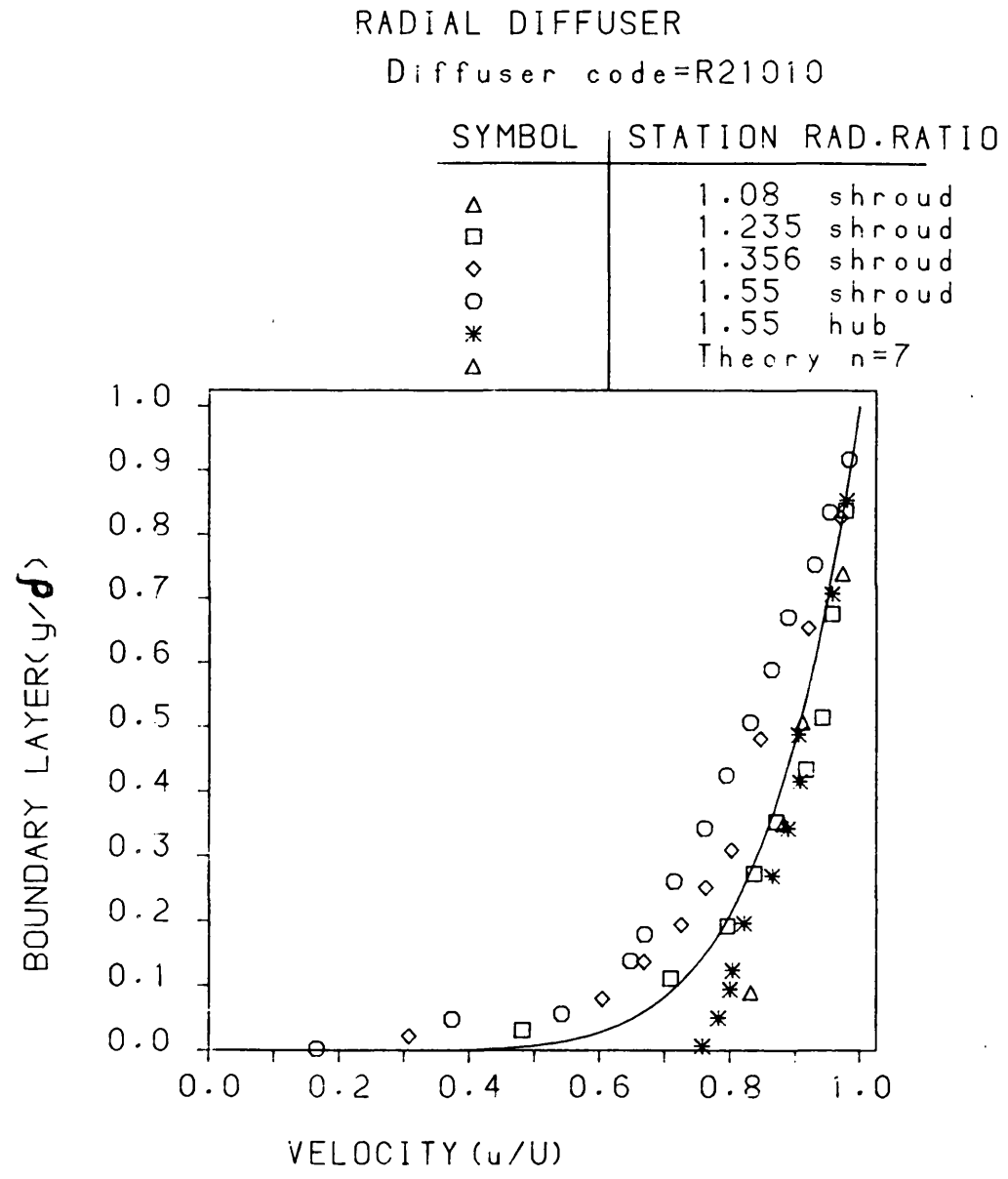

FIGURE 6.10: Velocity distribution in the boundary layer

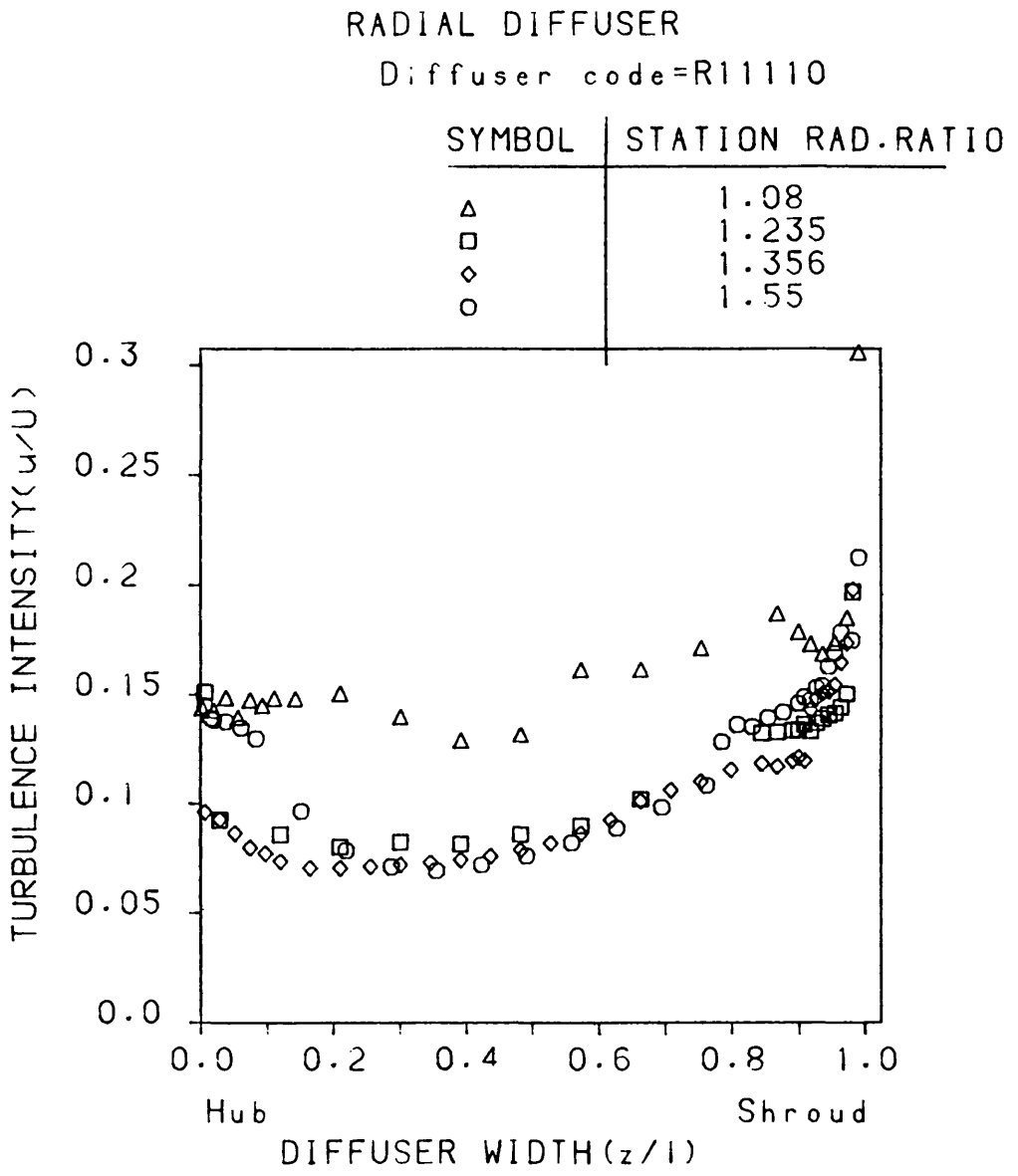

FIGURE 6.11: Turbulence intensity distribution in the radial diffuser.

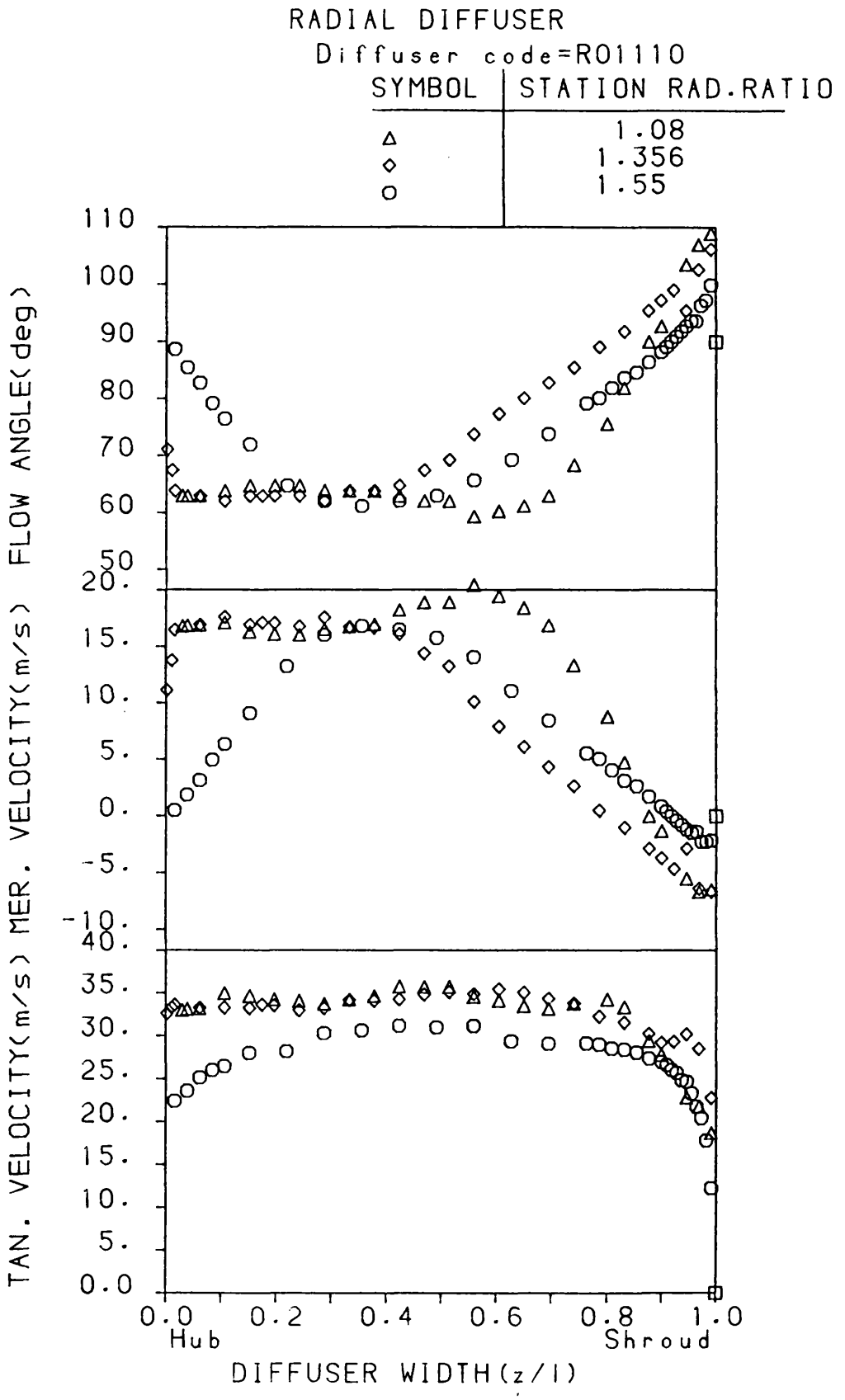

FIGURE 6.12: Velocity distribution throughout a radial diffuser with artificial separation at inlet.

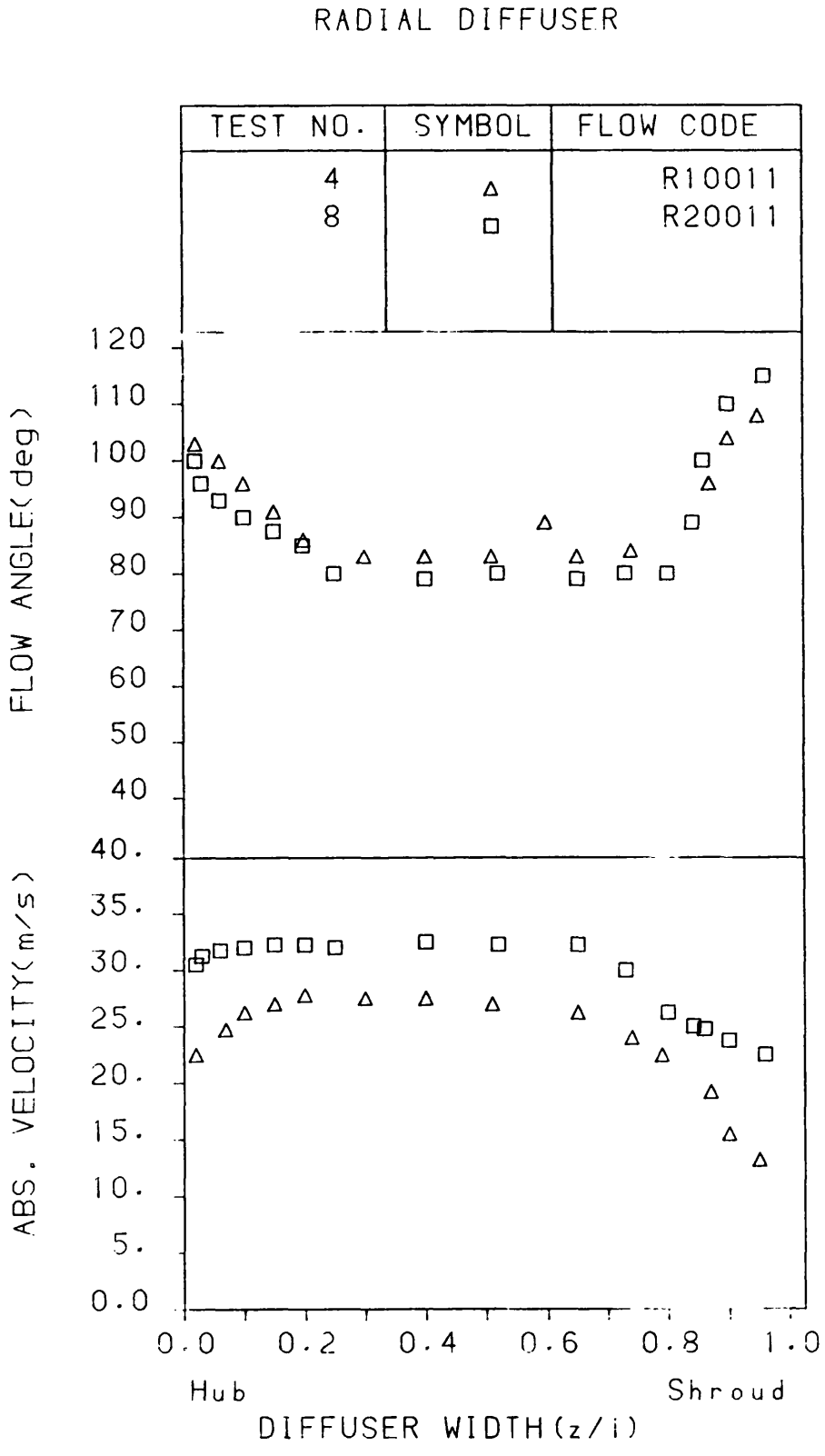

FIGURE 6.13: Absolute velocity and flow angle profiles at the diffuser inlet for unstable flow.

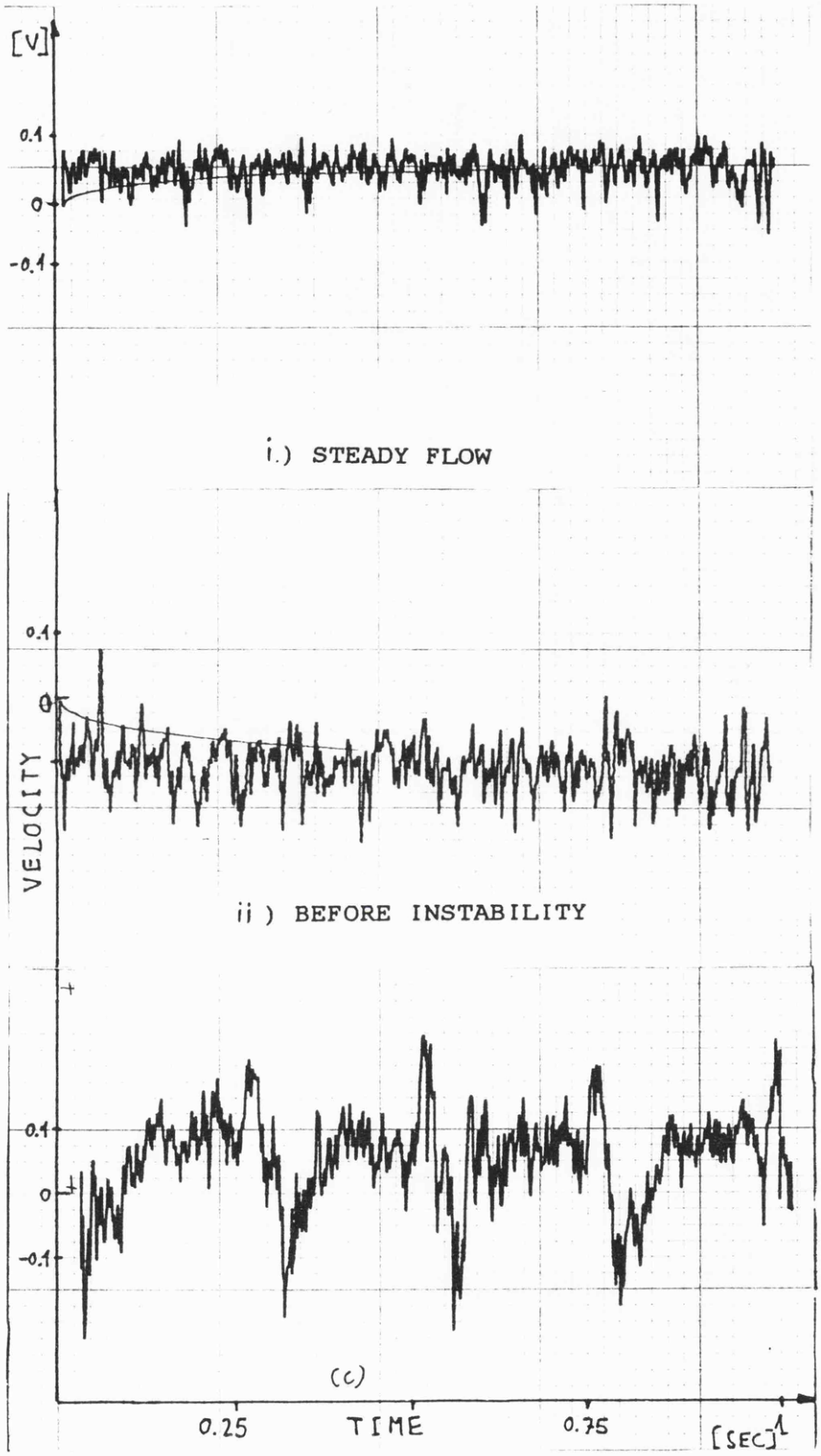

FIGURE 6.14: Hot-wire anemometer velocity fluctuations at inlet.

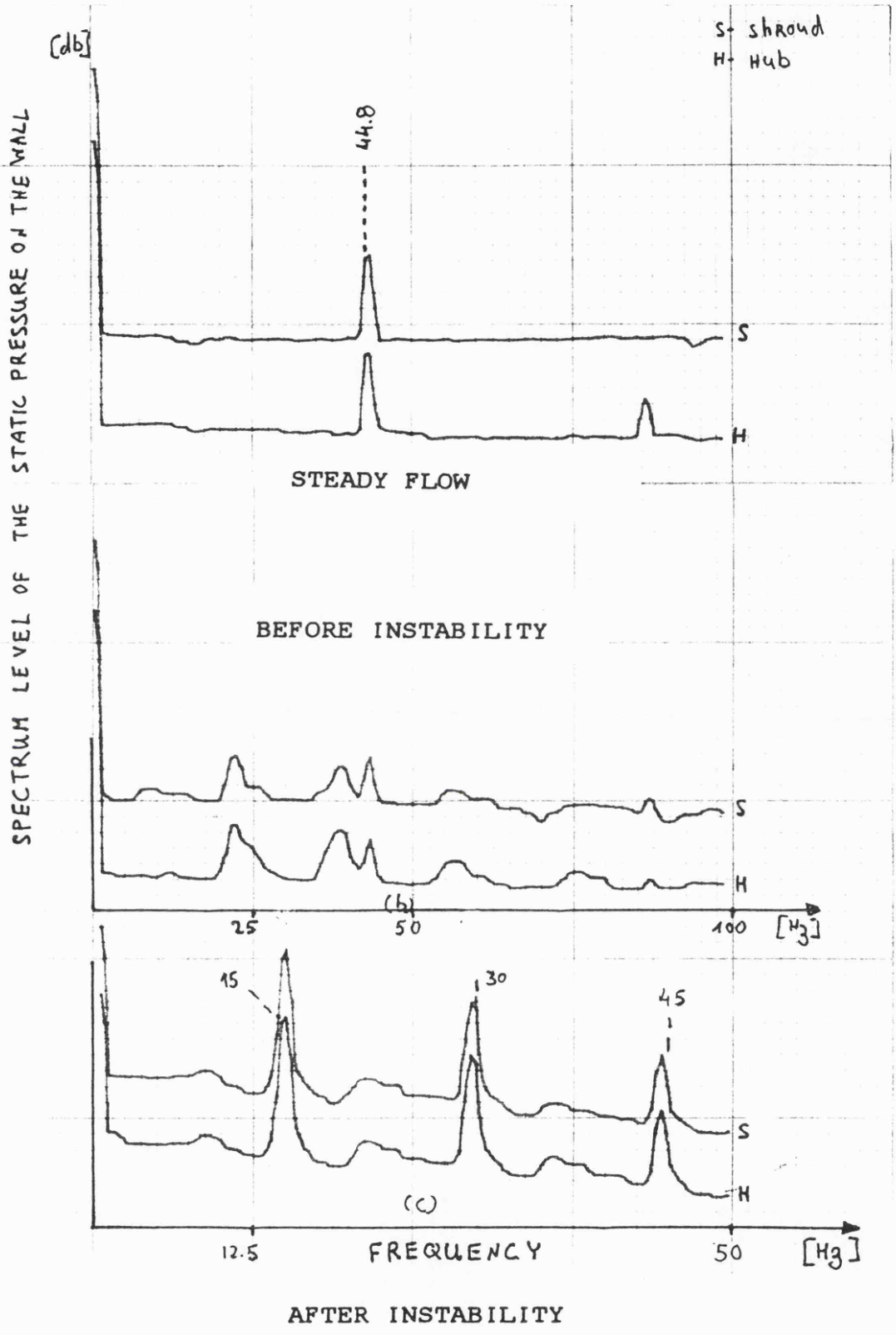

FIGURE 6.15a: Spectra of radial diffuser inlet pressure fluctuations.(2600 r.p.m screen speed)

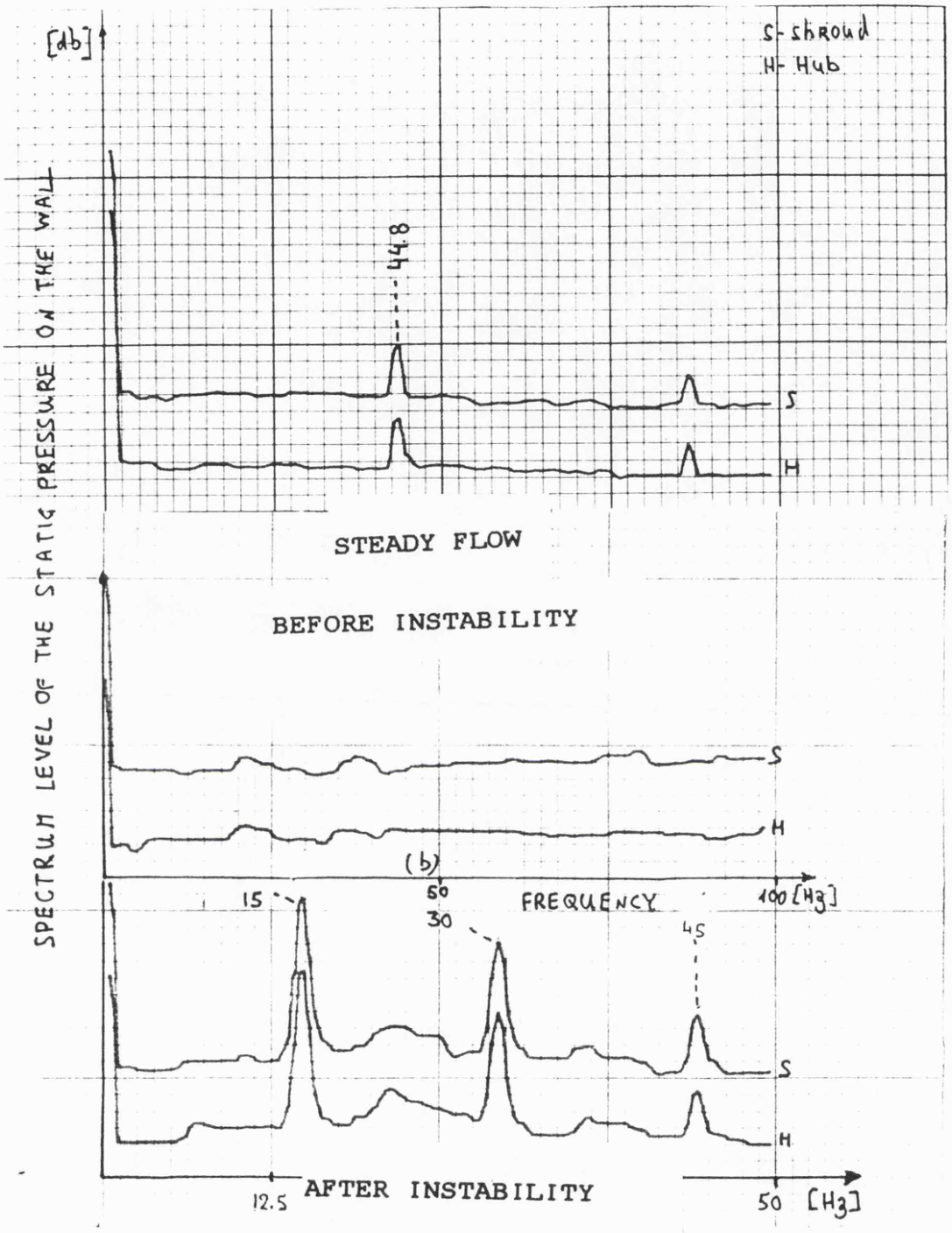

FIGURE 6.15b: Spectra of radial diffuser outlet pressure fluctuations.(2600 r.p.m screen speed)

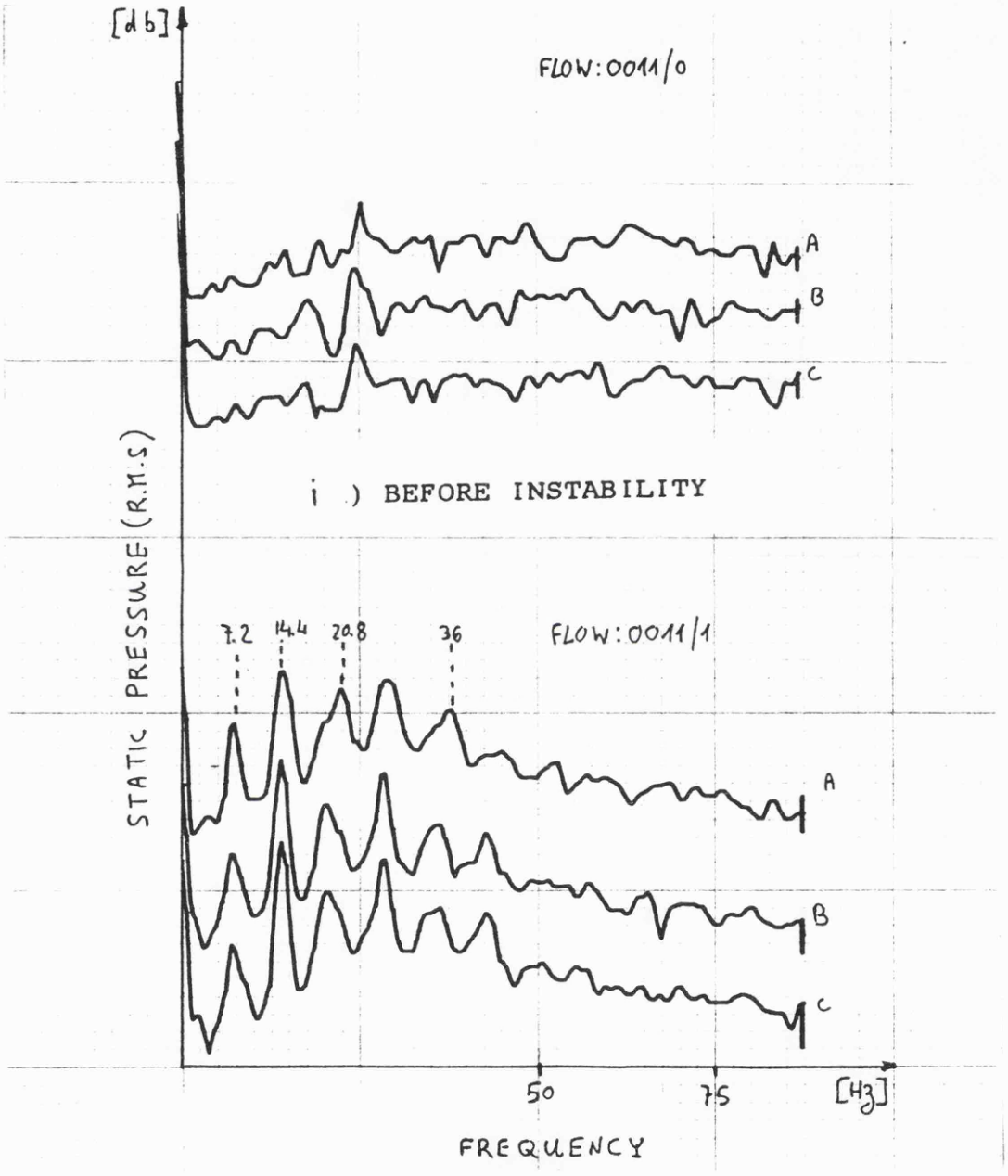

FIGURE 6.16: Spectra of radial diffuser inlet pressure fluctuations.(1789 r.p.m screen speed)

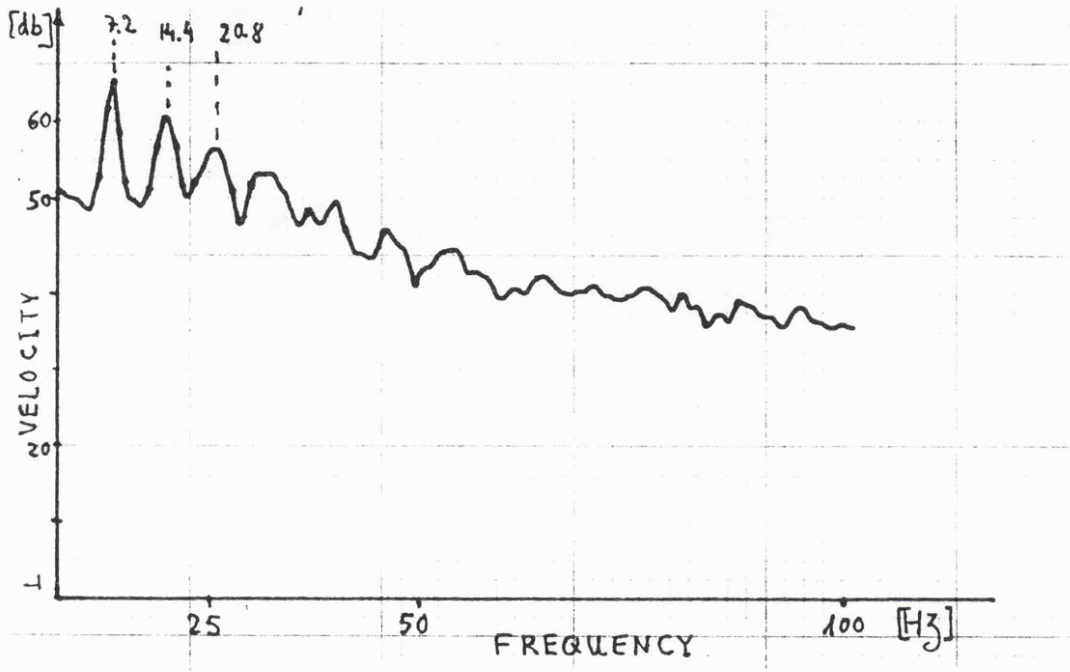

FIGURE 6.17: Spectra of radial diffuser inlet velocity fluctuations.(1789 r.p.m screen speed) Measured by hot-wire anemometer.

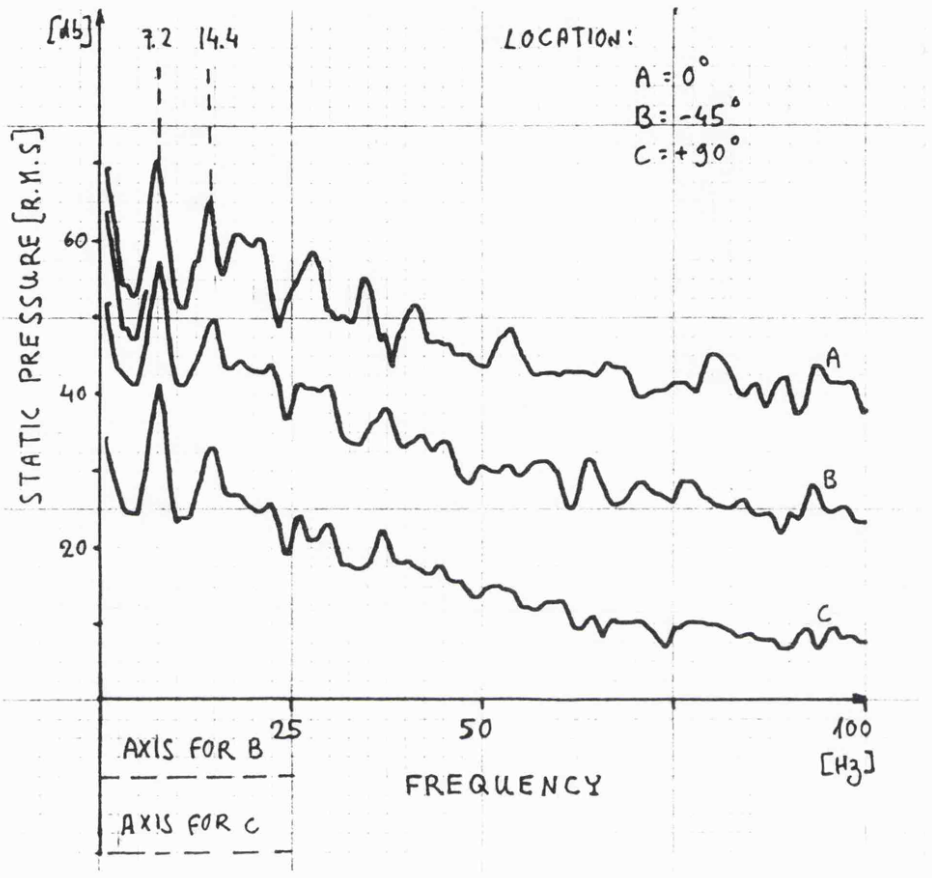

FIGURE 6.18: Spectra of radial diffuser outlet pressure fluctuations.(1789 r.p.m screen speed)

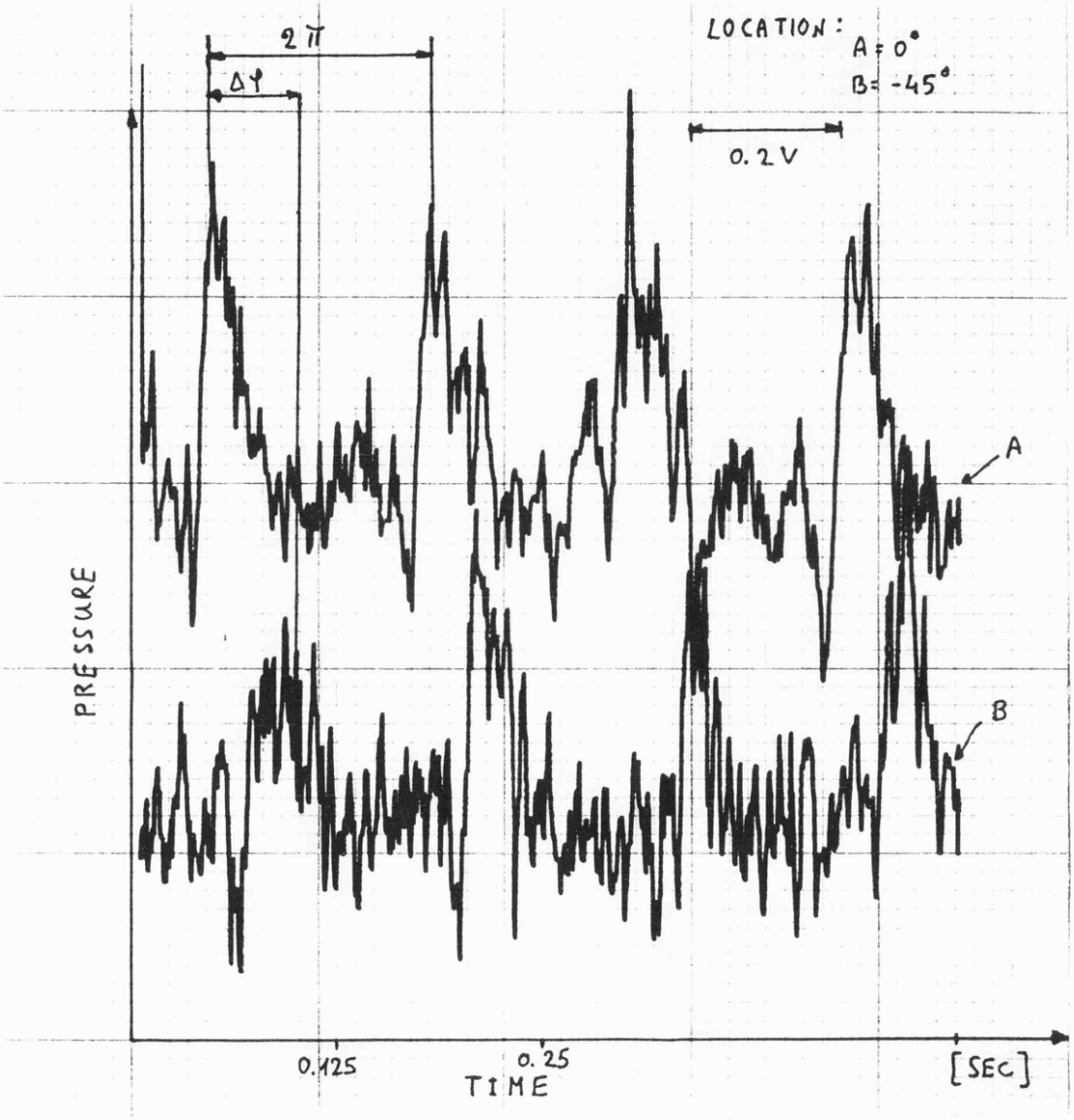

FIGURE 6.19: Phase difference of the pressure fluctuations between two pressure transducers located at the same radius (outlet), but offset by 45 degrees.

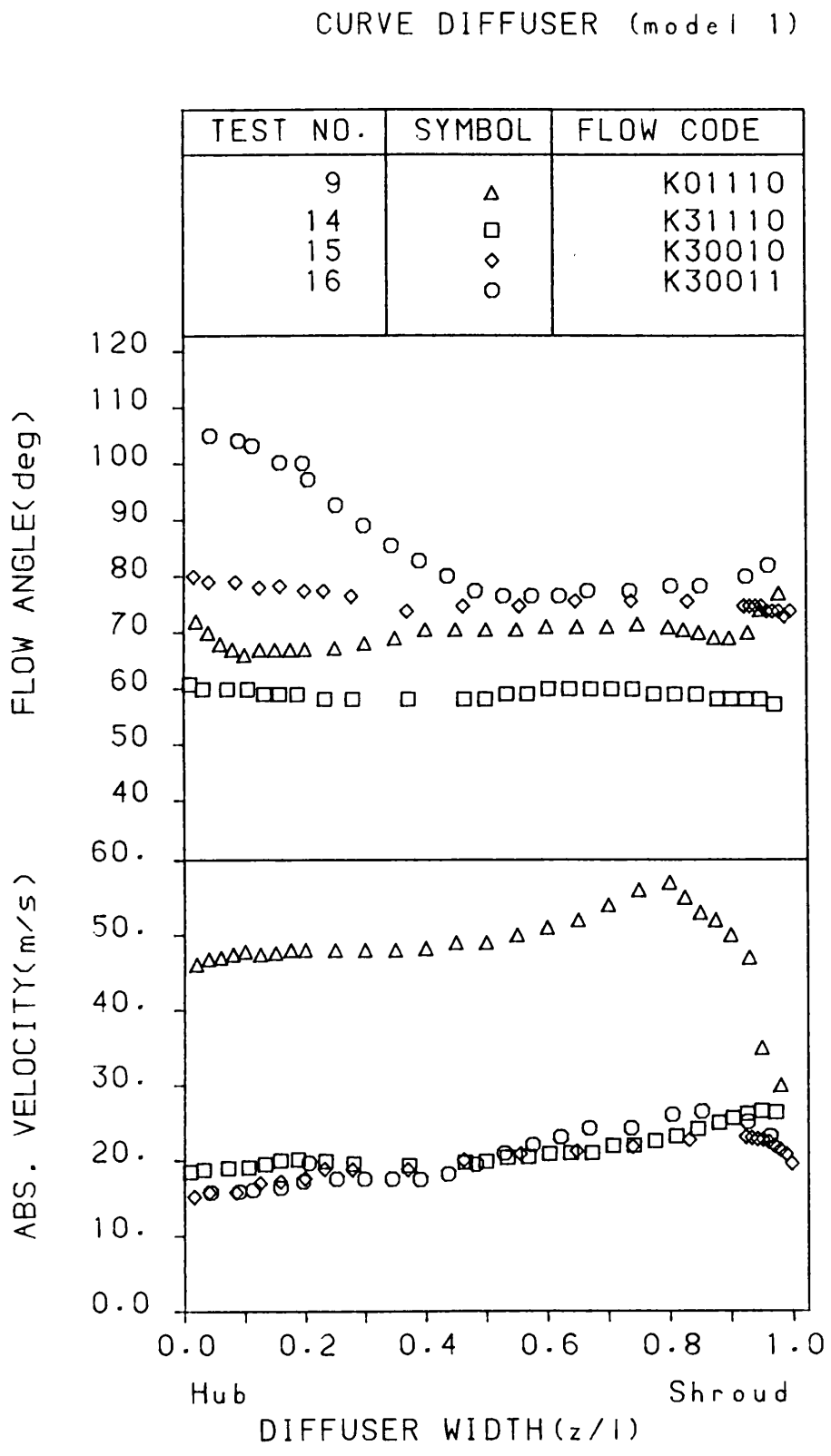

FIGURE 6.20: Inlet flow profiles for curved diffuser. (model 1)

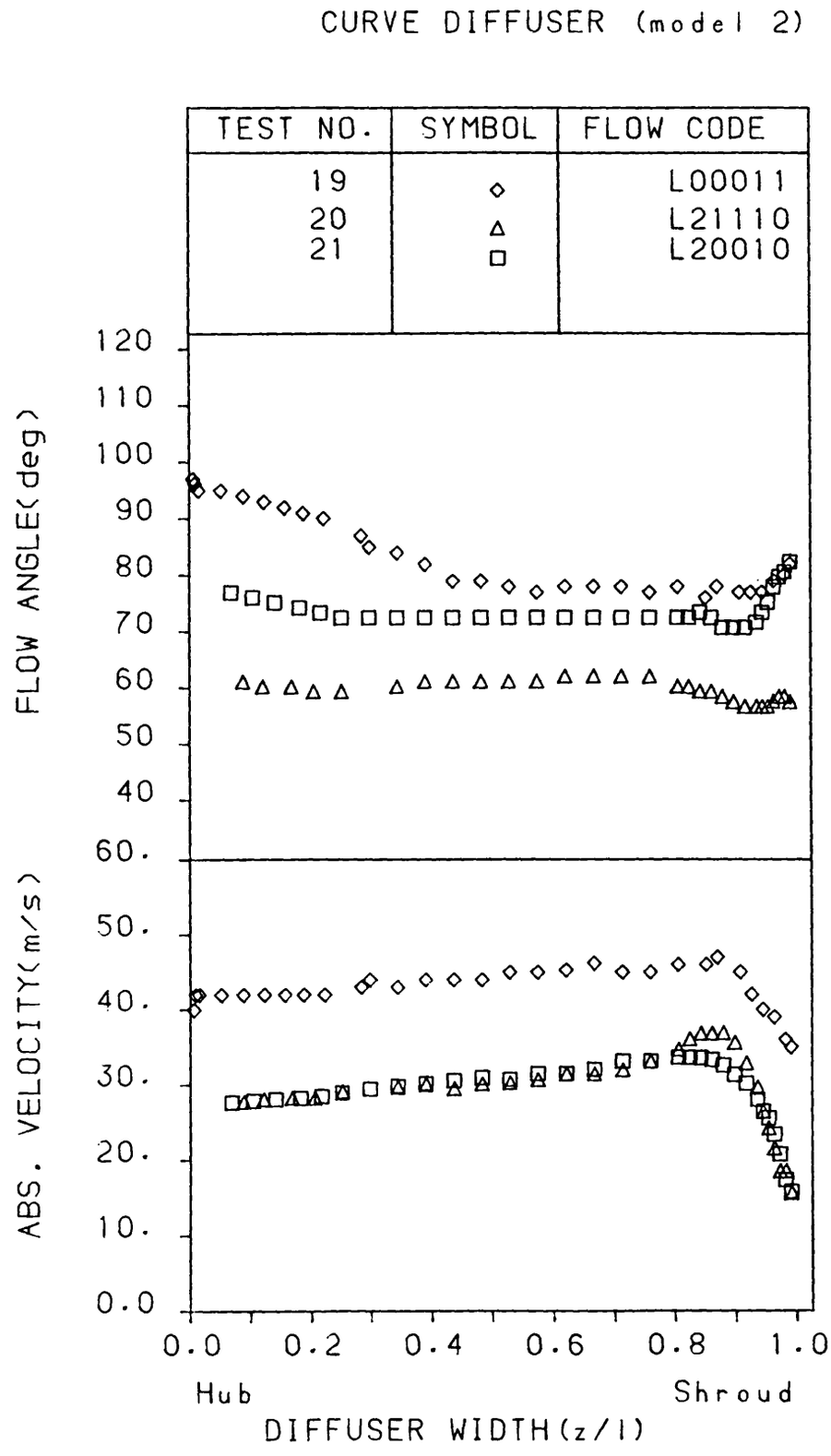

FIGURE 6.21: Inlet flow profiles for curved diffuser. (model 2)

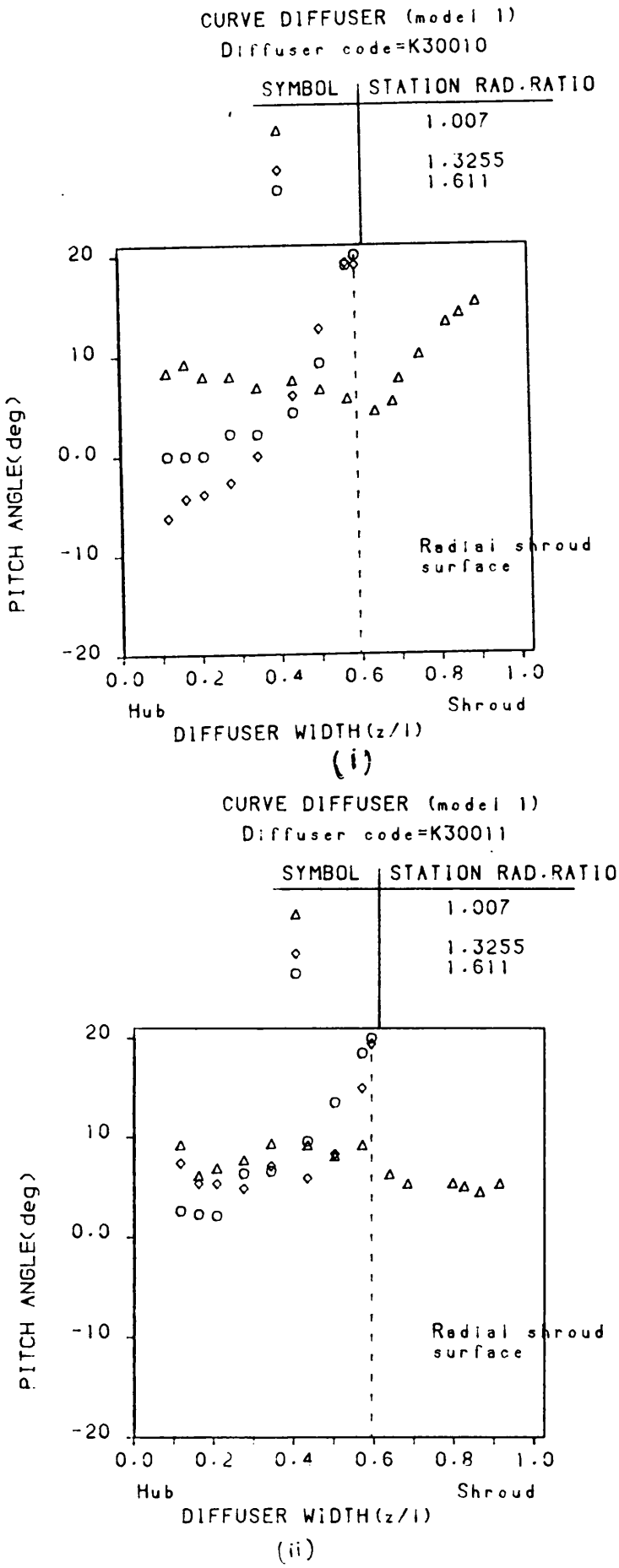

FIGURE 6.22: Pitch angle distribution at each cross section. (model 1)

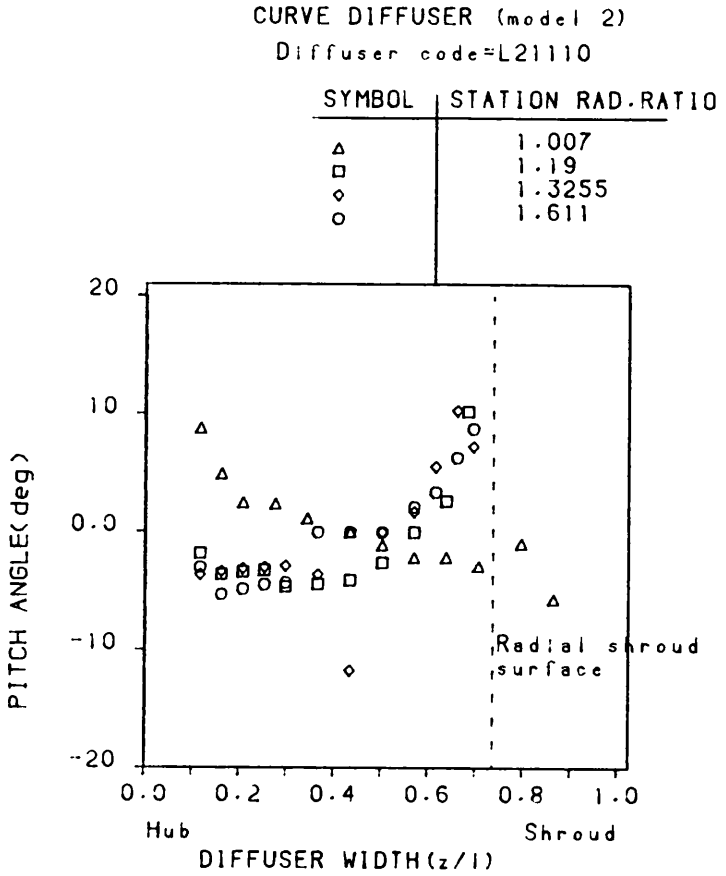

(i)

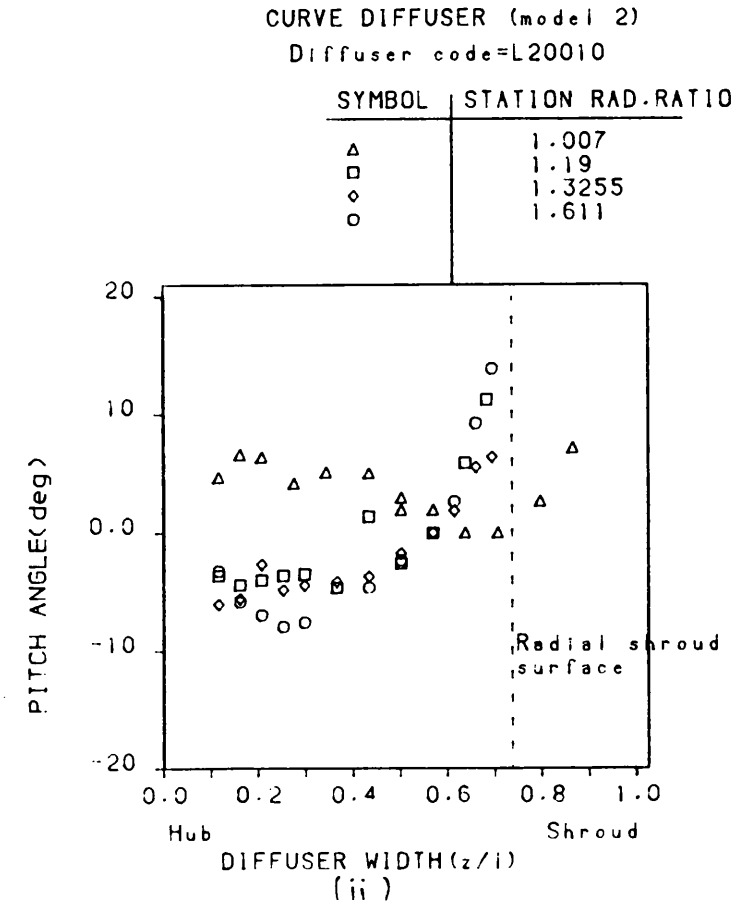

(ii)

FIGURE 6.23: Pitch angle distribution at each cross section. (model 2)

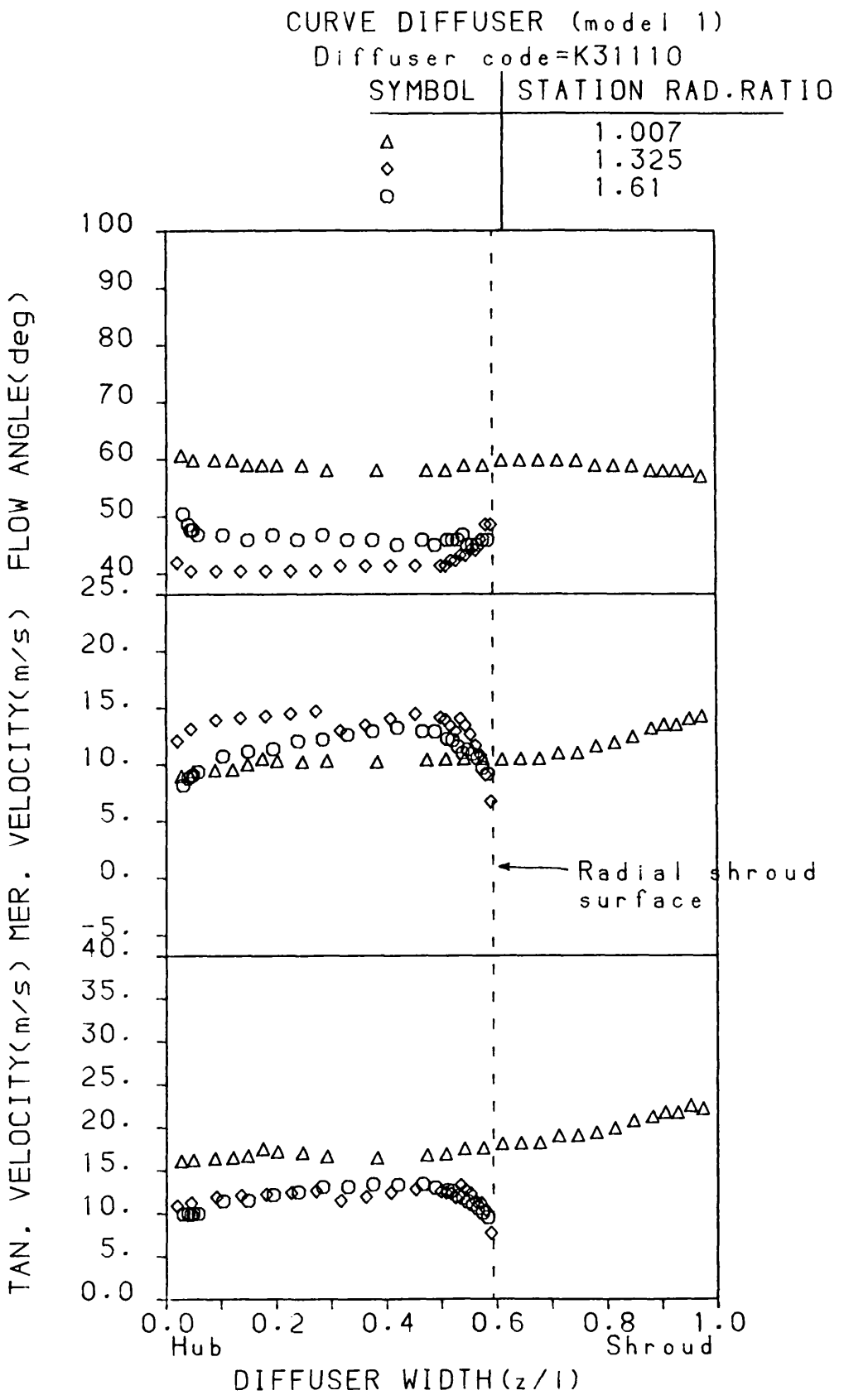

FIGURE 6.24: Velocity distribution throughout a curved diffuser. (model 1)

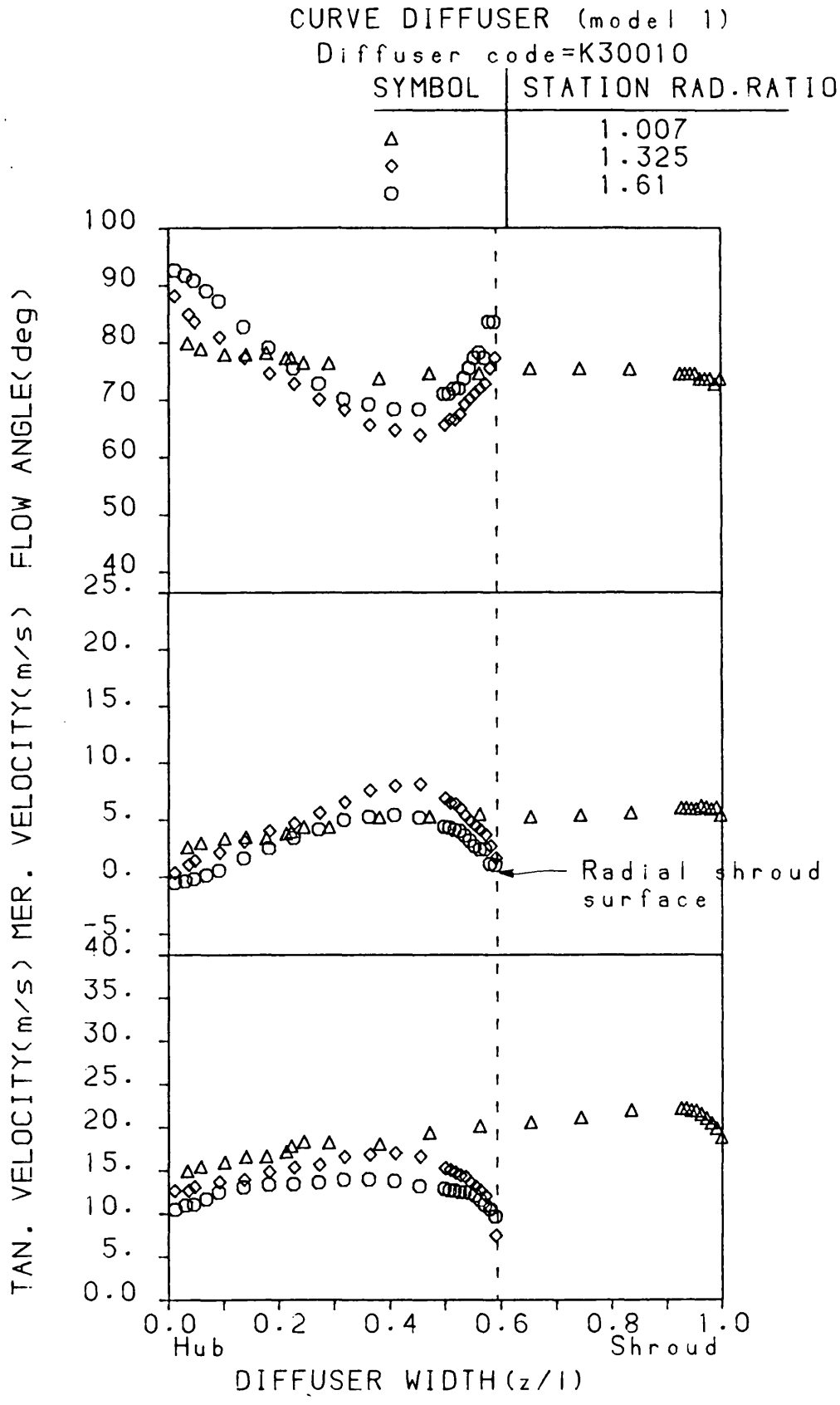

FIGURE 6.25: Velocity distribution throughout a curved diffuser. (model 1)

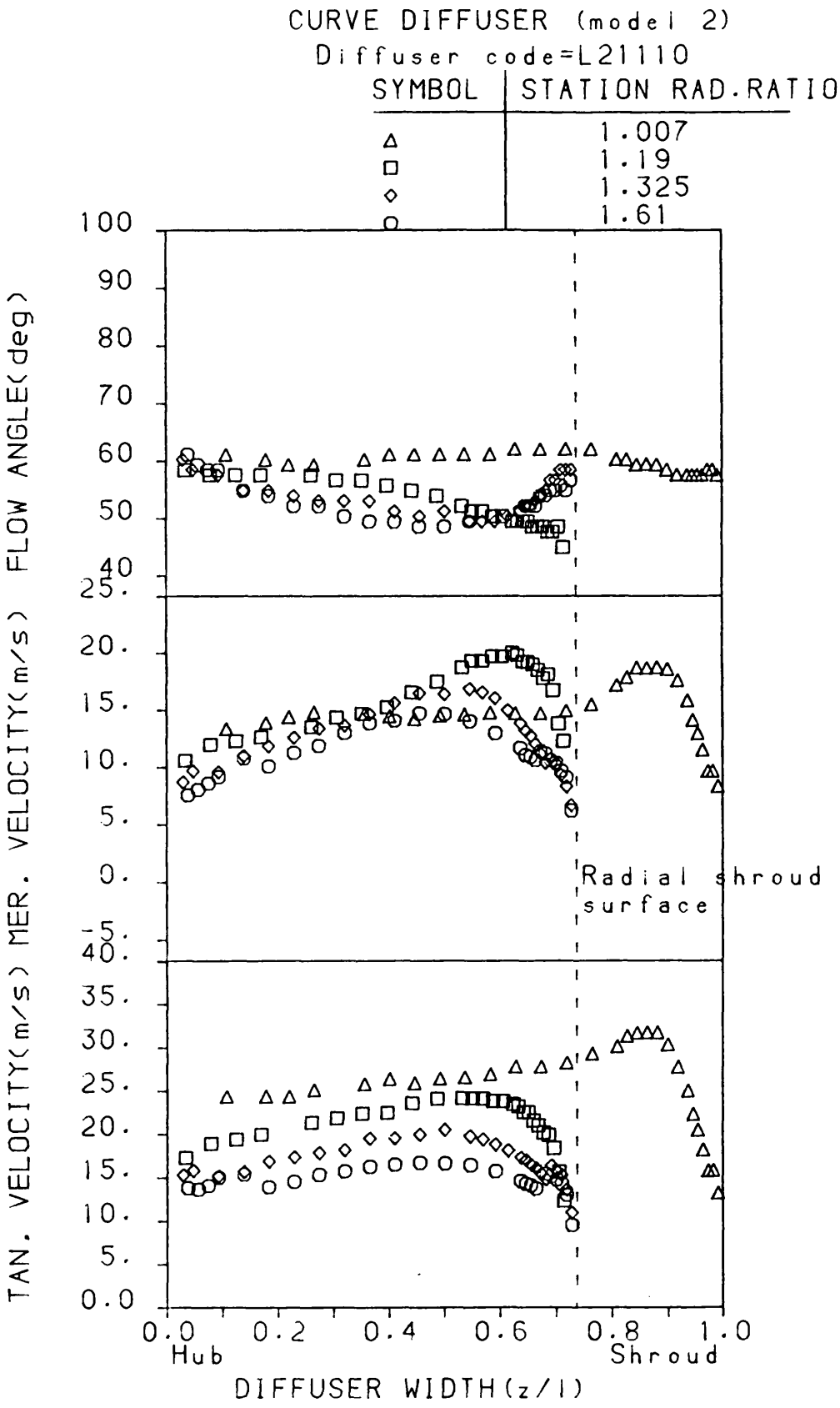

FIGURE 6.26: Velocity distribution throughout a curved diffuser. (model 2)

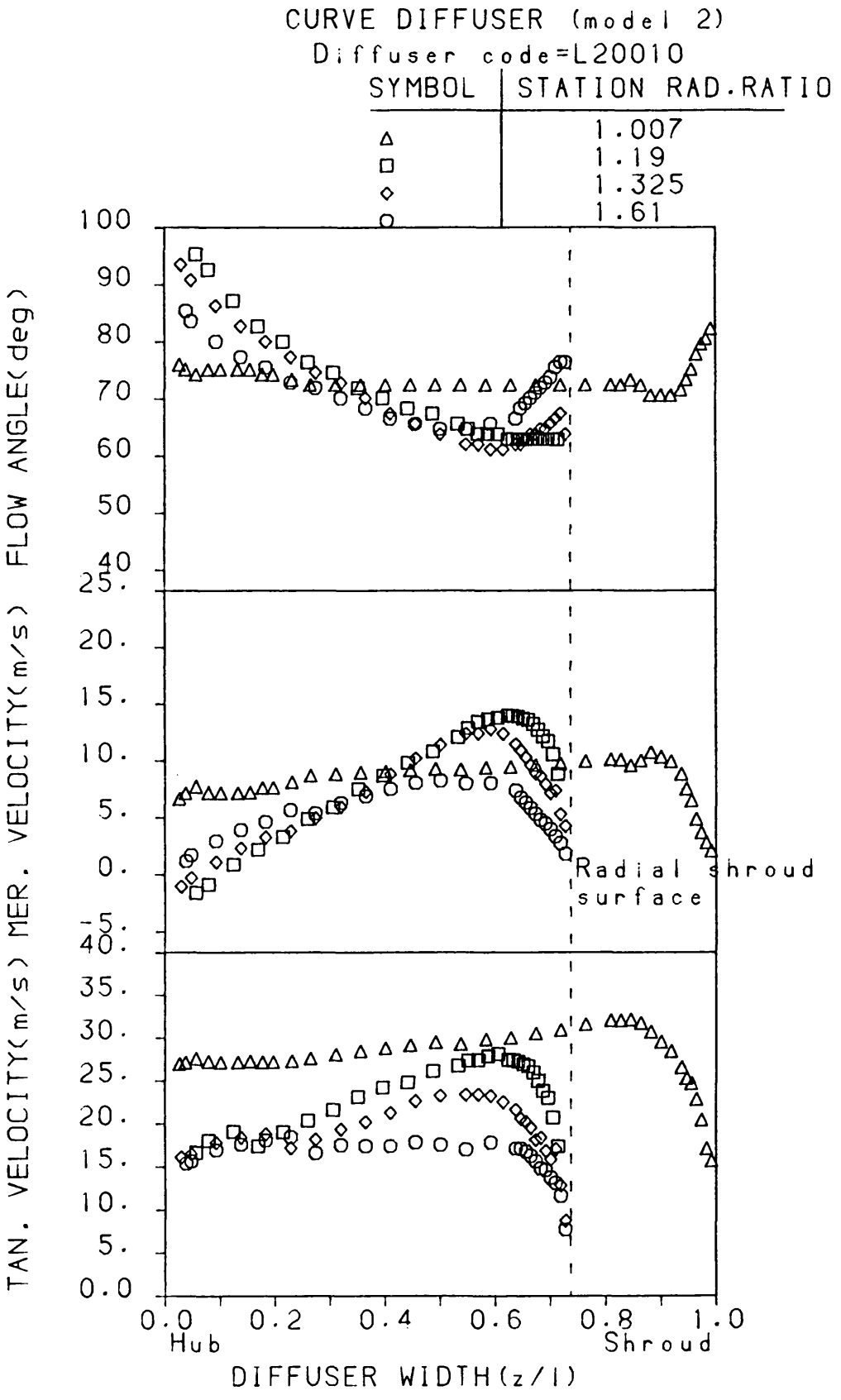

FIGURE 6.27: Velocity distribution throughout a curved diffuser. (model 2)

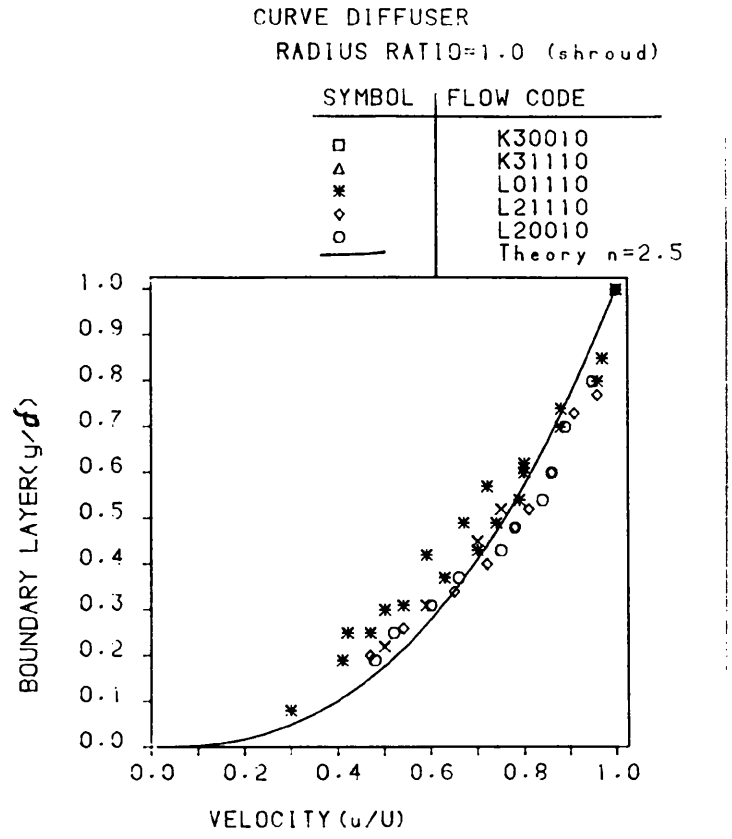

(i)

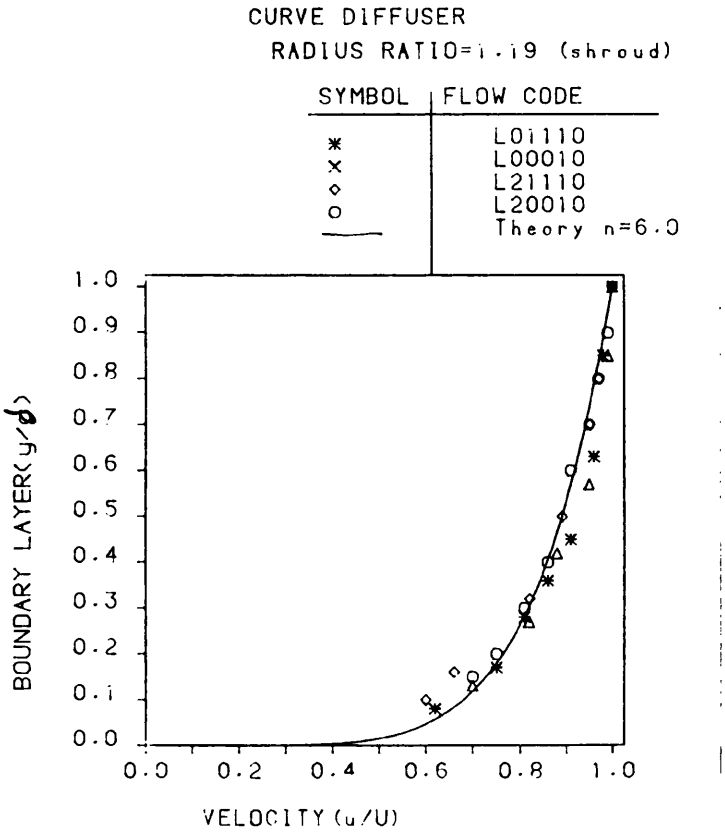

(ii)

FIGURE 6.28: Velocity distribution in the boundary layer near the shroud surface at different radial stations.

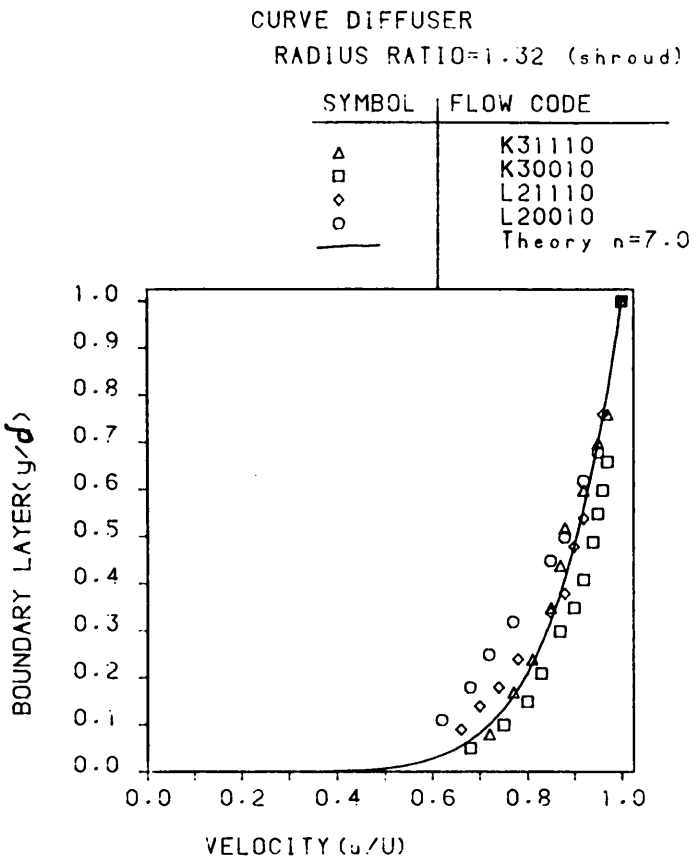
CURVE DIFFUSER
RADIUS RATIO=1.32 (shroud)
SYMBOL
FLOW CODE
K31110
K30010
L21110
L20010
Theory n=7.0
BOUNDARY LAYER(y/δ)
VELOCITY(u/U)
0.0
0.1
0.2
0.3
0.4
0.5
0.6
0.7
0.8
0.9
1.0

(iii)

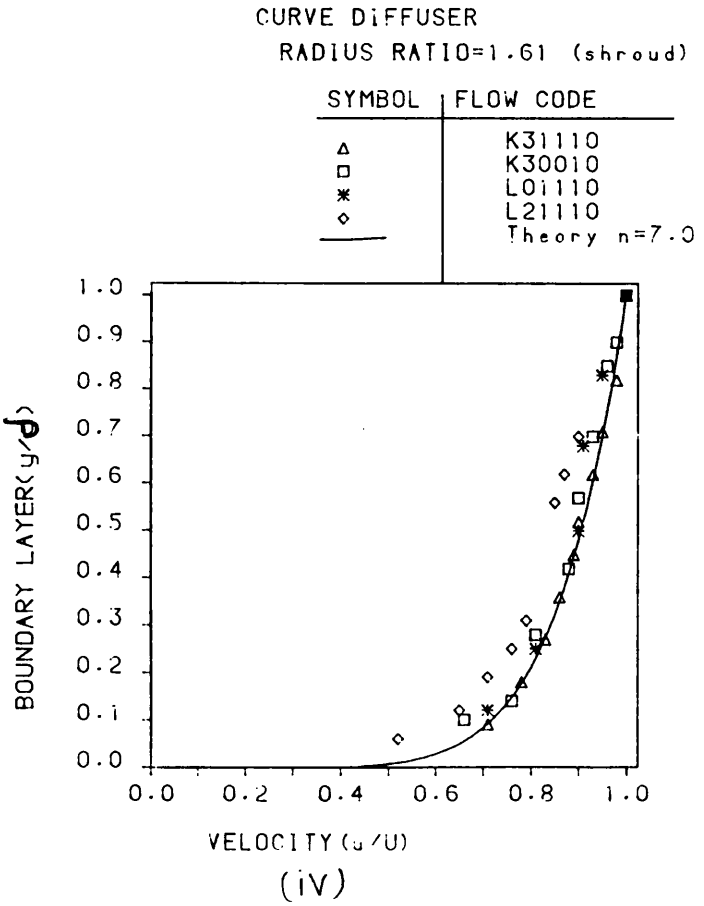
CURVE DIFFUSER
RADIUS RATIO=1.61 (shroud)
SYMBOL
FLOW CODE
K31110
K30010
L01110
L21110
Theory n=7.0
BOUNDARY LAYER(y/δ)
VELOCITY(u/U)
0.0
0.1
0.2
0.3
0.4
0.5
0.6
0.7
0.8
0.9
1.0

(iv)

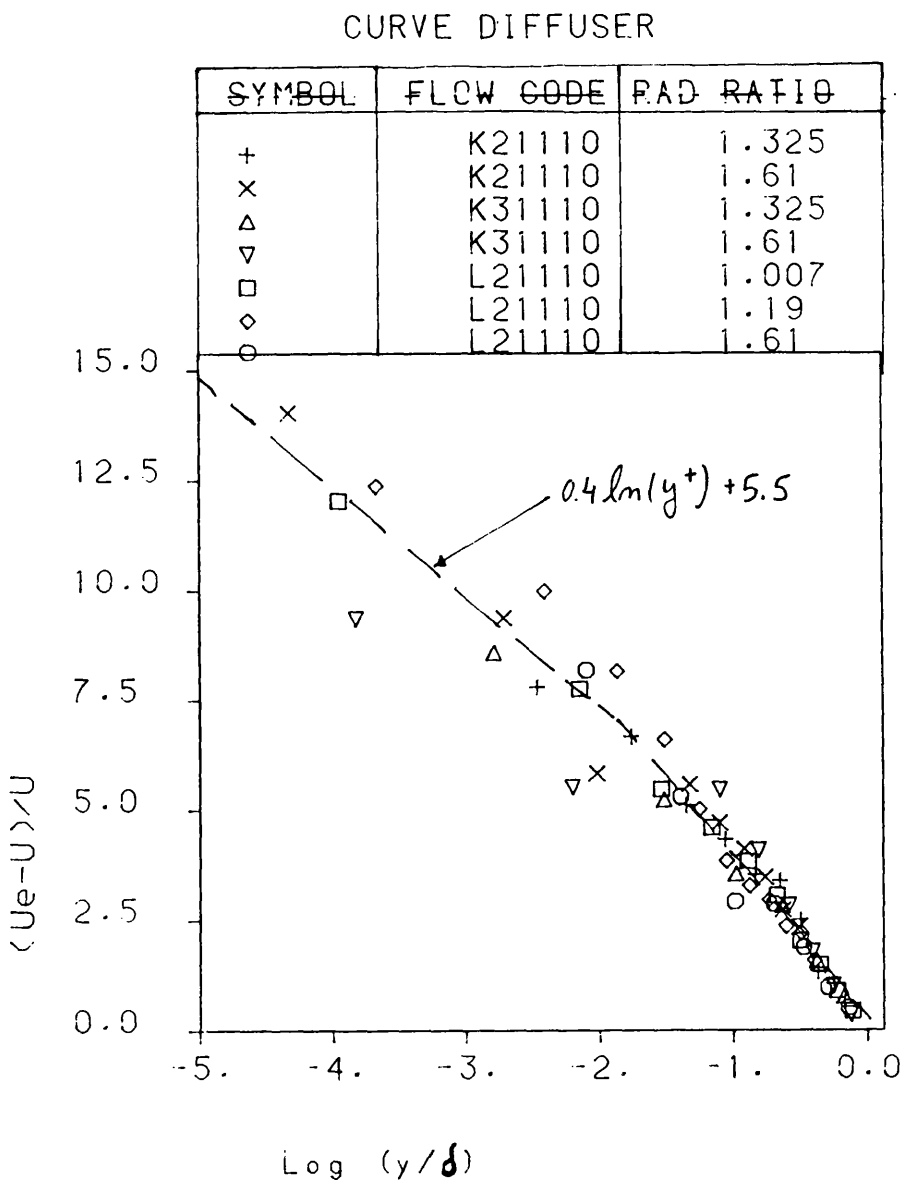

FIGURE 6.29: Comparison between the theoretical application of the "Lograrithmic law of the wall" and experimental results for the curved diffusers.

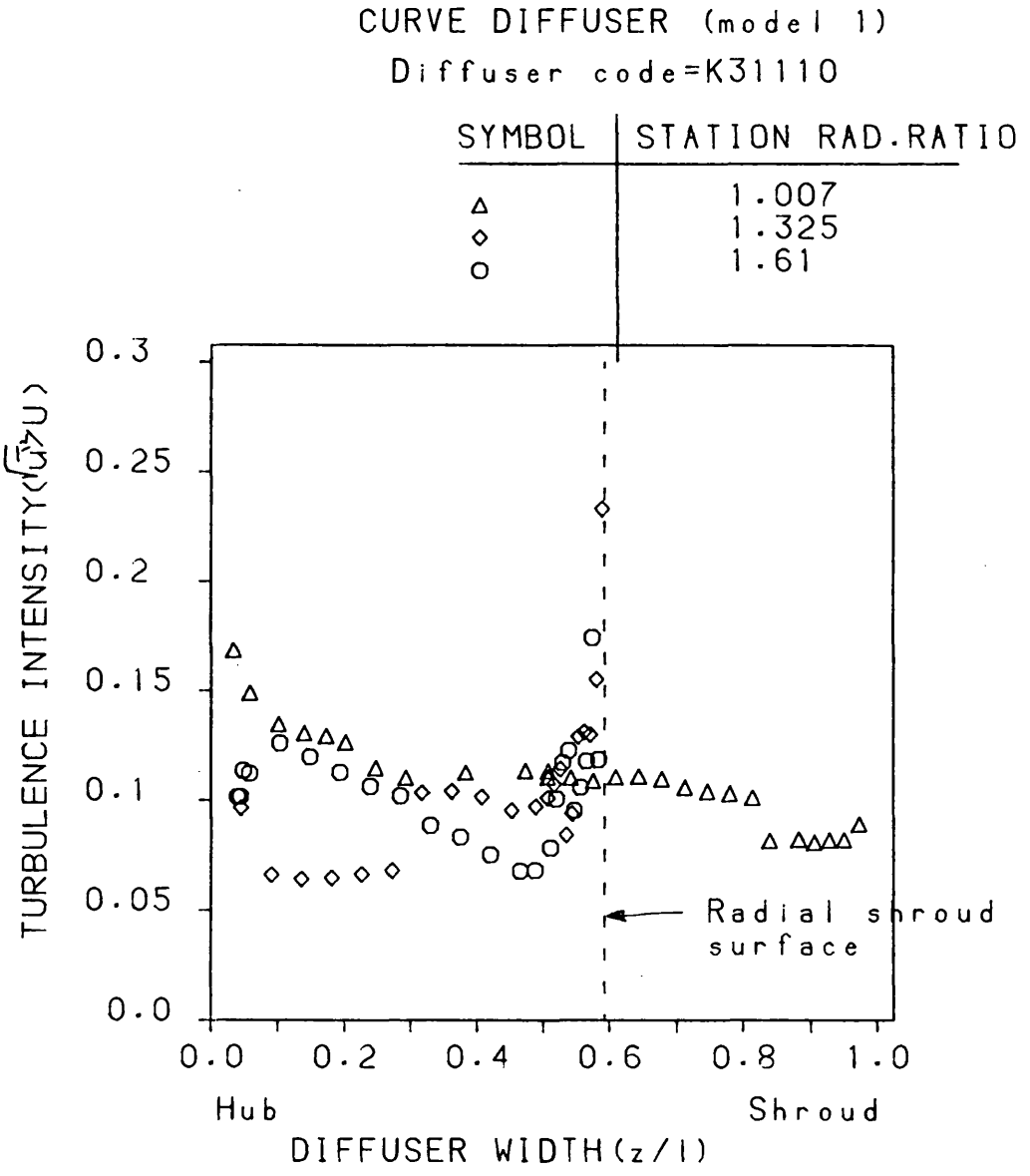

FIGURE 6.30a: Turbulence intensity distribution in curved diffuser. (model 1)

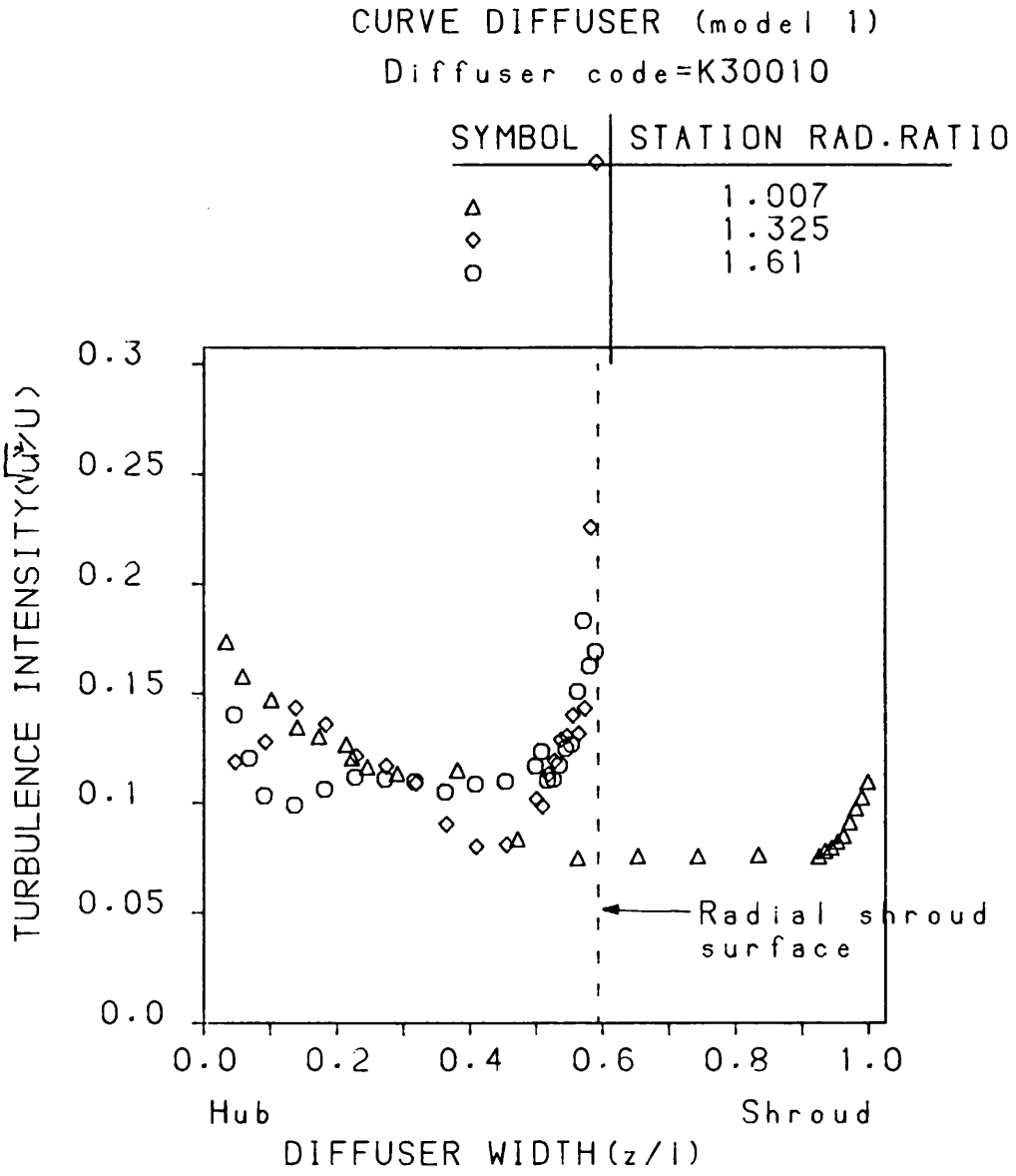

FIGURE 6.30b: Turbulence intensity distribution in curved diffuser. (model 1)

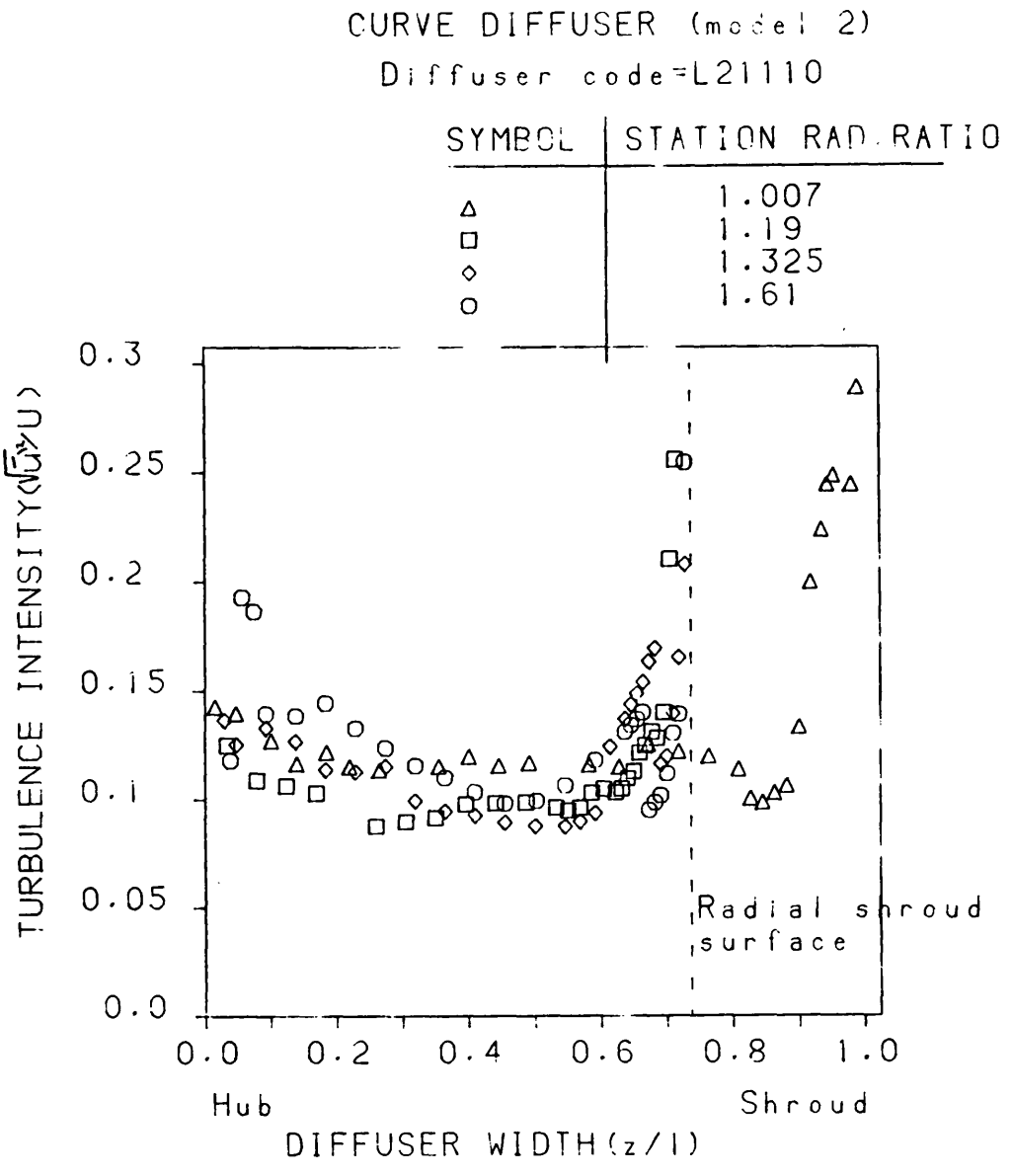

FIGURE 6.31a: Turbulence intensity distribution in curved diffuser. (model 2)

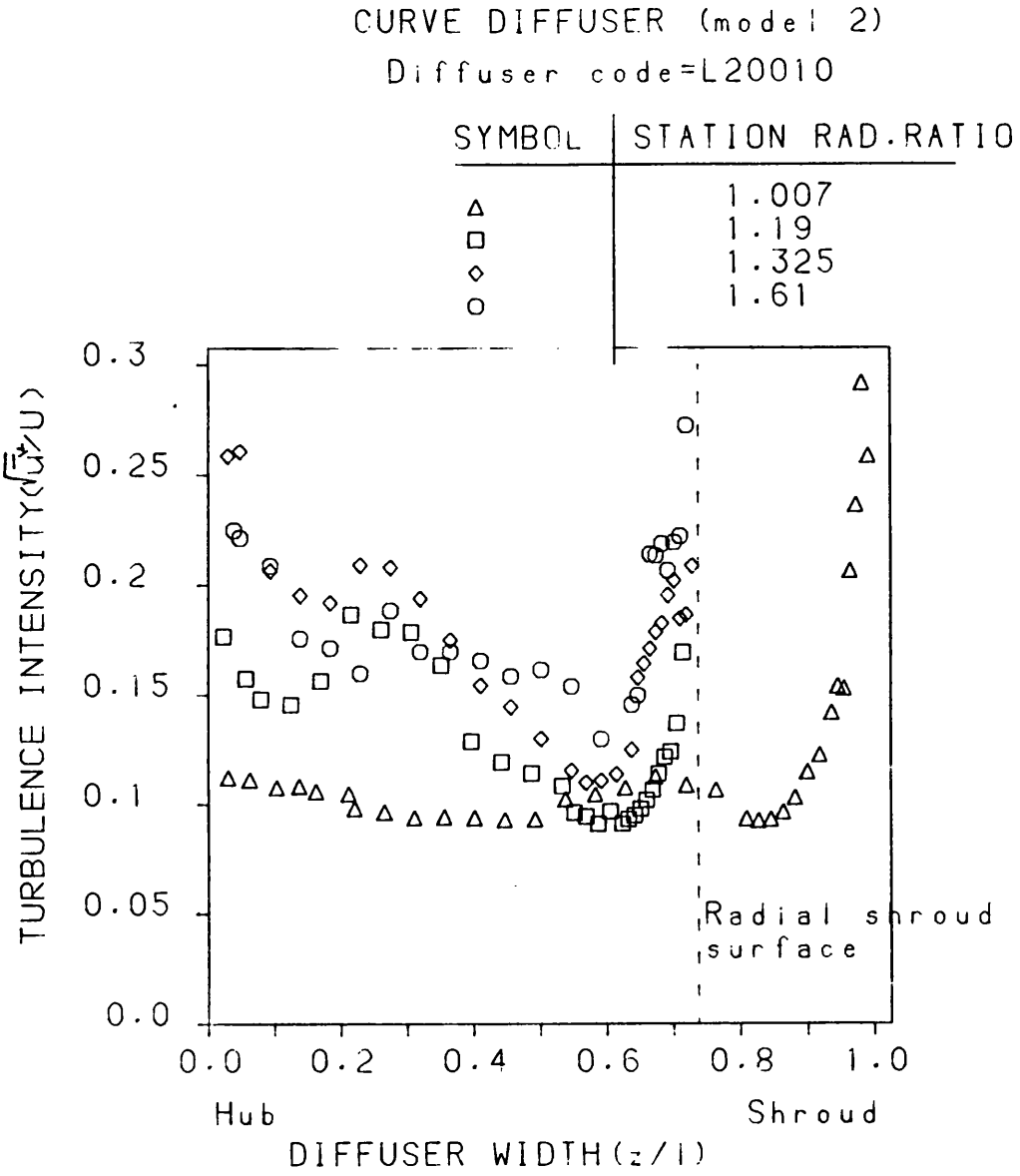

FIGURE 6.31b: Turbulence intensity distribution in curved diffuser. (model 2)

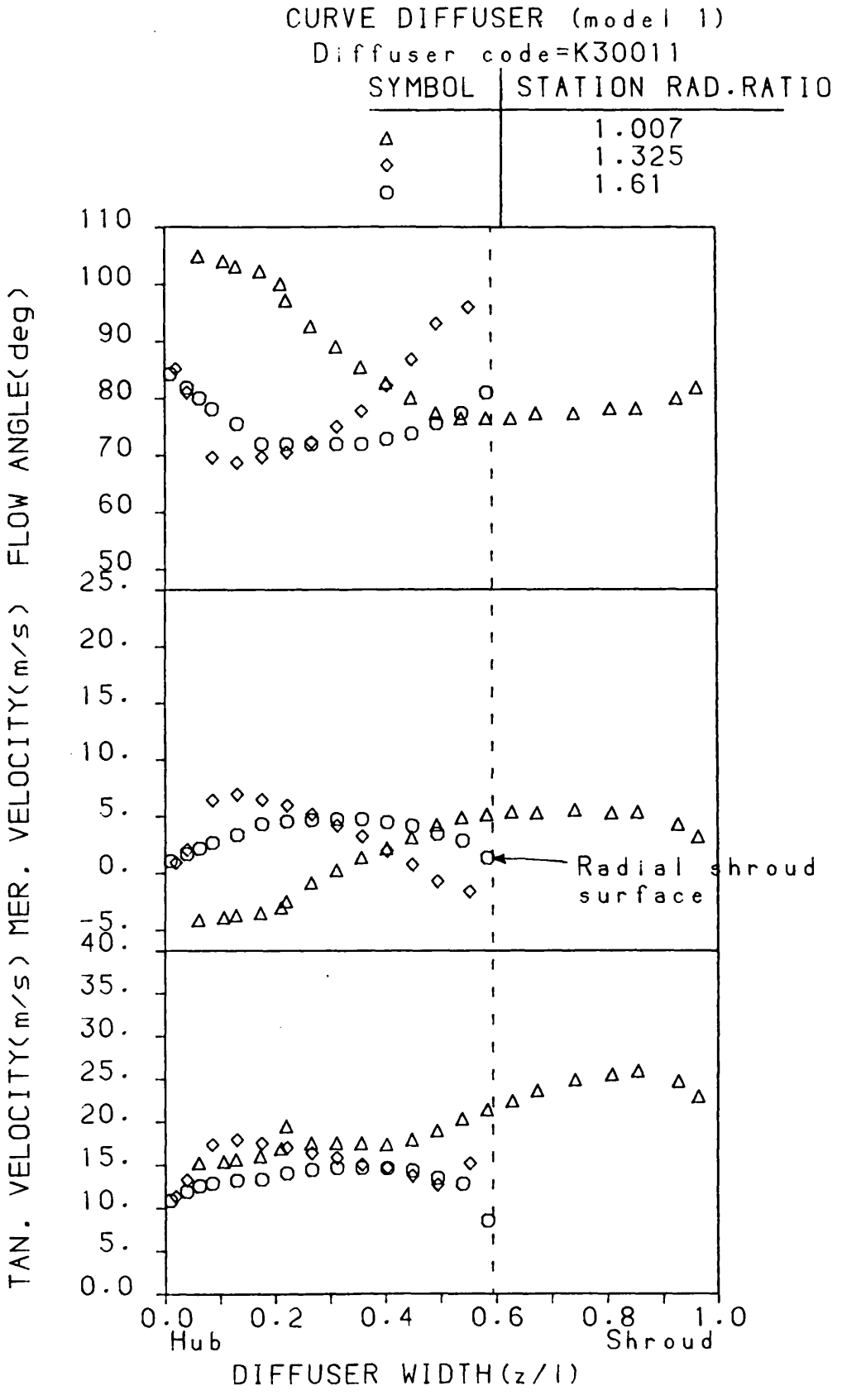

FIGURE 6.32: Flow profiles distribution for an unstable flow. (model 1)

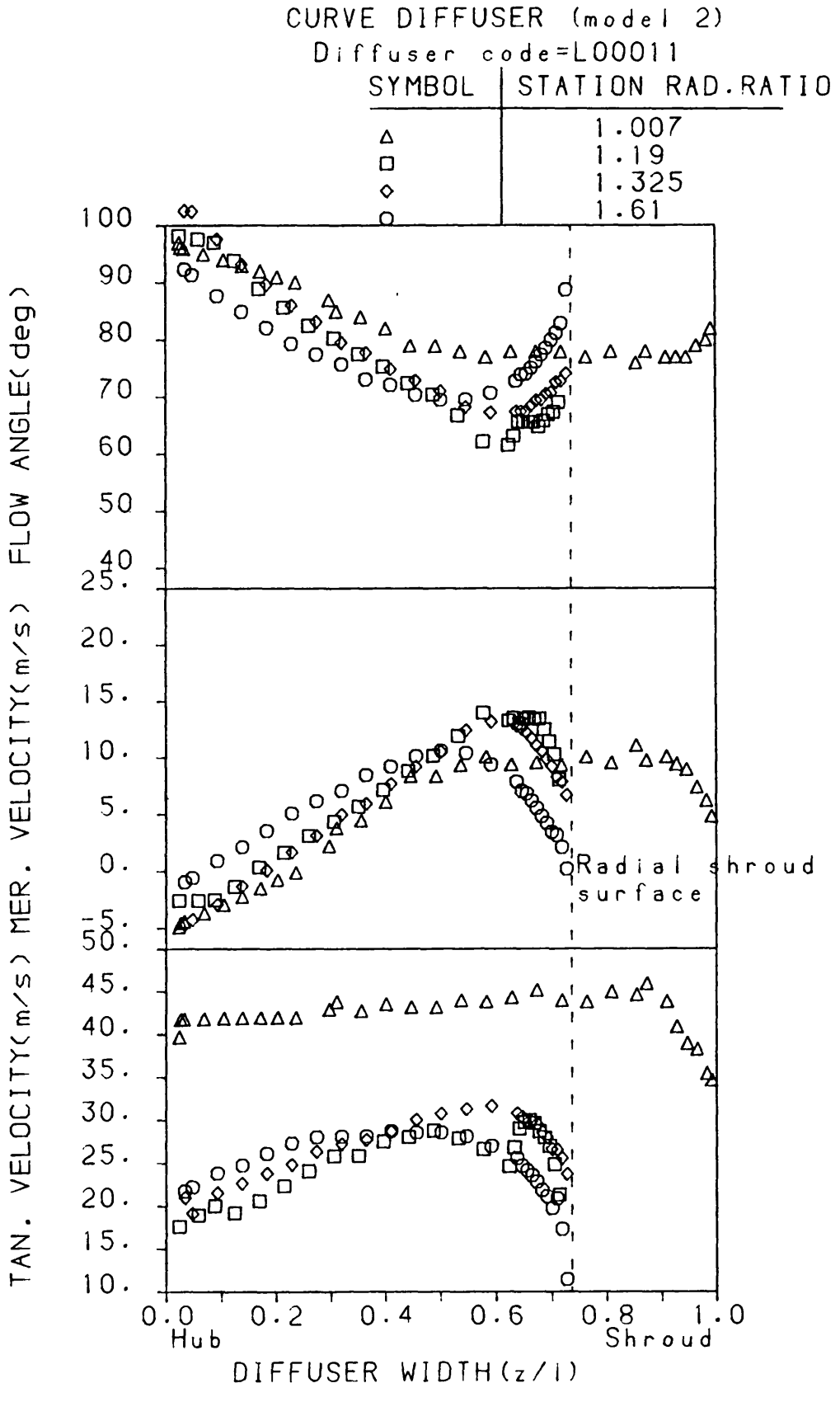

FIGURE 6.33: Flow profiles distribution for an unstable flow. (model 2)

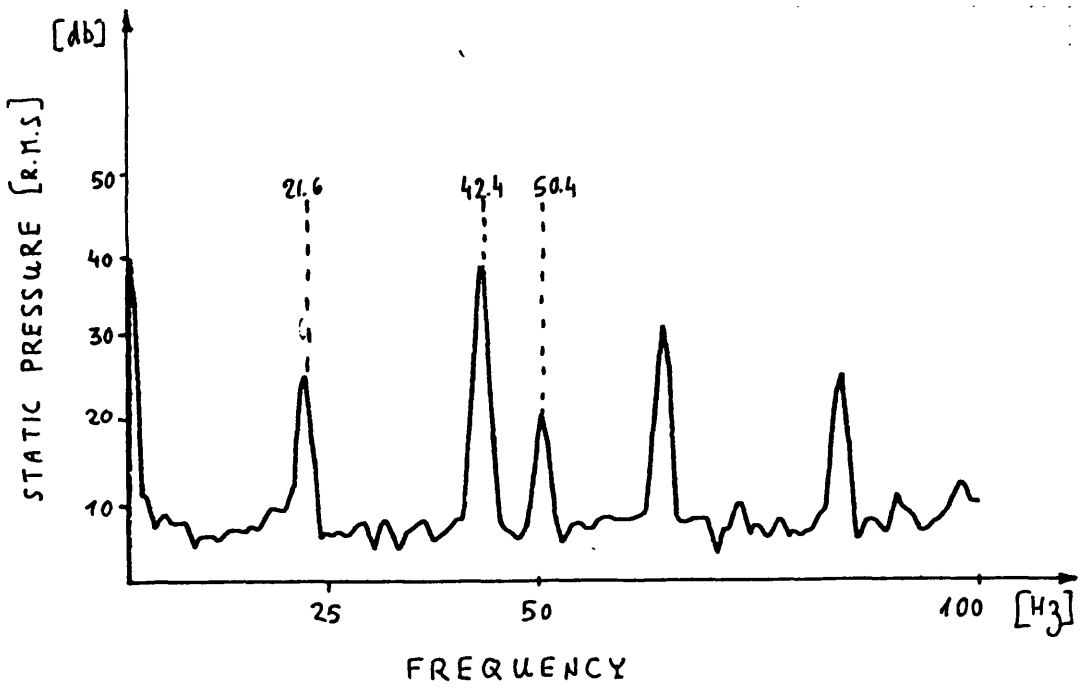

i) STEADY FLOW

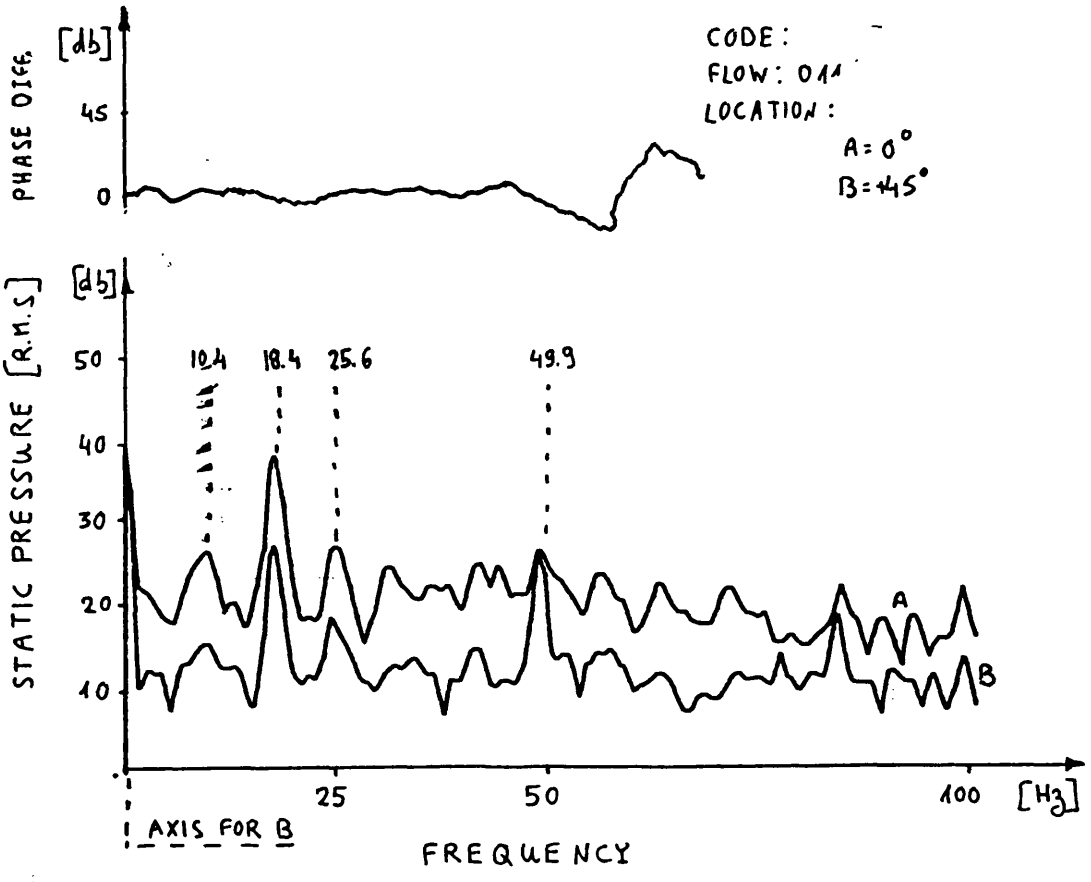

ii) BEFORE INSTABILITY

FIGURE 6.34: Spectra of curved diffuser (model 1) pressure fluctuations.

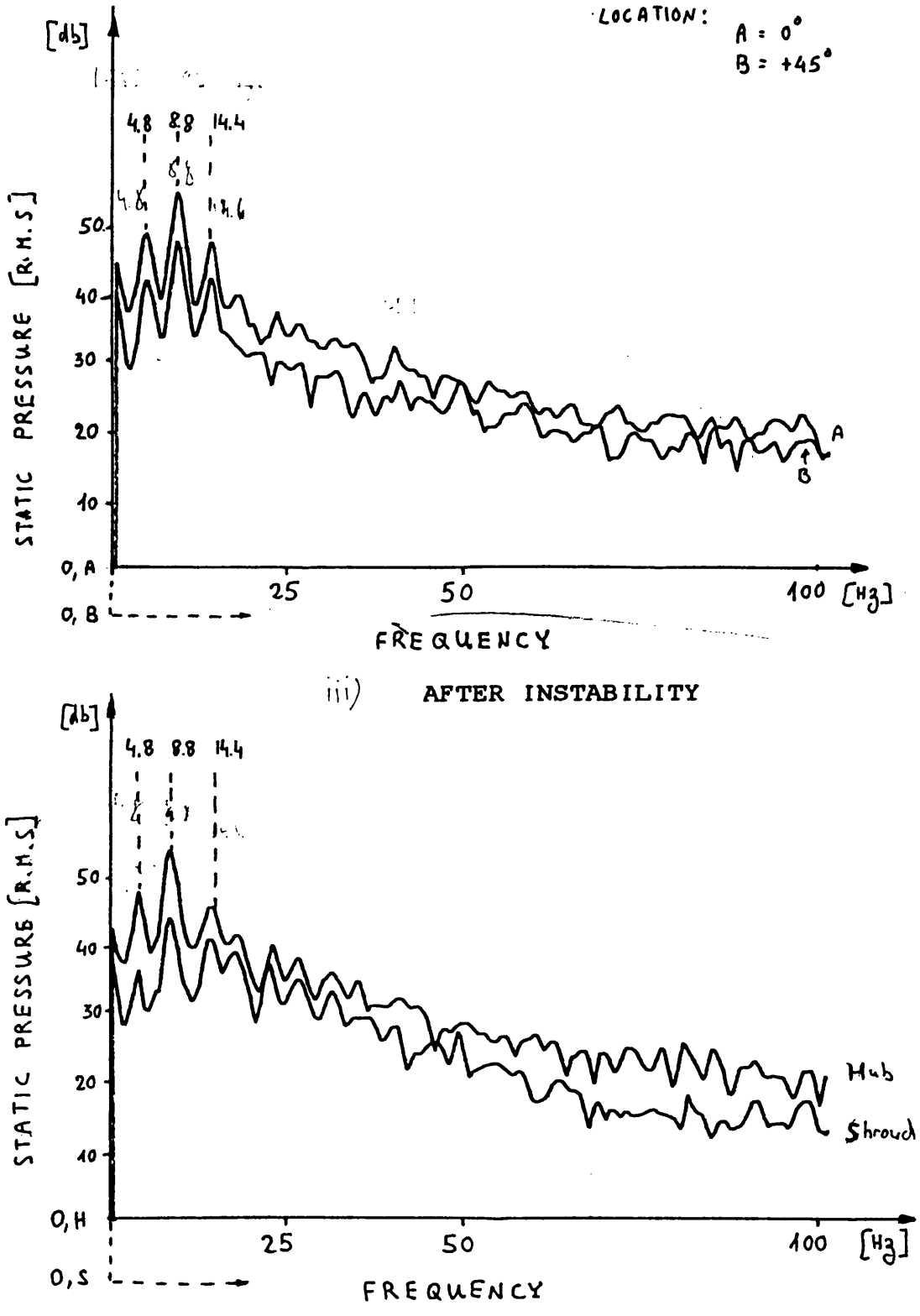

FIGURE 6.34: Continued

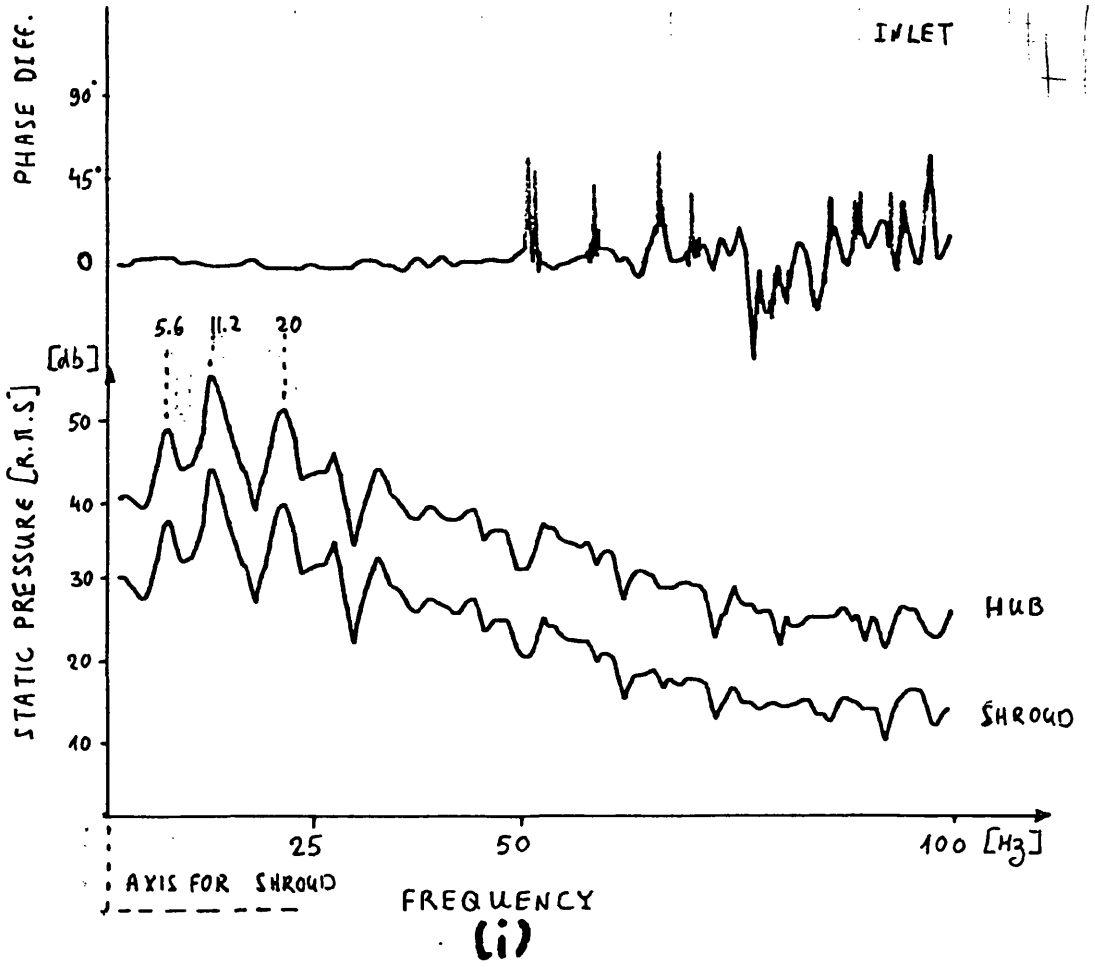

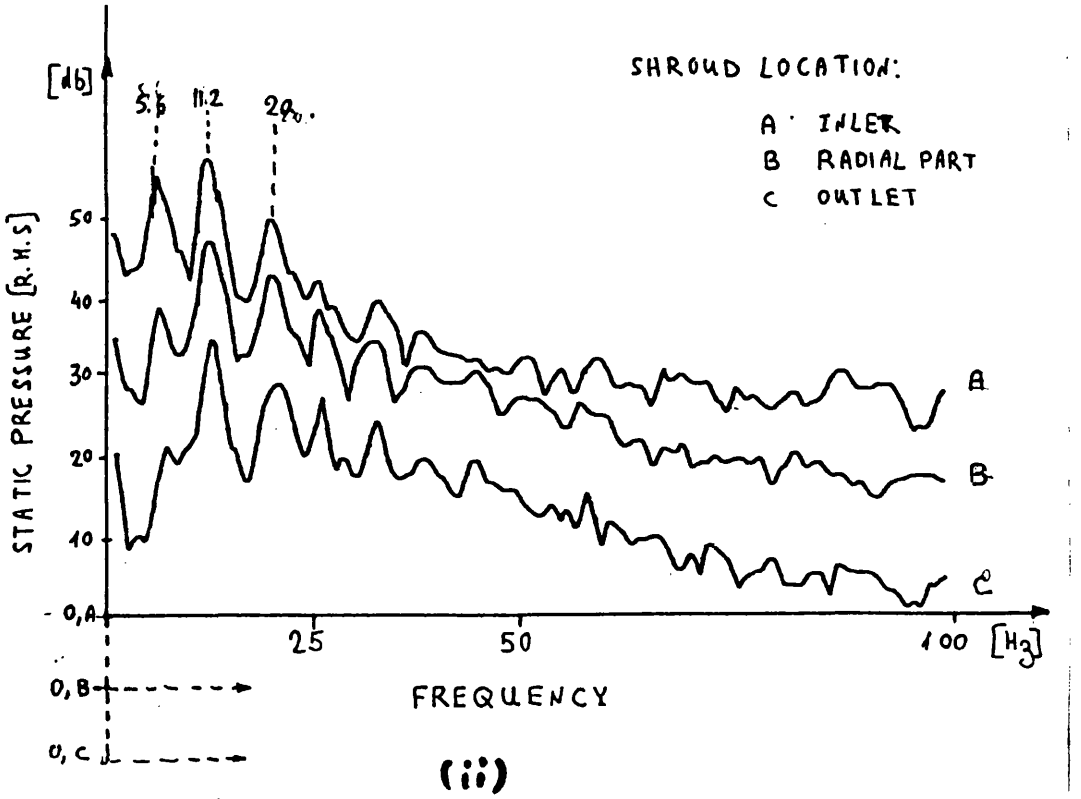

FIGURE 6.35: Spectra of curved diffuser (model 1) pressure fluctuations in unsteady flow.

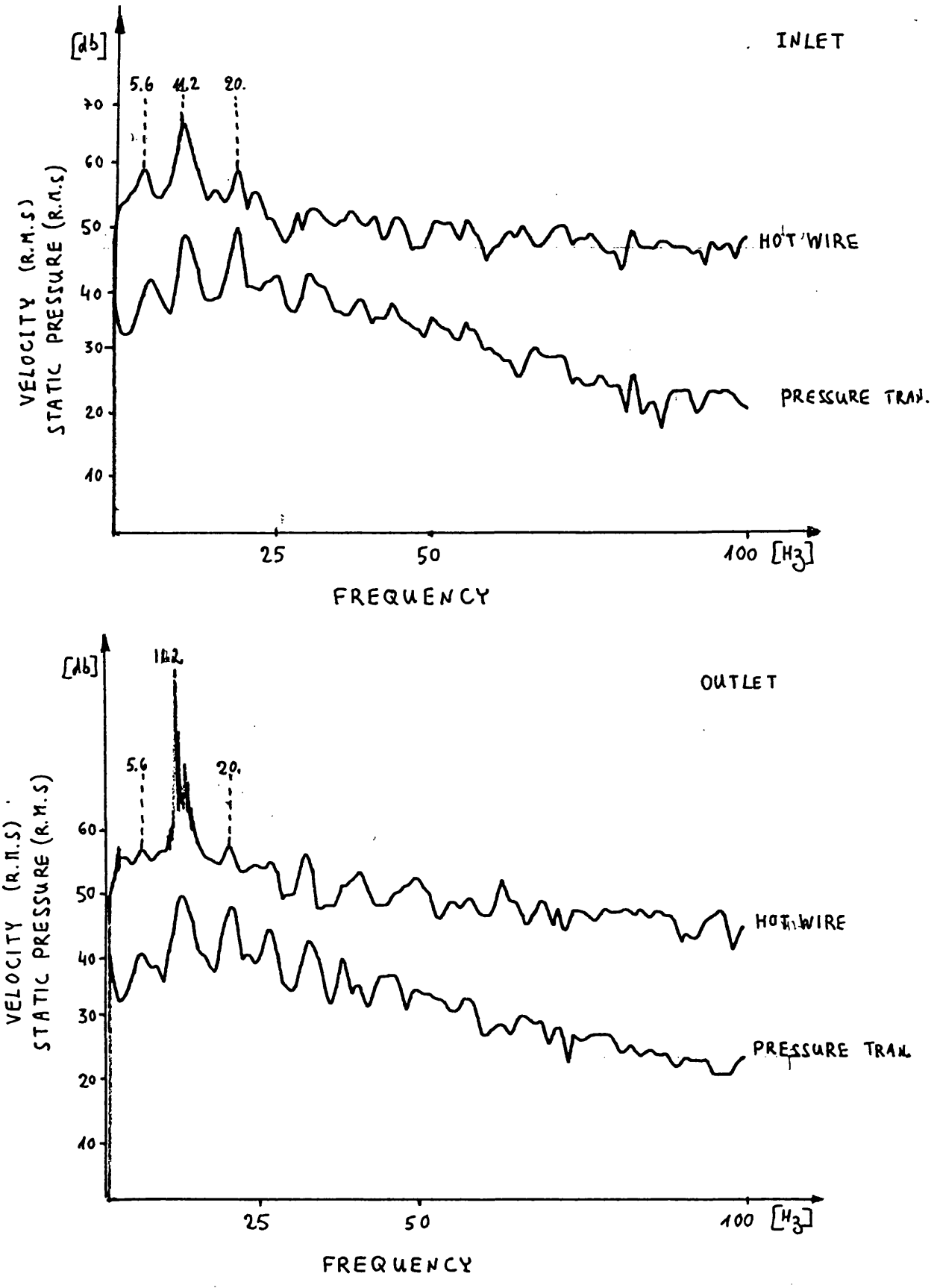

FIGURE 6.36: Comparison between hot-wire anemometer and pressure transducers spectra. (model 1)

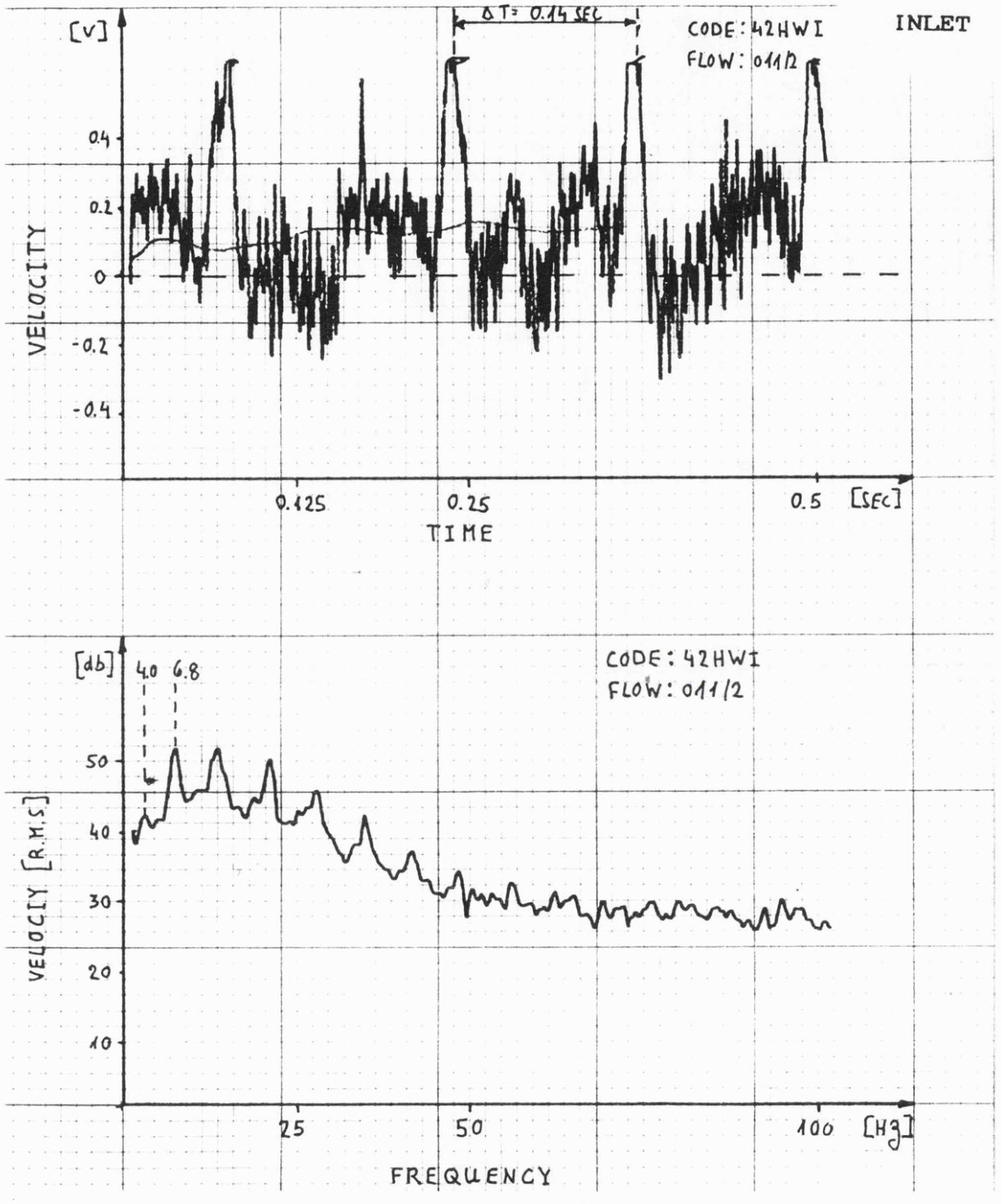

FIGURE 6.37: Spectra and fluctuation of hot-wire anemometer output in the curved diffuser. (model 2)

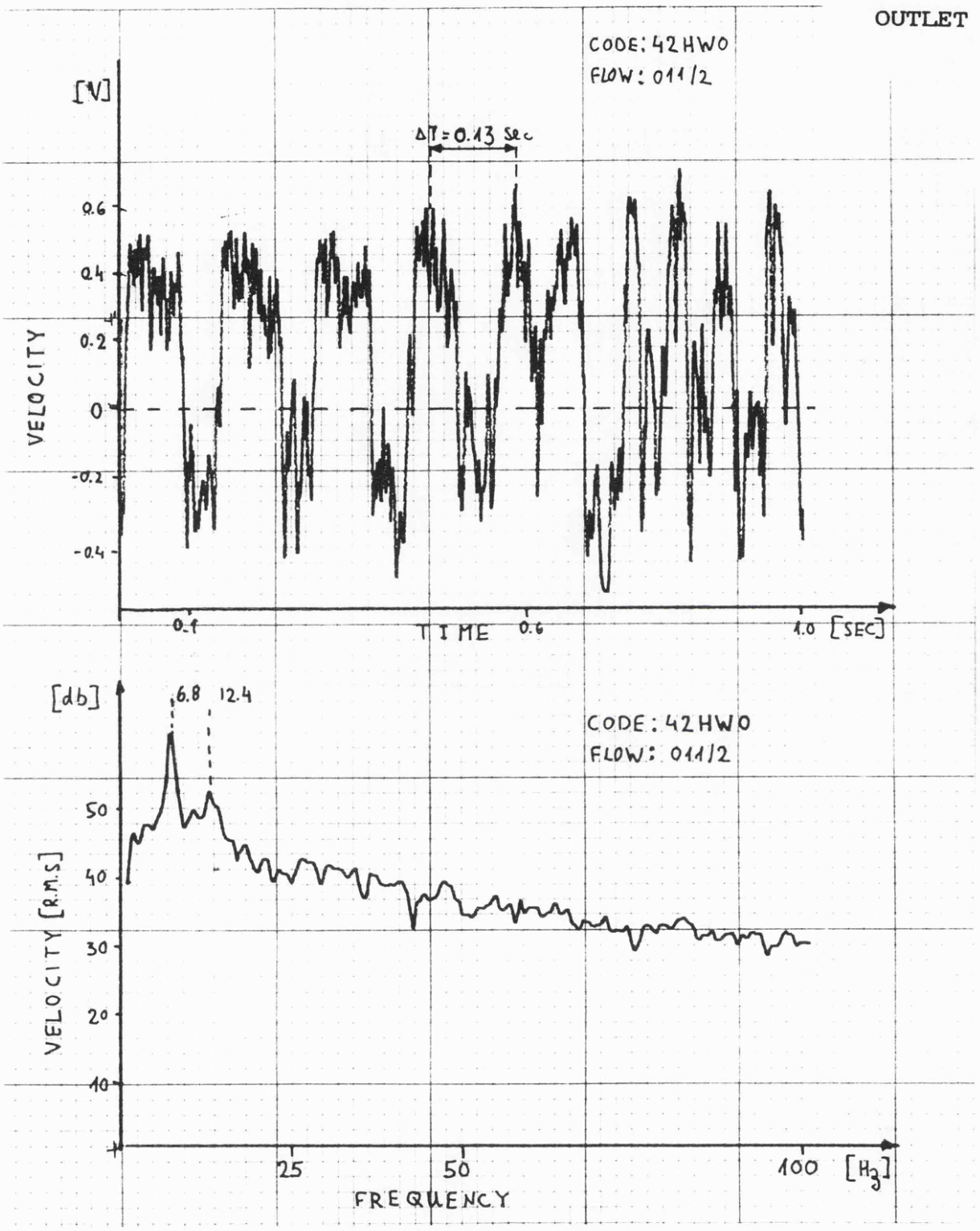

FIGURE 6.37: Continued

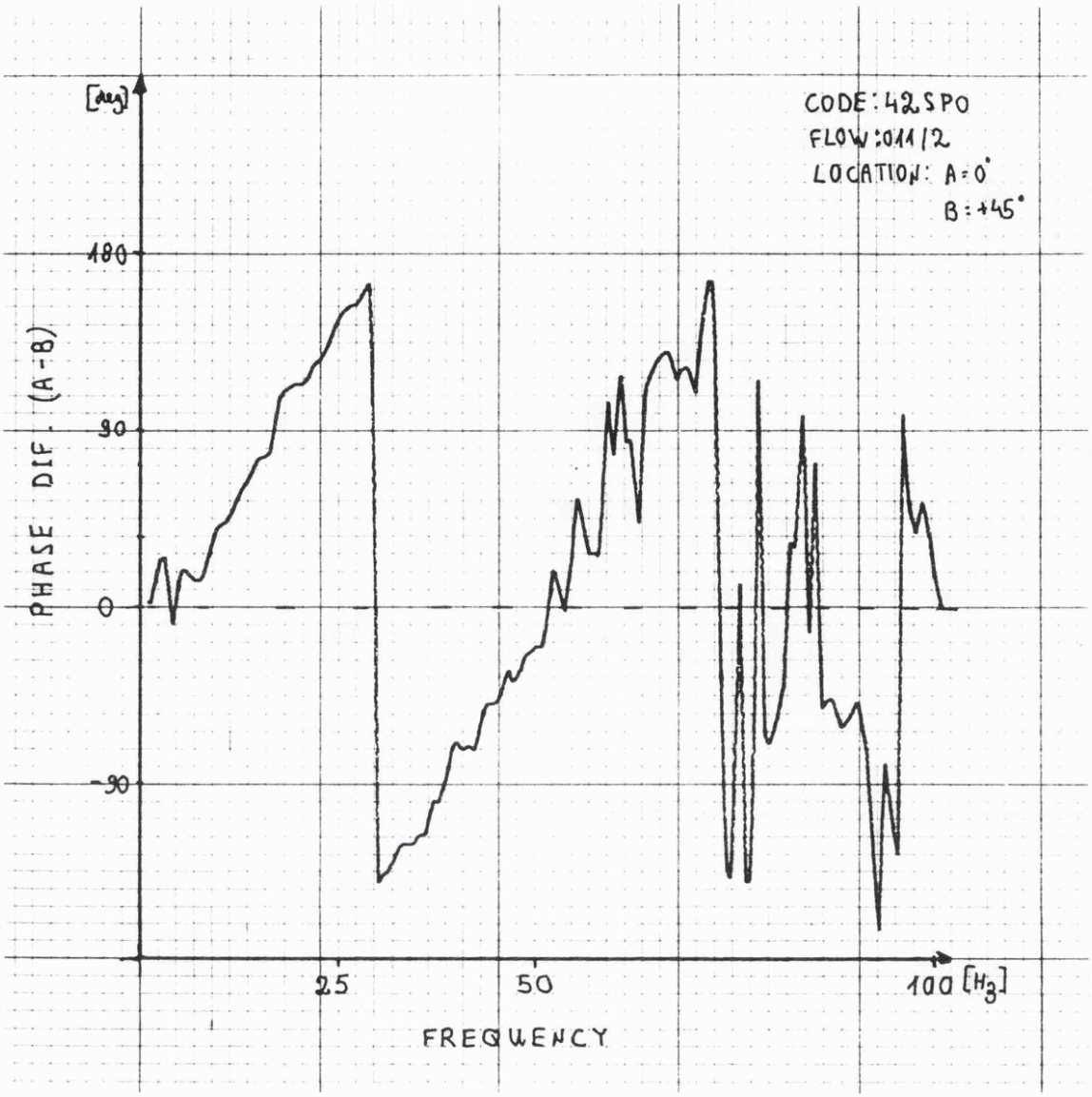

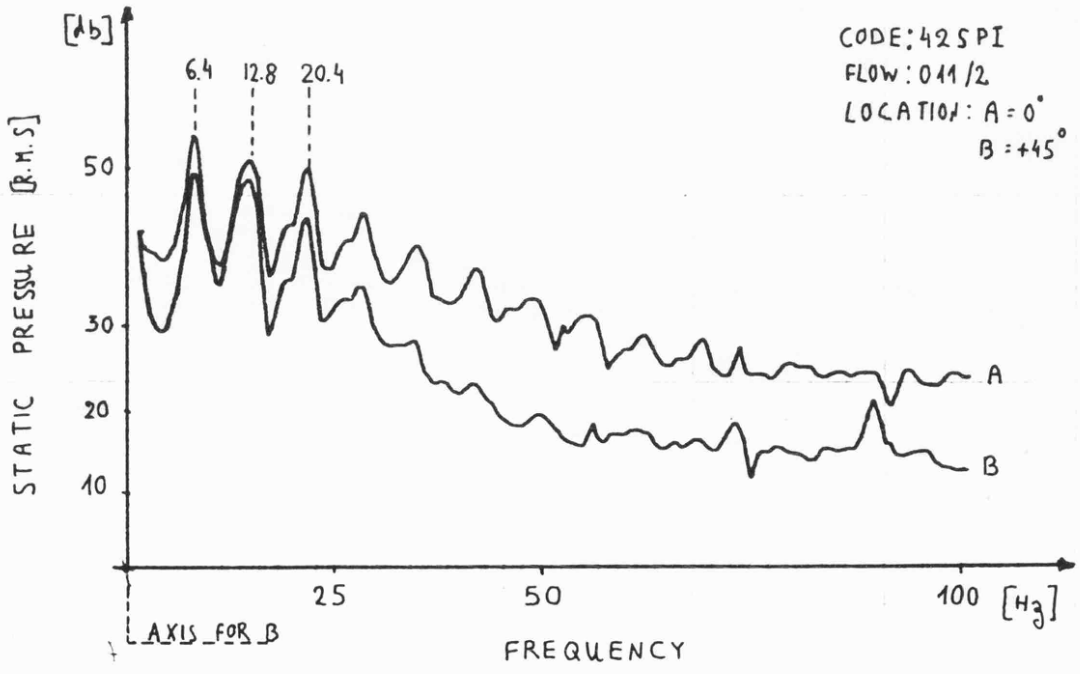

FIGURE 6.38: Presusser fluctuations and phase different measurments between two pressure transducers in curved diffuser. (model 2)

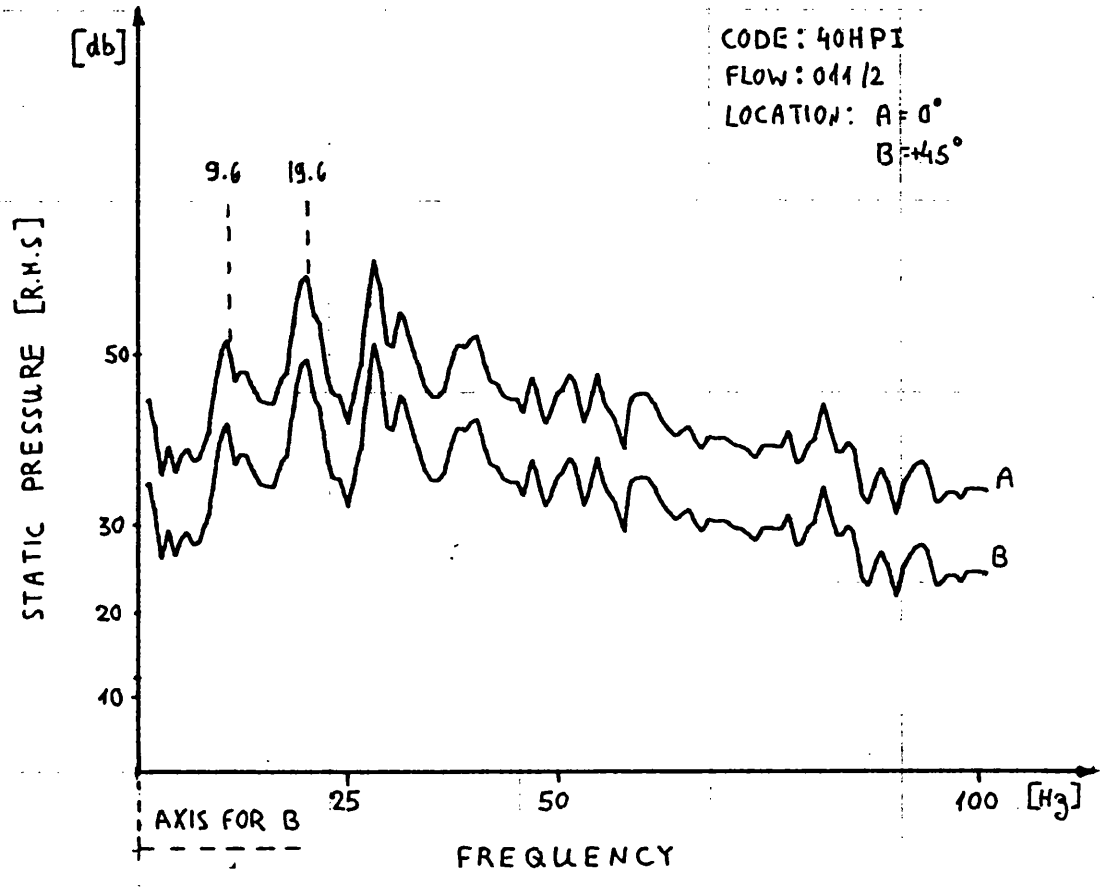

FIGURE 6.39: Spectra of curved diffuser (model 2) pressure fluctuations.

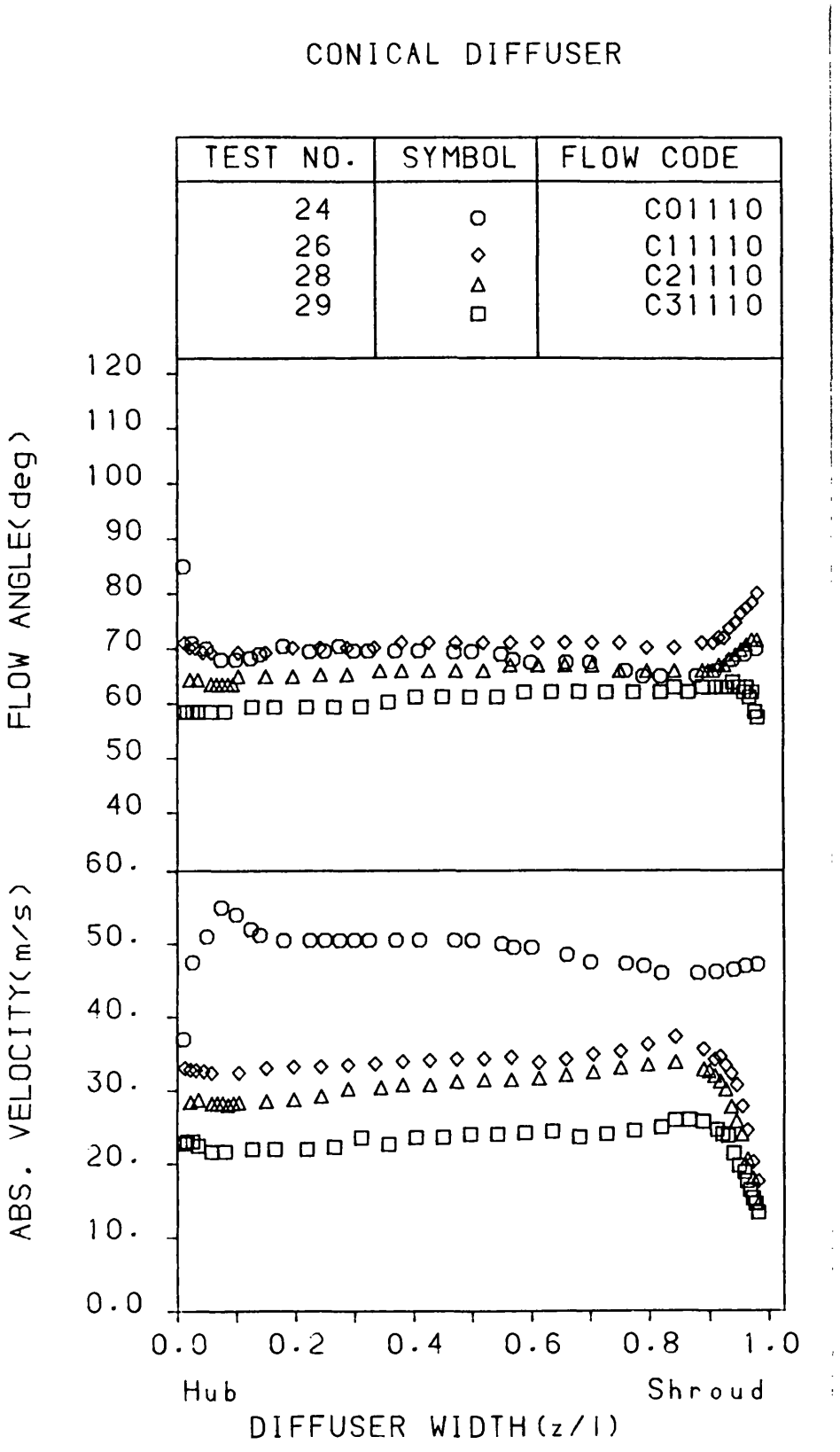

FIGURE 6.40: Absoulute velocity and flow angle distributions at the inlet of the conical diffuser.

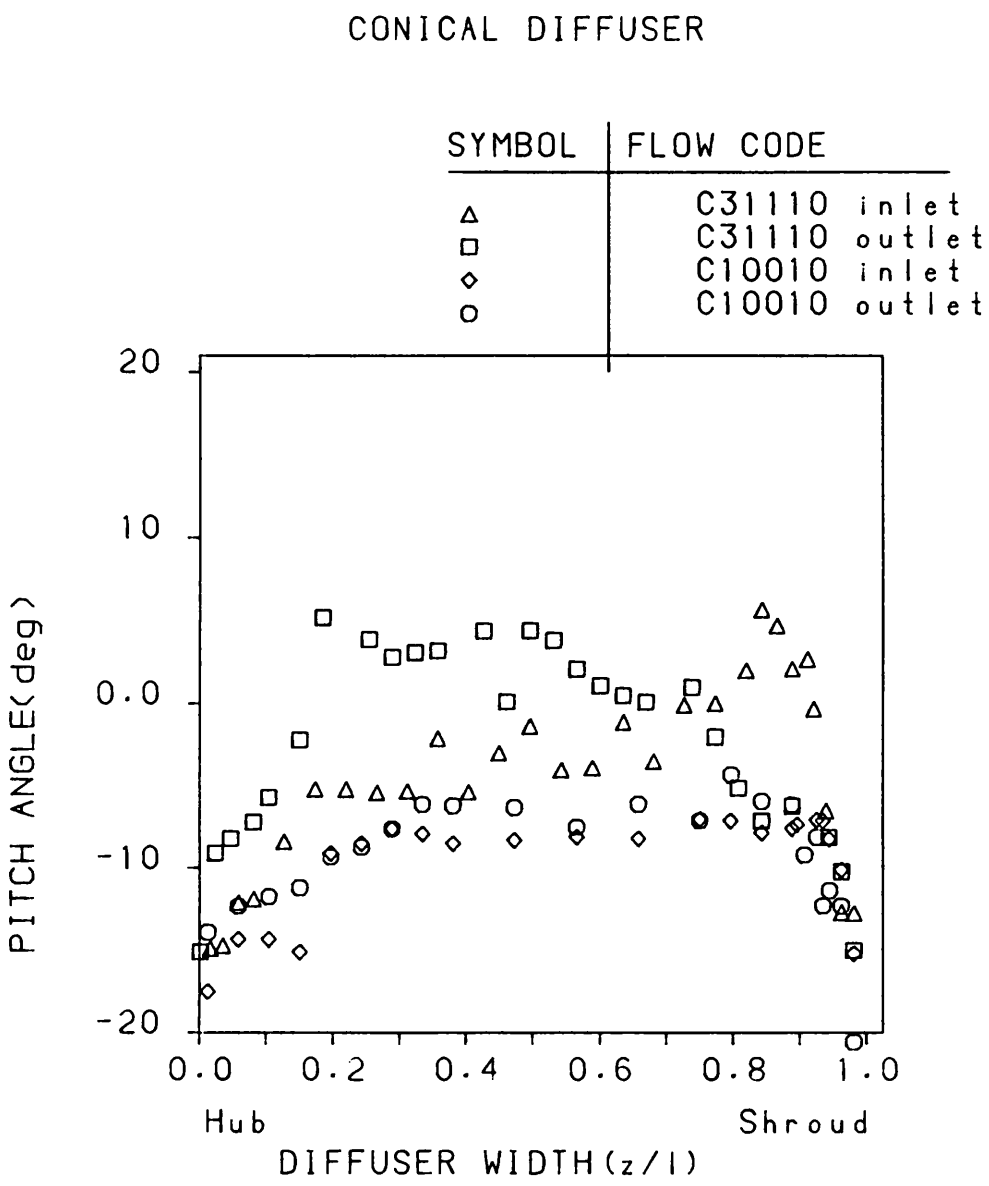

FIGURE 6.41: Pitch angle distributions for different flow rates.

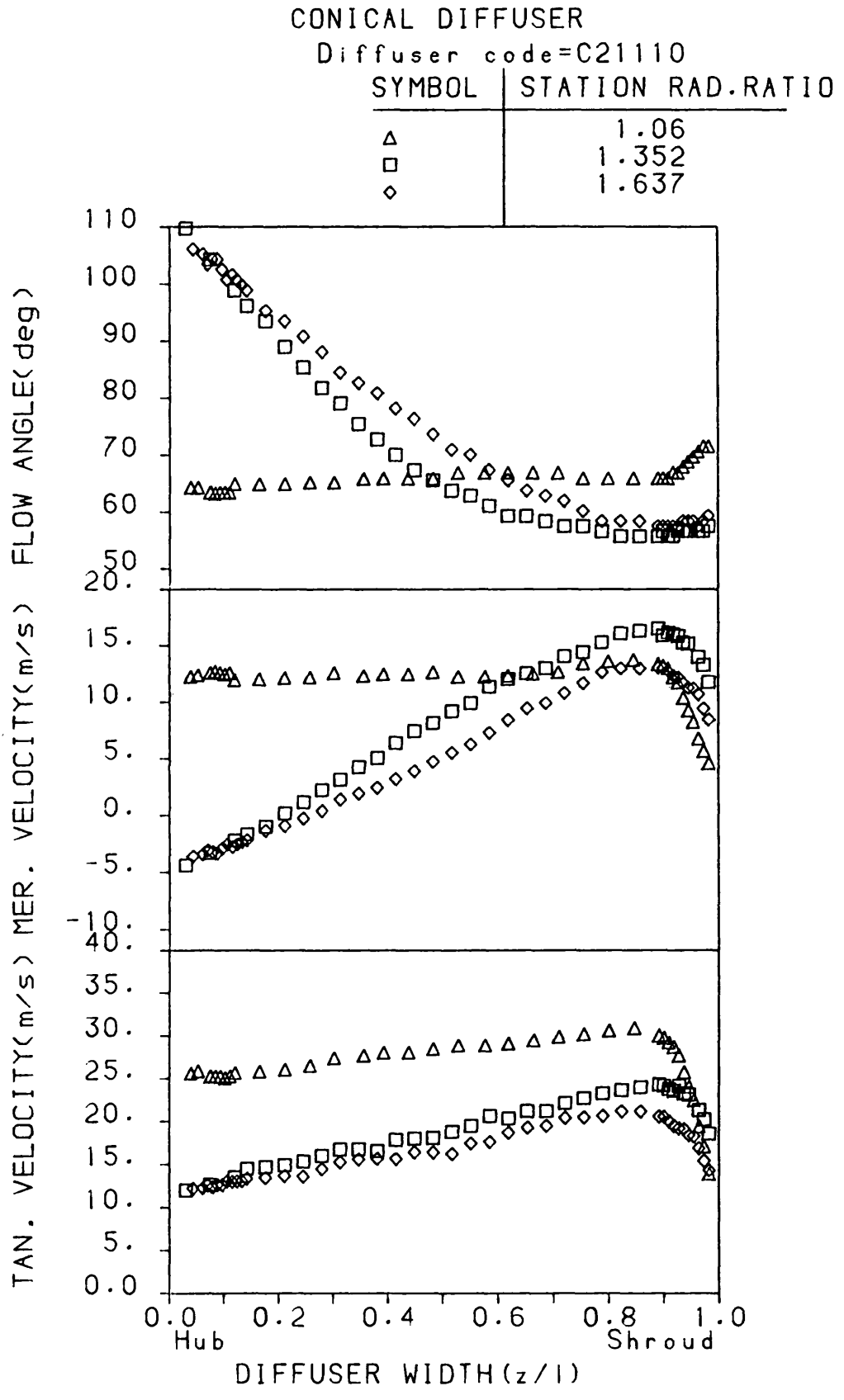

FIGURE 6.42: Velocity distributions in the conical diffuser at different radial stations.

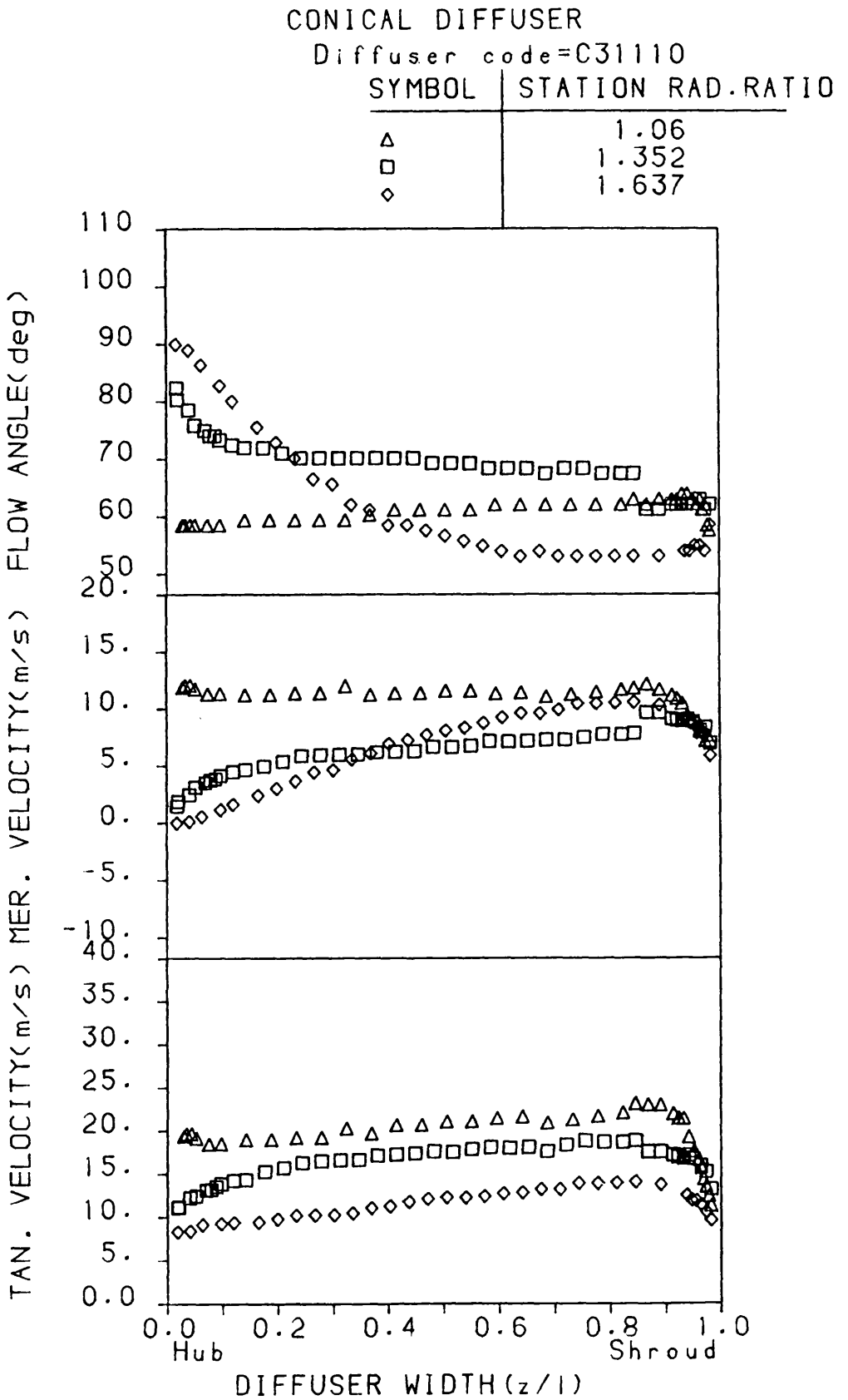

FIGURE 6.43: Velocity distributions in the conical diffuser at different radial stations.

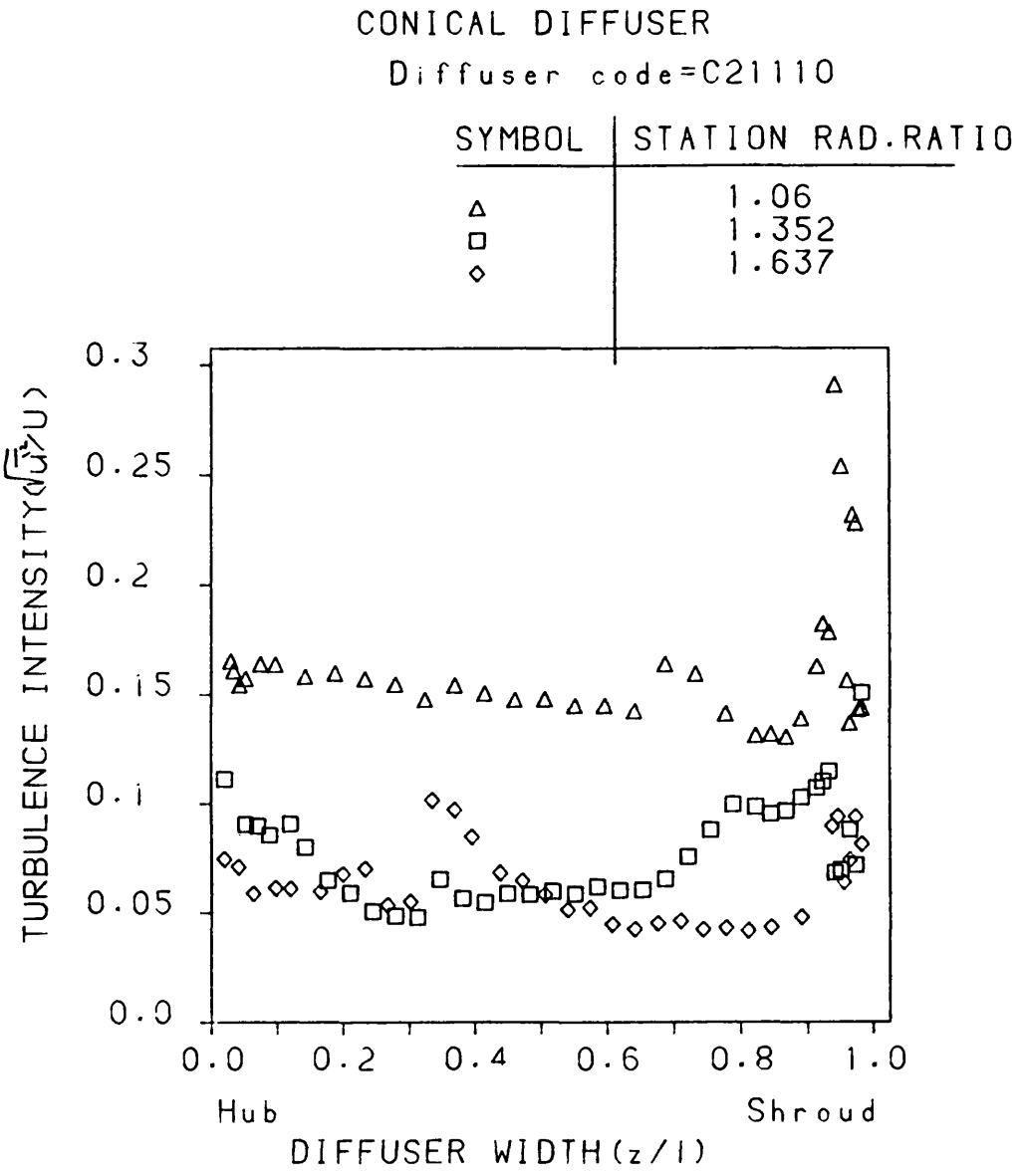

FIGURE 6.44: Turbulence intensity distribution in the conical diffuser.

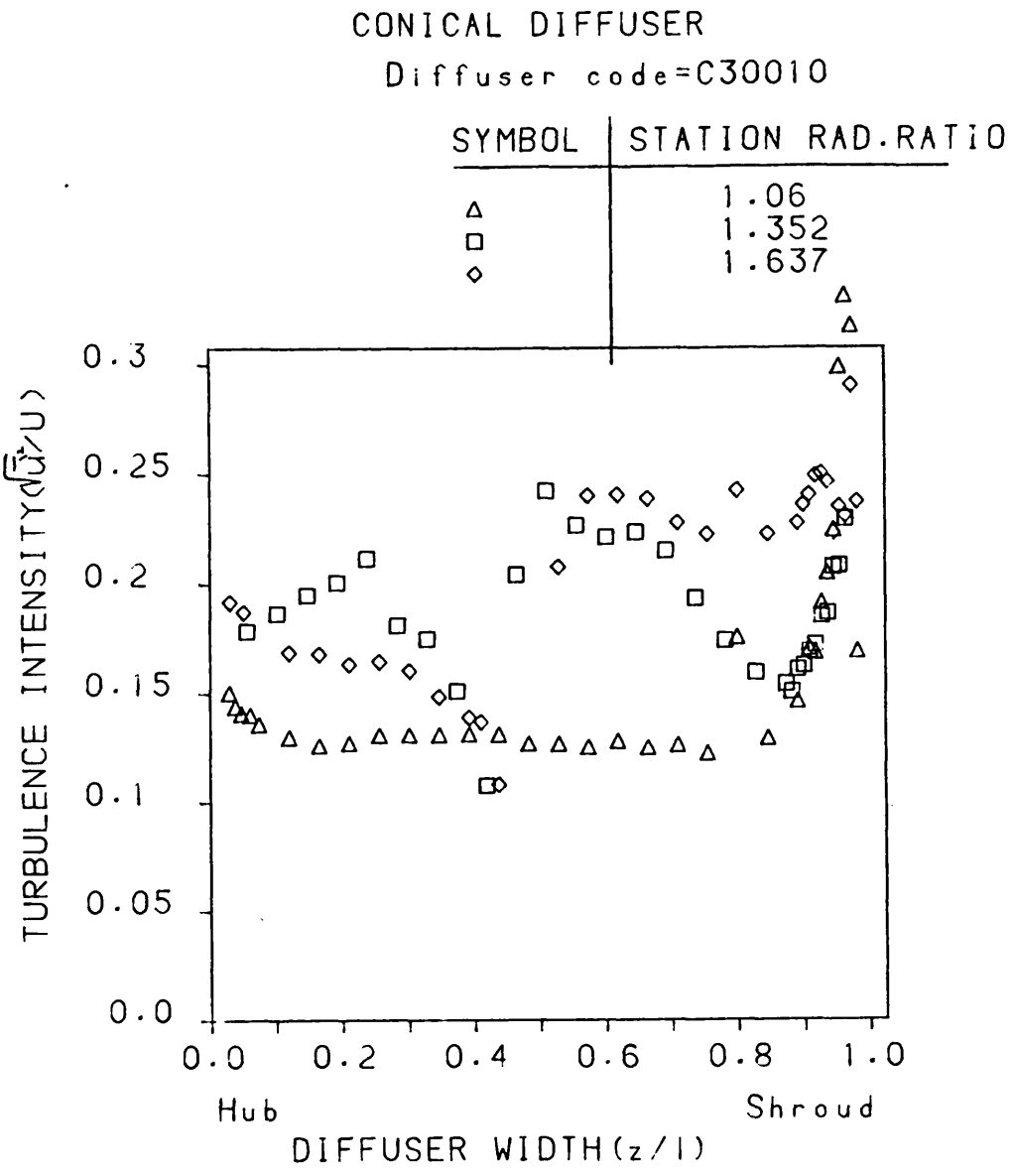

FIGURE 6.45: Turbulence intensity distribution in the conical diffuser.

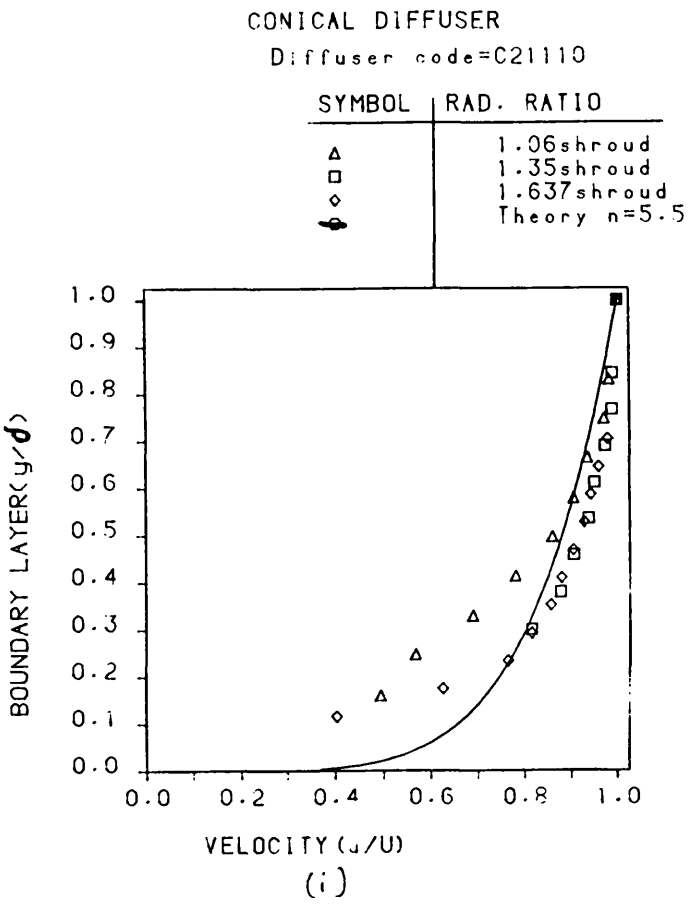

(i)

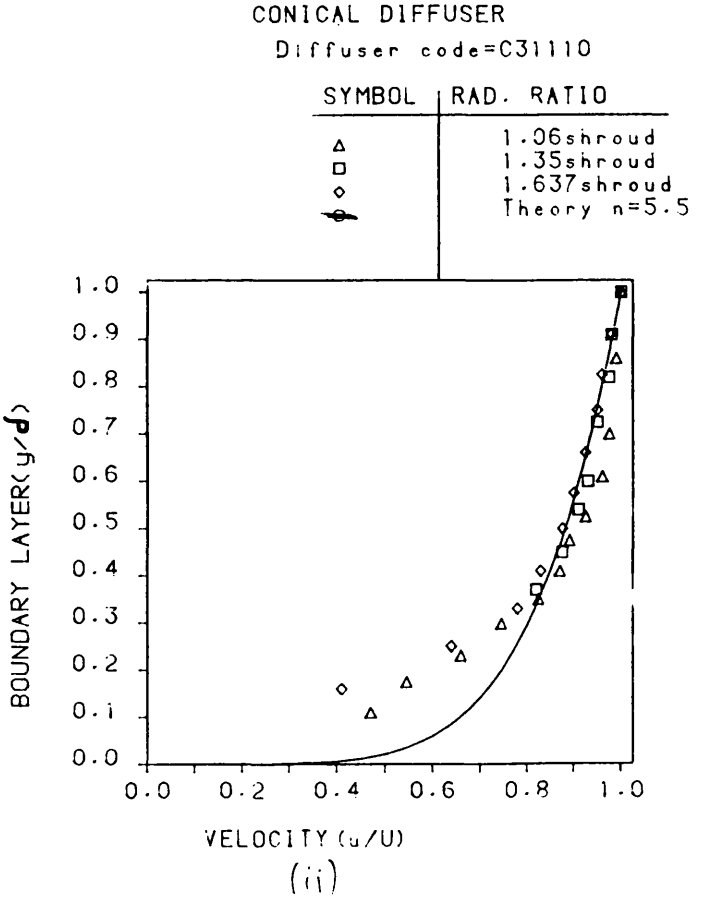

(ii)

FIGURE 6.46: Velocity distribution in the boundary layer.

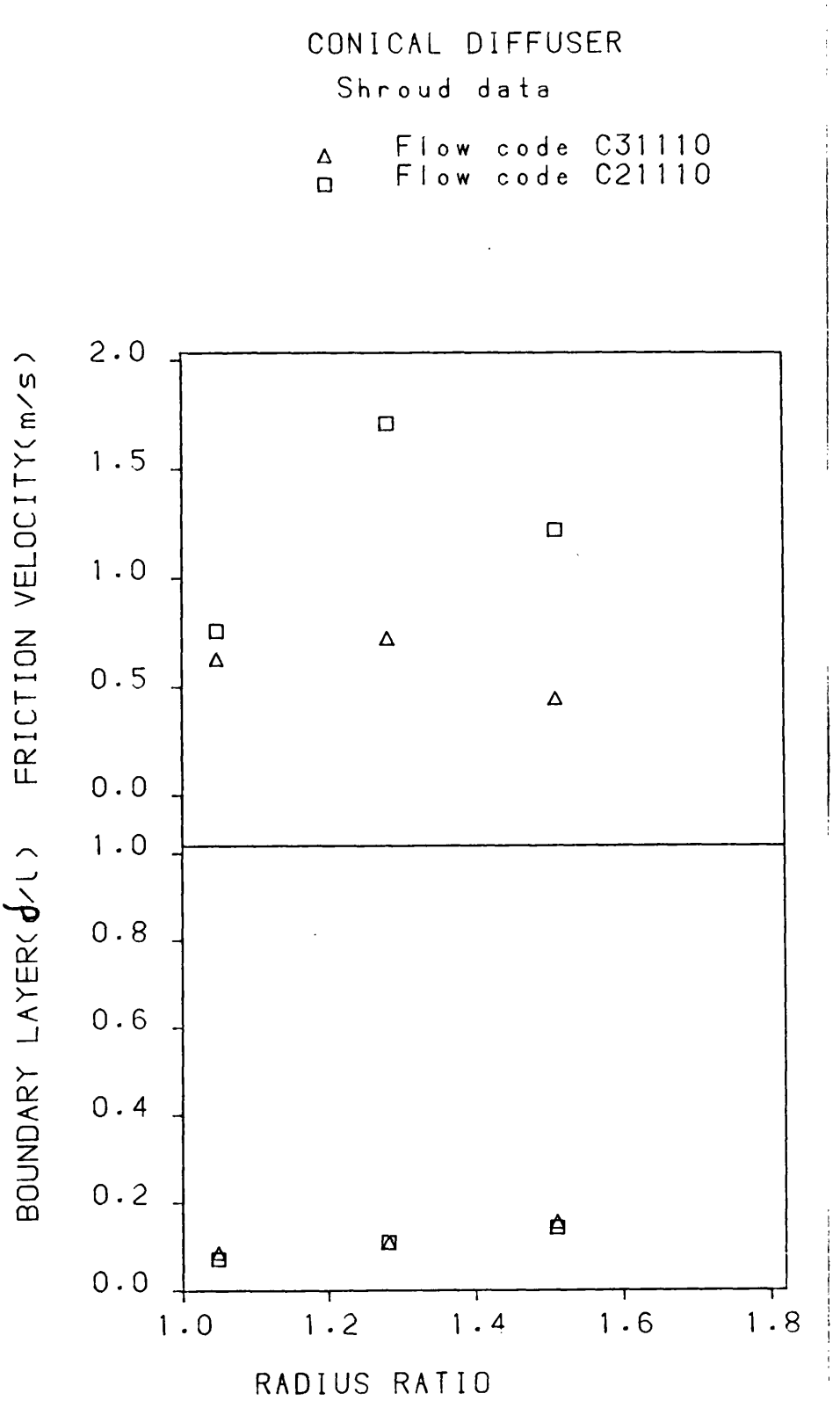

FIGURE 6.47: Boundary layer thickness and friction velocity for different flow rates in the conical diffuser.

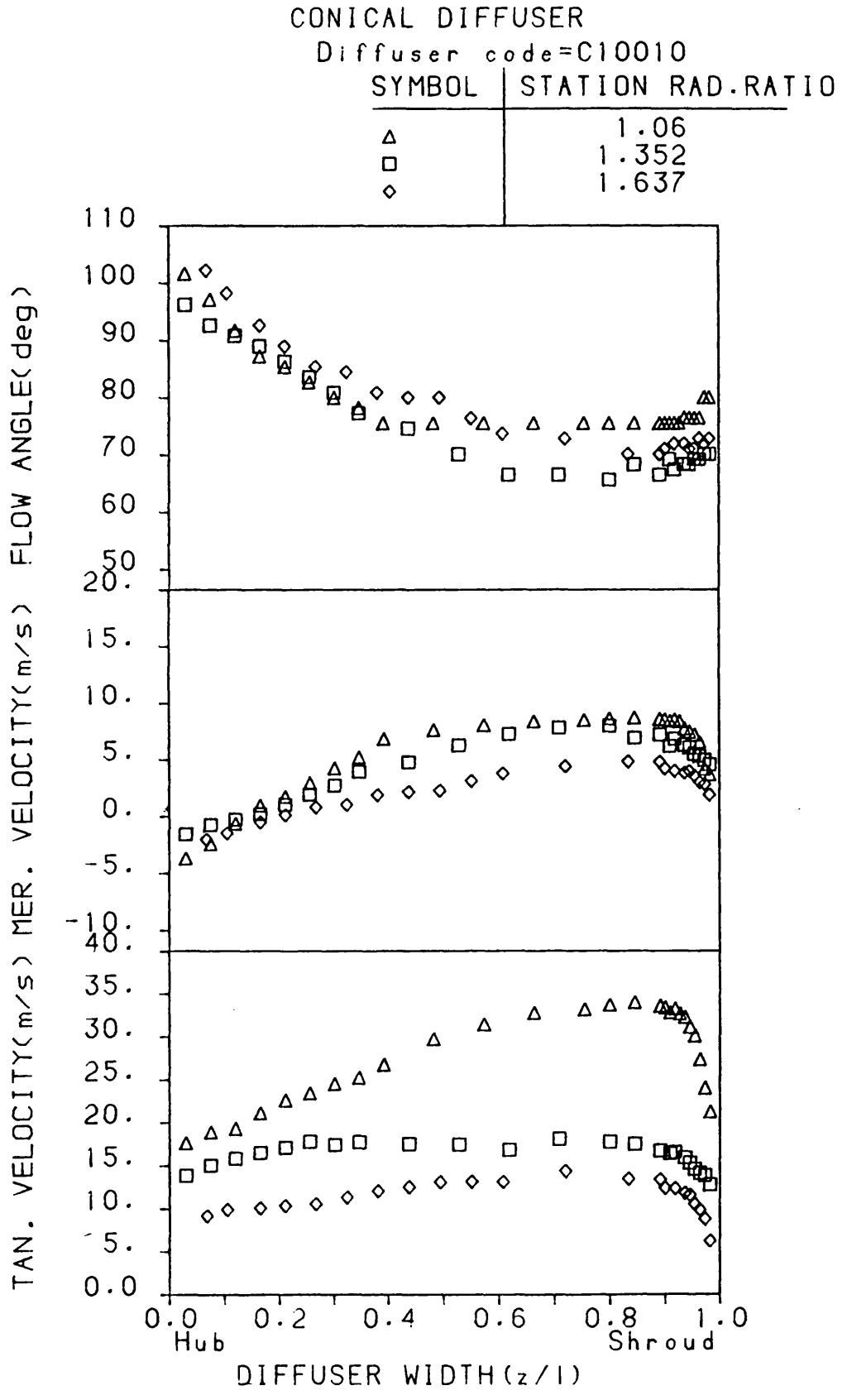

FIGURE 6.48: Flow profile distributions in unsteady flow.

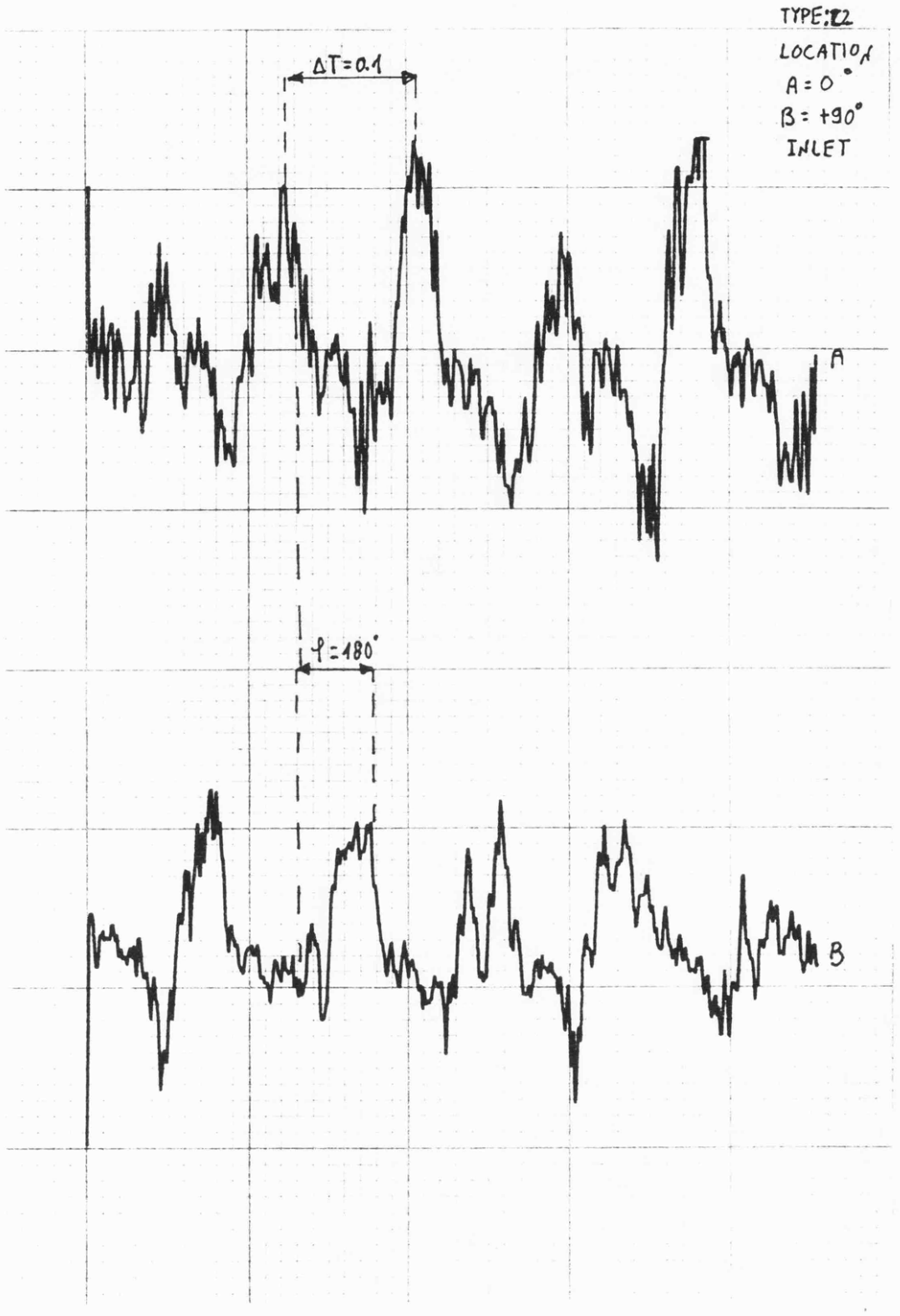

FIGURE 6.49a: Pressure traces on the hub surface.

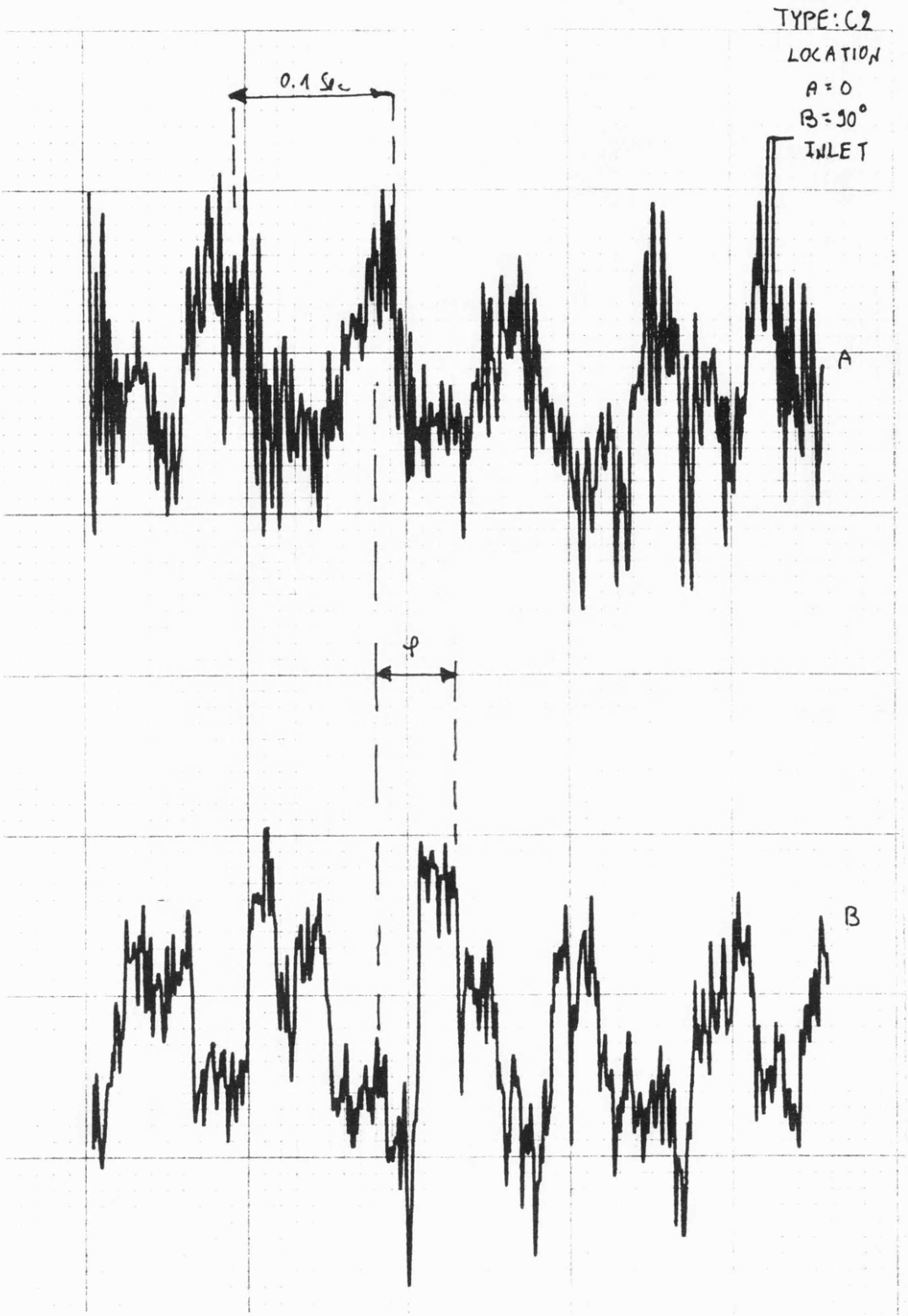

FIGURE 6.49b: Pressure traces on the shroud surface.

(i)

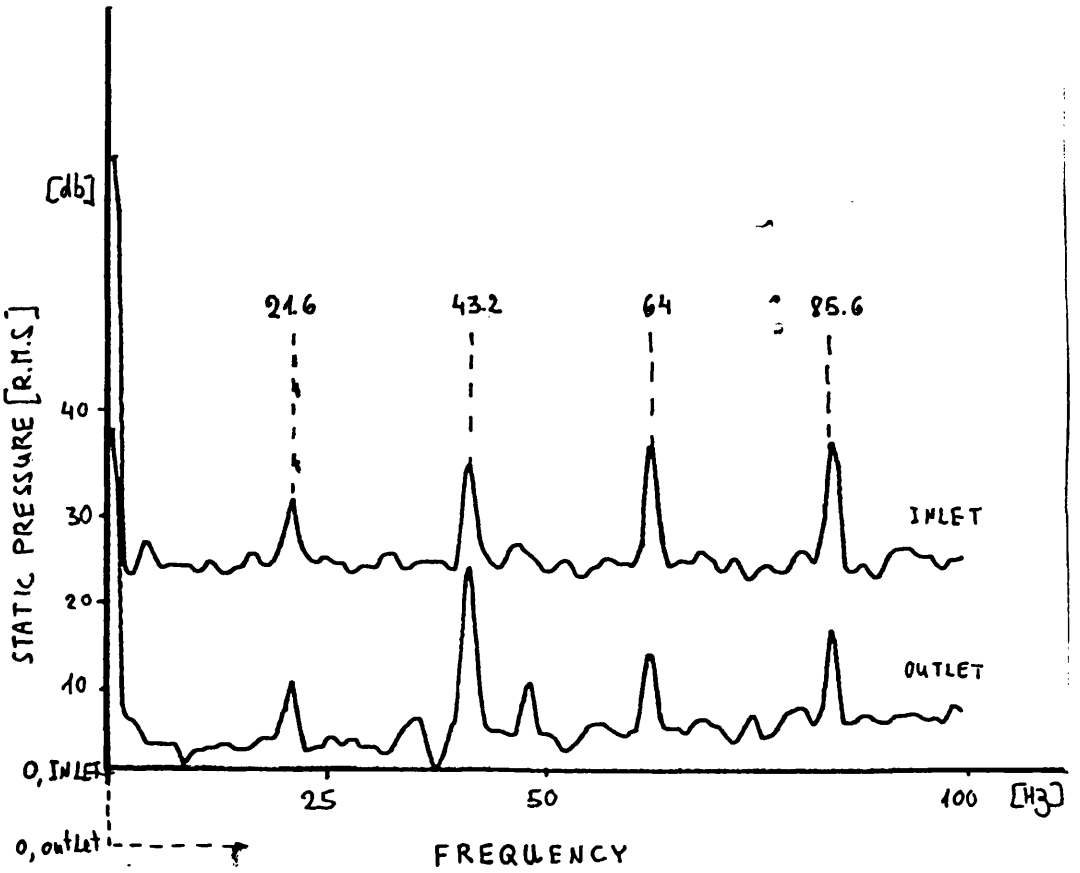

i) STEADY FLOW

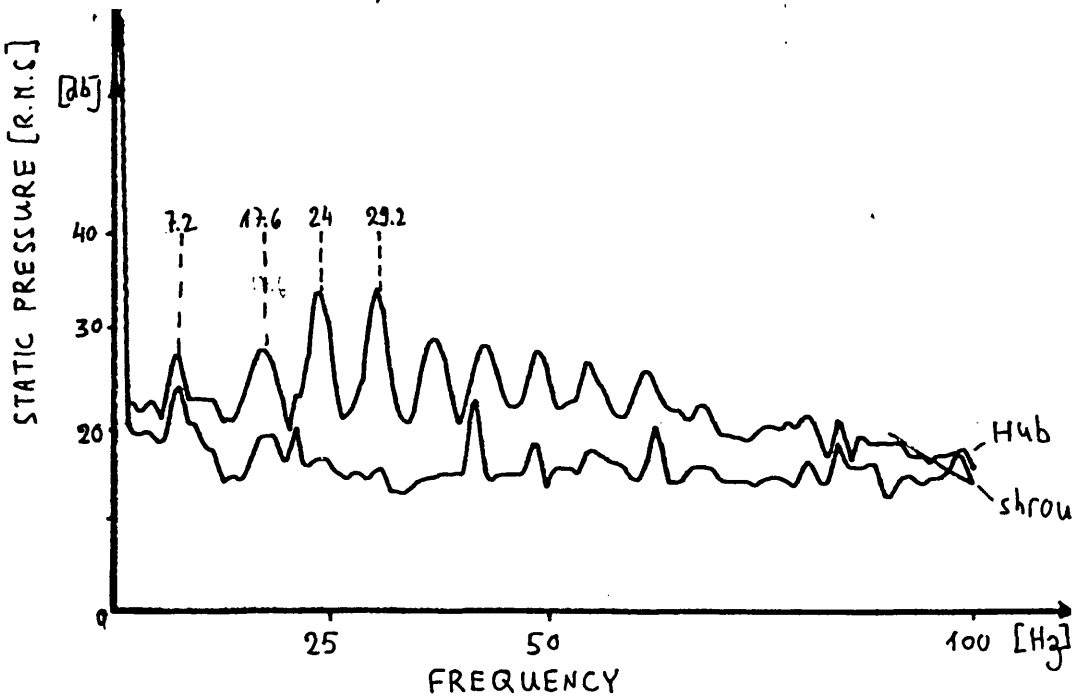

ii) AFTER INSTABILITY

FIGURE 6.50: Spectra of conical diffuser pressure fluctuations.

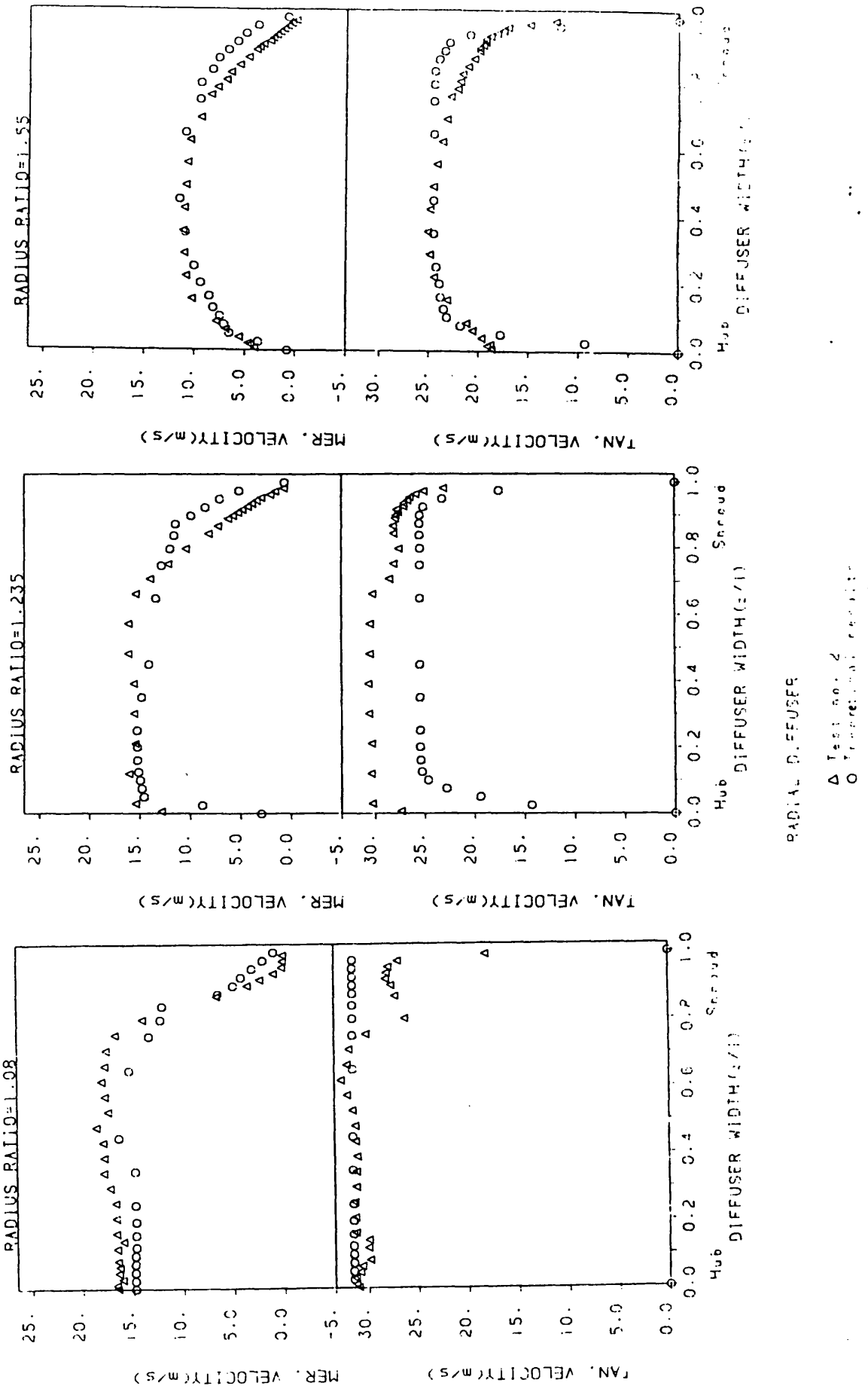

FIGURE 6.51: Comparison between theoretical and experimental results in the radial diffuser.

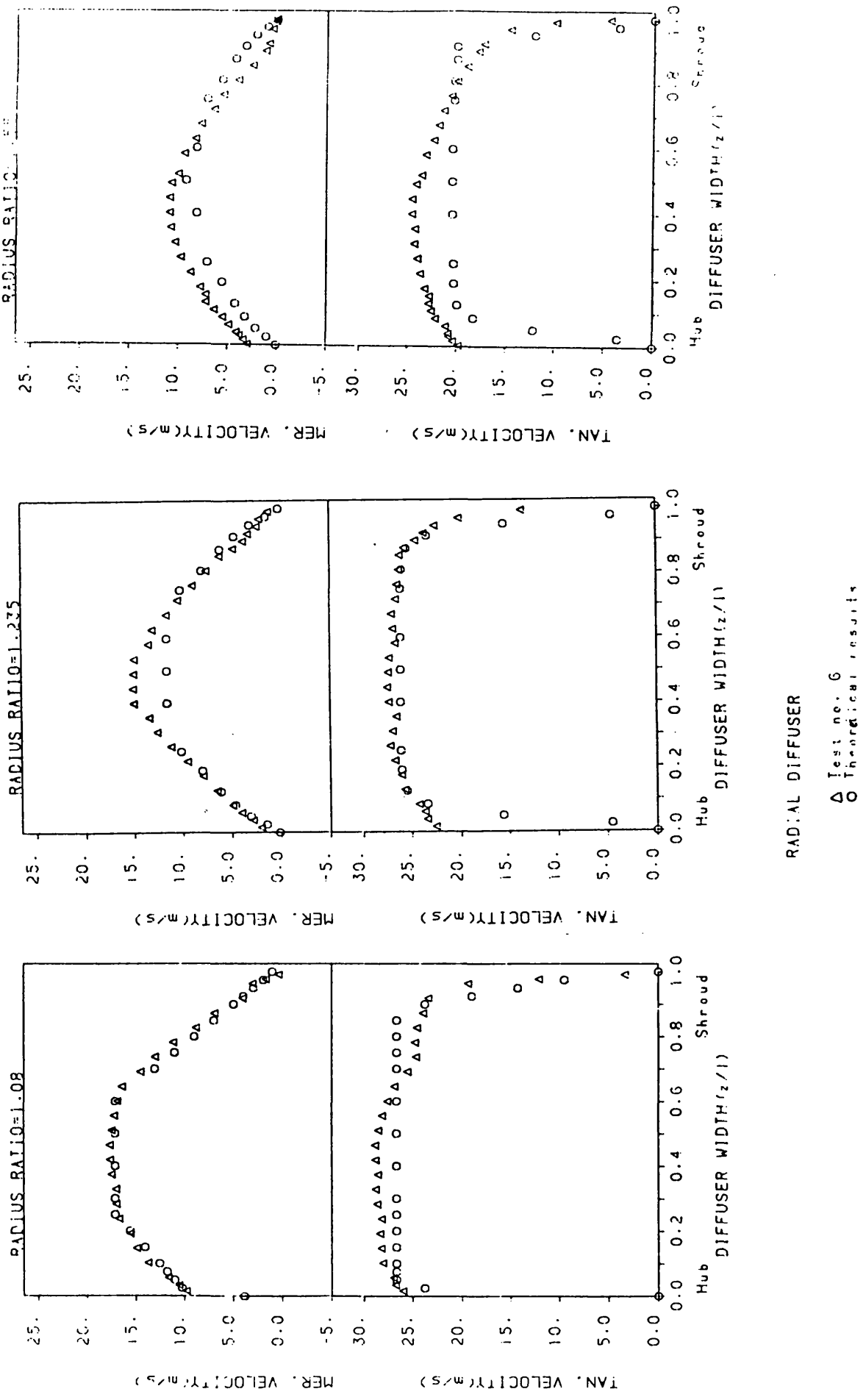

FIGURE 6.52: Comparison between theoretical and experimental results in the radial diffuser.

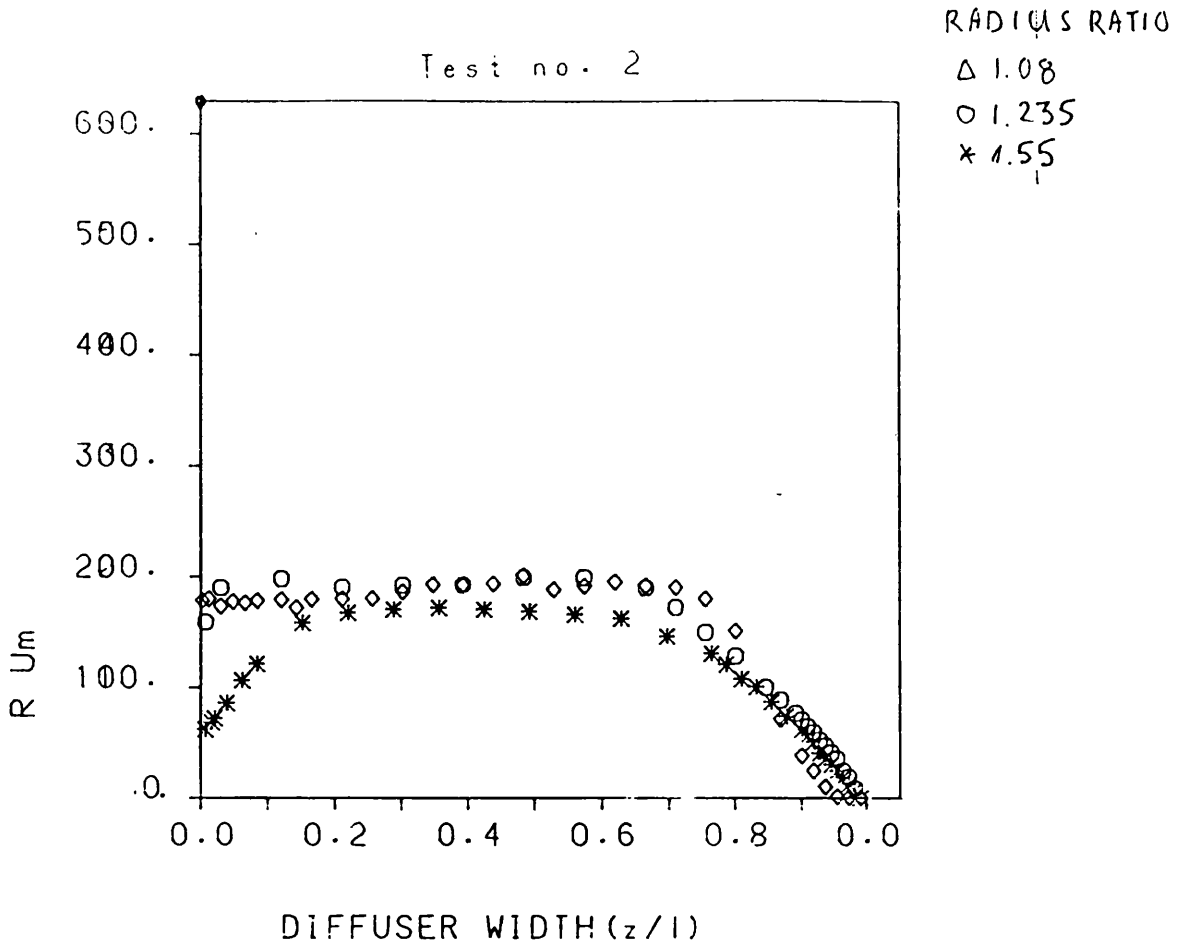

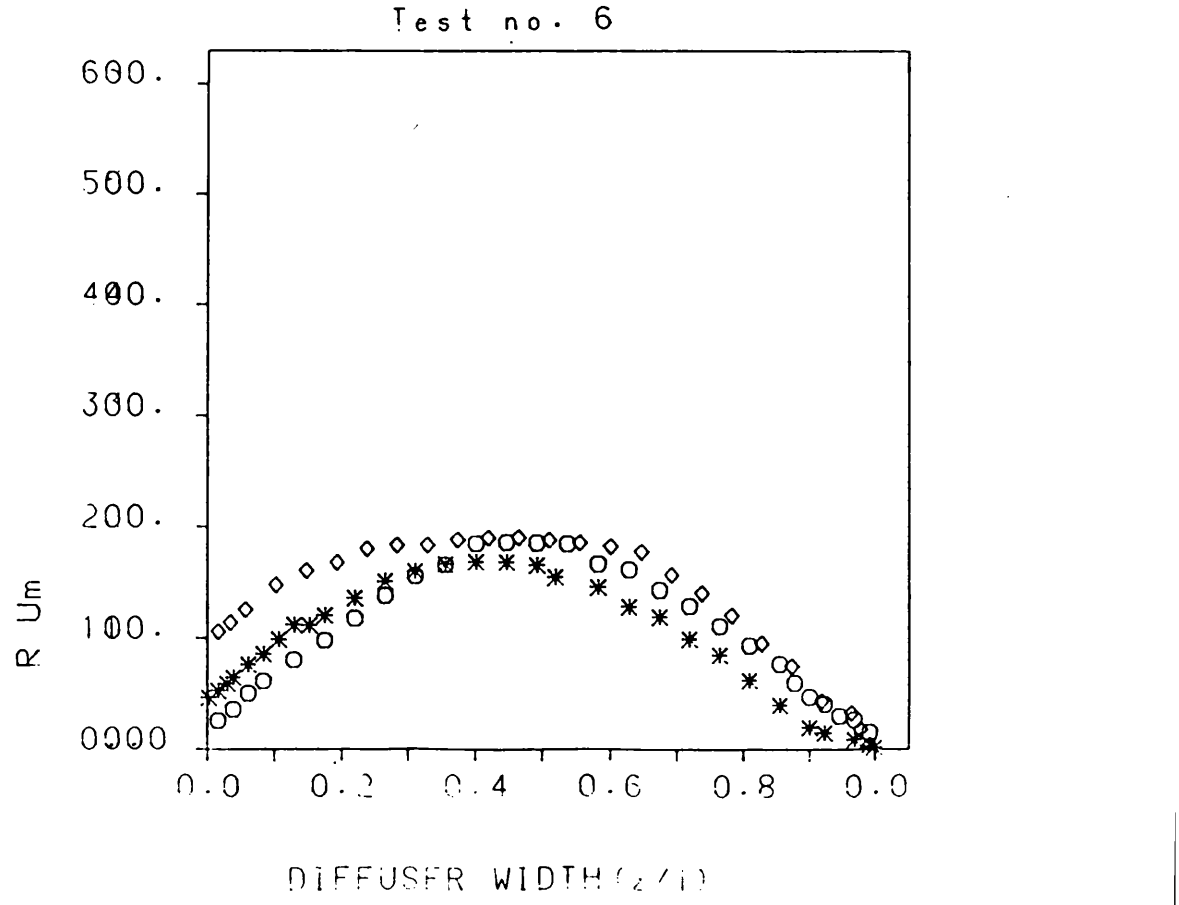

FIGURE 6.53: Variation of rUm across the radial diffuser cross section.

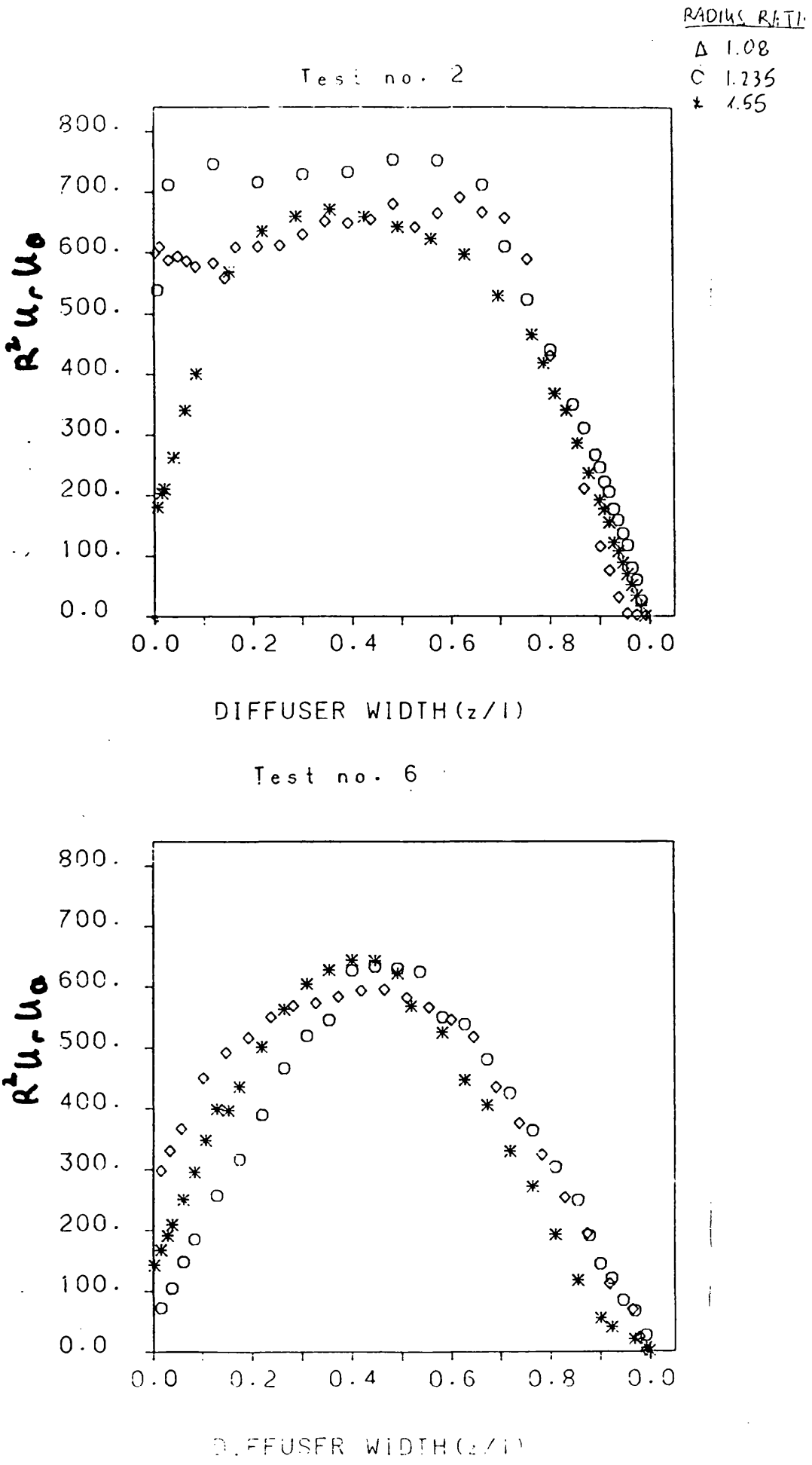

FIGURE 6.54: The experimental angular momentum distribution at each cross section of the radial diffuser.

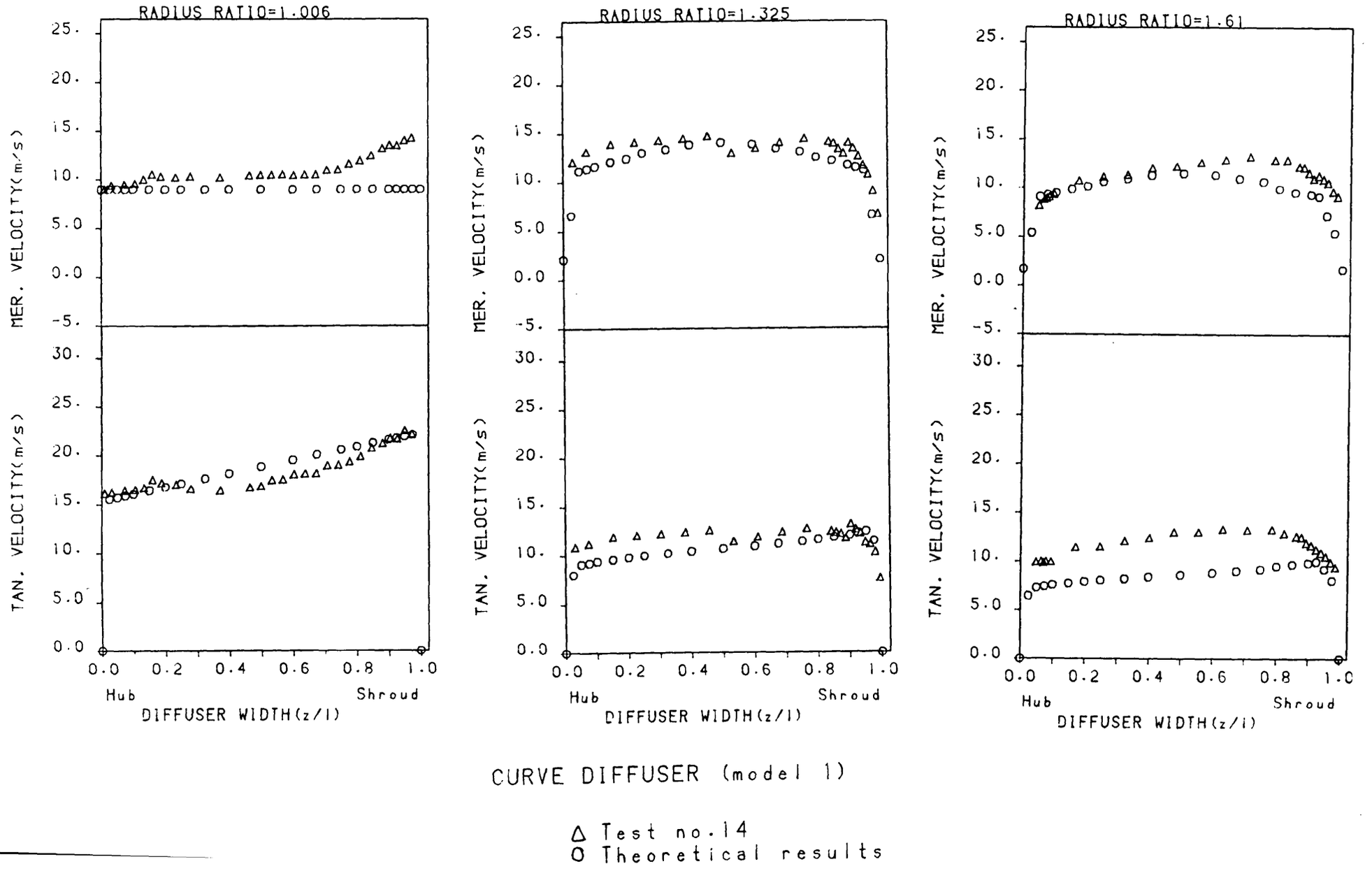

FIGURE 6.55: Comparison betwen theoretical and experimental results in the curved diffuser. (model 1)

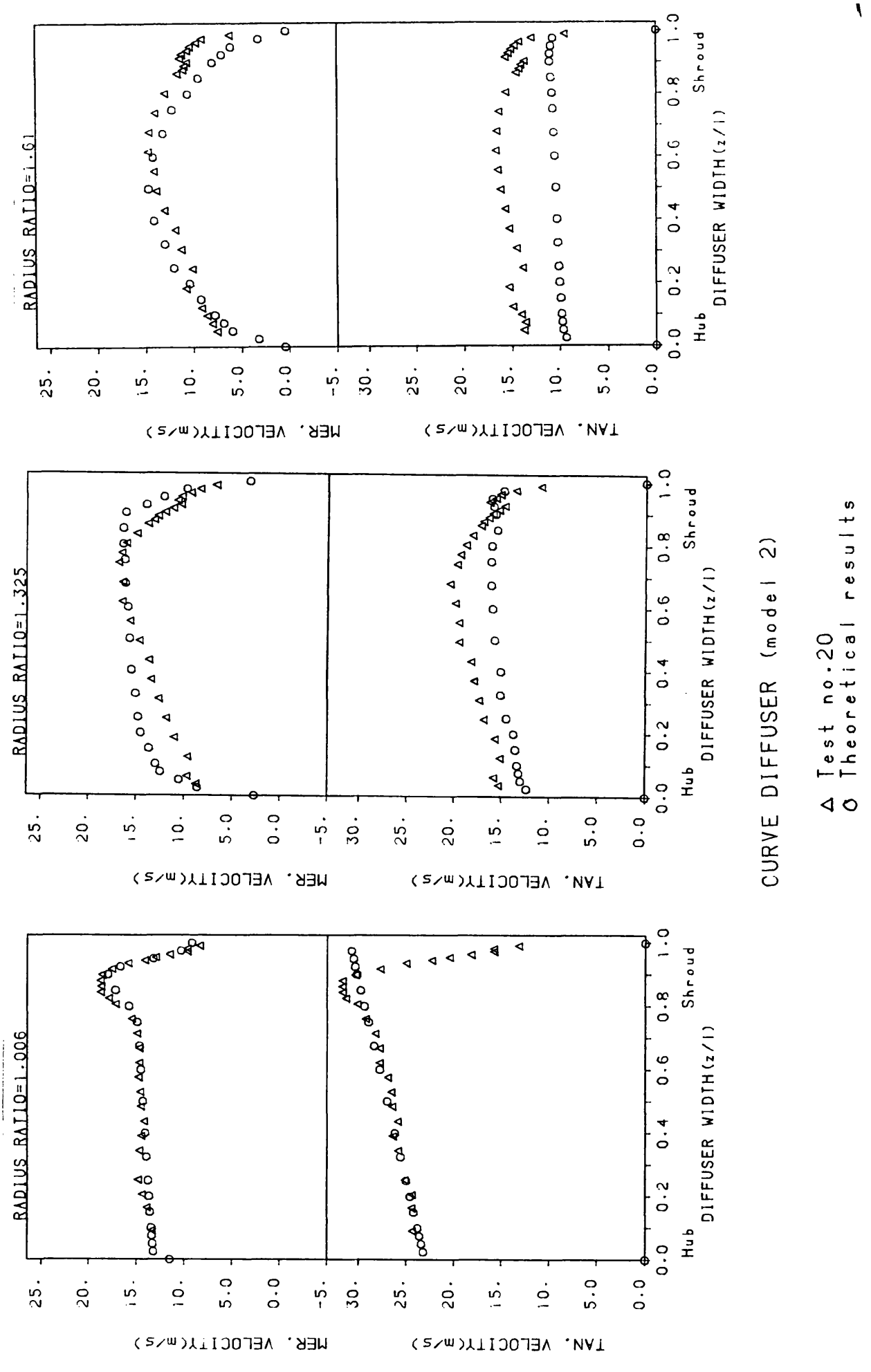

FIGURE 6.56: Comparison between theoretical and experimental results in the curved difuuser. (model 2)

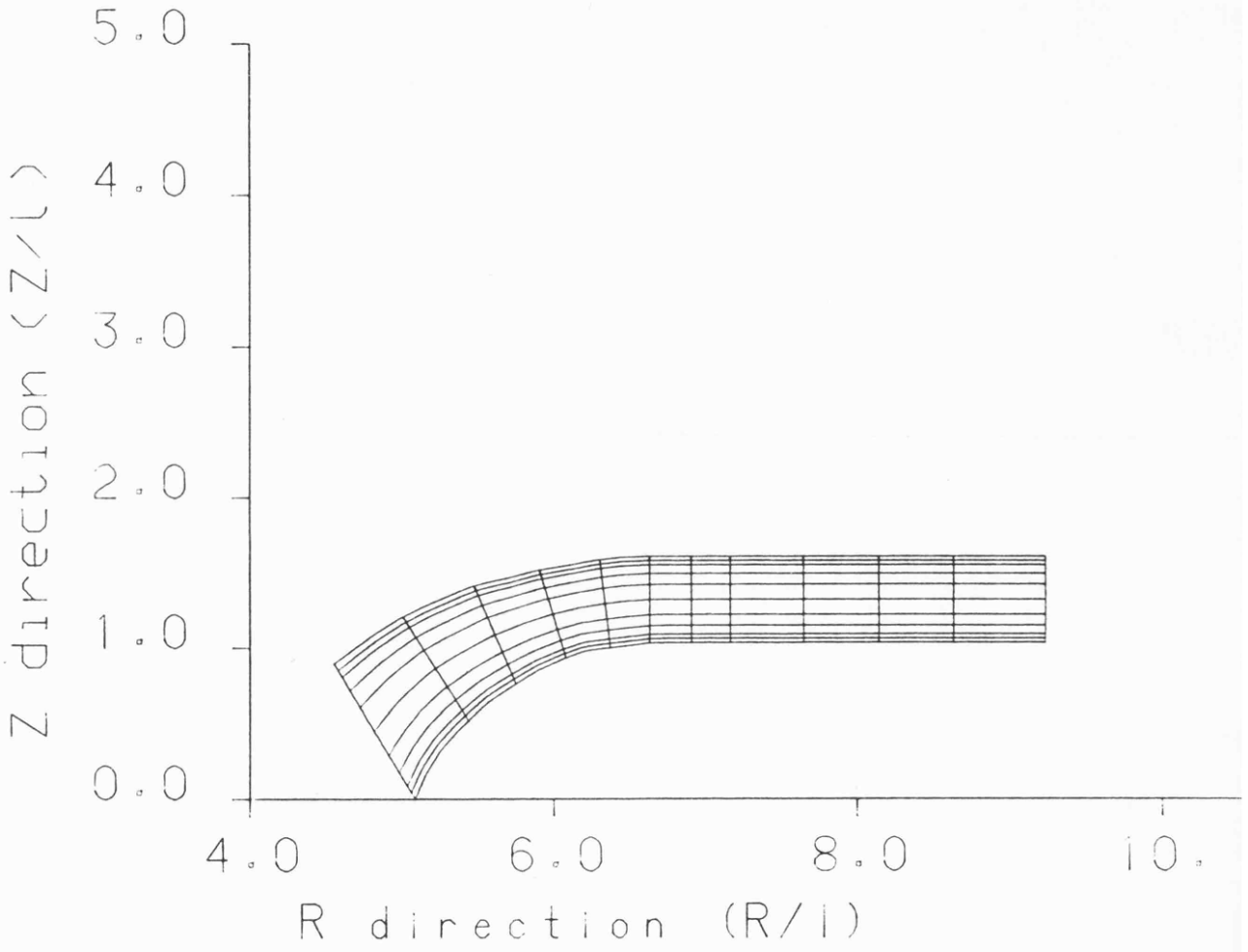

FIGURE 6.57: Fine mesh used with the curved diffuser.

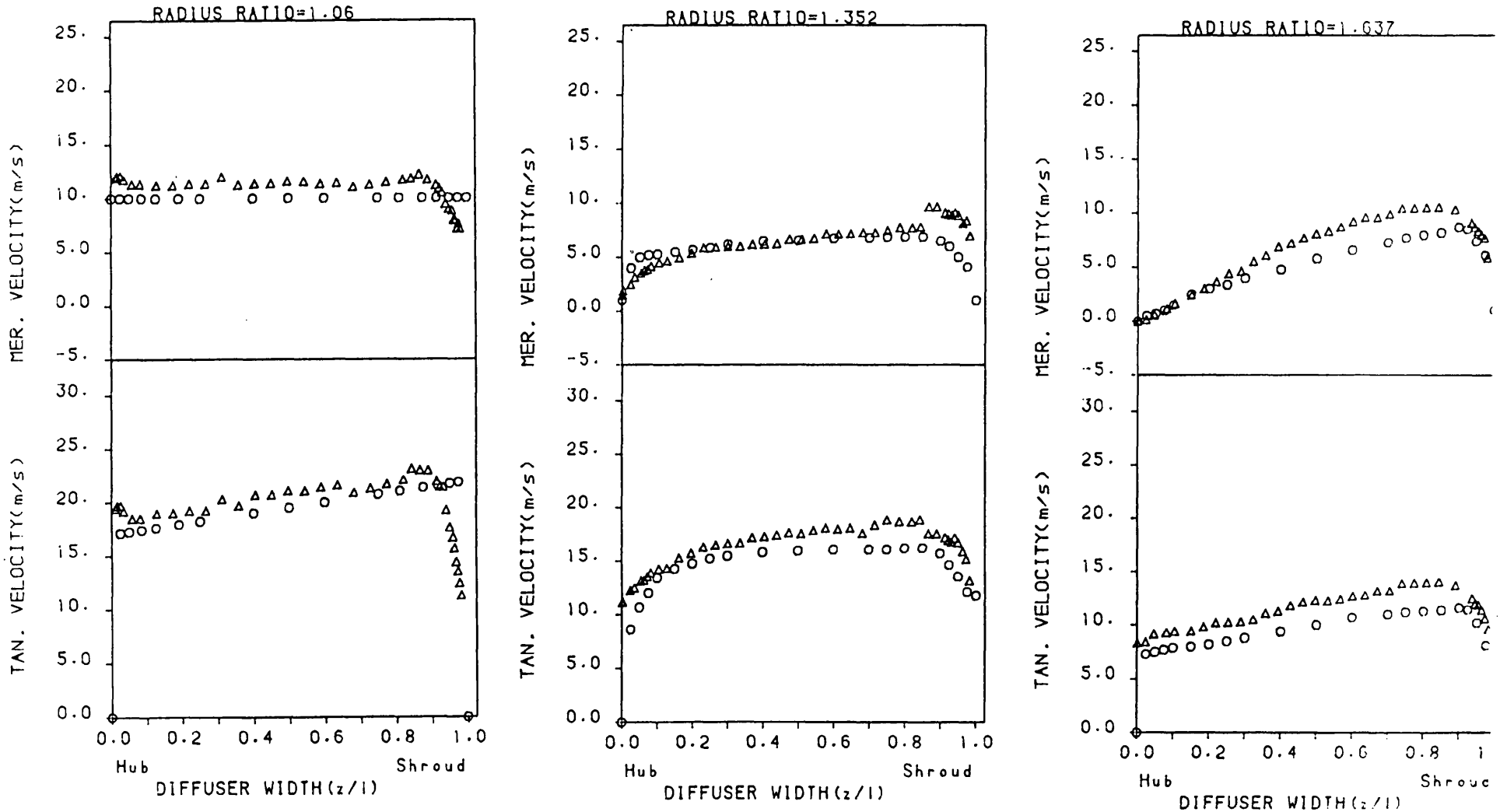

FIGURE 6.58: Comparison between theoritical and experimental results in the conical diffuser.

CHAPTER 7

CONCLUSIONS AND SUGGESTIONS FOR FURTHER WORK

7.1: CONCLUSIONS

The three types of vaneless diffusers associated with radial and mixed flow compressors have been studied both experimentally and theoretically.

The experimental investigation was carried out on six times full size models of turbocharger diffusers. For the mixed flow compressor designs it is quite clear that the simple straight conical diffuser is the least stable design, it being very difficult to develop a totally steady flow condition. Of the two alternative curved annular diffusers tested it was shown that contraction of the passage width led to a clear improvement in the flow stability. For mixed flow impellers it is, therefore, necessary to design a curved annular diffuser with contraction of the passage width such that the ratio of inlet to discharge cross sectional area is approximately unity. For radial flow impellers the commonly employed radial vaneless diffuser proved to have better stability characteristics than the curved annular diffusers. The

necessity to employ curved annular diffusers with mixed flow impeller designs is, therefore, a distinct disadvantage, and mixed flow design can only be justified if clear improvements are available from the mixed flow impeller design.

A theoretical investigation, based upon a stream function-vorticity formulation of the Navier-Stokes equations, has been developed to analyse the flow in each type of diffuser. The theoretical procedure has employed the two equation, k-ϵ, turbulence model, and used the finite element numerical solution technique. Numerical convergence problems arose with high Reynolds number flow situations; this was overcome by using the "upwind technique" and by employing a variational principle solution procedure with a dynamic mesh system. The theoretical procedure was used to assess the effect of different inlet flow conditions upon the diffuser preformance. Whilst the turbulence model employed was not able to predict directly the point of separation and recirculating flows it was possible to indentify regions of low velocity where separation would be encountered. It was shown that a gradient in the inlet meridional velocity profile led to a tendency to flow separation. Gradients in the tangential component of velocity did not

prove to be as critical. For flow situations where instabilities did not occur the predicted flow profile agreed well with those obtained experimentally.

7.2 SUGGESTION FOR FURTHER WORK.

Stability of diffuser flows is only part of the general problem of surge in turbocharger compressors. In order to suppress surge and extend the operating range of the compressor it is necessary to improve the stability of each component. To this end the investigation should be continued on a turbocharger compressor so that the stability and interaction of each component can be studied. The small size high speed turbocharger compressor leads to a difficult instrumention problem; however development of improved techniques associated with miniture pressure transducers, telemetry, and laser anemometery will aid with this work.

The theoretical study needs further detailed investigation with particular reference to the turbulence model and its applicability to curved surfaces and recirculating flows. If the theoretical techniques are to be extended to impeller and volute interaction with the vaneless diffuser it will be necessary to investigate

both time dependent and three dimensional flow problems. For this purpose a numerical procedure based upon a pressure-velocity model, inplace of the stream function-vorticity model, may well prove to be advantageous.

REFERENCES

ABIR A. (1978)
Three dimensional stress and deformation analysis of symmetric finned bodies.
MSc. Thesis Technion Hifa ISREAL (in Hebrew)

ABDELHAMID A.M.,COLWILL W.,BARROWS J. (1979)
Experimental investigation of unsteady phenomena in vaneless radial diffusers
J. of Engineering of Power January, p.p 52-60

ABDELHAMID A.M. (1980a)
Distinction between two type of self excited gas oscillations in vaneless radial diffusers.
Canadian Aeronautics and Space Journal Vol. 26 No.2 p.p 105-117

ABDELHAMID A.M. (1980b)
Analysis of rotating stall in vaneless diffusers of centrifugal compressors.
Canadian Aeronautics and Space Journal Vol. 26 No.2 p.p 118-128

ABDELHAMID A.M. (1981)
Effects of vaneless diffusers geometry on flow instability in centrifugal compression system.
ASME paper 81-GT-10

ABDELHAMID A.M. (1982)
Control of self excited flow oscillations in vaneless diffuser of centrifugal compression systems.
ASME paper 82-GT-188

ACRIVLELLIS M. (1977)
Hot wire measurements in flows of low and high turbulence intensity.
DISA Information No.22 December

ACRIVLELLIS M. (1978)
Flow field dependence on hot-wire probe cooling law and probe adjustment.
DISA Information No.23 September

ADLER D. (1980)
Status of cenrifugal impeller internal aerodynamics. (part 1 and 2)
J. of Engineering for Power July p.p 728-746

ANTONIA A. (1968)
Radial diffusion with swirl.
Mechanical and Chemical Engineering Transaction Australia May p.p 127-131

ATKEY R. (1975)
Computer aided design of radial and mixed flow compressors.
Ph.D. Thesis University of BATH

AZIZ A.K. (1972)
THE MATHEMATICAL FOUNDATION OF THE FINITE ELEMENT METHOD.
Academic Press, N.Y

BAKER A.J. (1972)
Finite Element computational theory for three dimensional boundary layer.
AIAA paper 72-108

BAKER A.J. (1973)
Finite element solution algorithm for viscous incompressible fluid dynamics.
I.J. for Numerical Method in Engineering, Vol. 6 p.p 89-101

BAKER A.J. (1976)
Finite Element solution of turbulent and reacting compressible three dimensional flows.
ICCAD 2 International symposium on Finite Element in flow problem. ITALY June 14-18

BAMMERT K., RAUTENBERG M., WITTEKINOT W. (1978)
Vaneless diffuser flow with extremely distorted inlet profile.
ASME paper 78-GT-47

BARINA F.J. (1947) Comparative performance of two vaneless diffusers designed with different rates of passage curvature for mixed flow impellers.
NACA Technical Note No. 1490

BARBOTIN D. (1977)
Experimental and theoretical evaluation of flow pattern in curved annular diffusers
M.Sc. Thesis BATH University

BAR YOSEPH P. (1978)
Finite element solution of Navier-Stokes equation in rotating flow. (In HEBREW)
D.Sc. Thesis TECHNION HIFA ISRAEL

BEARMAN P.W. (1971)
Corrections for the effect of ambient temperature drift on hot-wire measurements in incompressible flow.
DISA Information No.11 MAY p.p 25-30

BERCOVIER M. ENGELMAN M. (1979)
A finite element for the numerical solution of viscous incompressible flows.
J. of Computational Physics, No. 30 p.p 181-201

BOBKOV V., IBZAGIMUV M.K., SABELEV G.T. (1968)
Correlation of experimental data on the pulsation velocity intensity for turbulent flow in channels of different form.
Fluid Dynamics Vol.3 p.p 111-118

BRADSHAW P., YOUNG A.D. (1973)
Effects of stream line curvature on turbulent flow.
AGARD-AG-169

BROWN W.B. (1947)
Friction coefficients in a vaneless diffuser.
NACA TN1311

BROWN W.B., BRADSHAW G.R. (1947)
Method of designing vaneless diffusers and experimental investigation of certain undetermined parameters.
NACA Technical Note No. 1426.

CAMPION-RENSON A., CROCHET M.J. (1978)
On the stream function-vorticity finite element solution of Navier-Stokes equation.
I. J. for Numerical Method in Engineering, Vol. 12 p.p 1809-1818

CEBECI T., SMITH A.M. (1975)
ANALYSIS OF TURBULET BOUNDARY LAYERS.
Academic Press

CHENG R.T. (1972)
Numerical solution of the Navier-Stokes equations by the finite element method.
The Physics of Fluid Vol. 15, Number 12 p.p 2098-2105

CHUNG T.J. (1978)
FINITE ELEMENT ANALYSIS IN FLUID DYNAMICS.
McGraw Hill INC. U.S.A. 1978

CHAMPAGE F.H., SLEICHER C.A., WEHRMANN O.H. (1967)
Turbulence measurements with inclined hot-wire(part 1 & 2)
J. of Fluid Mech. Vol. 28 p.p. 153-182

COCKRALL D.J., MARKLAND E. (1963)
A review of incompressible diffuser flow.
J. of Aircraft Engineering, Oct. p.p 286-292

COMBER P.M., TOUZOT G.,COCHET J.F. (1978)
A comparison of different elements and formulations for thesolution of steady viscous flow.
Int. Conf. of Numerical Method in Laminar and Turbulent Flow.
Univ. of SWEANSEA U.K.

CRANE C.M., BURLEY D.M. (1974)
Numerical studies for viscous swirling flow through annular diffusers. (part 1 and 2)
J. of Engineering Math., Vol. 8 p.p 181-192

DAVIS W.R. (1976)
Three dimensional boundary layer computation on the stationary end walls of centrifugal turbomachinery.
J. of Fluid Engineering, Sept. p.p 431-442

DAVIS W., MILLAR D. (1975)
A comparision of the matrix and streamline curvature methods of axial flow turbomachinery analysis from user's point of view.
J. of Engineering for Power Oct. p.p 549-560

DEAN R.C., SENOO Y. (1960)
Rotating wakes in vaneless diffusers.
J. of Basic Engineering, Sept. p.p 563-574

DENNIS S.C.R., CHANG C. (1969)
Numerical intrgration of the Navies Stoke equation for steady two dimensional flow.
Physics of Fluid Supp.II p.p 89-93

DHATT G., BONAVENTURE K.F., BOURQUE C. (1981)
A stream function-vorticity finite element formulation for the Navier-Stokes equations.
I. J. for Numerical Method in Engineering, Vol. 17 p.p 199-212

DODGE P.R. (1977)
Numerical method for 2D and 3D viscous flow.
AIAA Journal, Vol. 15 No.7 July p.p 961-967

ELLIS G.O. (1964)
A study of induced vorticity in centrifugal compressors.
J. of Engineering for Power Janu. p.p 63-76

EL-GERESY B. (1982)
Theoretical and experimental study of flow in annular vaneless diffusers.
Ph.D. Thesis BATH University

FRAZER R.A., JONE W.P. (1937)
Approximation to function and to solutions of differential equation.
G.B. Tech Rept 1 p.p 517-549

FENNER R.T. (1975)
FINITE ELEMENT METHOD FOR ENGINEERS.
The MACMILLAN PRESS L.T.D U.K

FISER W., ZAHN G., TASCHE J. (1982)
Theoretical and experimental investigation about vaneless return channel of multistage radial flow turbomachines.
ASME paper 82-GT-267

GALERKIN B.G (1915)
Trans 63-18924
Fed. Sci. Tech. Info.

GARDOW E.B. (1958)
The three dimensional turbulent boundary layer in a free vortex diffuser.
Gas Turbine Laboratory, Report No.42, M.I.T.

GOLDSTEIN S. (1965)
MODERN DEVELOPMENT IN FLUID DYNAMICS.
Dover Publication

GOSMAN A.D., PUNN W.M., RUNCHAL A.K., SPALDING D.B., WOLFSHTEIN M. (1969)
HEAT and MASS TRANSFER IN RECIRCULATING FLOW.
Academic Press London

HEINRICH J.C., HUYAKORN P.S., ZIENKIEWICZ O.C, MITCHELL A.R. (1977)
An Upwind finite element scheme for two dimensional convective transport equation.
I.J. for Numerical Method in Engineering Vol. 11 p.p 131-143

HEINRICH J.C., ZIENKIEWICZ O.C. (1977)
Quadratical finite element scheme for two dimensional convective trasport problem.
I.J. for Numerical Method in Engineering Vol.11 p.p 1813-1844

HINZE J.O. (1959)
TURBULENCE
McGraw Hill N.Y

HIRSCH C.H., WARZEE G. (1976)
A finite element method for through flow calculation in turbomachines.
J. of Fluid Engineering, Sept. p.p 403-421

HIRSCH C.H., WARZEE G. (1978)
An integrated quasi-3D finite element calculation program for turbomachinery flows.
ASME paper 78-GT-56

HONAMI S., TSUKAGOSHI K., SAKAI T., WATANABE I. (1971)
Investigation concerning the fluid flow in the mixed-flow diffuser.
ASME paper 71-GT-40

HOOD P., TAYLOR C.(1974)
Navier-Stokes equations using mixed interpolation.
FINITE ELEMENT IN FLOW PROBLEM ,U.A.H. press
University of ALABMA

HUTTON A.G. (1971)
A finite difference method for analysing the flow in the entrance section of a duct.
MSc. Thesis University of WALES

HUTTON T.G. (1976)
Finite element analysis of turbulent incompressible flow bounded by smooth walls.
Int. Symp. of Finite Element Problem ICCAD 2nd.
Italy June 14-18.

HUYAKORN P.S., TAYLOR C., LEE R.L., GRESHO P.M. (1978)
A comparison of various mixed interpolation finite elements in the velocity pressure formulation of the Navier-Stokes equations.
Computer and Fluid, Vol. 6 p.p 25-35

IKEGAWA M. (1979)
A new finite element technique for the analysis of steady viscous flow problems.
I.J. for Numerical Method in Engineering Vol.14 p.p 103-113

IMAICHI K., TSURUSAKI H. (1979)
Rotating stall in a vaneless diffuser of a centrifugal fan.
ASME Winter Annual meeting Dec.2-7 N.Y.

IRON B.M., ZIENKIEWICZ O.C. (1968)
Curved isoparametric quadrilateral element for finite element analysis.
Int. J. Solids Structures, Vol. 4 p.p 31-42

IRONS B.M. (1970)
Frontal solution program for finite element analysis.
I.J. for Numerical Method in Engineering Vol.2 p.p 5-32

JANSEN W. (1964a)
Steady fluid flow in a radial vaneless diffuser.
J. of Basic Engineering Sept. p.p 607-619

JANSEN W. (1964b)
Rotating stall in a radial vaneless diffuser.
J. of Basic Engineering Dec. p.p 750-758

JOHNSTON J.P., DEAN R.C. (1966)
Losses in vaneless diffuser of centrifugal compressors and pumps.
J. of Engineering for Power Janu. p.p 49-60

JAPIKSE D. (1976)
REVIEW Progress in numerical turbomachinery analysis.
J. of Fluid Engineering Dec. p.p 592-606

JORGENSEN F.E. (1971)
Directional sensitivity of wire and fiber-film probes.
DISA Information NO.11 May

KAWAHARA M., OKAMOTO T. (1976a)
Finite element analysis of steady flow of viscous fluid using stream function.
Proc. of JSCE No.247 p.p 123-135

KAWAHARA M., YOSHIMURA N., NAKAGAWA K.,
OHSAKA H. (1976b)
Steady and unsteady finite element analysis of incompressible viscous fluid.
I.J. for Numerical Method in Engineering, Vol. 10 p.p 437-456

KAWAGUCHI T., FURUYAY Y. (1966)
The rotating flow in a vaneless diffusers having two parallel discs.
Bulliten of J.S.M.E, Vol No. 36 Nov., p.p 711-718

KINNS R. (1973)
Calibration of a hot-wire anemometer for velocity perturbation measurement.
J. of Physics E:Scientific Instruments Vol.6 p.p253-256

KRIMERMAN J., ADLER D. (1975)
The numerical calculation of the meridional flow field in turbomachine using finite element method.
Israel J. of Technology, Vol No. 12 p.p 268-274

KRIMERMAN J. (1978)
Calculation of the fully three dimensional flow field in turbo impellers using the finite element method.
DSc. Thesis Technion Hifa Isreal (in Hebrew)

KUBO T. (1980)
Unsteady flow phenomena in centrifugal fans.
Bulletin of JSME Vol. 23 No.185-7

KOCH F.A., GARTSHORE I.S. (1972)
Temperature effects on hot-wire anemometer calibrations.
J. of Physics E:Scientific Instruments Vol. 5 p.p58-61

KOSUGE H., TAKANE H., NAKANISHI K. (1982)
A consideration concerning stall and surge limitations within centrifugal compressors.
ASME paper 82-GT-15

LASKARIS T.E. (1978)
Finite element analysis of the three dimensional potential flow in turbomachines.
AIAA Journal, Vol. 16

LEMNEMANN E., HOWARD J. (1970)
Unsteady flow phenomena in rotating centrifugal impeller passages.
J. of Engineering for Power Janu. p.p 65-72

LIGRANI D.M., BRAEMBUSSCHEL R.V., ROUSTAN M. (1982)
Rotating stall measurement in the vaneless diffuser of a radial flow compressor.
ASME paper 82-GT-257

MAGER A. (1952)
Generalization of boundary layers momentum integral equations to three dimensional flow including those of rotating systems.
NACA Report 1067

MATES R.G. (1963)
Three dimensional flow in the diffuser of a mixed flow compressor.
Ph.D. Thesis CORNELL University

METU A. (1982)
A quasi three dimensional finite element solution for steady

compressible flow through turbomachines.
ASME paper 82-GT-261

MORGAN K., HUGHES T.G., TAYLOR C. (1977)
Investigation of a mixing length and a two equation turbulence model, utilizingthe finite element method.
Appl. Math. Modelling Vol. 1 Dec. p.p 395-400

MOULT A. (1975)
Application of the finite element method in calculation of flow patterns in liquids and glasses.
Ph.D. Thesis University of SHEFFIELD

MOULT A., BURLEY D., RAWSON H. (1979)
The numerical solution of two dimensional steady flow problem by the finite element method.
I.J. for Numerical Method in Engineering Vol.14 p.p 11-35

NASH J.F., PATEL V.C. (1972)
Three dimensional turbulent boundary layers.
S.B.C Technical books

ODEN J.T., WELLFORD L.C. (1972)
Analysis of flow of viscous fluid by the finite element method.
J. AIAA Vol. 10 p.p 1590-1599

OLIVER A.J. (1975)
The prediction of heat transfer and fluid flow in the entrance region of an annulu with the inner cylinder rotating.
Ph.D. Thesis C.E.R.L LEATHERHEAD

OLIVER A.J. (1980)
The prediction of turbulent flow and heat transfer over backward facing steps.
Computer Method in Fluids, Pentech Press London. p.p 309-338

OLSEN M.D., TUAMN S.Y. (1976)
Primitive variable verus stream function in finite element solution of Navier-Stokes equation.
Finite Element Method in Flow Problem, S.Margherita Ligure p.p 57-68

PICONE M. (1928)
Rend. Circ. Mat. Palermo 52, p.p 225-253

PATANKAR S.V., SPALDING D.R. (1972)
A calculation procedure for heat and mass momentum transfer in three dimensional parabolic flow.
Int. J. of Heat and Mass Transfer, Vol. 15 p.p 1787-1806

PFOERTNER H., RAABE J. (1977)
Solution of flow problem with boundaries by two and three dimensional isoparametric finite element.
PROC. 17th Congress of the IAHR Vol 2 paper A138 p.p 499-505

REBERNIK B. (1972)
Investigation on induced vorticity in vaneless diffusers of radial flow pumps.
Proceedings of the Fourth Conference on Fluid Machinery BUDAPEST p.p 1129-1140

RODI W., SPALDING D.R. (1970)
A two parameter model of turbulence and its application to free jets.
Turbulence transport modeling AIAA 1973

RODI W. (1975)
A new method of analysing hot-wire signals in highly turbulent flow, and its evaluation in a round jet.
DISA Information No.17 February p.p 9-18

SAKAI T., WATANABE I., TSUKAGOSHI K. (1971)
Investigation concerning the fluid flow in the mixed flow diffuser.
ASME paper 71-GT-40

SAKAI T., MIZAKI S., WATANABE I. (1971)
A study on flow pattern within the centrifugal and mixed flow impellers.
ASME paper 71-GT-41

SAKAI T.,SANBE M., NAKAYAMA T. (1978)
Experimental study on diffusers for mixed flow machine.
ASME paper 78-GT-120

SAUSTRUP KRISTENSEN H. (1973)
Hot-wire measurements in turbulent flows.
DISA InformationDepartment November

SANDBORN V.A., KLINE I.J. (1961)
Flow Models in boundary layer stall inception.
J. of Basic Engineering, Sept. p.p 317-328

SCHNEIDER G.E., RAITHBY G.D., YOVANOVICH M. (1978)
Finite element analysis of incompressible fluid flow incorporating equal order pressure and velocity interpolation.
Inter. Conf. Numerical Method in Laminar and Turbulent Flow.
University of SWANSEA p.p 89-102

SENOO Y., KINOSHITC Y. (1977a)
Influence of inlet flow conditions and geometrics of centrifugal vaneless diffusers on critical flow angle for reverse flow.
J. of Fluid Engineering March p.p 99-103

SENOO Y., KINOSHITC Y., ISHIDA M. (1977b)
Asymmetric flow in vaneless diffuser of cenrifugal blowers.
J. of Fluid Engineering March p.p 104-113

SENOO Y., KINOSHITC Y. (1978)
Limits of rotating stall and stall in vaneless diffuser of centrifugal compressors.
ASME paper 78-GT-19

SHEORAN Y. TABAKOFF W. (1982)
A study of viscous flow in stator and rotor passages.
ASME paper 82-GT-248

SPALDING D.B., PATANKER S.V. (1967)
HEAT MASS TRANSFER IN BOUNDARY LAYERS.
LONDON Morgan Granpian.

STARSMORE N. (1977)
Of a fence immersed in a boundary layer.
Ph.D Thesis BATH University

TAYLOR C., HOOD P. (1973)
A numerical solution of the Navier-Stocks equations using Finite Element technique
Computer and Fluid Vol. 1 p.p 73-100

TAYALOR C., HUGHES T.C., MORGAN K. (1977)
A numerical analysis of turbulent flow in pipe.
Computer and Fluid Vol. 5 p.p 191-204

TAYLOR C., HARPER J.J., HUGHES T.G., MORGAN K.(1978a)
An analysis of developing turbulent flow in a circular pipe by the finite element method.
Int. conf. of Numerical Method in Laminar and Turbulent Flow
University of SWEANSEA

TAYLOR C., HUGHES T.C., MORGAN K.(1978b)
Finite element solution of one equation model of turbulent flow.
J. of Comutational Physics No. 29 p.p. 163-172

TAYLOR C., THOMAS C.E., MORGAN K.(1980)
Confined turbulent flow utilising the finite element method.
ASME A.M.D. Vol. 34 p.p. 213-224

TAYLOR C., HUGHES T.G. (1981)
FINITE ELEMENT PROGRAMMING OF THE NAVIER-STOKES EQUATIONS.
Pineridge Press L.T.D THOMAS C.E., MORGAN K., TAYLOR C.(1981)
A finite element analysis of flow over a backward facing step.
Computer and Fluid Vol.9, p.p. 265-279

VAN DRIEST E.R. (1956)
On turbulent flow near a wall
J. Aero. Sci. 23 p.p 1007-1011

VOLOV V.T., SHAKHOV V.G. (1978)
Study of radial diffusers with flow swirl.
Soviet Aeronautics, Vol. 21 No.3 p.p 111-112

VOORDE C.B., BOS J. (1972)
Measured and caculated turbulent boundary layer flow in a vaneless radial diffuser.
AGARD-164-1972 p.p 293-310

VRIES G., BALASUBRAMANIAN R., NORRIE D.H. (1974)
The application of the pseudo-functional finite element method to viscous flow problem.
Fifth Australasian Conf. on Hydraulics and Fluid Mechanics p.p 561-571

WALLACE F.J., ATKEY R.C., WHITFIELD A. (1975)
A psedudo three dimensional analysis of flow in vaneless diffuser for mixed flow compressors.
J. of Mechanical Engineering Science Vol.17 No.6 p.p 348-356.

WACHZPZESS E.L. (1975)
A "RATIONAL" FINITE ELEMENT BASIS.
Academic Press Inc. N.Y., San Francisco, London

WATSON N., INGHAN D.R. (1971)
Compressible flow in radial vaneless diffuser.
Symposim on Internal FlowSALFORD University paper 8 p.p 56-65

WHITFIELD A., WALLACE F.J., ATKEY R.C. (1976)
The effect of variable geometry on operating range and surge margin of centrifugal compressor.
ASME paper 78-GT-98

WHITFIELD A., ATKEY R.C., WALLACE F.J. (1979)
The design and performance of vaneless curved annular diffusers for mixed flow turbocharger compressor.
Presented at the Isreal Joint Gas Turbine Congress, Haifa, ISREAL.

WOLFSHTEIN M. (1967)
Convection process in turbulent impinging jet.
Ph.D Thesis University of LONDON

WU Ch. H. (1952)
A general theory of three dimensional flow in subsonic and supersonic turbomachines of Axial, Radial and Mixed flow types.
NASA report TN2604

YAMAMOTO A. (1978)
A method for calculating laminar and turbulent swirling flow in cylindrical annuli
MSc. Thesis CARLETON University

ZIENKIEWICZ O.C., GULLAGHER R.H., HOOD P. (1975)
Newtonian and non-newtonian viscous incompressible flow temperature induced flow.
MAFFLAP by WHITEMAN p.p 235-267

ZIENKIEWICZ O.C. (1978)
THE FINITE ELEMENT METHOD
McGraw Hill L.T.d

APPENDIX 1

THE FINITE ELEMENT METHOD

1A1 THE NATURE OF THE FINITE ELEMENT METHOD

The finite element method has been developed for solving general continuum problems. A discretization of the continum through the finite element
can give an approximate for all problems of motion of continuous media, linear or non-linear, steady or unsteady, and in particular flow problems.

The finite element method is applied to a variational equivalent or an integral equivalent of a differential equation and does not use the differential equation directly.

The mathematical background of the finite element method has been given by many investigators such as ODEN(1971), CHUNG(1978), ZIENKIEWICZ(1978).

The formulation of physical problems leads in most cases to an equation of the type

$$\frac{\partial \phi}{\partial t} + A\phi = g \qquad \text{in all the domain } (D)$$

and (1A.1)

$$B\phi = 0 \qquad \text{on the boundary } (\partial D)$$

where A is an operator with partial derivatives, and B is an operator of the first order which does not cover the operator A. The vector valued function Φ has to satisfy, inside the domain D, the field equation, and on the boundary ∂D the boundary condition.

The finite element solution for such a problem requires the following basic assumptions:

a) Any domain can be divided into small elements which are interconnected at a discrete number of points known as nodes. These are the basic points for the unknown parameters to the problem.

b) Inside the domain the physical and geometrical variables can be describe by a selected base interpolation which is referred to as the "shape function". Therefore for the whole domain all the

the variables in the basic equation can be represented as

$$\phi = \sum_{i=1}^{m} \phi_i N_i(r,z)$$
$$r = \sum_{i=1}^{m} r_i N_i(r,z) \qquad (1A.2)$$
$$z = \sum_{i=1}^{m} z_i N_i(r,z)$$

where N is the interpolation function

and m is the total number of mesh points.

This set of base functions is chosen to define uniquely the state of physical and geometric variables inside the element as a function of the nodal values. The functions have to be continuous and to have a first derivative inside the element and on the boundary. If the definitions of the element geometry and the base function are such that realization of this condition at the node and the boundary is satisfied, the element is said to be conforming. Another condition for base functions, which is sufficient but not always necessary, is that for convergence of the finite element method, when the size of element tends to zero, the base functions must be able to represent any constant value of the field variables and derivatives.

The choice of different base functions for each variable defines the type of element used, such as

a) A subparametric element, is an element in which the

physical variable uses more nodes to define it than is necessary for the element.

b) An isoparametric element, is an element in which the shape function used for physical and geometric variables are the same.

c) A superparametric element, is an element in which the variation of geometry is represented by more nodes than that for the physical unknown.

The choice of the shape function is tied to the type of element as well as to the number of nodes within each element. Although many functions can be found satisfying the finite element condition, in most cases the theory of the piecewise polynomial interpolation function is used. This can be divided into two main groups a) For continuity the shape function will be continuous across the element boundary but not the derivatives, b) Elements with shape function which their first derivative will be also continuous.

1A2 TYPES OF ELEMENT

The different types of element are shown in fig. 1A.2. The decision as to which type of element to use is not straight forward and depends largely upon the particular problem and geometry involved. A small number of simple

triangular elements may in many cases lead to a satisfactory solution. If, however, a high degree of accuracy is required it is necessary to employ a more complicated element or a large number of simple elements. The relative merits of type and number of element has to be assessed for each particular problem, considering both the required accuracy and computation time involved.

1A2.1 Linear triangular elements

A linear triangular element is used extensively in the application of the variational method and is therefore described here in detail. A typical triangular element defined by node i,j,k is shown in fig. 1A.3. The value of the variable Φ can be uniquely specified in the element by the values at its three nodes and a linear interpolation function of the coordinates r,z.

Thus within the element

$$\phi = a_i\phi_i + a_j\phi_j + a_k\phi_k \qquad (1A.3)$$

where a_i a_j a_k are functions of the coordinates r and z

and $a_i = b_i + c_i*r + d_i*z$

where

$$b_i = (r_j*z_k - r_k*z_j)/2d$$

$$c_i = (z_j - z_k)/2d$$

$$d_i = (r_k - r_j)/2d$$

and d =area of triangle i j k.

In the triangle i j k the interpolation function is linear, for this reason the first derivative is constant and can be calculated by

$$\frac{\partial Q}{\partial r} = \frac{1}{2d}\left[Q_i(z_k - z_j) + Q_j(z_i - z_k) + Q_k(z_j - z_i)\right]$$
$$\frac{\partial Q}{\partial z} = \frac{1}{2d}\left[Q_i(r_j - r_k) + Q_j(r_i - r_k) + Q_k(r_j - r_i)\right] \qquad (1A.4)$$

1A2.2 Isoparametric elements

The application of the finite element method for problems with curved boundary shapes leads to the necessity to use isoparametric elements with curve sides instead of a large number of linear elements. These elements, are widely used in the finite element method, see IRON et.al(1968), ZIENKIEWICZ(1978), and many other investigators use quadratic or higher order shape functions to specify the shape of the element sides.

In this work Lagrangian isoparametric elements were used when the Galerkin method was applied. The element had nine nodal points and a quadratic function described the shape of the element. By using a normalized coordinate system for each element the value of the axes in the

element varied between -1 to +1, see fig. 1A.4.

The shape function selected was a commonly used second order polynomial, see ZIENKIEWICZ(1978) which yield

$$N_i = \frac{1}{4}(1+\xi_0)(1+\eta_0)\xi_0\eta_0$$

for nodes 1, 3, 5, 7

$$N_i = \frac{1}{2}(1+\xi_0)(1-\eta^2)\xi_0$$

for nodes 2, 6

$$N_i = \frac{1}{2}(1+\eta_0)(1-\xi^2)\eta_0$$

for nodes 4, 8

$$N_i = (1-\xi^2)(1-\eta^2)$$

for node 9

where $\xi_i\xi = \xi_0$ and $\eta_i\eta = \eta_0$

and ξ_i , η_i is the coordinate of node point i.

The shape function should be 1 at the node point and zero at other nodes. This condition satisfies the convergence criterion of the finite element method.

The coordinates at any point within the element are given by

$$\xi = \langle N_1, N_2 \ldots\ldots N_m \rangle \begin{Bmatrix} \xi_1 \\ \xi_2 \\ \vdots \\ \xi_m \end{Bmatrix} \qquad (1A.5)$$

Once the shape functions are known in the normalized coordinates they must be transformed into the global coordinates system. This can be carried out by using the

rule of partial differentiation i.e.

$$\frac{\partial N_i}{\partial \xi} = \frac{\partial N_i}{\partial r}\frac{\partial r}{\partial \xi} + \frac{\partial N_i}{\partial z}\frac{\partial z}{\partial \xi} \qquad (1A.6)$$

Doing the same differentiation with respect to the η coordinate and writting it in a matrix from gives

$$\begin{Bmatrix} \frac{\partial N_i}{\partial \xi} \\ \frac{\partial N_i}{\partial \eta} \end{Bmatrix} = \begin{bmatrix} \frac{\partial r}{\partial \xi} & \frac{\partial z}{\partial \xi} \\ \frac{\partial r}{\partial \eta} & \frac{\partial z}{\partial \eta} \end{bmatrix} = [J] \begin{Bmatrix} \frac{\partial N_i}{\partial r} \\ \frac{\partial N_i}{\partial z} \end{Bmatrix} \qquad (1A.7)$$

The matrix [J] is known as the Jacobian matrix and can be calculated explicity in terms of the local coordinates. More detail about this transformation and the Jacobian matrix can be found in ABIR(1978), ZIENKIEWICZ(1978).

1A3 THE APPROXIMATION METHOD FOR SOLUTION.

The most general method for obtaining an integral formulation equivalent to the basic equation are:

a) The Variational method

b) The method of Weighted Residuals.

1A3.1 The Variational Method

The variational method is based on the principle that a physical law can often be deduced from concise mathematical principles, to the effect that certain

integrals attain extreme values.

Define a scalar functional χ which can be written as

$$\chi = \int_{O} F\left(\phi, \frac{\partial \phi}{\partial x}, \ldots .\right) dD + \int_{\partial D} E\left(\phi + \frac{\partial \phi}{\partial x} \ldots\right) ds$$

where F and E are specified operators.

This functional has to satisfy the differential equation 1A.1 and the solution is a function of Φ which makes χ stationary (miminised) with respect to small changes of Φ, $\delta\Phi$. This minimisation is necessary to satisfy the prerequisite of the continuity of Φwhich is defined at the nodal points. When minimising the functional it is only necessary to have conditions for a typical element, and the effect of other elements on the general minimisation equation will be in an identical pattern. To obtain the general equation it is necessary to add the contribution of all the elements in the domain. If the equivalent functional is a function of the nodal value Φ_i then the minimising of χ with respect to Φ_i is:

$$\frac{\partial \chi}{\partial \phi_i} = 0 \qquad (1A.8)$$

and the general solution for all the domain is obtain by

$$\sum_{k=1}^{e} \frac{\partial \chi^k}{\partial \phi_i} = 0$$

where e is the number of elements in the domain.

Equation 1A.8 creates a set of linear simultaneous equations, where the number of equations is equal to the total number of nodes. This set of equations can be represented by

$$\frac{\partial \chi}{\partial \phi} = \begin{Bmatrix} \frac{\partial \chi}{\partial \phi_1} \\ \frac{\partial \chi}{\partial \phi_2} \\ \vdots \\ \frac{\partial \chi}{\partial \phi_m} \end{Bmatrix} = 0 \qquad (1A.9)$$

1A3.2 The Weighted Residuals Method

In many physical phenomena, a variational principle either does not exist or its existence is not obvious, then the Weighted Residual method can be applied.

Consider a general non-linear differential equation as equation 1A.1 with two types of boundary condition, Dirichelet and Neuman. Trial function Φ can be approximated over the whole domain by

$$\phi^* = \phi_D + \sum_{i=1}^{m} C_i Q_i \qquad (1A.10)$$

where c_i is a function described in terms of independent variables such as the coordinates. Φ_D is prescribed and satisfies the boundary condition where $\Phi_i = 0$

The function Φ^* satisfies the differential equation as an approximate solution within an error or residual R i.e.

$$R = A(\phi^*) - g \neq 0 \qquad (1A.11)$$

The residual R is the zero when Φ^* is the exact solution. The best solution will be one which reduces the residual to a small value at all points in the domain. An obvious way to achieve this the condition is to find a set of "arbitrary" weighting functions M such that over the whole domain

$$\int_D M \cdot R \cdot dD = 0 \qquad (1A.12)$$

Since there are n unknowns it is necessary to have a set of n weight functions and equation 1A.12 can be rewritten as

$$\int_D M_j R \, dD = \int_D M_j (A(\phi^*) - g) dD = 0 \qquad (1A.13)$$
$$j = 1, \ldots n$$

The integration of equation 1A.13 leads to a set of algebraic equations equal in number to the number of nodes in the domain.

The choice of the Weighting functions corresponds to various criteria of the method, such as:

a) The point collection method developed by FRAZER(1937).

b) The least square method which has been presented by PICOME(1928). He used the weighting function $d(\Phi^*)/dC_i$, the corresponding interpretation is that the mean square residual

$$I = \int_D [R(\phi^*)]^2 dD$$

must be minimized with respect to the constant Ci.

c) The Galerkin method was developed first by GALERKIN(1915) and is the most widely used technique for the weighted residual method. The weight functions are chosen to be equal to the shape function N of the variable, that is

$$M = N$$

For all the different methods the only limitation is that the weight function must be positive, single valued and finite.

1A.4 THE "UPWIND" METHOD

The differential operator A in equation 1A.1 includes in elliptic problems, terms of the first and second derivative. In some cases the first derivative becomes significant and difficulties with respect to the stability of the numerical solution occurs. The instability of the solution occurs because the matrix of coefficients (after the problem transfer to a set of linear equations) cease to be diagonally dominant.

In finite difference methods this problem has led to the development of the "upwind difference schemes" as presented by GOSMAN et. al(1969), SPALDING(1969) and

other investigators. This procedure has been applied in the finite element when using a weight residual formulation such as the Galerkin-Petrov method by many authors e.g. CHRISTIC et.al(1977), ZIENKIEVICZ(1978). The "upwind method" ensure that the matrix of coefficients will remain diagonal dominant, therefore a solution can be obtained to the problem.

To explain the principle of the upwind method first consider of one dimensional problem given by

$$Q\frac{\partial\phi}{\partial X} - \frac{\partial^2\phi}{\partial X^2} = 0 \qquad (1A.14)$$

and let Q be a function of Φ

Equation 1A.14 can be written in the finite difference way as

$$(1-\tfrac{Q}{2})\phi_{i+1} - 2\phi_i + (1+\tfrac{Q}{2})\phi_{i-1} = 0 \qquad (1A.15)$$

If γ is defined as a control parameter of distortion equation 1A.15 can be rearrange to

$$\left[1+(1+\gamma)\tfrac{Q}{2}\right]\phi_{i-1} - 2(1+\gamma Q)\phi_i + \left[1+(\gamma-1)\tfrac{Q}{2}\right]\phi_{i+1} = 0 \qquad (1A.16)$$

It can be seen that γ can be equal to -1,0,+1, then equation 1A.16 is identical to a backward, central or forward finite difference solution. Thus for a diagonally dominant problem the exact difference solution is of the form

$$\phi_i = A + B\left[\frac{1+(\gamma+1)\frac{Q}{2}}{1-(\gamma-1)\frac{Q}{2}}\right]_i \qquad (1A.17)$$

where A and B are constant.

The solution is not oscillatory if $\gamma = 0$ and $Q < 2$, or when $Q > 2$ and $\gamma > 1-2/Q$ (1A.18)

For a two dimensional problem the solution will not be oscillatory if $Q < 4$ or $\gamma_1 > 1-4/Q$ (1A.19)

where γ_1 is the control parameter of distortion in the Y direction. By keeping the conditions of equations 1A.18, 1A.19 a finite element or finite difference solution will converge without oscillation.

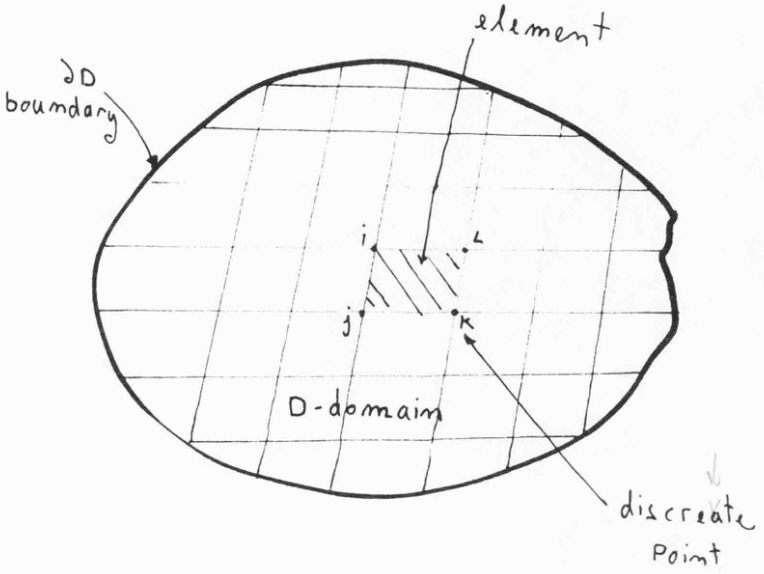

FIGURE 1A.1: Two dimensional domain divided into elements.

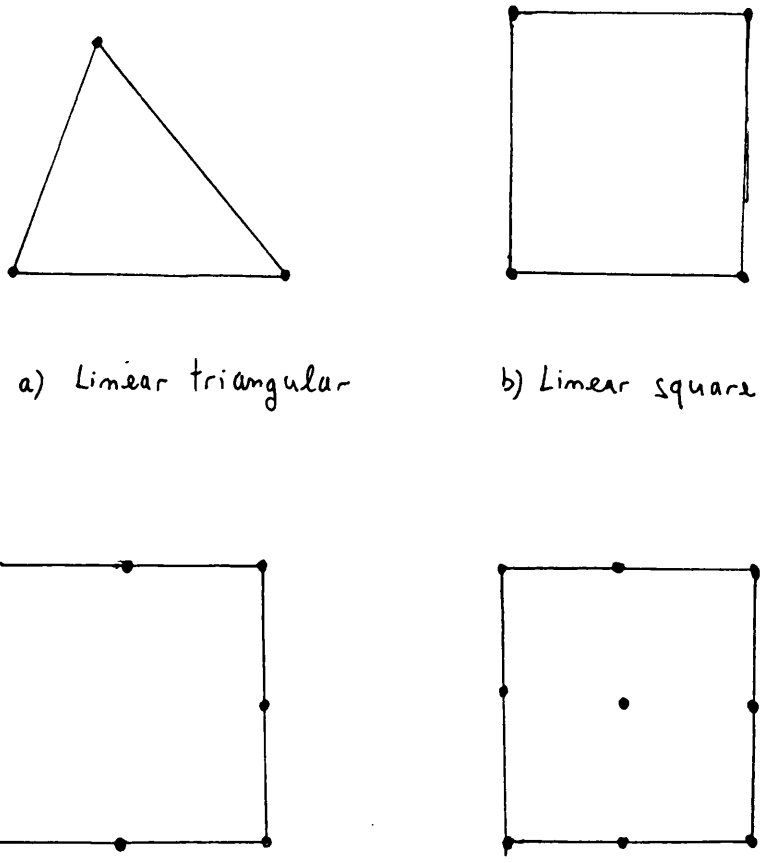

FIGURE 1A.2: Different types of element.

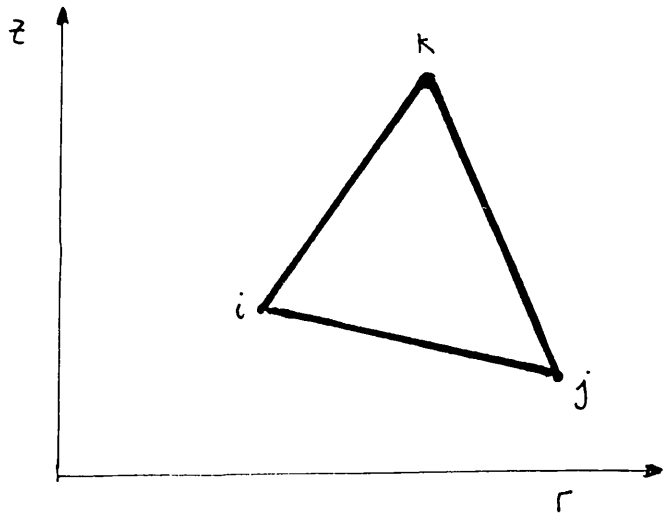

FIGURE 1A.3: A triangular element.

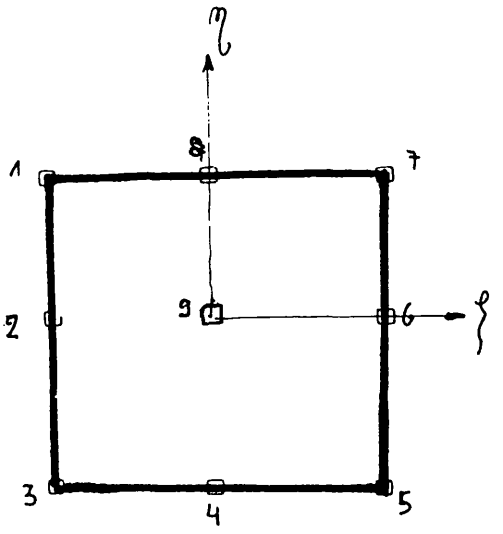

FIGURE 1A.4: A Lagrangian element.

APPENDIX 2

THE TURBULENT FLOW DIFFERENTIAL EQUATIONS AND TURBULENCE MODELLING.

The definition of turbulence is given by HINZE(1959) as "Turbulent fluid motion is an irregular condition of flow in which the various quantities show a random variation with time and space coordinates so that statistically distinct average values can be discerned". Turbulence can be generated by friction forces at fixed walls or by the flow of layers of fluids with different velocities past or over one another. By using this definition an average mathematical model to the problem of turbulent flow can be developed.

The Navier-Stokes equations for a compressible viscous flow and perfect gas may be written in the following form

$$\frac{\partial}{\partial t}(\rho \tilde{u}_i) + \frac{\partial}{\partial x_j}(\rho \tilde{u}_i \tilde{u}_j) = -\frac{\partial \tilde{P}}{\partial x_i} + \frac{\partial \tilde{\tau}_{ij}}{\partial x_j}$$

$$\frac{\partial \rho}{\partial t} + \frac{\partial}{\partial x_j}(\rho \tilde{u}_j) = 0 \qquad (2A.1)$$

where the stress tensor τ_{ij} is given by

$$\tilde{\tau}_{i,j} = -\frac{2}{3}\mu \delta_{i,j} \frac{\partial \rho_i}{\partial x_i} + \mu\left(\frac{\partial \tilde{u}_i}{\partial x_j} + \frac{\partial \tilde{u}_j}{\partial x_i}\right)$$

where δ_{ij} is the Kronecker delta having the value of 1 for i=j and 0 for i not equal j.

Equation 2A.1 can be applied to laminar as well as to turbulent flows. For turbulent flow it is necessary to replace the dependent variables by their instantaneous values as

$$\tilde{U} = U + u'$$

$$\tilde{P} = P + p'$$

where u' and p' are the velocity and pressure fluctuation terms, and U and P are the average values.

The usual approach used to solve turbulent flow is to time average the instantaneous equations and to solve the resulting equations for the time average quantities U and P. The time average quantities can be expressed as

$$U = \frac{1}{\Delta t_{12}} \int_{t_1}^{t_2} u(t)\, dt$$

and (2A.2)

$$\overline{u_i' u_j'} = \lim_{\Delta t_{12} \to \infty} \frac{1}{\Delta t_{12}} \int_{t_1}^{t_2} u_i'(t)\, u_j'(t)\, dt$$

Equation 2A.1 can be modify to a time average equation for axisymmetric flow with constant density to yield

$$U_r \frac{\partial U_r}{\partial r} + U_z \frac{\partial U_r}{\partial z} - \frac{U_\theta^2}{r} = -\frac{1}{\rho}\frac{\partial P}{\partial r} + \frac{\mu}{\rho}\left[\frac{1}{r}\frac{\partial}{\partial r}\left(r\frac{\partial U_r}{\partial r}\right) - \frac{U_r}{r^2}\right] + \frac{\mu}{\rho}\frac{\partial^2 U_r}{\partial r^2} - \frac{1}{r}\frac{\partial}{\partial r}\left(r\,\overline{u_r'^2}\right) - \frac{\partial}{\partial z}\left(\overline{u_r' u_z'}\right) + \frac{\overline{u_\theta'^2}}{r}$$

$$U_r \frac{\partial U_z}{\partial r} + U_z \frac{\partial U_z}{\partial z} = -\frac{1}{\rho}\frac{\partial P}{\partial z} + \frac{\mu}{\rho}\frac{1}{r}\left(r\frac{\partial U_z}{\partial r}\right) + \frac{\mu}{\rho}\frac{\partial^2 U_z}{\partial z^2} - \frac{1}{r}\frac{\partial}{\partial r}\left(r\,\overline{u_r' u_z'}\right) - \frac{\partial}{\partial z}\left(\overline{u_z'^2}\right) \quad (2A.3)$$

$$U_r \frac{\partial U_\theta}{\partial r} + U_z \frac{\partial U_\theta}{\partial z} + \frac{U_r U_\theta}{r} = \frac{\mu}{\rho}\left[\frac{1}{r}\frac{\partial}{\partial r}\left(r\frac{\partial U_\theta}{\partial r}\right) - \frac{U_\theta}{r}\right] + \frac{\mu}{\rho}\frac{\partial^2 U_\theta}{\partial z^2} - \frac{\partial}{\partial r}\overline{u_r' u_\theta'} - \frac{\partial}{\partial z}\left(\overline{u_z' u_\theta'}\right) - \frac{2\,\overline{u_r' u_\theta'}}{r}$$

$$\frac{\partial}{\partial z}\left(r U_z\right) + \frac{\partial}{\partial r}\left(r U_r\right) = 0$$

There are now more unknown variables than equations available for solution, for this reason further assumptions have to be made to eliminate the turbulence components from the transport equations.

Most of the present day methods for modelling turbulent flows are based upon the turbulent viscosity model, where all the Reynolds stresses could be significant (see HINZE(1959)) which leads to

$$
\begin{aligned}
\rho \overline{u_r' u_z'} &= -\mu_t \left(\frac{\partial u_z}{\partial r} + \frac{\partial u_r}{\partial z} \right) \\
\rho \overline{u_z' u_\theta'} &= -\mu_t \left(\frac{\partial u_\theta}{\partial z} \right) \\
\rho \overline{u_r' u_\theta'} &= -\mu_t \left(r \frac{\partial}{\partial r} \left(\frac{u_\theta}{r} \right) \right) \\
\rho \overline{u_z'^2} &= -\mu_t 2 \frac{\partial u_z}{\partial z} + \delta_t \\
\rho \overline{u_r'^2} &= -\mu_t 2 \frac{\partial u_r}{\partial r} + \delta_t \\
\rho \overline{u_\theta'^2} &= -\mu_t 2 \frac{u_r}{r} + \delta_t
\end{aligned}
\qquad (2A.4)
$$

where the term δ_t is according to HINZE, "an average turbulence pressure" needed to ensure that the sum of the normal stresses is non-zero in the terms of the Kronecker delta.

In this way the differential equation changes a problem dependent upon the Reynolds stresses to a problem based on the unknown turbulent viscosity. The turbulent viscosity in equation 2A.4 is introduced as a scalar, but OLIVER(1975) and YAMAMOTO(1980) indicated that the

turbulent viscosity is not necessarily a scalar especially of cases of strongly swirling flows. There are several ways to introduce the turbulent viscosity (or to calculate its value) and the most popular method is discussed in the next section.

2A1 THE TURBULENCE MODEL.

The turbulence models can be classified into two main categories,

a) The algebraic method.

b) The differential method.

The algebraic model is simple and does not introduce any further dependent variables because the turbulent viscosity is defined in terms of mean velocity gradients. The differential model however is based on the turbulence properties from the solution of a differential transport equation.

2A1.1 Algebraic model.

The algebraic model is based on Prandtl's mixing length hypothesis which introduces the turbulence viscosity as

$$\mu_t = \rho l \left| \frac{\partial u}{\partial y} \right| \qquad (2A.5)$$

where l is a length scale known as the mixing length given by (see SPALDING and PATANKAR(1967))

$$l = \kappa y \left[1 - \exp\left(-y^+/A\right)\right] \qquad \kappa y \le \lambda\delta$$

$$l = \lambda\delta \qquad \kappa y > \lambda\delta$$

with κ=0.4, A=26, λ=0.09 and δ is the boundary layer thickness. y is the distance in the direction prependicular to the surface.

This model was first introduced by VAN-DRIEST(1956) and derived from Prandtl's mixing length hypothesis for predicting boundary layer flows with zero pressure gradient. VAN-DRIEST assumed that near a wall the value of the shear stress equals the shear stress on the wall, and used the follow equation to represent the viscosity.

$$\frac{\mu_{eff}}{\mu} = 1 + \left\{1 + 4\left[\kappa y^+ \left(1 - \exp\left(-y^+/A^+\right)\right)\right]^2\right\}^{\frac{1}{2}} \qquad \kappa y \le \lambda\delta$$

$$\frac{\mu_{eff}}{\mu} = \frac{\lambda\delta u_\tau}{\nu} >> 1 \qquad \kappa y > \lambda\delta \qquad (2A.6)$$

This model and the mixing length hypothesis has been widely used in finite difference methods, HUTTON(1971),

and finite element approach, TAYLOR(1978).

2A1.2 The differential method

The differential method uses the Prandtl-Kolmogorov equation for the turbulent viscosity

$$\mu = \rho l k^{\frac{1}{2}} \qquad (2A.7)$$

where k is the turbulent kinetic energy, and l the mixing length.

If the rate of dissipation of turbulence is introduced as

$$\varepsilon = \frac{C_\mu k^{3/2}}{l_D} \sim \frac{C_\mu k^{3/2}}{l} \qquad (2A.8)$$

where l_D is the lenght scale.

the turbulent viscosity become

$$\mu_t = \frac{C_\mu \rho k^2}{\varepsilon} \qquad (2A.9)$$

where C_μ is an experimental constant.

Equation 2A.9 developed by RODI(1970) is based on the turbulence property from the solution of a differential transport equation. The model called the k-ϵ model which uses the kinetic energy of turbulence (k) and the rate of dissipation of turbulence (ϵ).

The equation for k may be obtained from the time dependent Navier-Stokes equations by the following method. Multiply each of the instantaneous Navier-Stokes equations by its corresponding instantaneous velocity,

then sum the resulting equations and time average. Subtract the sum of the equations formed by multiplying each of the time averaged Navier-Stokes equations by its corresponding average velocity.

The terms with turbulence components and it must be modified to introduce the basic variables of average velocity and pressure. Using equations 2A.4, which introduces the shear stress terms $\overline{u'_i u'_j}$ as products of turbulent viscosity, and assuming that the turbulent diffusion terms are represented by the diffusive transport of k, see WOLFSHTEIN(1967) given by the product of the spatial gradient of k and effective turbulent diffusively of k, $(\frac{1}{\rho}\frac{\mu_t}{\sigma_k})$ where σ_k is a form of Prandtl number for the diffusion of turbulence energy, the final equation can be written as

$$U_r\frac{\partial k}{\partial r} + U_z\frac{\partial k}{\partial z} = \frac{\mu}{\rho}\left[\frac{\partial^2 k}{\partial z^2} + \frac{1}{r}\frac{\partial}{\partial r}\left(r\frac{\partial k}{\partial r}\right) - \frac{1}{\rho}\left(\frac{\mu_t}{\sigma_k}\frac{\partial k}{\partial z}\right) - \frac{1}{\rho r}\frac{\partial}{\partial r}\left(\frac{\mu_t}{\sigma_k} r\frac{\partial k}{\partial r}\right)\right]$$
$$+ \left\{2\left(\frac{\partial^2 U_z}{\partial z^2}\right) + 2\left(\frac{\partial U_r}{\partial r}\right)^2 + \left(\frac{\partial U_\theta}{\partial z}\right)^2 + \left(\frac{\partial U_z}{\partial r} + \frac{\partial U_r}{\partial z}\right)\right. \qquad (2A.10)$$
$$\left. + \left[r\frac{\partial}{\partial r}\left(\frac{U_\theta}{r}\right)\right]^2 + 2\left(\frac{U_r}{r}\right)^2\right\} - C_\mu K^{3/2}/\ell_D$$

where l_D is the turbulence dissipation length scale.

The equation for the rate of dissipation of turbulence energy (ϵ) can also be constructed using the

Navier-Stokes equation modelled by HARLOW (see RODI(1970)),

and using the same assumptions as for the k equation, the transport equation becomes

$$U_r\frac{\partial\varepsilon}{\partial r}+U_z\frac{\partial\varepsilon}{\partial z}=\frac{\mu}{\rho}\left[\frac{\partial^2\varepsilon}{\partial z^2}+\frac{1}{r}\left(r\frac{\partial\varepsilon}{\partial r}\right)-\frac{1}{\rho}\left(\frac{\mu_t}{\sigma_\varepsilon}\frac{\partial\varepsilon}{\partial z}\right)-\frac{1}{\rho r}\frac{\partial}{\partial r}\left(\frac{\mu_t}{\sigma_t}r\frac{\partial\varepsilon}{\partial r}\right)\right]$$
$$+C_1\frac{\mu_t}{\rho}\frac{\varepsilon}{k}\left\{2\left(\frac{\partial^2 U_z}{\partial z^2}\right)+\left(\frac{\partial U_z}{\partial r}+\frac{\partial U_r}{\partial z}\right)^2+2\left(\frac{\partial U_r}{\partial r}\right)^2+\left(\frac{\partial U_\theta}{\partial z}\right)^2\right. \qquad (2A.11)$$
$$\left.+\left[r\frac{\partial}{\partial r}\left(\frac{U_\theta}{r}\right)\right]^2+2\left(\frac{U_r}{r}\right)^2\right\}-C_2\varepsilon^2/k$$

The coefficients in equations 2A.10 and 2A.11 can be obtain from experimental data and are assumed to be

$C_\mu = 0.09$, $\sigma_k = 1.0$, $\sigma_\varepsilon = 1.0$, $C_1 = 1.47$, $C_2 = 2.0$

Equations 2A.10 and 2A.11 give a set of differential equations which model turbulent as well as laminar flow and can be used for obtaining solutions for both cases.

2A.2 THE LOGARITHMIC LAW OF THE WALL.

The total shear stress in the turbulent boundary layer with zero pressure gradient can be written as (see CEBECI(1974))

$$\tau = \tau_l + \tau_t = \mu\frac{\partial u}{\partial y} - \rho\overline{u'v'} \qquad (2A.12)$$

By assuming that the laminar shear stress (τ_1) is small

compared to the turbulent shear stress (τ_t) in the part of the inner region where the flow is fully turbulent and by substituting the expression

$$\overline{u'v'} = \mu_t \left(\frac{\partial u}{\partial y}\right) \qquad (2A.13)$$

and using the eddy viscosity relation $\mu_t = \kappa U_\tau y$ (where U_τ is the friction velocity on the wall) equation 2A.13 yields

$$\kappa u_\tau y \left(\frac{\partial u}{\partial y}\right) = u_\tau^2 \qquad (2A.14)$$

where κ is Van Karman mixing lenght constant.
Integration yields

$$\frac{u}{u_\tau} = \left(\frac{1}{\kappa}\right) \ln\left(\frac{y u_\tau \rho}{\mu}\right) + C \qquad (2A.15)$$

where C is a constant and found from experimental work to be approximately 5.5.

Equation 2A.15 describes the velocity distribution in the boundary layer near the wall. By knowing the value of the velocity at distance y from the wall the friction velocity can be calculated.

APPENDIX 3

HOT-WIRE ANEMOMETER

3A.1 INTRODUCTION

The hot-wire anemometer has been used for many years in the measurement of mean and fluctuating velocities in turbulent and laminar flows. This technique depends on the convective heat loss from an electrically heated probe to the surrounding fluid. Assuming that only the velocity of fluid varies the heat loss can be interpreted as a direct measure of the velocity. If the heat loss is represented by the output of the anemometer bridge for a constant fluid temperature the mathematical expression can be written as

$$E^2 = A + B U_{eff}^{n} \qquad (3A.1)$$

where U_{eff} is the effective cooling velocity component which can be expressed as (see fig. 3A.1)

where $$U_{eff}^2 = U_x^2 + k_1 U_y^2 + k_2 U_z^2 \qquad (3A.2)$$

$$U_{eff}^2(\beta) = U^2(0)\left[\cos^2\beta + k_1^2 \sin^2\beta\right] \qquad \text{For } \theta = 0$$

$$U_{eff}^2(\theta) = U^2(0)\left[\cos^2\theta + k_2^2 \sin^2\theta\right] \qquad \text{For } \beta = 0$$

3A.2 HOT-WIRE CALIBRATION

The basic problem in hot-wire analysis is to relate the velocity components to the measured hot-wire signal. To do this it is necessary to calibrate the anemometer output voltage against a known flow velocity.

Generally probes were calibrated in an open test section of a low speed wind tunnel, with a probe orientation of both pitch angle and yaw angle equal to zero (β=0, Θ=0). By following the recommendations of KINNS(1972) and STARSMORE(1977) the parameter A, equation 3A.1, was assumed to be given by $A = 0.92 * E_0$, where E_0 is the anemometer output with zero flow. Rearranging and taking logarithms of equation 3A.1 yields

$$\mathrm{Log}(\Delta E^2) = \mathrm{Log}(B') + n\,\mathrm{Log}(U_{eff}) \qquad (3A.3)$$

where

$$\Delta E^2 = (E^2/(0.92E_0)^2) - 1$$

$$B' = B/(0.92E_0)^2$$

Plotting Log(ΔE^2) against Log(U_{eff}) should, according to equation 3A.3 yield a straight line. The exponent power n can then be found from the slope of the line. It was, however, recommend to calculate the exponent for each interval of 10 m/sec in the calibration curve. A typical example of a calibration curve is shown

in fig. 3A.2.

By rotating the probe about the Y and Z axes, the anemometer output voltage was read as a function of angle. In this way the constants k_1 and k_2 of the effective cooling velocity were obtained from

$$k_1 = \frac{1}{\sin\beta}\left\{\left[\frac{E(\beta)^2 - A}{E(0)^2 - A}\right]^{\frac{2}{n}} - \cos^2\beta\right\}^{\frac{1}{2}}$$

$$k_2 = \frac{1}{\sin\theta}\left\{\left[\frac{E(\theta)^2 - A}{E(0)^2 - A}\right]^{\frac{2}{n}} - \cos^2\theta\right\}^{\frac{1}{2}} \qquad (3A.4)$$

JORGENSEN(1971) and ACRIVLELLIS(1978) found that when the pitch factor k_2 corrections are neglected errors on U(0) between 5 to 12% occur. By using k_2, errors on U(0) are reduced to between 1-2%. The factor k_1 was found to vary with the angle and it was recommend to use the value for k_1 obtained when β =90 degrees; this results in errors on U(0) from 4% to 10%.

The hot-wire anemometer output was also a function of the fluid temperature; therefore any change in the ambient temperature conditions affected the heat loss from the wire and the calibration curve.

Assuming that the zero flow voltage output and β in equation 3A.1 varies linearly with the difference between the wire and ambient temperature, consider two cases, one at the calibration temperature T_{cal}, and the other at

some arbitrary temperature T_1, with a velocity identical in each case. The ratio between the two hot-wire outputs can be written, following WOOD(1981), KOCH et al(1972) and BEARMAN(1971) as

$$\left(\frac{E_1}{E_{cal}}\right)^2 = 1 + \frac{G}{\alpha_h} \qquad (3A.5)$$

where α_h is the overheat ratio at calibration.

and $G = \frac{T_1 - T_{cal}}{T_{cal}}$

With a knowledge of the temperature and the overheat ratio at calibration the calibration coefficients at any other temperature can be obtained.

3A.2.1 Calibration rig and calibration procedure.

A calibration rig as shown in fig. 3A.3 was used to calibrate the hot-wires. The calibration rig was an open nozzle type and the air velocity, over a range of approximately 1-75 m/sec, was measured with a pitot tube. An experimental investigation of the calibration rig indicated that the hot wire probe and pitot tube could be positioned up to 50 mm from the nozzle and 25 mm either side of the centre of the discharge. In these positions the hot-wire and pitot tube observed the same magnitude of velocity.

Before starting the calibration procedure two further steps had to be taken.

1) The system had to be compensated for the cable resistance by using a P.S.I. shorting probe.

2) The cold resistance of the wire R_c was measured using the decade resistance setting on the anemometer, and the running resistance calculated from the overheat ratio which was generally chosen as 0.8.

$$R = R_c (1+\alpha_h)$$

The calibration of a single probe required that the probe be set at a series of angles, approximately ± 70 degrees from the flow direction, for a series of velocities, for the direction coefficients to be found. This was done by using a rotary table in front of the nozzle. The calibration procedure was then:

1) The probe was turned until it was locanded normal to the flow direction and the mean maximum output recorded. The nominal zero flow voltage E_0 was also observed.

2) Generally approximately 30 points were taken in order to establish the calibration curve in the velocity range of the rig.

3) The probe was rotated to several angular positions in order to measure data for the calculation of the direction coefficients. Two tunnel speeds of approximately 10 and 30 m/sec were used , but the

calibration was found to be independent of the air velocity.

All the information was recorded on a tape in terms of left and right side of equation 3A.3, and used later as a data based for obtaining the velocity during the experimental tests.

3A.3 ANALYSIS OF TURBULENT FLOW.

Equation 3A.2 would still be valid if it included the fluctuating parts of all the velocities. The wire was placed in the X,Y plane, as seen in fig. 3A.4, and β is the angle between the mean flow direction and the normal to the wire, the velocity components of equation 3A.2 can then be written as

$$U_x = \left[(U+u_x)\cos\beta + u_y \sin\beta\right]$$

$$U_y = -(U+u_x)\sin\beta + u_y \cos\beta \qquad (3A.6)$$

$$U_z = u_z$$

The response equation which relates the hot-wire electrical signal to the velocity component is

$$\frac{E}{S} = \left\{\left[(U+u_x)\cos\beta + u_y \sin\beta\right]^2 + k_1^2\left[(U+u_x)\sin\beta + u_y\cos\beta\right]^2\right\}^{\frac{1}{n}} \qquad (3A.7)$$

where

$$S = \frac{1}{m}\left(\frac{E}{E^2-(0.92E_0)^2}\right)$$

SAUSTSUP(1973), ACRIVLELLIS(1977) showed by series expanding the right hand side of equation 3A.7 and introducing the mean square voltage output

$$\overline{\ell^2} = \overline{(E-\bar{E})^2}$$

that the mean output voltage E is given by

$$\frac{\bar{E}(\beta)}{S} = \overline{U}\cos\beta\left\{1+\frac{k_1^2}{2}\tan\beta\left[1+\left(2+\frac{1}{\tan\beta}+\tan^2\beta\right)\frac{\overline{u_y^2}}{U^2}\right]+\right.$$
$$\left.\frac{k_2^2}{2\cos^2\beta}\left[\frac{\overline{u_z^2}}{U^2}-\frac{\overline{u_x u_z^2}}{U^3}-\frac{\overline{u_y u_z^2}}{U^3}\tan\beta+\ldots\right]\right\} \qquad (3A.8)$$

and the root mean square output $\overline{e}^2$ is

$$\frac{\bar{\ell}^2}{S^2}(\beta) = \cos^2\beta\left\{\overline{u_x^2}\left(1+k_1^2\tan^2\beta+2\overline{u_x u_y}\tan\beta\,(1-k_1^2)\right.\right.$$
$$\left.\left.+\overline{u_y^2}\tan^2\beta\left[1-2k_1^2\left(1+\frac{\tan^2\beta}{2}\right)\right]\right\}$$

Neglecting all the third order terms from the equations U, $\bar{u}_x$, $\bar{u}_y$ and $\overline{u_x u_y}$ can be obtained directly from $\overline{E}$ and $\overline{e}^2$ for any given angle.

The same procedure can be applied in the X, Z plane to obtain $\bar{u}_z$.

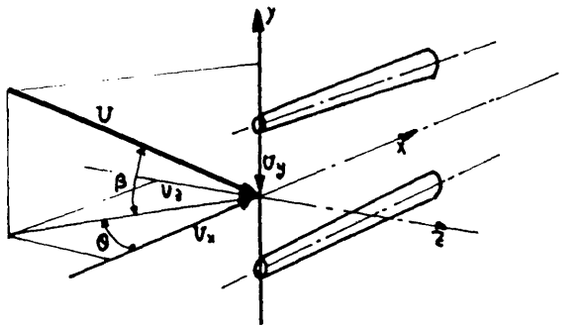

FIGURE 3A.1: General co-ordinate system for the hot-wire anemometer.

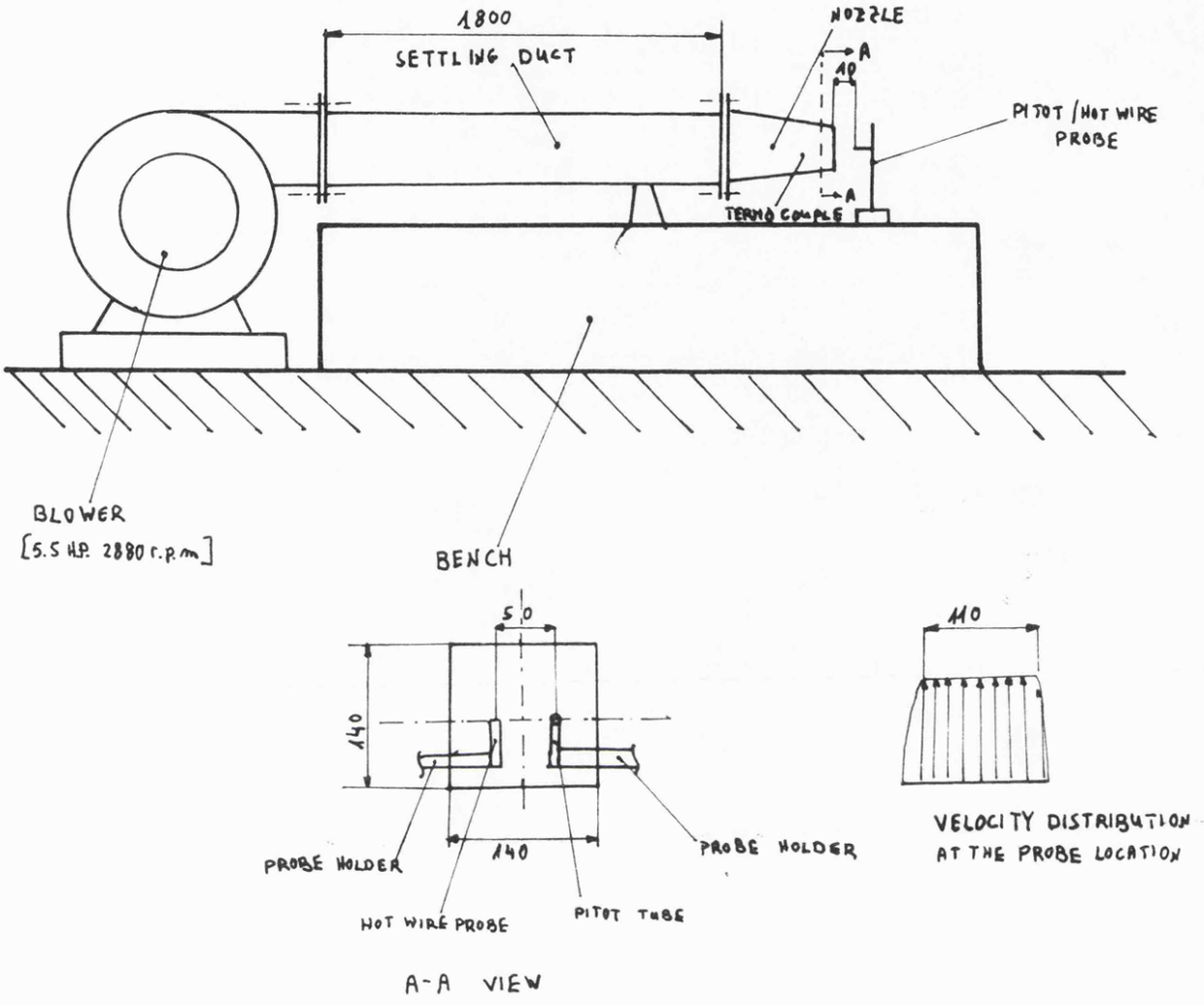

FIGURE 3A.2: Calibration rig.

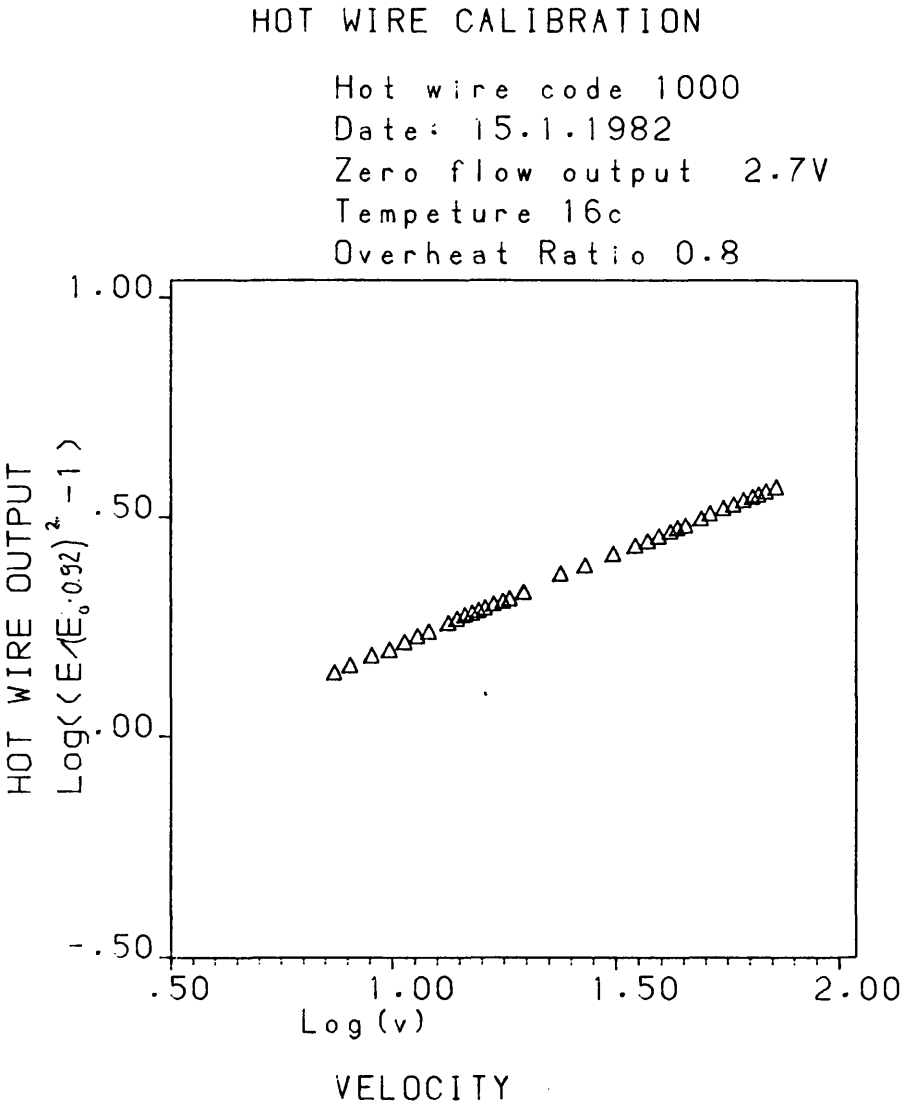

FIGURE 3A.3: Hot-wire calibration curve.

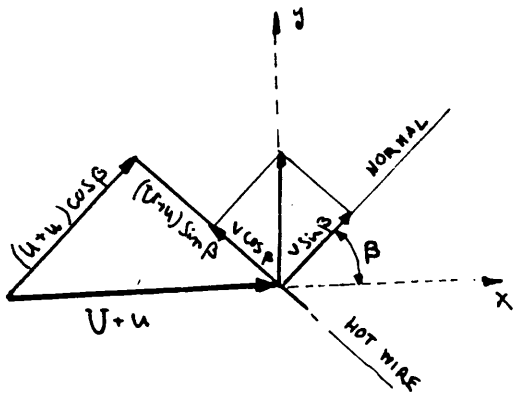

FIGURE 3A.4: Definition of velocity vectors.